Atomic-level understanding of co-based catalysts for CO preferential oxidation in H2-rich feedstock

Liping Zhong

UNIVERSITÉ DE STRASBOURG

ÉCOLE DOCTORALE DES SCIENCES CHIMIQUES
Institut de chimie et procédés pour l'énergie l'environnement et la santé (ICPEES)

THÈSE

présentée par :

Liping ZHONG

soutenue le : 15 **Décembre 2020**

pour obtenir le grade de : **Docteur de l'université de Strasbourg**

Discipline/ Spécialité : Chimie/Chimie Physique

Atomic-level understanding of Co-based catalysts for CO preferential oxidation in H_2-rich feedstock

Compréhension à l'échelle atomique du fonctionnement des catalyseurs à base de Co pour l'oxydation préférentielle du CO en milieu riche en H_2

THÈSE dirigée par :

[M. ZAFEIRATOS Spyridon]	Directeur de recherches, Université de Strasbourg

RAPPORTEURS :

[Mme. BERLIER Gloria]	Professeur, University of Turin, Turin
[M. BION Nicolas]	Chargé de recherches, Université de Poitiers, Poitiers

AUTRES MEMBRES DU JURY :

[M. CENTI Gabriele]	Professeur, University of Messina, Messina
[Mme. ROGER Anne-Cécile]	Professeur, Université de Strasbourg, Strasbourg
[M. TESCHNER Detre]	Max Plank Society Research Fellow, Fritz-Haber-Institut, Berlin
[M. VAJDA Stefan]	Professeur, Czech Academy of Science, Prague

Liping ZHONG

Compréhension à l'échelle atomique du fonctionnement des catalyseurs à base de Co pour l'oxydation préférentielle du CO en milieu riche en H_2

Résumé

Les performances d'un catalyseur sont connues pour être influencées par plusieurs facteurs, l'état d'oxydation de surface étant l'un des plus importants. Les catalyseurs à base de cobalt, qui apparaissent comme des matériaux prometteurs pour la réaction d'oxydation préférentielle du monoxyde de carbone dans un mélange riche en hydrogène (COPrOx), font cependant l'objet d'un débat intense ., au sujet de l'état d'oxydation de leurs sites actifs durant la réaction. Dans cette thèse, nous avons utilisé la technique de NAP-XPS en *operando* combinée avec d'autres méthodes de caractérisations *in* et *ex situ* pour corréler l'activité COPrOx à l'état d'oxydation du cobalt. Sur la base des résultats de NAP-XPS et NEXAF, CoO a été identifiée comme la phase optimale pour la COPrOx, tandis que les premiers calculs modélisation ont permis d'expliquer cettedécouverte. Il a également été noté que CoO est métastable et s'oxyde rapidement dans des conditions COPrOx conduisant à la désactivation du catalyseur.

Mots clés: Co_3O_4, CoO, NAP-XPS *in situ*, NEXAF *in situ*, oxydation préférentielle du CO, vanadium, manganèse, DRIFT *operando, pression atmosphérique NEXAFS, operando, site actif*

Résumé en anglais

Catalytic performance is known to be influenced by several factors, with the catalysts' surface oxidation state being the most prominent of all. Cobalt appears as one of the most promising materials for preferential oxidation of carbon monoxide in hydrogen rich mixtures (COPrOx). However, the oxidation state of the active sites on cobalt-based catalysts for COPrOx is a subject of intense debate. In this thesis, we use operando NAP-XPS and NEXAFS combined with DFT and other in situ and ex situ characterization methods to correlate COPrOx activity and cobalt oxidation state. Based on NAP-XPS and NEXAFs results, we identified CoO as the optimum cobalt oxidation state, while first principal calculations provided a rational explanation of this finding. We also noted that CoO is metastable and oxidizes fast under COPrOx conditions leading to catalyst deactivation.

Keywords: **Co_3O_4, CoO, in situ NAP-XPS, in situ NEXAFs, CO preferential oxidation, vanadium, manganese, active site, operando DRIFTs, atmospheric pressure NEXAFS, operando, active site**

Acknowledgement

The first person I would like to acknowledge is definitely my supervisor **Dr. Zafeiratos.** Although I'm afraid that I cannot express only with simple letters how grateful I am to him, I would still try my best to express my gratitude towards him. **Dr. Zafeiratos** has not only supervised my PhD work but also created more choices of my life. His professional attitude and abundant knowledge in science is the best example for my scientific career. He always believes in me and encourages me when I don't have faith into myself. Most importantly, he is always there to support me and answer my questions. I don't remember how many times I have knocked the door of his office, but I will never forget each of his smiles to me when I stepped into the office. Except for the support with work, his enthusiasm for life always reminds me to cherish every moment of life. For me, he is exactly the person we call "贵人" in Chinese, which means one of the most precious people in your life. However, except the gratitude to him, I'm also very sorry to him about my bad English writing. I cannot imagine how much he has suffered from my publications and final thesis. In a word, I cannot have an entire "thesis" with his corrections nor finish my PhD without his supports and efforts.

The second person whom I would like to thank is Alain. He is always so patient to help me resolve any technical problems I had in ICPEES and improve my French at the same time. Thanks to him and other people(**Domnique, Thierry, Michèle** and **Sécou** et al), I have enjoyed my work and life in this institute. In addition to them, I must thank **Vaso**, she is always being there to support me with her magic hands to deal with the problems in the lab. Moreover, she also helps me resolve the problems happened out of the lab.

Special thanks to the scientists **Dr. Michael Hävecker** and **Dr. Detre Teschner** in Fritz Haber Institute for their help with the NAP-XPS measurement and data analysis.

I'm also very grateful to my colleague/friend **Dr. Mathias Barreau**. He always encouraged me and listened to me when I'm anxious about the work. More importantly, he has helped me with a lot of things: correcting my writing, experiments, analysis and even eating the food I couldn't finish . I feel so lucky to have him in our team during my last year.

I would like to express my gratitude to my friends in Strasbourg: **Lulu, Maria, Kai, Xiong, Jiang and Yuhan**. We have spent great time together during last years.

Last but not least, I have to thank my boyfriend **Erwan Jubault** for his tremendous supports for all these years.

Table of content

List of Figures

List of Tables

Résumé

1) Introduction

L'oxydation préférentielle du monoxyde de carbone (COPrOx) est l'une des méthodes les plus simples et les plus efficaces pour l'élimination du monoxyde de carbone (CO) résiduel de l'hydrogène utilisé pour l'alimentation des piles à combustible à membrane échangeuse de protons (PEMFC). Un catalyseur PrOx idéal doit être très sélectif vis-à-vis de l'oxydation du CO, tout en évitant les réactions d'oxydation de H_2 et de méthanation du CO.[1] Parmi les catalyseurs PrOx rapportés, les catalyseurs à base de cobalt et de cuivre sont considérés comme des alternatives aux catalyseurs à base de métaux précieux (métaux du groupe du platine, PGM). Les catalyseurs à base d'oxyde de cobalt, actifs à très basse température (dès -77 °C) pour l'oxydation du CO,[2] sont considérés comme les catalyseurs COPrOx les plus prometteurs. Malgré l'évaluation de nombreuses formulations de matériaux dans la littérature (nanostructures Co_3O_4 de diverses morphologies,[3] oxydes de cobalt promus,[4] catalyseurs cobalt supportés) les catalyseurs à base de cobalt ne répondent pas encore aux exigences d'un catalyseur COPrOx efficace. Des inconvénients tels que la température élevée de début d'oxydation du CO dans un milieu riche en H_2, la possible méthanation du CO à température plus élevée et la désactivation rapide du catalyseur nuisent à leurs performances. Pour résoudre ces problèmes, la compréhension des mécanismes fondamentaux, tels que la phase active réelle du catalyseur et les interactions à l'interface entre le cobalt et son promoteur ou support, sont inévitablement nécessaires.

Dans le but de concevoir des catalyseurs à base de cobalt efficaces, il est essentiel d'identifier la phase la plus active du cobalt lors de la COPrOx. Dans la majorité des études, le Co_3O_4 est considéré comme la phase active [5]. Ce résultat est étayé par de récentes études de surface *in situ* montrant que le Co_3O_4 est stable en milieu réducteur COPrOx.[6] Au contraire, d'autres études ont montré que le Co_3O_4 réduit en monoxyde de cobalt (CoO) se révèle plus actif pour l'oxydation du CO.[7,8] Par ailleurs, d'autres études *in situ* ont montré que l'état de surface du cobalt pendant la réaction était non stœchiométrique (de type Co_3O_{4-x}).[9] La réponse ambiguë sur la phase active est due à la difficulté de définir l'état d'oxydation de surface du catalyseur dans les conditions de réaction COPrOx. Dans ce contexte, le chapitre 3 a été consacré à la comparaison des performances en COPrOx des phases CoO et Co_3O_4 obtenues à partir d'un même matériaux (poudre de cobalt pure). De cette manière, nous nous sommes concentrés

sur l'activité intrinsèque des oxydes de cobalt tout en contournant les effets liés au support et/ou à la morphologie du catalyseur. L'originalité de ces travaux réside également dans l'utilisation de la spectroscopie *operando* en complément de la caractérisation standard du matériau, permettant le suivi de l'évolution du matériau en conditions réactives.

Parmi les catalyseurs à base de cobalt prometteurs signalés, le système Co–Mn a montré une meilleure activité pour l'oxydation du CO par rapport aux oxydes de cobalt simples.[10,11] Notamment, le système Mn-Co-O a montré une excellente activité et stabilité en COPrOx.[12] Dans le but d'optimiser davantage la réactivité du système Co-Mn, il est essentiel de comprendre les interactions entre Co, Mn et les réactifs. L'étude de catalyseurs mixtes Co-Mn fait donc l'objet du quatrième chapitre, notamment *via* le suivi de l'évolution de l'état d'oxydation du manganèse et son effet sur le cobalt en conditions réactives.

Dans le chapitre 3, la spectroscopie photoémission à pression proche de l'ambiante (NAP-XPS) a révélé que la phase optimale de CoO est radicalement transformée, conduisant à la diminution de l'activité et à une mauvaise stabilité. En général, les ions métalliques à valence variable sont considérés comme des modificateurs actifs qui peuvent régler la liaison chimique ou l'état de surface des catalyseurs à oxyde métallique. Ainsi, dans le cinquième chapitre, nous nous sommes concentrés sur l'amélioration de la stabilité de la phase CoO pendant la réaction de COPrOx. Dans cette étude, le vanadium, qui a des états d'oxydation nombreux,[13] a été additionné à des nanoparticules de CoO commerciales. Les oxydes de CoO promus par V ont ensuite été évalués pour la réaction de COPrOx après un prétraitement réducteur. Après comparaison des performances catalytiques de catalyseurs simples Co et mixtes Co-V, les interactions entre V et les nanoparticules de cobalt réduites ont été élucidées par une série de caractérisations *ex situ* et *in situ*.

2) Résultats et discussions

a. La définition de la phase active optimale des catalyseurs à base d'oxydes de cobalt pour la COPrOx.

Dans le chapitre 3, nous comparons directement CoO et Co_3O_4 pour la COPrOx en utilisant la même poudre d'oxyde de cobalt non supportée après des prétraitements en milieu oxydant et réducteur. Les tests catalytiques démontrent que le Co pré-réduit (PreH_2-Co) présente une conversion de CO beaucoup plus élevée que le cobalt pré-oxydé (PreO_2-Co). L'activité spécifique de surface de deux catalyseurs au cobalt est représentée sur la Figure 1. A 200 °C,

l'activité spécifique du $PreH_2$-Co se révèle être environ 8 fois plus élevée que celle mesurée pour le $PreO_2$-Co. Lorsque la température de réaction augmente au-dessus de 250 °C, l'activité du $PreH_2$-Co est stabilisée, provoquant des activités spécifiques similaires pour les deux catalyseurs. De la même manière, le $PreH_2$-Co montre également une meilleure sélectivité envers de l'O_2 consommé par l'oxydation du CO.

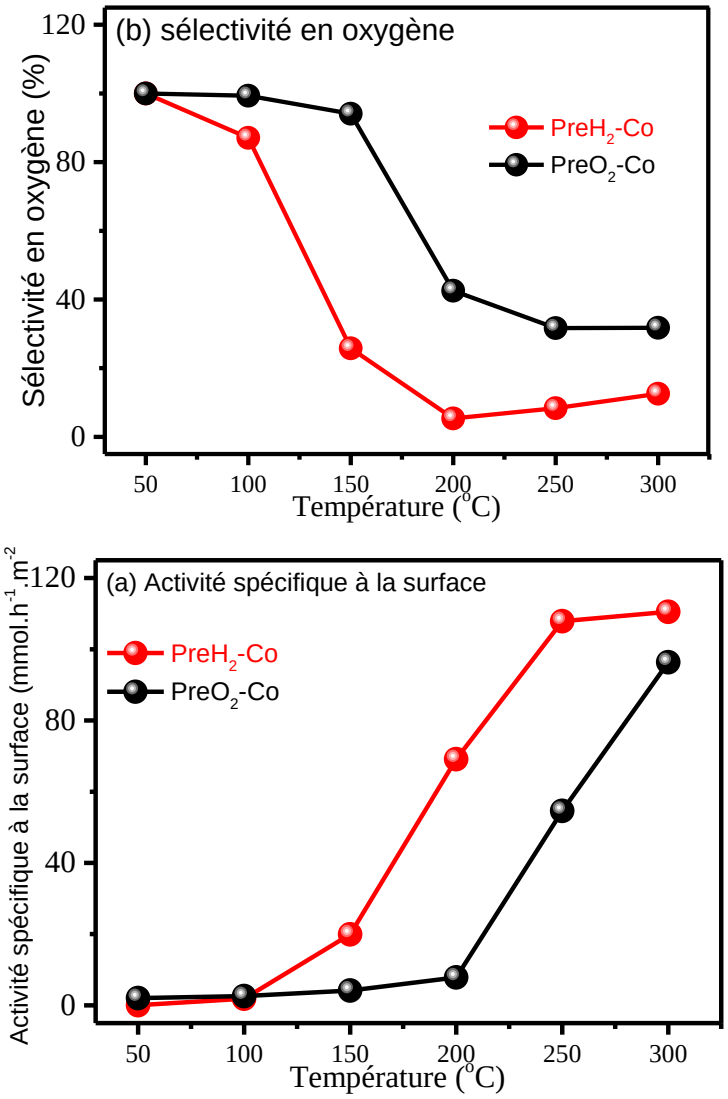

Figure 1. a) Activité spécifique de surface ou quantité de CO convertie par surface en mmol h^{-1} m^{-2} et b) Sélectivité O_2 en CO_2 pour $PreO_2$-Co et $PreH_2$-Co en fonction des mesures de chromatographie en phase gazeuse (GC) en fonction de la température.

Les images de la microscopie électronique à balayage (MEB) et microscope électronique en transmission (MET) démontrent que les différents prétraitements entraînent de petits changements sur la structure et la morphologie des particules de cobalt. Cependant, les

résultats de la caractérisation diffractométrie de rayons X (DRX) indiquent que la question de la phase active de $PreH_2$-Co pendant la réaction est ambiguë. Par exemple, le diffractogramme du $PreH_2$-Co usé est révèle la présence de pics de diffraction des phases CoO et Co_3O_4,[14] suggérant que la structure de cobalt est affectée par le prétraitement H_2 et oxydée davantage pendant la réaction COPrOx. Pour définir la phase active réelle du cobalt pendant la COPrOx, en particulier pour $PreH_2$-Co, des expériences synchrotron ont été réalisées en conditions réactives (P = 0,5 mbar). Comme présenté en Figure 2, l'étude *operando* de NAP-XPS illustre la prédominance de la phase CoO en surface du catalyseur $PreH_2$-Co pendant la réaction de COPrOx, tandis que Co_3O_4 est confirmé comme étant la seule phase active de $PreO_2$-Co.

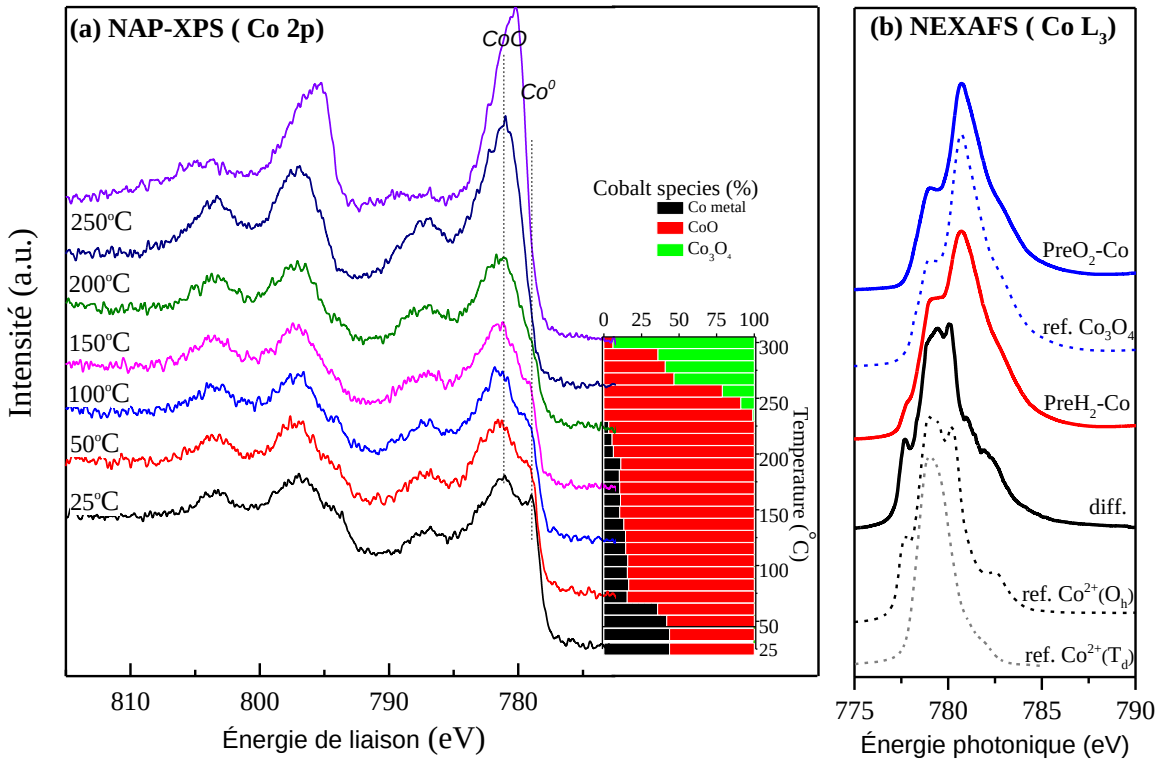

Figure 2. Spectres NAP-XPS *in situ* de Co 2p sur $PreH_2$-Co sous conditions de COPrOx à différentes températures sous 0.5 mbar. L'encart montre la distribution des phases de cobalt obtenues par déconvolution de pic de Co 2p. Conditions de réaction: 1% CO, 2% O_2 et 97% H_2 à 0,5 mbar avec une vitesse de montée en température de 5 ° C / min; avant la réaction, le cobalt a été réduit dans 1 mbar H2 à 400 oC pendant 30 min. b). Spectres NEXAFS in situ de $PreO_2$-Co et $PreH_2$-Co enregistrés à 300 ° C dans les conditions de réaction susmentionnées

Afin d'examiner l'effet de l'écart de pression entre les expériences spectroscopiques et catalytiques (0.5 mbar au lieu de 1 bar) sur la stabilité du CoO, la réaction COPrOx sur

PreH$_2$-Co a été réalisée à différents régimes de pression à l'aide d'un réacteur à pression variable. Les résultats obtenus fournissent des preuves solides en faveur d'un maintien de la phase CoO pendant la réaction de COPrOx à des températures d'environ 200 °C et des pressions de réaction réalistes. Au contraire, les mêmes expériences effectuées ont montré que seule la phase Co_3O_4 était détectée sur PreO$_2$-Co après réaction. Il est donc conclu que CoO est plus actif que Co_3O_4 pour la réaction de COPrOx. Le mécanisme de réaction impliquant ces deux phases a ensuite été élucidé par analyse infrarouge (DRIFTS) et calcul la théorie de la fonctionnelle de la densité (DFT).

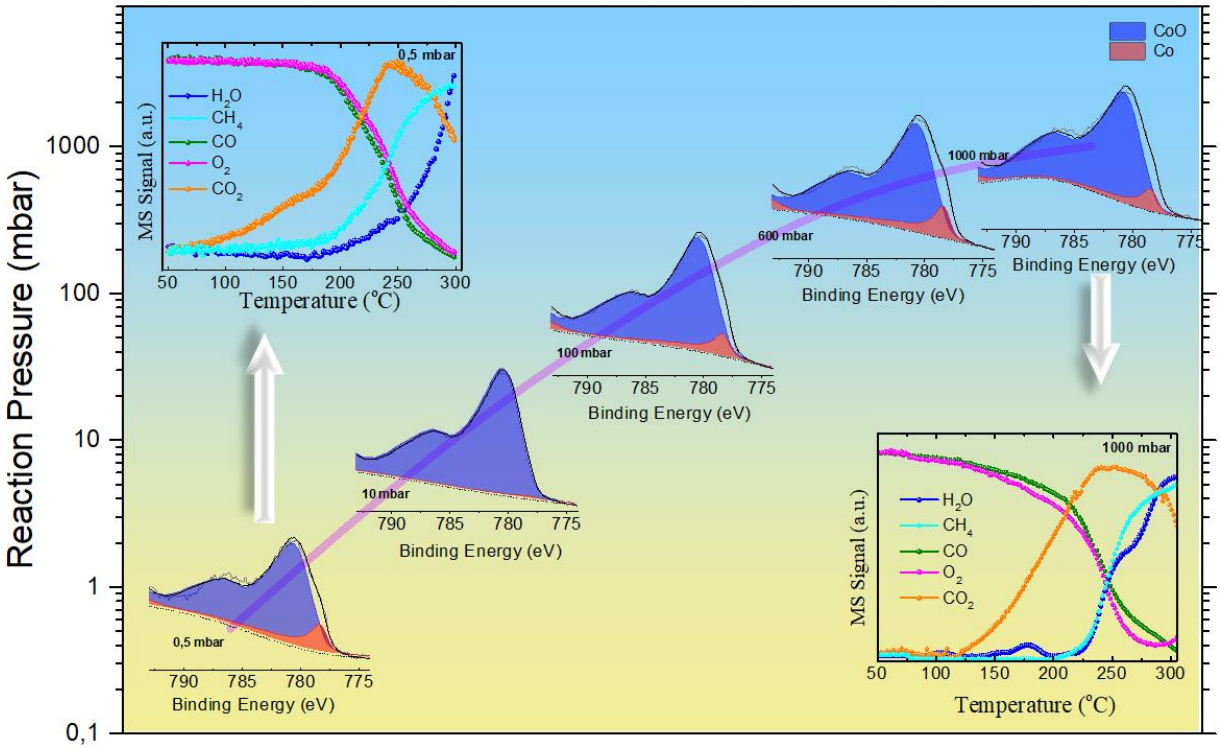

Figure 3. Les spectres XPS Co 2p$_{3/2}$ de PreH$_2$-Co mesurés après réaction COPrOx à 210 °C à différentes pressions totales. Le spectre Co 2p$_{3/2}$ à 0,5 mbar est NAP-XPS in situ, tandis que les spectres Co 2p$_{3/2}$ à pressions plus élevées ont été enregistrés ex situ après 30 min de réaction suivie d'une évacuation des réactifs et d'un transfert sous vide vers le spectromètre XPS. Les graphiques en médaillon montrent les données QMS correspondantes de la consommation de réactifs et des rendements en produits en fonction de la température de réaction enregistrée à 0,5 et 1000 mbar (la température de réaction dans ces expériences a été augmentée jusqu'à 300 °C)

b. L'effet promoteur du Mn sur CoO pour la réaction de COPrOx

Dans le chapitre 4, trois catalyseurs MnOx-CoOx non supportés ont été préparés avec différents pourcentages de Mn (0, 12,5 et 87,5 at.%) puis évalués par spectroscopie et méthodes de caractérisation standards. Les tests catalytiques montrent que la faible addition

de Mn au cobalt pur conduit à l'amélioration de sa réactivité vis-à-vis de l'oxydation du CO. Les profils de distribution des réactifs et des produits, suivis par analyse SM de la phase gazeuse à l'intérieur de la chambre de le spectrométrie photoélectronique X rayon (XPS), sont présentés sur la figure 4. Il est observé que la production de CH_4 est inhibée en présence de Mn, alors que l'oxydation du CO et l'oxydation H_2 sont favorisées.

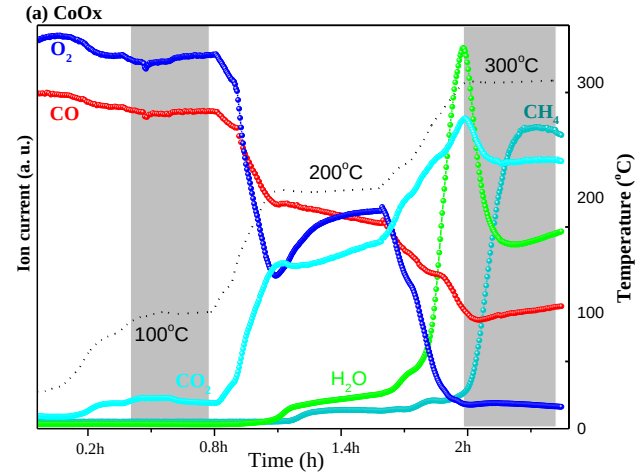
(a) CoOx
O2
CO
CO2
H2O
CH4
100°C
200°C
300°C
Ion current (a. u.)
Temperature (°C)
Time (h)
0.2h
0.8h
1.4h
2h
0
100
200
300

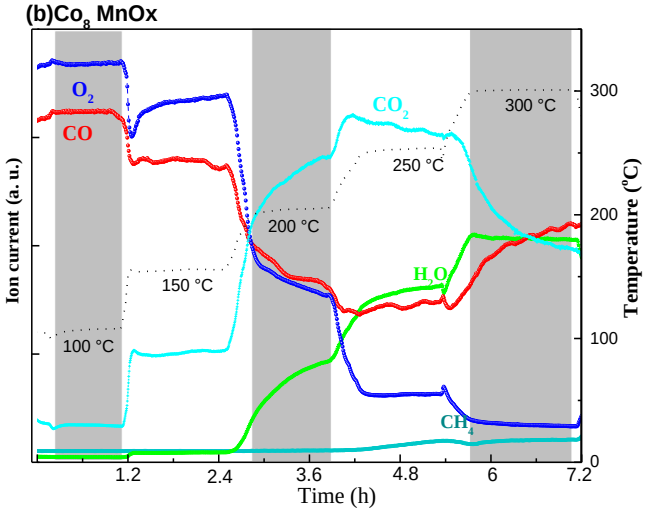
(b)Co8 MnOx
O2
CO
CO2
H2O
CH4
100 °C
150 °C
200 °C
250 °C
300 °C
Ion current (a. u.)
Temperature (°C)
Time (h)
1.2
2.4
3.6
4.8
6
7.2
0
100
200
300

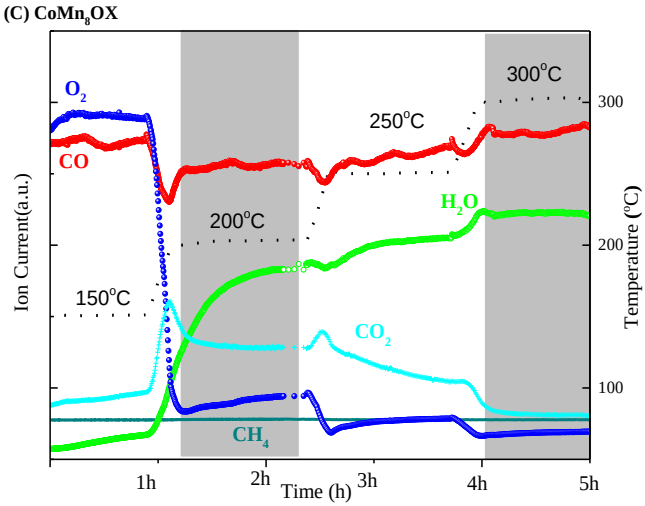
(C) CoMn8OX
O2
CO
CO2
H2O
CH4
150°C
200°C
250°C
300°C
Ion Current(a.u.)
Temperature (°C)
Time (h)
1h
2h
3h
4h
5h
100
200
300

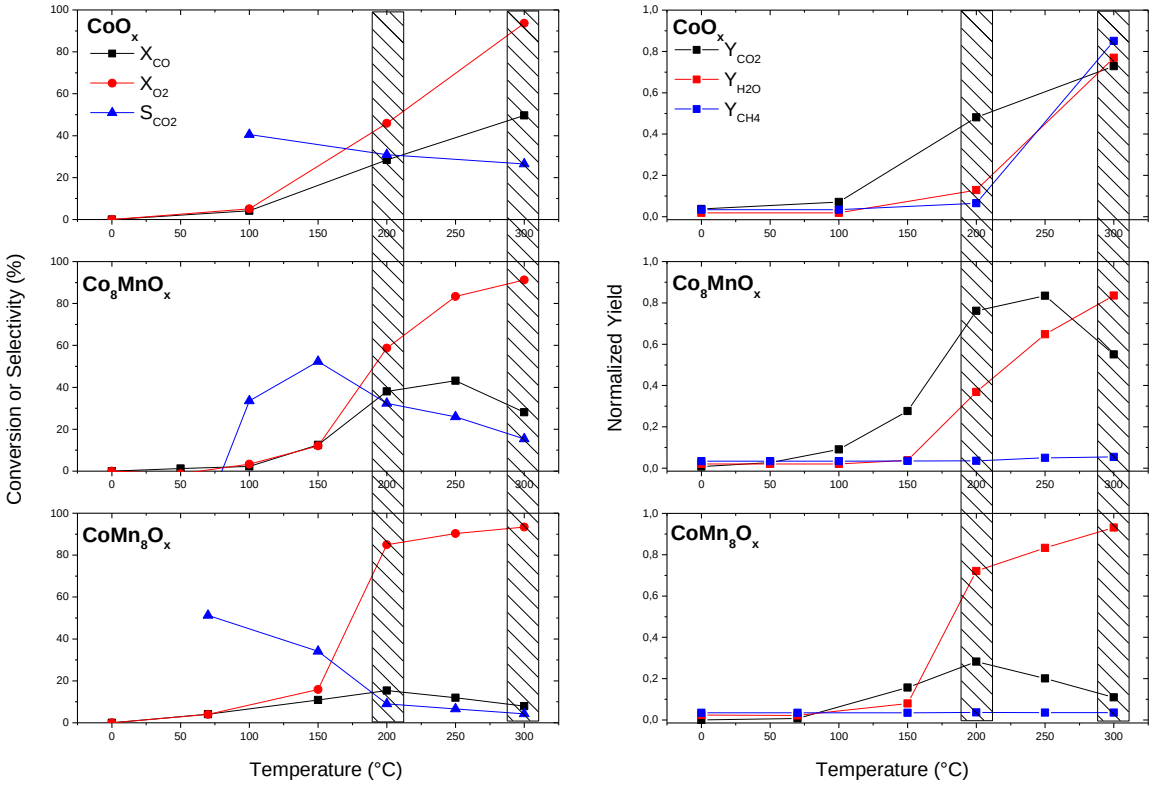

Figure 4. Données spectromètre de masse à quadrupôle(QMS) (a), (b), (c) des CoOx-MnOx. Conditions: 1 mbar de 1% CO, 1% O_2 et 98% H_2, plage de température entre 50 et 300 °C avec une vitesse de chauffe de 10 °C / min entre chaque étage de température. Avant les tests d'activité, les échantillons ont été prétraités dans la chambre XPS sous 1 mbar de H_2 à 400 °C pendant 1 h.

Dans la Figure 4 sont également présents les résultats de l'étude *operando* de NAP-XPS sur les catalyseurs mentionnés ci-dessus en conditions de COPrOx à 1 mbar. Les spectres XPS de Mn et Co correspondants indiquent l'évolution de leur état d'oxydation en fonction de la température au cours du COPrOx. (Figure 5) Après déconvolution des spectres correspondants, la distribution des différentes espèces de cobalt et de manganèse sur chaque catalyseur est clairement clarifiée. A basse température, le cobalt et le manganese se révèle être principalement présentes à l'état d'oxydation 2+. Le chauffage du catalyseur en condition de COPrOx entraîne alors l'oxydation du Mn^{2+} en Mn^{3+}, tandis que le Co^{2+} est relativement stable dans les mêmes conditions. Ce comportement d'oxydation du Mn se traduit par plus de production d'eau et de CO_2 par rapport à une seule phase Co^{2+} dans les mêmes conditions. En outre, une seconde étude spectroscopique basée sur le synchrotron a indiqué que l'état de coordination de Co^{2+}, Mn^{2+} et Mn^{3+} dans le système Co-Mn. Le

comportement de ségrégation du Co-Mn dans H_2 et pendant la COPrOx est défini par une analyse de profil en profondeur des spectres XPS.

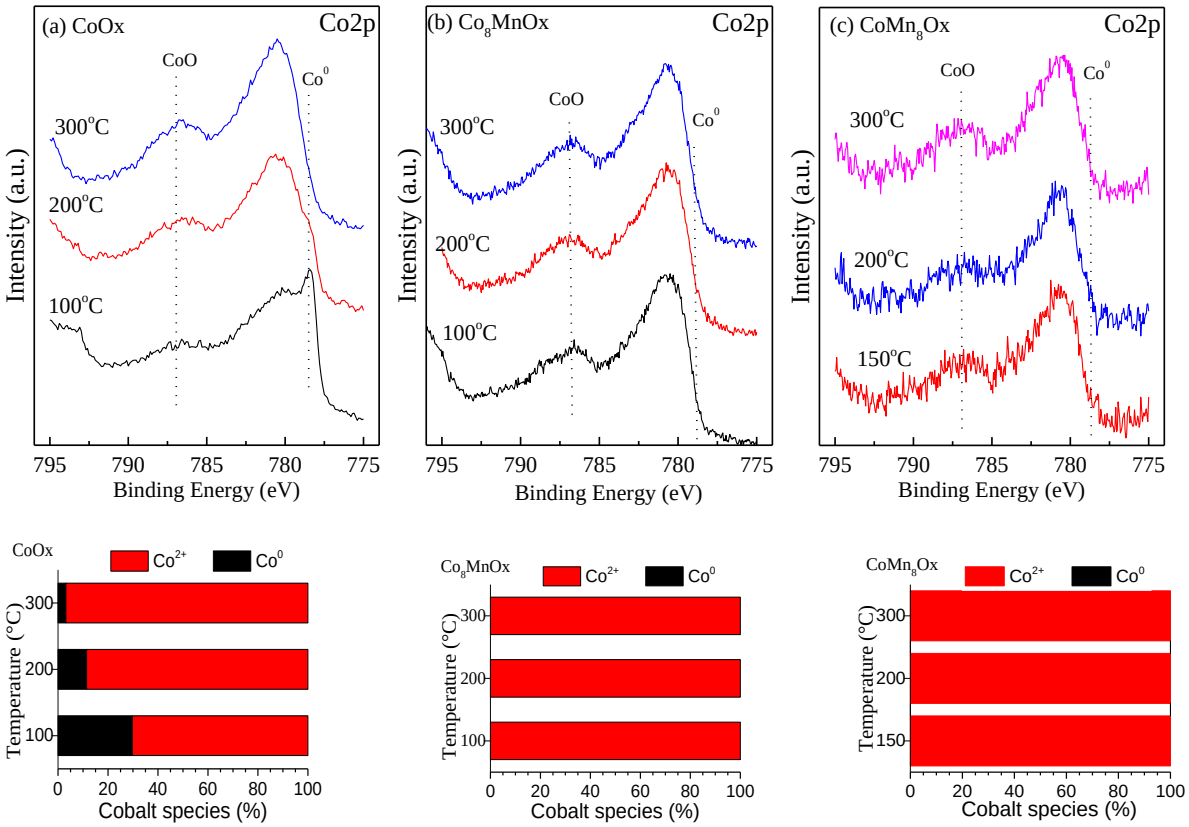

Spectres NAP-XPS in situ de Co $2p_{3/2}$ sur (a) CoOx pur, (b) Co_8MnOx et (c) $CoMn_8Ox$ enregistrés pendant COPrOx à différentes températures. Répartition des espèces de cobalt résultant de la déconvolution Co $2p_{3/2}$. Conditions de fonctionnement: 1 mbar de 1% CO, 1% O_2 et 98% H_2, de la température ambiante à 300 °C

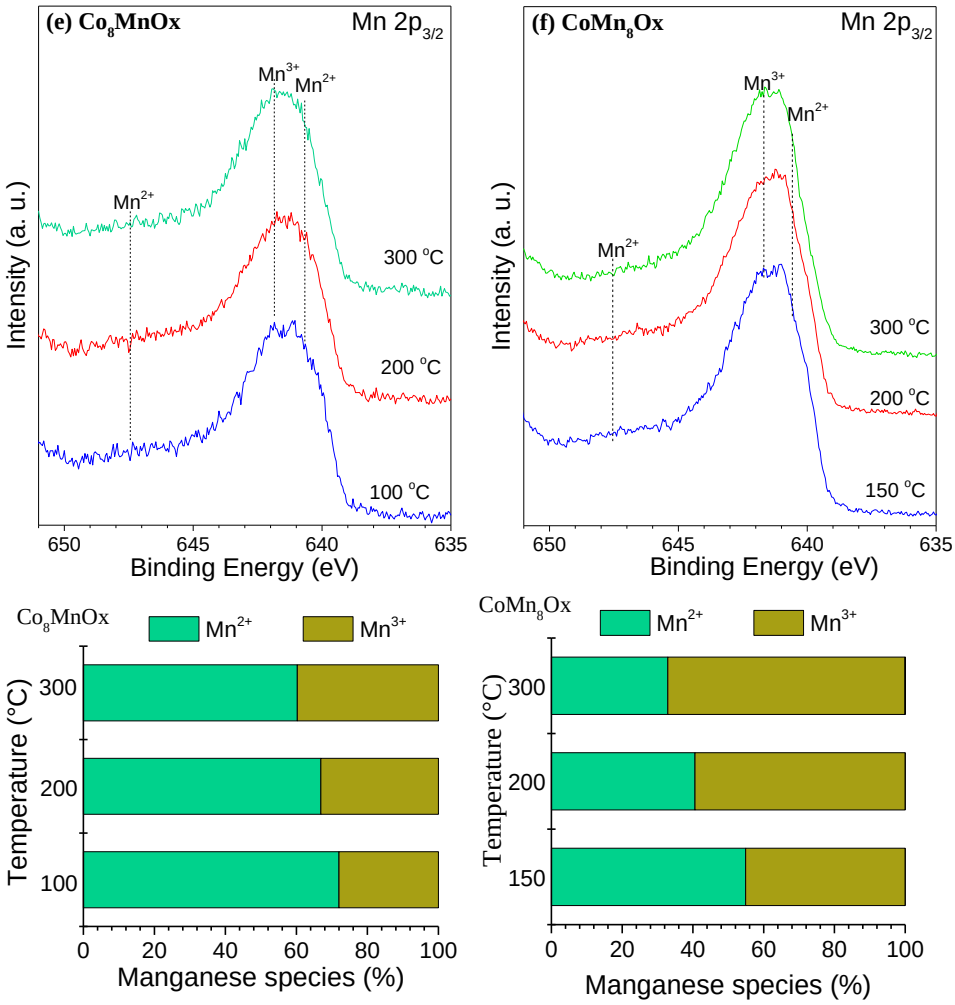

Figure 5. Les spectres XPS de Co $2p_{3/2}$ et Mn $2p_{3/2}$ de différents catalyseurs des Co-MnOx pendant la réaction COPrOx à 1 mbar.

c. La stabilisation de la phase CoO par incorporation de vanadium

Dans le chapitre 5, nous avons constaté que l'ajout de vanadium à l'oxyde de cobalt entraîne une amélioration significative des performances catalytiques en COPrOx. Comme le montre la figure 6, l'addition de vanadium à l'oxyde de cobalt donne un matériau avec une activité intrinsèque plus élevée en conversion de CO. Une analyse DRX après le prétraitement sous H_2 puis la réaction a montré que les catalyseurs CoO et $V_{0.125}$CoO contiennent tous deux la phase Co^0. Bien que la phase de vanadium ait été indistinctement observée par DRX, de la cartographie la spectroscopie de rayons X à dispersion d'énergie(EDS) a permis de mettre en évidence une dispersion homogène du vanadium dans les oxydes de cobalt. Les mesures de H_2-RTP ont ensuite permis de constater que la température de réduction des oxydes de cobalt était décalée vers de plus hautes températures, mettant en évidence une interaction forte entre

Co et V. Toutes les recherches sur la structure et la morphologie indiquent que le vanadium exerce son effet promotionnel comme une phase de surface amorphe plutôt que comme une phase cristalline.

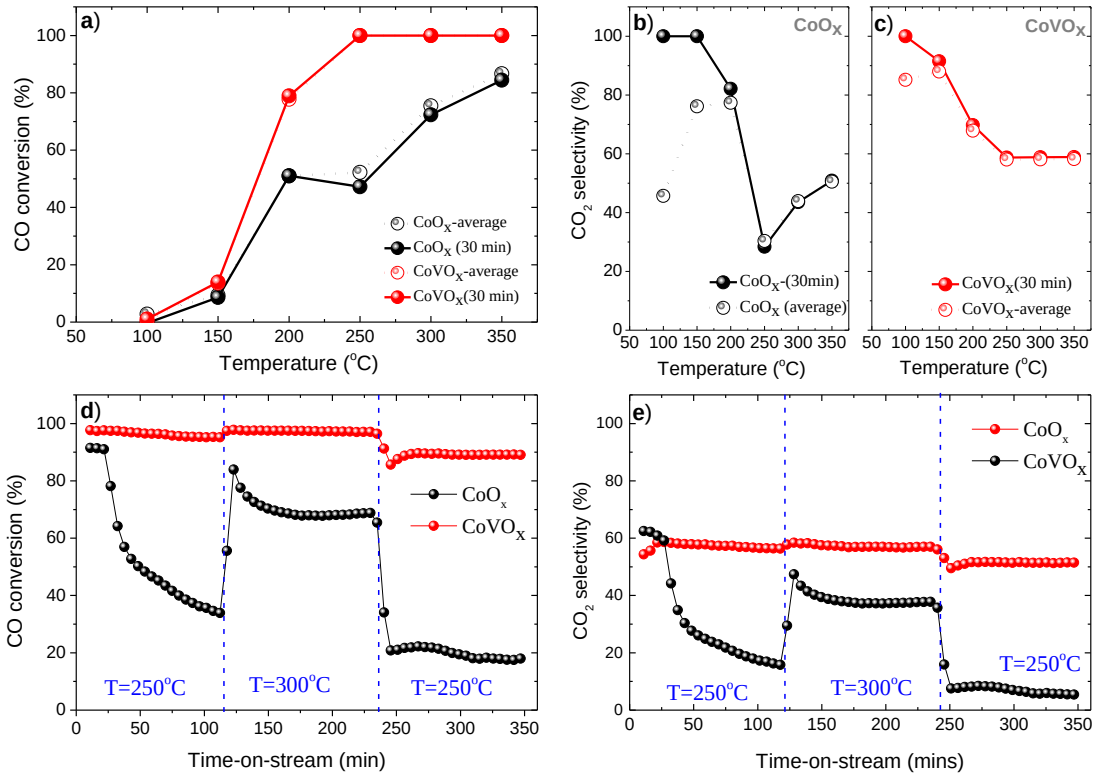

Figure 6. Tests de activité et durabilité des catalyseurs CoOx et CoVOx en fonction des mesures de chromatographie en phase gazeuse (GC) en fonction de la température en 1bar. (a) conversion du CO et (b) sélectivité du CO_2 en fonction de la température de réaction COPrOx. (c) conversion du CO et (d) sélectivité du CO_2 en fonction du temps de fonctionnement à 2 températures caractéristiques. Conditions expérimentales: 1% CO, 1% O_2 et 50% H_2 en débit He-équilibré; 50 mg de catalyseur; 50 ml / min de débit total à pression atmosphérique.

Une étude de XPS *in situ* a révélé que la phase active du cobalt modifié par V était composée de Co^{2+} et V^{5+}. La surface de cobalt du catalyseur sans V subit notamment une oxydation suivie d'une réduction, entraînant une déstabilisation de la phase Co^{2+}, tandis que la surface en cobalt du PreH_2-$V_{0.125}$CoO est plus stable, maintenant le Co^{2+} comme état d'oxydation de surface dominant. La présence de V^{5+} améliore considérablement la conversion du CO en améliorant donc la stabilité duCo^{2+} en surface. En complément, une analyse par spectroscopie d'adsorption des rayons X a directement mis en évidence la formation d'une phase de vanadate de cobalt amorphe (contenant V^{5+} et Co^{2+}) à la surface de $V_{0.125}$CoO. L'analyse *in situ* XPS de V 2p (figure 5a) illustre que le vanadate de cobalt formé est stable pendant la

COPrOx, fournissant ainsi une certaine quantité de Co^{2+} en position octaédrique. De plus, les résultats de la déconvolution démontrent que la phase de surface la plus élevée du cobalt se maintient sous forme de Co^{2+} octaédrique (figure 7c). Cela indique que la couverture de vanadate de cobalt sur la surface empêche l'oxydation / réduction supplémentaire de la phase Co^{2+} isolée en profondeur. Dans l'ensemble, la formation de vanadate de cobalt amorphe à la surface des nanoparticules de cobalt se traduit par plus de sites Co^{2+} octaédriques en surface du $V_{0.125}CoO$ comparé au CoO pur, améliorant ainsi l'activité de COPrOx.

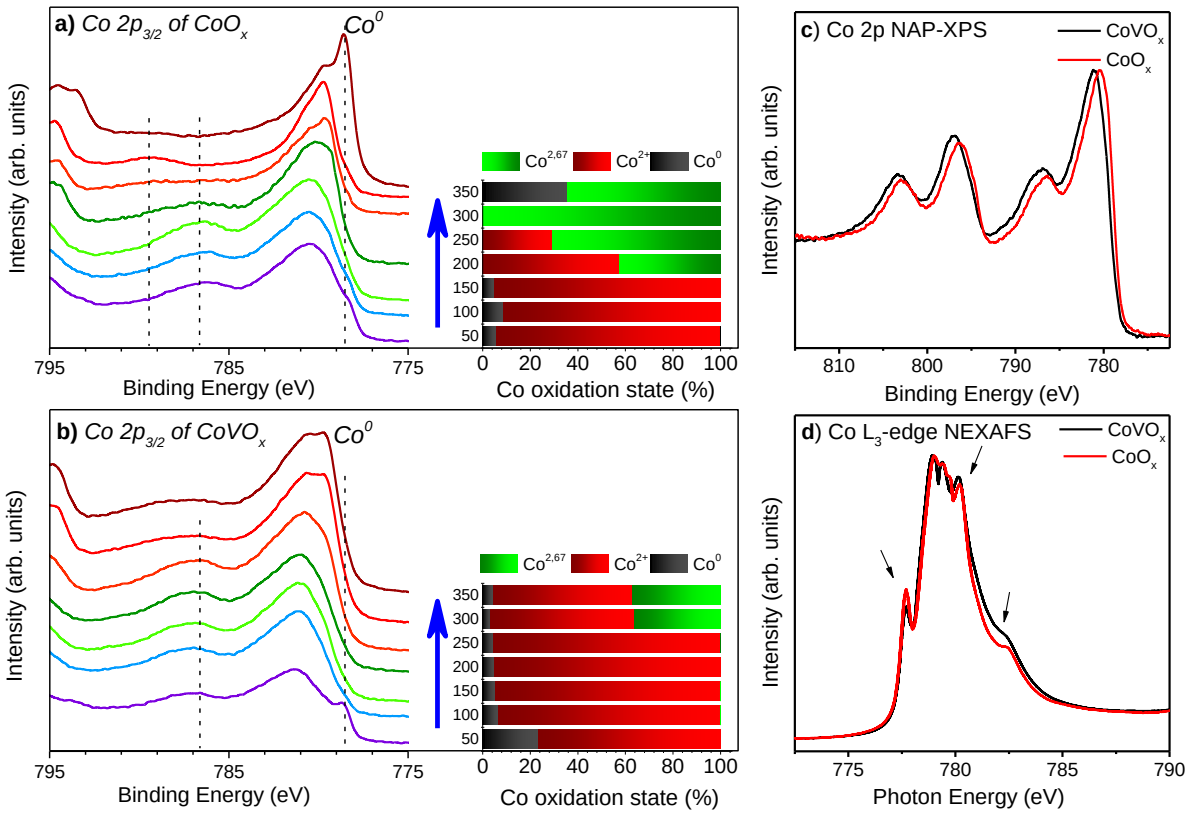

Figure 7. Spectres Operando NAP-XPS de Co 2p sur catalyseurs CoOx (a) et CoVOx (b) enregistrés à différentes températures pendant la réaction COPrOx: 1% CO, 1% O_2 et 50% H2 dans He, à une pression totale de 0.5 mbar. Chaque spectre a été enregistré après environ 10 minutes de réaction. La distribution des espèces de cobalt obtenues par déconvolution de pic de Co 2p est indiquée dans les graphiques à barres insérés. (c) Co 2p NAP-XPS et (d) Spectres NEXAFS de bord Co L_3 de catalyseurs CoOX et CoVOx dans des conditions qui favorisent la formation de l'état Co^{2+}, c'est-à-dire à 150 ° C dans un mélange COPrOx.

3) Conclusion générale

Les travaux de cette thèse ont été consacrés à la définition d'une phase active optimale à base de cobalt pour la COPrOx. Dans un premier temps, nous avons comparé directement l'activité des phases CoO et Co_3O_4 en combinant des méthodes analytiques *ex situ* et *operando* avec de

la modélisation moléculaire. Le CoO a été identifié comme la phase favorisant le plus le procédé COPrOx, fournissant un élément critique pour la conception rationnelle de catalyseurs COPrOx efficaces et durables. Le chapitre suivant a ensuite été consacré à la définition de la phase la plus active du système Co-Mn, qui est considérée comme le catalyseur COPrOx à base de cobalt le plus prometteur. Les résultats ont révélé que l'effet promotionnel du manganèse était fortement lié à son état d'oxydation. Même si plus d'espèces Co^{2+} sont formées à la surface de CoMn par rapport au cobalt pur en raison de la formation d'oxydes mixtes, la formation de Mn_2O_3 entrave la réactivité vis-à-vis de l'oxydation du CO en favorisant l'oxydation de H_2. La phase CoO-MnO a été identifiée comme la phase la plus active du système Co-Mn pour la réaction de COPrOx. Cependant, la stabilisation de CoO-MnO est également difficile. Ainsi, plus d'efforts ont été réalisés pour stabiliser la phase CoO dans les conditions de réaction. Dans ce contexte, le cobalt modifié au vanadium a démontré une excellente stabilité et réactivité vis-à-vis de l'oxydation du CO en milieu riche en hydrogène. Des 'études de XPS et de l'adsorption des rayons X (NEXAFs) *in situ* ont révélé que le vanadium se combine avec une certaine quantité de cobalt, formant une phase de vanadate de cobalt amorphe en surface du catalyseur. Cette phase est formée par la coordination des espèces V^{5+} et Co^{2+} octaédriques. Le vanadate de cobalt formé empêche non seulement l'oxydation ou la réduction des espèces Co^{2+}, mais fournit également une certaine quantité de sites Co^{2+} octaédriques actifs stables pour la COPrOx. Dans cette mesure, le système Co-V-O réduit peut être considéré comme un nouveau système prometteur pour la COPrOx.

References

(1) Bion, N.; Epron, F.; Moreno, M.; Mariño, F.; Duprez, D. Preferential Oxidation of Carbon Monoxide in the Presence of Hydrogen (PROX) over Noble Metals and Transition Metal Oxides: Advantages and Drawbacks. *Top. Catal.* **2008**, *51* (1–4), 76–88.

(2) Xie, X.; Li, Y.; Liu, Z. Q.; Haruta, M.; Shen, W. Low-Temperature Oxidation of CO Catalysed by Co_3O_4 Nanorods. *Nature* **2009**, *458* (7239), 746–749.

(3) Khasu, M.; Nyathi, T.; Morgan, D. J.; Hutchings, G. J.; Claeys, M.; Fischer, N. Co3O4 Morphology in the Preferential Oxidation of CO. *Catal. Sci. Technol.* **2017**, *7* (20), 4806–4817.

(4) Ma, L.; Seo, C. Y.; Chen, X.; Sun, K.; Schwank, J. W. Indium-Doped Co3O4nanorods for Catalytic Oxidation of CO and C3H6towards Diesel Exhaust. *Appl. Catal. B Environ.* **2018**, *222* (September 2017), 44–58.

(5) Bao, T.; Zhao, Z.; Dai, Y.; Lin, X.; Jin, R.; Wang, G.; Muhammad, T. Supported Co_3O_4-CeO_2 Catalysts on Modified Activated Carbon for CO Preferential Oxidation in H_2-Rich Gases. *Appl. Catal. B Environ.* **2012**, *119–120*, 62–73.

(6) Lukashuk, L.; Föttinger, K.; Kolar, E.; Rameshan, C.; Teschner, D.; Hävecker, M.; Knop-Gericke, A.; Yigit, N.; Li, H.; McDermott, E.; et al. Operando XAS and NAP-XPS Studies of Preferential CO Oxidation on Co_3O_4 and CeO_2 -Co_3O_4 Catalysts. *J. Catal.* **2016**, *344*, 1–15.

(7) Teng, Y.; Sakurai, H.; Ueda, A.; Kobayashi, T. Oxidative Removal of Co Contained in Hydrogen by Using Metal Oxide Catalysts. *Int. J. Hydrogen Energy* **1999**, *24* (4), 355–358.

(8) An, K.; Alayoglu, S.; Musselwhite, N.; Plamthottam, S.; Melaet, G.; Lindeman, A. E.; Somorjai, G. A. Enhanced CO Oxidation Rates at the Interface of Mesoporous Oxides and Pt Nanoparticles. *J. Am. Chem. Soc.* **2013**, *135* (44), 16689–16696.

(9) Nguyen, L.; Zhang, S.; Yoon, S. J.; Tao, F. F. Preferential Oxidation of CO in H_2 on Pure Co_3O_{4-x} and Pt/Co_3O_{4-X}. *ChemCatChem* **2015**, *7* (15), 2346–2353.

(10) Guo, Q.; Liu, Y. MnOx Modified Co_3O_4-CeO_2 Catalysts for the Preferential Oxidation of CO in H_2-Rich Gases. *Appl. Catal. B Environ.* **2008**, *82* (1–2), 19–26.

(11) Gómez-Cuaspud, J. A.; Schmal, M. Nanostructured Metal Oxides Obtained by Means Polymerization-Combustion at Low Temperature for CO Selective Oxidation. *Int. J. Hydrogen Energy* **2013**, *38* (18), 7458–7468.

(12) Zhao, Z.; Bao, T.; Li, Y.; Min, X.; Zhao, D.; Muhammad, T. The Supported CeO_2/Co_3O_4-MnO_2/CeO_2 catalyst on Activated Carbon Prepared by a Successive-Loading Approach with Superior Catalytic Activity and Selectivity for CO Preferential Oxidation in H_2-Rich Stream. *Catal. Commun.* **2014**, *48*, 24–28.

(13) Abbate, M.; Pen, H.; Czyzyk, M. T.; de Groot, F. M. F.; Fuggle, J. C.; Ma, Y. J.; Chen, C. T.; Sette, F.; Fujimori, A.; Ueda, Y.; et al. Soft X-Ray Absorption Spectroscopy of Vanadium Oxides. *J. Electron Spectros. Relat. Phenomena* **1993**, *62* (1–2), 185–195.

(14) Glaspell, G. P.; Jagodzinski, P. W.; Manivannan, A. Formation of Cobalt Nitrate Hydrate, Cobalt Oxide, and Cobalt Nanoparticles Using Laser Vaporization Controlled Condensation. *J. Phys. Chem. B* **2004**, *108* (28), 9604–9607.

Abstract

Catalytic performance is known to be influenced by several factors, with the catalysts' surface oxidation state being the most prominent of all. Cobalt appears as one of the most promising materials for preferential oxidation of carbon monoxide in hydrogen rich mixtures (COPrOx). However, the oxidation state of the active sites on cobalt-based catalysts for COPrOx is a subject of intense debate. In this thesis, we use operando NAP-XPS and NEXAFS combined with DFT and other in situ and ex situ characterization methods to correlate COPrOx activity and cobalt oxidation state. An important effort is devoted to evaluating the effect of the pressure gap between NAP-XPS measurements (0.5mbar) and realistic reaction conditions (1 bar). Moreover, the reactant residence time is found to play an essential role on the surface evolution of cobalt oxidation state. Based on NAP-XPS and NEXAFs results, we identified CoO as the optimum cobalt oxidation state, while first principal calculations provided a rational explanation of this finding. We also noted that CoO is metastable and oxidizes fast under COPrOx conditions leading to catalyst deactivation.

In the attempt to stabilize the CoO phase during COPrOx reaction, two promoted cobalt-based catalysts (CoMnOx and CoVOx) have been studied for CO oxidation in the presence of H_2. BET, H_2-TPR, electronic microscopy and XRD were used to investigate the effect of Mn and V promotion on structural and morphological properties of cobalt NPs, while in situ NAP-XPS and NEXAFS were applied for the identification of surface active phases of two promoted cobalt-based catalyst. In situ NAP-XPS demonstrated that Co^{2+} phase can be only partially stabilized in the presence of Mn. Operando NAP-XPS combined with mass spectrometry results over $CoMnO_x$ catalysts indicated that the addition of Mn does improvement the CO conversion on cobalt, but the transformation of Mn^{3+} to Mn^{2+} enhances the unwanted H_2 oxidation reaction. Similar study on Co_8VO_x catalyst for COPrOx reaction proved that the introduction of V into CoO NPs can stabilize the CoO phase under COPrOx gas environment, thus Co_8VO_x has exhibited remarkable improvements of reactivity and stability for COPrOx. Simulation of the NEXAFS results using multiplet calculations demonstrated that the distance of Co^{2+}-O is modified by the V, thus properly enhances the oxygen mobility on cobalt surface, leading to increase of the CO oxidation reactivity. Herein this thesis, we have firstly identified the optimum oxidation state of cobalt for CO conversion in H_2 feed stock and in a second step we tried to optimize the reactivity and stability of the most active phase via introduction of another component as a promoter.

Keywords: **Co_3O_4, CoO, in situ NAP-XPS, in situ NEXAFs, CO preferential oxidation, vanadium, manganese, operando DRIFTs, atmospheric pressure NEXAFS, operando**

Chapter 1

Literature Review

1.1 **Importance of CO preferential oxidation (COPrOx) for hydrogen purification**

Fossil fuels, which include coal, oil, and natural gas, supply about 80 percent[15] of the world's energy. When these non-renewable fuels, are burned, they release greenhouse gases (mainly carbon dioxide and methane), which in turn trap heat in our atmosphere, making them the primary contributors to global warming and climate change.[16] This fact has driven scientific community and governmental agencies to put an increasing attention to the development of environmentally friendly technologies for energy production. This combines, clean and renewable energy sources, to replace fossil fuels as well as energy conversion devices with high efficiency. In order to meet these requirements in transportation sector, automotive companies have developed new technologies and prototype vehicles adopting fuel cells to power the "zero emission" vehicles of the future. Fuel cells are currently one of the most promising energy conversion systems and are expected to play a key role in the energy transition process. A variety of fuel cell types for different applications has been developed, including proton-exchange membrane fuel cells (PEMFCS) operating at ~80^{o}C, alkaline fuel cells (AFC), operating at ~100^{o}C, phosphoric acid fuel cells (PAFCs) for ~200^{o}C operation, molten carbonate fuel cells (MCFC) at ~650^{o}C, solid oxide fuel cells (SOFC) for high temperature operation, 800-1100 ^{o}C, *etc.*.[17] Among them, PEM fuel cells, has been considered maybe as the most promising technology for future due to its advantages of low operating temperature, operation at high current density, potential for low cost and volume *etc*.. Moreover, PEM fuel cells using hydrogen fuel as energy carrier are becoming a competitive technology to batteries, for future electrical vehicles. This is because hydrogen used in fuel cells has energy to weight ratio that is ten times greater than lithium-ion batteries. Consequently, it offers much greater range while being lighter and occupying smaller volumes. It can also be recharged in a few minutes, similarly to gasoline vehicles. Recently, the application of PEM fuel cells has been significantly developed and demonstrated in fuel cell vehicles.[18]

PEMFC is an energy conversion device that directly converts chemical energy into electricity by an electrochemical reaction. The key component of a PEMFC is the membrane electrode assembly (MEA). MEA is composed of a proton exchange membrane (PEM)

placed between two electrodes (anode and cathode), as shown in **Figure 1-1.** The electrodes are typically made from a porous, electrically conducting carbon layer serving also as a high surface area support for the electro-catalyst. Hydrogen supplied at the anode is ionized into positively charged hydrogen ions (protons) and electrons in the presence of catalyst. The catalyst facilitates the electrochemical reactions and the adsorption of the reactant species. Electrons from the anode and protons that have crossed the membrane combine with oxygen at the cathode to form water that flows out of the fuel cell.

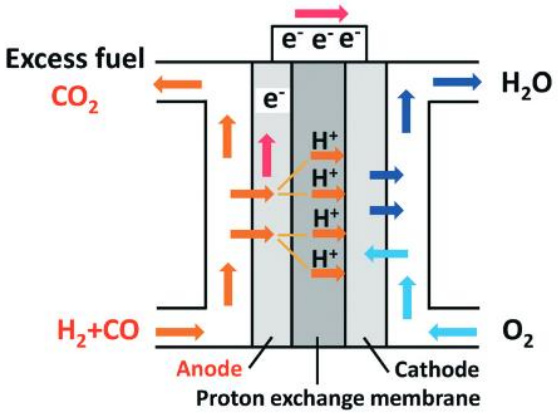

Figure 1-1. The reaction scheme of PEMFC. Taken from [19]

The electrocatalyst, typically platinum (Pt) or a Pt-based alloy (e.g. PtRu) and the membrane, usually a fluorocarbon-based polymer, are both sensitive to impurities that exist in the hydrogen fuel and oxidant feed streams.[20] As it is a transportable and storable zero-carbon-emission energy carrier, H_2 is the primary fuel for PEMFC applications.[21] Because of the rising demands of hydrogen, many technologies for hydrogen production has been developed, including steam methane reforming (SMR), partial oxidation processes including auto-thermal reforming (ATR) of methane and coal gasification. Due to excess of intermitted electricity produced by photovoltaics, water electrolysis is also considered as an alternative method for hydrogen production. Even though, hydrogen production from renewable sources is the choice of the future, currently the majority of hydrogen worldwide is produced by industry is based on catalytic steam reforming (SR) processes.[22] In the SR method hydrocarbons (mainly methane from natural gas feedstock), reacts with water vapors to produce syngas (hydrogen and carbon monoxide), according to the reaction: $CH_4 + H_2O \rightleftharpoons CO + 3H_2$. Inevitably H_2 obtained by the SR process contains carbon monoxide (CO), carbon

dioxide (CO_2) and methane (CH_4). Among them, carbon monoxide is the most critical impurity for PEMFC applications. This is because CO tends to adsorb onto the active sites of the platinum catalyst and to decrease the number of sites available for hydrogen adsorption blocking the electroxidation reaction.[23] 10 ppm of CO in the feed gas can deactivate the catalysts, decreasing fast the output voltage of the cell.[24] Undoubtedly, wide commercialization of PEM fuel cells demands of high durability of the electrocatalysts, therefore the elimination of CO in H_2 feed gas is significantly required.

The recommended CO content in H_2 feed gas for PEM fuel cells is less than 0.5 ppm.[25] This surges the development of diverse H_2-purification technologies. Membrane technology appears as an energy efficient solution for purifying H_2 required for fuel cells. However, the slow diffusion of the gases in the membrane barriers its industrial application.[21] Catalytic methanation of CO is considered as another alternative to remove traces of CO in H_2 at the very beginning of the purification procedure. Nickel based catalysts were the most effective catalysts for CO methanation but there are several bottlenecks to overcome including carbon formation which causes deactivation of catalyst due to coking.[26] Moreover, the use of Ni in mobile applications is considered a potential health hazard.[27] As a result, CO methanation is not viewed as a compatible method neither. Thus, CO preferential oxidation in the presence of H_2 (COPrOx) has been considered as the most straightforward and efficient approach to lower the CO level to meet the operational requirements of PEMFC.[19,28]

1.2 COPrOx catalysts

The origin of CO-PrOx reaction lies in the Haber–Bosch process, which is used for production of ammonia. As in the case of PEMFCs, the Haber–Bosch reaction has also a strict requirement of CO-free hydrogen, as CO is a strong catalyst poison for platinum-based catalysts used in this process. The reactions involved in the COPrOx process are described in the following list:

$$CO + 0.5O_2 \rightarrow CO_2;\ \Delta H^{\circ}_{298} = -283.6\ kJmol^{-1} \qquad \textbf{Eq. 1-1}$$

$$H_2 + 0.5O_2 \rightarrow H_2O;\ \Delta H^{\circ}_{298} = -243.5\ kJmol^{-1} \qquad \textbf{Eq. 1-2}$$

$$CO + 3H_2 \rightarrow CH_4 + H_2O;\ \Delta H^{\circ}_{298} = -206.2\ kJmol^{-1} \qquad \textbf{Eq. 1-3}$$

$$CO_2 + 4H_2 \rightarrow CH_4 + 2H_2O;\ \Delta H^{\circ}_{298} = -164.6 kJmol^{-1} \qquad \textbf{Eq. 1-4}$$

$$2CO \rightarrow C + CO_2;\ \Delta H^{\circ}_{298} = -172.3\ kJmol^{-1} \qquad \textbf{Eq. 1-5}$$

$$CO + 3H_2 \rightarrow CH_4 + H_2O;\ \Delta H^{\circ}_{298} = -41.4\ kJmol^{-1} \qquad \textbf{Eq. 1-6}$$

CO conversion to CO_2 (equation 1-1) at low temperature in the presence of H_2 is the target of COPrOx reaction. However, in addition to the desired reaction of CO oxidation, COPrOx involves undesired H_2 consumption because of H_2 oxidation and CO methanation depending the type of catalyst and the temperature. Herein, the two side reactions should be highly minimized to avoid the consumption of H_2. Moreover, the water produced from the two reactions is considered as a poison the catalysts.[10] Thus, a desirable COPrOx catalyst should be highly effective for CO conversion to CO_2 but inert for H_2 conversion and CO methanation. Since last century, considerable efforts have been invested into searching for efficient COPrOx catalysts.[7] To date, catalysts for COPrOx can be basically classified into noble metal-based catalysts and non-noble transition metal oxides.[1] The most active noble metal catalysts for COPrOx are Pt and Au. The effect of preparation method, morphology, structure, promoters and support on the catalytic performance of Pt and Au-based COPrOx catalysts have been thoroughly reviewed in the past. Herein, the next part summarizes the reports of CO preferential oxidation over noble and no-noble metal-based COPrOx catalysts.

1.2.1 Noble metal-based catalyst

Noble metal-based catalysts have attracted considerable attention for COPrOx due to their superior CO thermal oxidation activities. The noble metals in group VIII (Pt, Ir, Ru, and Rh) and group IB (Au and Ag) are considered as the most active catalysts for CO oxidation in the absence or presence of H_2.[29] Furthermore, their catalytic performance have been dramatically improved after supporting them on different oxides or combining them with another components. Among them, Au and Pt supported on different oxide carriers and combined with transition metals, they have shown impressive CO conversion even at room

temperature.[1]

1.2.1.1 Platinum-based catalysts

It is known that pure Pt has very low activity towards CO oxidation due to the poisoning effect of CO, which adsorbs and covers Pt's active surface sites, competing with O_2 adsorption.[30,31] However, Pt based supported catalysts (on alumina, silica, silica gel, etc.) have exhibited excellent activity and have been commercialized. The first patent for the COPrOx catalyst was awarded to Engelhard Industries Inc. in the 1960s,[32] in which supported Pt/Al_2O_3 catalysts were applied to purify the hydrogen for the application of ammonia synthesis. In this patent, the CO can be efficiently removed by using Pt/Al_2O_3 around 100 ˚C. After that, Pt-supported catalysts became one of the most heavily studied catalysts for CO oxidation in the absence, or in the presence, of H_2. To date, various Pt-based catalysts have been developed for COPrOx in a wide operation temperature window (e.g., 80−180 °C) for the PEMFCs applications. In 1987, Los Alamos National group published a study for COPrOx over 0.5% Pt supported on alumina (Al_2O_3), revealed that the higher the content of O_2, the higher the conversion of CO and H_2 achieved.[33] When the molar ratio of O_2 to CO was 2, the conversion of CO reached 100% above 160℃, but when the molar ratio of O_2 to CO was 1, the conversion of CO was less than 100% under identical reaction conditions. This report indicated that the gas composition of COPrOx reactants plays a role of catalytic performance of Pt-based catalysts. In addition to the influence of feed gas ratio, the catalytic performance of Pt based catalysts can be promoted by pretreatment of Pt/Al_2O_3 catalyst in water vapors. It was found that the pretreatment in H_2O vapor can reduce the particle size of Pt and enhance the CO activity of the catalyst at low temperatures.[34]

In early stage, inert compounds such as SiO_2, Al_2O_3, and zeolites were used as supports to immobilize Pt particles. Among these supports, Igarashi et al.[35] have shown that the activity of Pt catalyst can be improved by using zeolites instead of Al_2O_3 support. In the presence of large amount of hydrogen and low concentration of oxygen, Pt supported on molecular sieves can selectively oxidize more CO compared to the traditional Pt/Al_2O_3 catalyst. [35] Moreover, comparison of the reactivity of Pt supported on different zeolites shown that Pt supported on Faujasite (FAU-type) zeolites is more active than on MOR, ZSM and ETS-10 type zeolites. [36] The superior activity of Pt supported on FAU is attributed to the large pore size and pore volume of FAU zeolites, leading to higher dispersion of Pt particles.

More recently, reducible oxides such as CeO_2 and FeO*x* gradually replaced the inert supports for Pt supported catalysts and received increasing attention. Among these catalysts, Pt/CeO_2 was not only considered as the most active but also the most selective catalyst for COPrOx, reaching near 100% of CO conversion and CO_2 selectivity at low temperature of about 100 °C.[3738] It is proposed that the highly hydrated ceria with significant vacancy density provides an oxidizing agent at the interface between Pt and Ce. This agent reacts with the nearby surface carbonyls formed on the Pt particles yielding CO_2. Another study on the mechanism of the COPrOx reaction over Pt/ceria catalysts, via multiple steady-state in situ spectroscopy (DRIFTS and XPS) at different partial pressures of O_2 and/or CO, indicated that the oxygen vacancy formation is correlated with the enhanced CO oxidation activity. Therefore the water desorption is hindered due to preferential oxidation of CO instead of H_2. More studies on Pt/CeO_2 system demonstrated that a Pt-O-Ce interface is formed in $Pt\text{-}CeO_2$ catalyst, while ionic Pt species is formed on $CeO_2\text{-}Co_3O_4$ supports due to the transfer of lattice oxygen from reducible oxides, indicating the strong interaction between Pt and its supports. Bugaev's group have recently illustrated the evolution of the atomic structure of Pt/CeO_2 during COPrOx by application of extended X-ray absorption fine structure (EXAFS) and X-ray absorption near-edge (XANES) spectroscopies.[39] As illustrated in **Figure 1-2**, the structure of Pt atom is varying with different reaction temperature from α-PtO_2 stacked layers to single layer and eventually forms alloyed Pt particle bonded to Ce due to exposure to CO and H_2 in PrOx composition, indicating the dynamic behavior of Pt phase during COPrOx reaction.

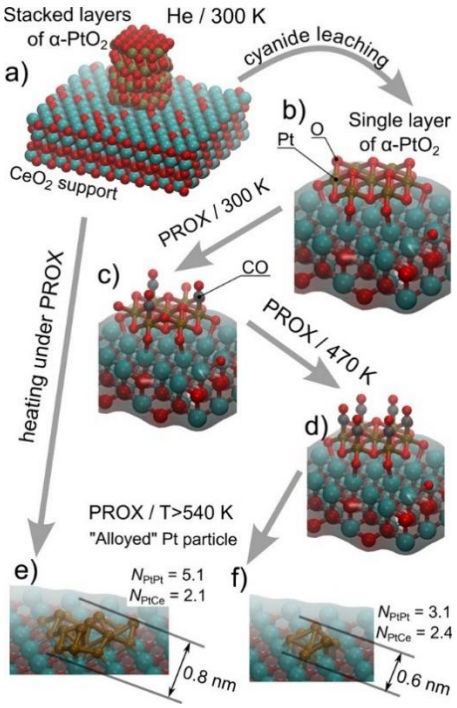

Figure 1-2. Illustration of the evolution of an atomic structure of the Pt/CeO_2 under PrOx conditions and at elevated temperature: (a, b) 4% Pt/ceria and 2% Pt/ceria in helium at room temperature; (b–d, f) 2% Pt/ceria at elevated temperature under PrOx; (e) reduced 4% Pt/ceria under PrOx. Taken from [39]

In addition to the effects of the support and the feed gas ratio, the addition of another metal (such as Ru, Fe, Co, Cu, Sn, Mn, Ce, Nb, Ni, and even alkali metals) to Pt-based catalysts can considerably improve the COPrOx activity.[40,41] Both Co and Cu has shown a promotional effect on Pt supported on SiO_2 for COPrOx by forming intermetallic compounds (IMCS).[42] The formation of IMCS weakens the Pt-Pt bond and promotes electron charge transfer from Pt to Co or Cu. The charge transfer results in weaker adsorption of CO on the IMCS surface as compared to the pure Pt. Although both catalysts exhibited 100% CO conversion from 80°C-180°C, $PtCo_3$ has better selectivity of O_2 towards CO_2 than that of PtCu. The promotion effect of Co on supported Pt catalysts has been also studied over $PtCo/TiO_2$ and $PtCo/Al_2O_3$.[43,44] Among various PtCo supported catalysts, PtCo supported on YSZ (Pt:Co = 1:5, 0.5 wt.% Pt) shows the best COPrOx reactivity which can reduce CO content in H_2-feed gas below 10 ppm at 110-150 ˚C even with reactants containing water and carbon dioxide.[45]

To date, there is still an open debate about the active phase in PtCo-based catalyst for CO conversion. Ko et al.[45] reported that the formation of isolated bimetallic Pt-Co nanoparticles is responsible for the observed high PrOx activity at room temperature (RT). On the contrary,

Komatsu et al. found that the maximum PrOx activity over these PtCo catalysts was related to the appearance of Pt_3Co or Pt-Co phases.[42,46] Besides, the critical role of the Pt, Co intermetallic compound in PtCo catalysts for PrOx of CO was investigated by Li et al,[47] suggesting that the surface Co oxides interacts with Pt and induce a promotional effect during the reaction, which is consistent with the findings in another work from Yuan's team.[48] On the contrary, Xu et al. proposed that the active PtCo catalyst phase is an architecture consisting of Pt nanoparticles decorated with highly dispersed CoO nanostructures. This architecture is formed after exposure to a reductive atmosphere, while similar structures have been observed on $PtCo/TiO_2$ in H_2 and methanol atmosphere.[44]

Bao's group found that the combination of Pt-Fe supported on SiO_2 exhibit almost 100% CO conversion at room temperature (RT) under COPrOx atmosphere by forming an ''FeO-on-Pt'' surface structure.[49] Their later investigation on Pt-Fe system for CO catalytic oxidation via XPS and XANES indicated that the surface architecture of Pt–Fe bi-component catalyst can be controlled by reducing the catalyst in H_2 at various temperatures.[50] As shown in **Figure 1-3**, the reducing pretreatment of Pt-Fe catalyst results in different COPrOx activity due to the different surface architecture formed at different H_2 reduction temperature. In case of Fe-Pt bi-component supported catalysts, Pt forms a single atom catalyst directly dispersed on the surface of FeO_x support. This catalyst showed 2-3 times higher activity for CO conversion than the cluster-sized catalyst. Strikingly, Cao's group prepared atomically dispersed iron hydroxide deposited on Pt/SiO_2 nanoparticles. They show that the activity of this catalyst is 10 times higher than the Pt-single atom catalyst supported FeO_x. This superior activity was attributed to the high reducibility of isolated $Fe_1(OH)_x$ on Pt.[28] So far, this is the most active Pt-based catalyst reported for COPrOx, with 100% selectivity to remove CO over a broad temperature range from -75^{o}C-110 °C. Such a high conversion of CO has been only reported over certain surface planes of Co_3O_4 but without the presence H_2 in the feed gas.[51]

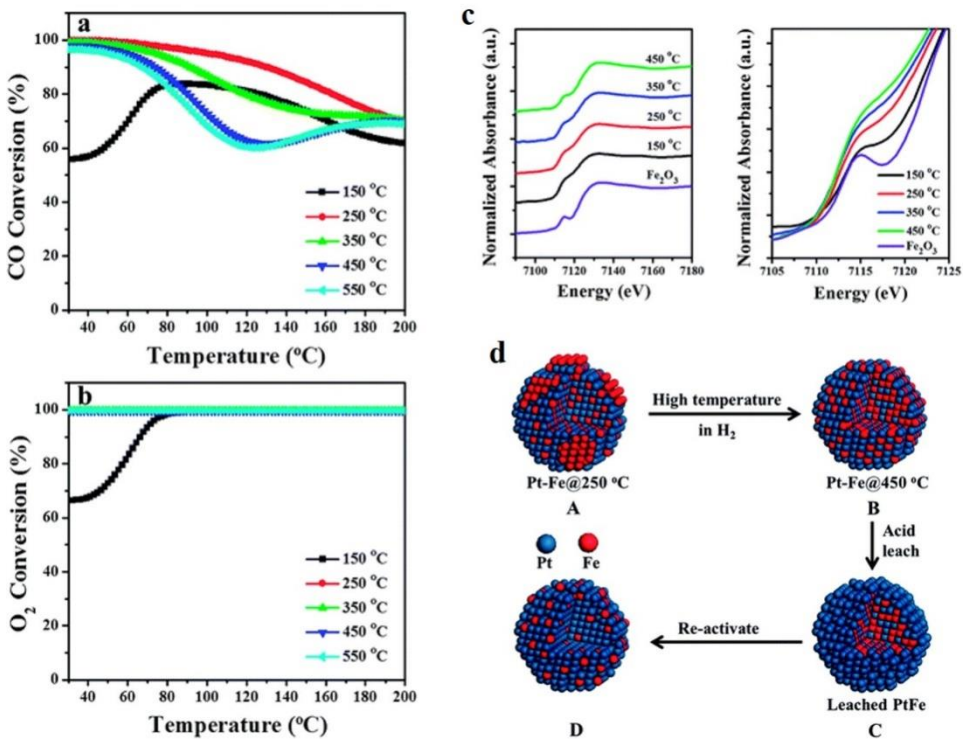

Figure 1-3. CO conversion (a) and O_2 conversion(a) in the PrOx reaction (1% CO, 0.5% O_2, 50% H_2 and He balance) over the Pt–Fe/CB catalysts reduced at the indicated temperatures. (c) Fe K-edge XANES spectra recorded in air from the Pt–Fe/SiO_2 catalysts reduced at the indicated temperatures and (d) schematic diagrams of the structures of Pt–Fe nanoparticles treated under various conditions. Taken from [50]

1.2.1.2 Au-based catalysts

Although bulk Au catalysts are inactive for CO oxidation, supported Au nanoparticles have shown a 100% of CO conversion at room temperature.[52,53] Many researchers have indicated that the properties of the support play an essential role on the performance of Au-based catalysts. It was commonly reported that the catalytic activity of Au supported on reducible oxides was higher than that on non-reducible oxides. Among these reducible oxides, TiO_2,[54] Fe_2O_3,[55,56] MnO_2 and Co_3O_4[57] are the most promising carriers for Au nanoparticles. These oxides not only aid to the better dispersion of Au particles on their surfaces, but also facilitate electron exchange due to facile changes of their oxidation state in the COPrOx atmosphere. A thoroughly study system of supported Au catalysts is the case of Au/ CeO_2. This catalyst exhibits high catalytic activity for CO oxidation due to the existence of highly dispersed Au particles formed by the interaction with surface defects of CeO_2.[58] Moreover, the strong interaction between Au and CeO_2 results in electron density transfer from Ce to Au, leading to the partial oxidation of Au and partial reduction of Ce(IV) into Ce(III), affecting the

catalytic activity.[59] Notably, the interaction of Au with the support (e.g. TiO_2 or ZrO_2) defines also the shape of Au particle.[60] In turn, the difference of Au particles shape on the two supports influences the number of low-coordination active centers, resulting in differences at the CO conversion.

In addition to the influence of the support, the preparation method of supported Au catalysts play a vital role for the reactivity as well. It is reported that the different preparation methods do not only modify the crystal structure of Au and the support, but may also affect the size of Au particles and their interaction with the support.[61,62] Khoudiakov et al[56] found that the Au content over the Au/Fe_2O_3 catalyst prepared by the deposition-precipitation was higher than that that prepared by co-precipitation method. A simple reason for that in the former method, all Au in the solution of precursor is completely precipitated, avoiding the waste of Au-containing sources. Moreover, as-prepared catalyst is more stable for CO oxidation after longer heating treatment.

Heterogeneous catalytic reactions are classified into two groups based on the sensitivity of catalytic activity to particle size.[63,64] The reactions in which the intrinsic activity of active sites is dependent on the particle size are classified as structure-sensitive reactions, while the rest of the reactions are structure-in sensitive reactions. It has been established for a long time that CO oxidation over supported Au is structure-sensitive reaction, which means that the catalytic activity and/or the selectivity of Au-based catalysts strongly depends on the particle size of gold. As mentioned above, the size of Au particles is a function of several factors, but primarily depend on the preparation method.[65,66]

For a good COPrOx catalyst, the nanosized Au particles should be highly dispersed on the surface of a metal oxide support and the optimum size of Au particles should be less than 5 nm. Bamwenda et al.[67] reported that the CO oxidation activity of Au catalyst prepared by deposition precipitation method is about 4 times that of catalyst prepared by photodegradation precipitation method. They found that the Au particle size of the catalyst prepared by photodegradation precipitation method is more than two times larger than that prepared by deposition precipitation method and used this difference in size to explain the effect on the reactivity. Bethke et al. found that when the particle size of Au was 5-10 nm, the $Au/\gamma\text{-}Al_2O_3$ catalyst had the best catalytic activity and selectivity in the selective catalytic oxidation of CO.[68] In addition, for Au catalyst, the catalytic activity of bimolecular layer

catalyst is better than that of single molecular layer and multi molecular layer structure.[69]

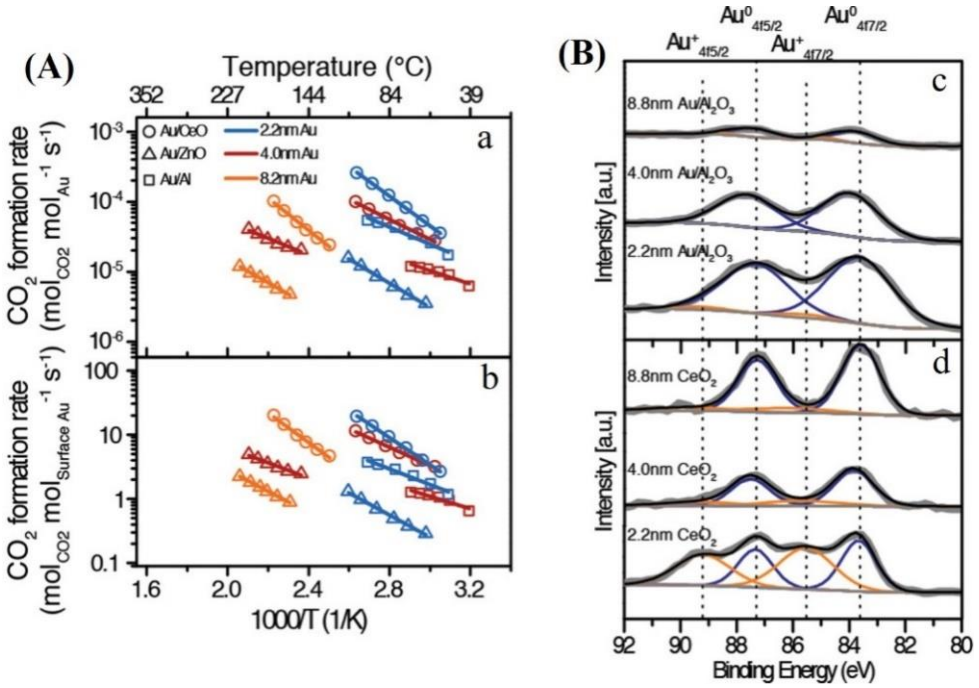

Figure 1-4. Kinetic data (A). Arrhenius-type plot of CO oxidation rate normalized by total amount of Au (a) and exposed Au surface atoms (b); XP spectra for Au/Al_2O_3 (c) and Au/CeO_2 (d) catalysts. Taken from[70]

More recently, Cargnello's group investigated the effect of size and support on the Au-catalyzed PrOx reaction using size-controlled Au nanoparticles.[70] Compared to Al_2O_3 and ZnO, CeO_2-supported Au shows better performance for CO oxidation in the temperature range of 30–280 °C. For all the examined supports, Au particle sizes of 2–5 nm shows the highest rates, whereas for larger sizes the rates drop. As shown in **Figure 1-4**, XPS study revealed that Au/CeO_2 exhibits a highest ratio of Au^+/Au^0 at smallest particle diameter, indicating that Au^+ is the active sites for COPrOx on Au-supported catalysts. All the above studies have well established that the activity of Au-supported catalysts is a strong function of the size, shape, and morphology of Au active phase.

1.2.2 Non-noble metal-based COPrOx catalysts

Although noble metal catalysts have demonstrated excellent activity for selective oxidation of CO, their high price and scarcity restricts their wider application. In addition, the selectivity and resistance to water and carbon dioxide of noble metal-based catalysts for COPrOx reaction are limited at high temperature. In order to reduce the cost of the whole

process, the research of an abundant, economic non-noble metal catalyst for COPrOx reaction has gained considerable attention among researchers in industry and academia. Among various transition metals, Cu and Co are the most promising and the mostly studied non-noble metal-based catalysts.

1.2.2.1 Copper-based catalyst

Among all the non-noble metal-based catalysts, Cu-Ce is considered as a promising alternative to noble metals for PrOx because of its superior activity, selectivity and resistance to CO_2 and H_2O. It is worth noting that when used individually, both copper and cerium have very limited activity for the COPrOx reaction. To date, three different types of Cu-Ce based catalysts have shown the most promising performance for COPrOx. These are i) copper supported on CeO_2 (referred as Cu/CeO_2), cerium supported on CuOx (referred as CeO_2/CuO) and CuO_x-CeO_x composites (referred as Cu-Ce-O). Among these Cu-Ce systems, Cu/CeO_2 catalysts for COPrOx have been those that are more extensively studied. In the early studies, researchers have focused on optimizing the reactivity of Cu/CeO_2 via using various synthesis strategies for the preparation of the catalysts. Cu/CeO_2 can be easily obtained by incipient wetness impregnation method using copper nitrate aqueous solution as one of precursors and CeO_2 nanoparticles as a support.[71] Cu/CeO_2 rod catalysts prepared by an ethanol thermal method exhibited superior reactivity for COPrOx due to highly dispersed CuO species on CeO_2, forming abundant oxygen vacancies and strong synergistic effect between CuO and CeO_2. More studies have focused on addressing the effects of preparation methods on catalytic activity of Cu/CeO_2. The comparison of Cu/CeO_2 performance obtained by different methods and the effects of support and morphology have been well summarized in a recent paper contributed by Jing et al.,[19] therefore will not be discuss further in this thesis.

Recently, the identification of active sites of copper-ceria system for CO conversion via using *in situ* and *operando* techniques is gaining ground among the researchers. Regarding the active sites of Cu-Ce system, most reports indicate that Cu^+ or CuO are the active sites for CO adsorption. For example, Luo and co-workers confirmed that the finely dispersed CuO was the main active site, while the Cu^{2+} in the CeO_2 lattice played the least role for CO oxidation.[72] Similar conclusions were also proposed in other works. For example, Gamarra and co-workers illustrated that CO oxidation occurs at the interfacial area between dispersed copper oxides and cerium oxides, while H_2 oxidation proceeds only after the formation of

Cu^{+}.[73] In addition, Martínez-Arias et al. proposed that the strong electronic interaction between the reduced ceria and small metallic copper particles led to the decreased CO adsorption capability of copper.[74] A strong synergistic effect between Cu-Ce and surface-dispersed Cu^{+} species rather than Cu^{0} was confirmed to form the active species for CO conversion by using fluorescence, XANES, and DRIFTS techniques.[75–77] More examples of in situ study over Cu-based catalysts for CO oxidation are discussed in section 1.3.3 in the perspective of *operando* near ambient pressure XPS studies.

1.2.2.2 Cobalt-based catalysts

Instead of copper based catalysts, cobalt-based catalysts are considered as another cheap and readily available alternative to noble metals for COPrOx reaction. Moreover, cobalt oxide has shown better activity and selectivity than that of copper for CO oxidation at least up to 200 °C.[11,78] In a study where CuO, NiO and Co_3O_4, were synthesized by using the same method of polymerization-combustion, it was found that the activity for COPrOx reaction follows the order: Co_3O_4 > NiO > CuO. The intrinsic activities at 100 °C are: 0.20 x $10^{-3}s^{-1}$ for the Co_3O_4 and 0.08 x $10^{-3}s^{-1}$ for NiO and CuO. Herein, pure cobalt oxide is 3 times more active than pure CuO and NiO, demonstrating the promising property of cobalt for CO oxidation in excess of H_2. In a comparative CO oxidation study of various metal oxides (CoO_x, CuO, MnO_2, NiO, Cr_2O_3, Fe_2O_3 and V_2O_5) supported over CeO_2, it was found that CoO_x/CeO_2 was superior to all the other catalysts.[79] However, a later study of cobalt supported on different metal oxides (ZrO_2, CeO_2, SiO_2, Al_2O_3, and TiO_2) found that ZrO_2-supported cobalt is most active for COPrOx as compared to other supports including CeO_2[80]. In addition to pure metal oxides supports, cobalt oxide supported on a mixed ceria–zirconia oxide has also shown very good activity for COPrOx.[81,82] The outstanding catalytic performance of cobalt for COPrOx reaction depends mainly on the redox behavior of the catalyst and the cobalt oxide dispersion. The latter is affected by specific ceria-zirconia support features, such as the atomic ratio of Ce/(Ce + Zr) and the cobalt oxide loading. The addition of transition metal oxides MO*x* (M = Mn, Fe, Ni or Cr) to $Co_3O_4/Ce_{0.85}Zr_{0.15}O_2$ could further improve the CO conversion as well as the resistance to CO_2 and H_2O. Notably, the modification of $Co_3O_4/Ce_{0.85}Zr_{0.15}O_2$ with MnO_x with a ratio of Co/Mn = 8:1 remarkably broadened the temperature window of 100% CO conversion. The analytic results presented proposed that the existence of Mn^{4+} and Mn^{3+} was favorable to the reaction acting as

stabilizers of the Co^{3+} phase, which for the authors is the surface active sites.[83] We will see later in this thesis that this assumption is not based on credible experimental facts and is confronted by our in situ analysis of the catalytic surface.

Like in the case of copper-based COPrOx catalysts, ceria seems to be the support of choice also for cobalt catalysts. The Co/CeO_2-based system has gained considerable attention for CO selective oxidation in H_2 feed gas. Co_3O_4-CeO_2 supported on modified activated carbon (AC) exhibits excellent reactivity towards COPrOx reaction, which is critically depends on the dispersion and reducibility of Co_3O_4. The latter is affected by the Ce/Co loading ($n_{Ce/Co}$) and the pretreatment temperature of the activated carbon.[5] It is concluded that the addition of cerium with an appropriate $n_{Ce/Co}$ can improve the catalytic performance of the supported Co_3O_4 catalyst on AC, ascribed to the increase in the amount of reducible Co^{3+}. Interestingly, despite having extremely low surface area (7 m^2/g) and low Co-dispersion (< 0.1%), the CoO_x (10 wt.%)/CeO_2 catalyst has shown promising PrOx reactivity. The COPrOx activity of CoO_x supported on CeO_2 has been further improved by increasing the surface area of CeO_2, resulting in higher Co-dispersion on the catalyst's surface.[84,85]

A recent study of preferential oxidation of CO over cobalt-based catalysts has also shown that promotion of Co_3O_4 with 10 wt.% CeO_2 increases the reduction temperature of Co_3O_4 phase in CO and H_2 and enhances the PrOx activity.[6] An operando XANES and NAP-XPS study indicated that Co_3O_4 can be reduced to metallic Co above 300 °C under COPrOx reaction conditions, leading to the formation of methane. As shown in **Figure 1-5**, the Co 2p NAP-XPS spectra of CeO_2-Co_3O_4 catalyst during COPrOx demonstrated that the Co^{3+} phase is stable from room temperature up to 300 °C, while XANES shows that Co_3O_4 is reduced to metallic Co phase above 250 °C. The gas evolution recorded by mass spectrometer during two experiments (XANES and NAP-XPS) show different products distribution (**Figure 1-5**(a) and (b)) due to the different oxidation state of cobalt. Overall, it is agreed that addition of CeO_2 to Co_3O_4 promoted the PrOx activity despite that CeO_2 is much less active than Co_3O_4.

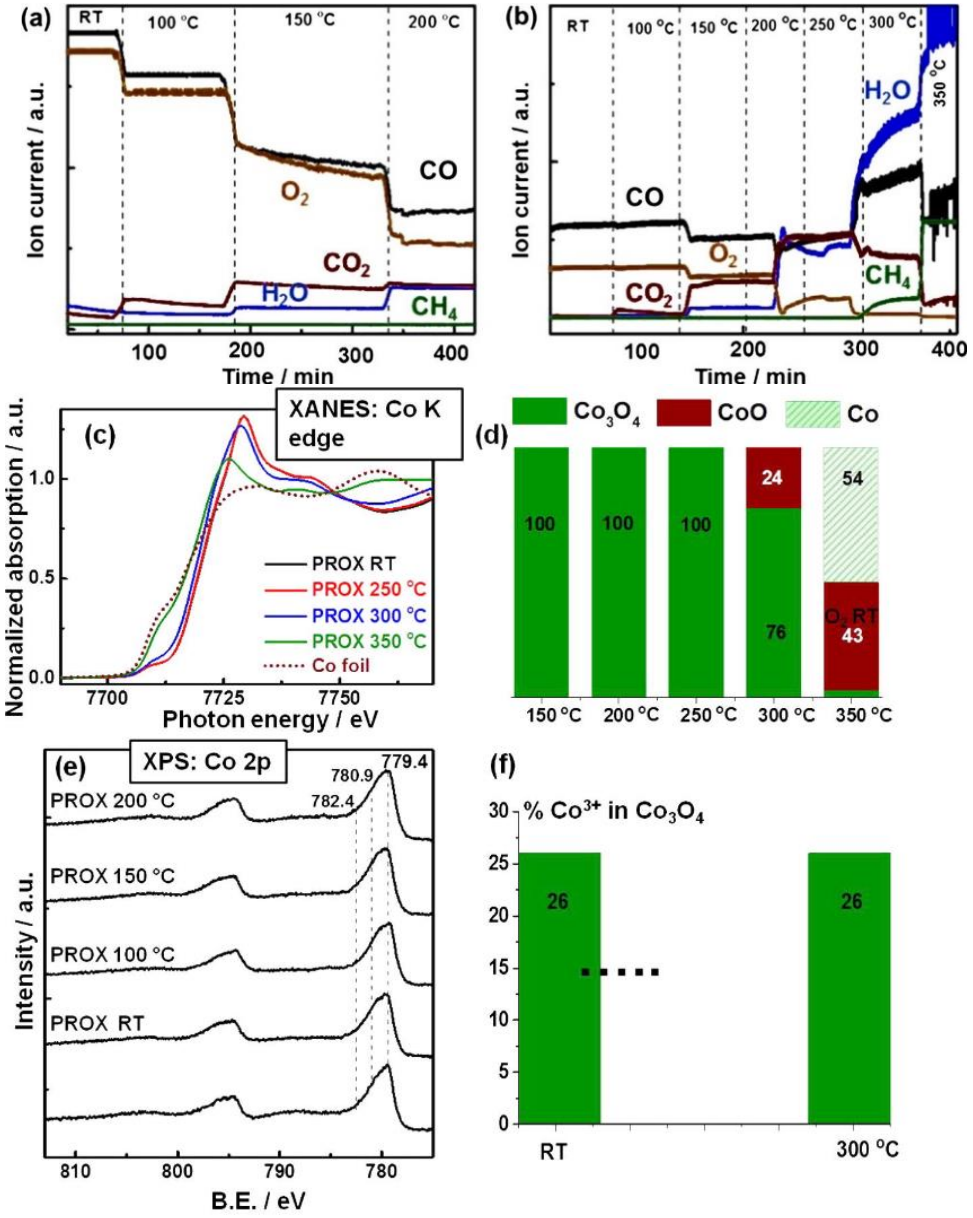

Figure 1-5. MS data of PrOx on CeO_2-Co_3O_4 recorded during (a) operando NAP-XPS; (b) operando XAS at the Co K edge. (c) XANES spectra at the Co K edge of CeO_2-Co_3O_4 under PrOx conditions (1 vol.% CO, 1 vol.% O_2 50% H_2 in He, total flow 50 mL min^{-1}) and (d) amount of reduced versus oxidized cobalt calculated by linear combination of reference spectra. (e) Operando NAP-XPS during PrOx over CeO_2-Co_3O_4 (1.5 ml/min O_2 + 1.5 ml/min CO + 17 ml/min H_2, 0.5 mbar): Co 2p region (hν = 1015 eV); (f) amount of oxidized cobalt calculated from linear peak fitting procedure. Taken from [6].

As discussed above the performance of catalytic nanoparticles strongly depends on their size, the morphology and their shape. Regarding the effect of morphology, Khasu and co-authors[3] have recently probed the relationship between Co_3O_4 morphology and its COPrOx reactivity. In contrast to sheets and belts shape cobalt particle, the Co_3O_4/SiO_2 model catalyst composed by cobalt nanotubes shows superior activity towards CO oxidation

in excess of H_2. The excellent activity of nanotubes was attributed to the formation of $Co^{3+/2+}$ pair on (100) planes of Co_3O_4. A similar conclusion has been reached by Gabriela et al, in a study of the impact of the spinel active phase faceting on Co_3O_4/Al_2O_3 for COPrOx.[86] The (100) termination has been found to be the most active surface plane of Co_3O_4 among all the other low-index (111) and (110) planes. The yield of CO_2 was linearly correlated to the abundance of Co^{3+} cations on exposed planes, with the (100) planes containing the most abundant Co^{3+} cations on the surface.

Before the morphology effect was investigated, the effect of size of Co_3O_4 nanoparticles has already been substantiated by Nyathi et al.[87] using model catalysts consisting of Co_3O_4 crystallites with different size and a narrow size distribution supported on γ-Al_2O_3. The best mass-specific CO conversion was obtained over Co_3O_4 with the smallest crystallite size. The reduction behavior of the different Co_3O_4 crystallites as a function of temperature under COPrOx indicates that catalysts with larger crystallites showed higher degrees of Co_3O_4 reduction. The fast reduction of larger Co_3O_4 crystallite is unfavorable for CO oxidation, as less CO_2 was formed, and instead, CH_4 was produced due to the presence of the metallic Co. The formation of CH_4 caused by metallic cobalt is consistent with the conclusion in the COPrOx study over Co_3O_4-CeO_2 catalysts.[6]

Recently, the impact of the nanoparticle–support interactions (NPSI) in Co_3O_4/Al_2O_3 catalysts for the PrOx of CO has been directly elucidated via using in situ XANES and quasi in situ XPS.[88] In this study, it is reported that the strength of NPSI leads to different reactivity and stability of Co_3O_4 for COPrOx. Catalyst with weak NPSI between unreduced Co_3O_4 and support shows a higher CO conversion and CO_2 yield at low temperature (50 ^oC -225 ^oC). Above 250 ^oC though the reduction from Co_3O_4 to metallic Co is facilitated with negative effects to the selectivity. The catalyst with strong NPSI does not favor Co_3O_4 reduction at elevated reaction temperatures and consequently the unwanted formation of CH_4. The differences in the redox behavior are typically ascribed to the differences of NPSI between the various crystallites of Co_3O_4 and the Al_2O_3 support.

1.3 **Catalytic reactions on non-noble, late transition metal catalysts studied by *in situ* near-ambient pressure XPS**

Transition metals can have multiple oxidation states, depending on the surrounding

environment (gas atmosphere, pressure and temperature) and the ionic species they are bonded to. Understanding the relationship between catalytic surfaces and their performance is crucial for the design of new transition metal catalysts and the optimization of those already in use. X-ray photoelectron spectroscopy (XPS) is one of the most powerful spectroscopic tools to obtain chemical information of solid surfaces. However, conventional XPS instruments operate under ultra-high vacuum conditions ($<10^{-8}$ mbar) limiting the characterization of catalysts, before and after reaction. The last 15 years, a new type of XPS apparatus has emerged, allowing in situ measurements of catalysts in gaseous environments in the mbar pressure range. These "environmental XPS" systems, commonly referred to as near ambient pressure XPS (NAP-XPS), have opened up new opportunities to study dynamic modifications at surfaces and correlate them with the catalytic performance. In this thesis the NAP-XPS technique plays a central role in the establishment of the relation between cobalt surface oxidation state and its COPrOx catalytic performance. Therefore, it is of great interest to review the previous NAP-XPS studies of non-noble, late transition metal catalysts (Fe, Co, Ni and Cu) in reactive gas or vapor phase environments. Such a review is missing in the literature and it is useful to include it here, since cobalt is the core catalyst of this thesis. The aim is to describe the rich chemistry of transition metal surfaces (including also cobalt) under conditions resembling the catalytic reaction in the prism of NAP-XPS technique. This review can give the greatest context in the study described in this thesis. A short introduction in the NAP-XPS technique can be found in *Chapter 2*.

1.3.1 Catalytic hydrogeneration

Direct hydrogenation of CO and CO_2 into valuable chemicals has attracted considerable efforts as fossil fuels continue to dominate the energy sector.[89] Inspired by demands for low-cost catalysts, several investigations of transition metals for the hydrogenation of C1 molecules into liquid fuels exist. Among the various transition metals examined so far, Co, Cu and Ni based catalysts have been found to be extremely active for CO_2 and CO hydrogenation reactions and here it is provide an outlook of the recent information obtained by NAP-XPS.

1.3.1.1 CO_2 dissociation and hydrogenation on Cu surfaces

Cu-based catalysts, typically supported on ZnO carriers, are widely utilized for reverse

water−gas shift reaction (RWGS) and methanol synthesis from CO_2 hydrogenation.[90–92] The groups of M. Salmeron and G.A. Somorjai used Cu single crystals as model catalysts to understand the effect of surface termination on the adsorption and dissociation of CO_2. In particular, synchrotron-based NAP-XPS, combined with high pressure scanning tunnelling microscopy (STM), were employed to investigate CO_2 interaction with Cu(100) and Cu(111) surfaces at room temperature and pressure up to 10 Torr for NAP-XPS and 20 Torr for STM.[93] The photoemission spectra shown in **Figure 1-6**a and b illustrate the coexistence of several O 1s and C 1s peaks induced by various adsorbed species on copper surfaces. Notably, the spectral shape is adjusted according to the CO_2 pressure, while there is also an effect of the surface termination (i.e. (111) vs. (100)) on the measured binding energies of the adsorbed species. The O 1s peak related to surface atomic oxygen (AO) on Cu appears around 529.7±0.1 eV, while the peak at 531.4 eV is induced by adsorbed $CO_2^{\delta-}$ species. Interestingly, later studies correlated the O 1s peak BE of adsorbed AO with its coverage on the Cu (100) surface.[94] In the C 1s region two adsorbed carbon species were found: hydrocarbon species located at 284.4 eV and $CO_2^{\delta-}$ species at 288.1 eV. The contribution of CO_2 in the gas phase above the sample is visible at higher binding energies in both O 1s and C 1s spectra (around 536 and 293 eV, respectively). Due to the relatively high coverage of AO followed by a relatively low signal of the $CO_2^{\delta-}$ species on the Cu (100) as compared to the (111) surface, it was concluded that open Cu surface planes, such as Cu (100), can dissociate CO_2 more efficiently than the close-packed ones (i.e.Cu(111)). The relevant STM images showed a significant reconstruction of Cu (100) surface in the presence of 20 Torr CO_2 and the production of a high density of kink and step sites. Taking into account that industrial CO_2 hydrogenation takes place at significant higher pressures than the spectroscopic studies, the above mentioned NAP-XPS results should be used to understand the general trends of copper reactivity, but cannot be directly extrapolated to describe the function of the technical CO_2 hydrogenation catalysts.

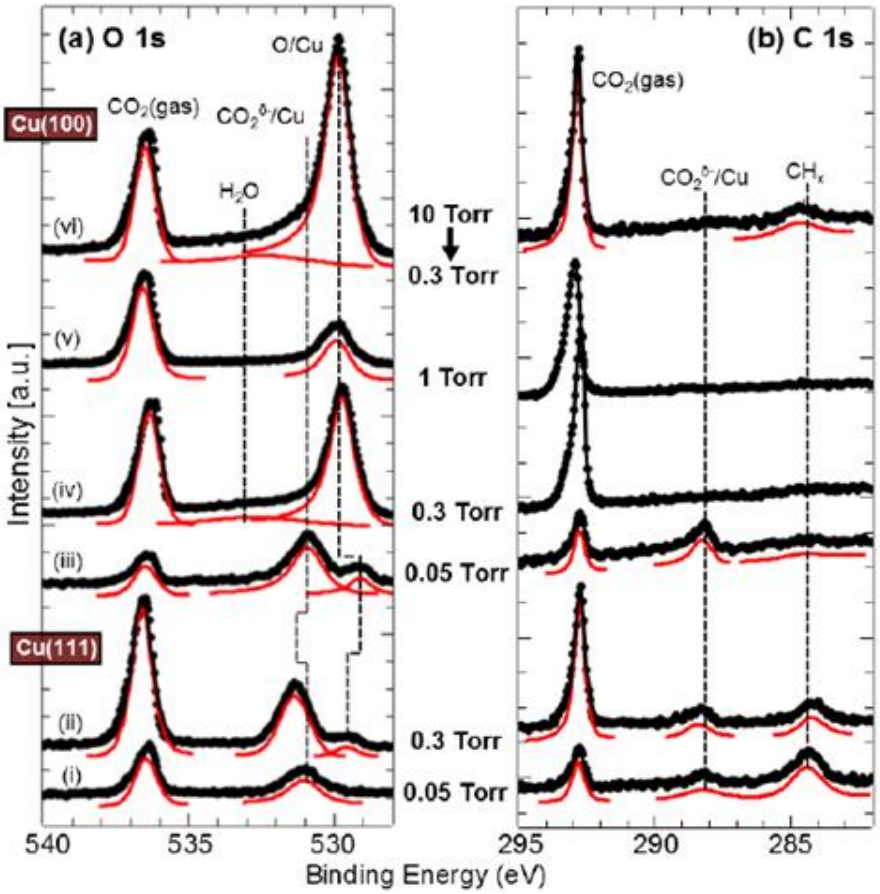

Figure 1-6. O 1s and (b) C 1s regions of the NAP-XPS spectra in the presence of CO_2 at RT on the Cu(111) surface (lower two panels) and on the Cu(100) surface (upper four panels): (i, iii) 0.05 Torr CO_2; (ii, iv) 0.3 Torr CO_2; (v) 1 Torr CO_2; (vi) 0.3 Torr CO_2 after the sample was kept for 5 min in 10 Torr CO_2. From[93]

These results were confirmed in a more recent study of CO_2 dissociation over Cu(100),[95] where the evolution of the oxygen layer induced by CO_2 dissociation was investigated in detail. With the aid of DFT calculations it was proposed that CO_2 dissociation take place preferentially over step sites on Cu surface (i.e. Cu atoms with lower coordination number).[95] This conclusion can be connected with an earlier work of CO_2 interaction with a welled defined vicinal Cu (997) substate.[96] Upon exposure to CO_2 at 67 °C carbonate species (CO_3^{2-}) were formed on copper through the reaction of CO_2 with oxygen derived from CO_2 dissociation. After saturation of adsorbed CO_3^{2-}, the spectroscopic signature of AO appeared, indicating that CO_2 dissociation to CO and O continue to take place even after saturation.[96] Dissociation of CO_2 into CO+O, was also noticed on Cu(111) after prolonged exposure to CO_2. This process can build up a layer of AO which passivates the Cu(111) surface and hinders further CO_2 activation.[97] On the contrary, fine control of the adsorbed oxygen species

in CO_2+H_2 mixture (e.g. by tuning the CO_2 and H_2 partial pressures) can have a beneficial impact by preventing the formation of graphitic carbon and sustain Cu catalytic activity.[97] Similar oxygen species were also reported during CO_2 interaction with polycrystalline copper surfaces, while when O_2 is co-fed with CO_2, metallic Cu is oxidized to Cu_2O followed by a net increase of CO species.[98] Besides gas phase oxygen, bulk-dissolved oxygen in copper can participate to the reaction by diffusion on the surface at critical temperatures (around 580 °C) and formation of chemisorbed oxygen.[99]

Apart from surface and bulk-dissolved oxygen, a third type of oxygen species may influence the reactivity of copper catalysts. This species are related to subsurface copper oxides (or oxygen inserted between the outermost copper layers) identified already in an early NAP-XPS work of methanol oxidation over polycrystalline Cu catalysts.[100] The important role of subsurface oxygen also for CO_2 activation on copper was highlighted by Favaro et al.,[101] who showed that CO_2 dissociation on Cu (111) is controlled by the formation of a subsurface oxide. This type of "suboxide" was defined as oxygen atoms inserted between the top two atomic layers of the Cu (111) crystal. Its presence is essential for converting chemisorbed CO_2 to a more active state designated by the authors as "bent (chemisorbed) CO_2". In the presence of adsorbed water, "bent CO_2" on copper is transformed to formate and CO species which is the first step towards CO_2 reduction.[101] However, the NAP-XPS study performed by Rodriguez's group on Cu/CeO_2 nano-catalysts proposed that the active state of copper during CO_2 reduction by H_2 or H_2O is not CuO_x, but metallic Cu^0, while species formed on the ceria support participate to the reaction.[102] This scenario seems to be in line with *ex situ* studies applying XPS analysis on post mortem CuCe composite catalysts.[103]

The Cu/ZnO system under CO_2 gas environment was studied using inverse catalysts, consisting of ZnO particles supported on a polycrystalline Cu foil. It was proposed that the addition of Zn on Cu promotes complete conversion of $CO_2^{\delta-}$ to carbonates resulting in consequent improvement of the CO_2 conversion.[104] In 0.1 torr of CO_2 the coexistence of $CO_2^{\delta-}$ and carbonates was observed by NAP-XPS only on clean metallic Cu surface, but not on Cu_2O. As soon as very small amounts of Zn were deposited on Cu the adsorbed $CO_2^{\delta-}$ species were converted to carbonates (CO_3^{2-}). When the model catalyst is exposed to a 1:1 mixture of CO_2: H2O, new adsorbed species are formed, with H_2O providing the hydrogen needed for the formation of hydrogenated species.

The same interface was later investigated by Rodriguez and co-workers[105] using copper single crystals instead of a polycrystalline foil. The NAP-XPS results over inverse ZnO-Cu(111) and ZnO-Cu(100) model catalysts showed that the copper substrate influences CO_2 hydrogenation, with ZnO-Cu(100) to be the preferred configuration for the high catalytic activity.[105] In particular, they proposed that formate species is an important intermediate of the reaction and their formation necessitates the presence of surface ZnO in a configuration similar to ZnO-CuO_x/Cu(111). According to the authors this indicates that the strong interaction between ZnO and Cu is essential for the activity. However, although the presence of formate species on copper catalysts exposed to CO_2 has been verified in several studies, there is no consistency if these species are spectators or reaction intermediates for methanol synthesis. For example, Yang et al. proposed that formate species on Cu are just spectator species, while methanol production goes through carboxyl intermediates, on the basis of FTIR experiments.[106] A recent report of H. Bluhm and co-workers highlighted possible complications in identification and quantification of adsorbed carbon species due to adventitious carbon readily adsorbed on copper surfaces even if precautions are taken during surface preparation.[107]

Copper is also a promising electrocatalyst for solid oxide electrochemical cells (SOEC), which motivated Bozzini et al. to build a model SOEC and use it to study carbon deposition on copper cathodes under CO_2 and CO_2/H_2O electrolysis at 600 °C.[108] Interestingly, the NAP-XPS and Near Edge X-Ray Absorption Fine Structure (NEXAFS) results show an analogous behaviour with the observations discussed above for copper heterogeneous catalysts. In particular, at intermediate potentials (2 V) electrochemical dissociation of CO_2 produces CO and AO on copper. AO reacts with pre-adsorbed carbon to form CO and when all carbon is removed oxidizes copper yielding Cu_2O. When the potential increases to 4 V then CO dissociation to C+O becomes feasible and carbon accumulation at the surface occurs. In CO_2/H_2O coelectrolysis conditions, surface deposit of C has a constant rate which does not depend on the applied potential.[108] Table 1 summarizes the binding energies of O 1s and C 1s photoelectron peaks for different types of adsorbed species formed on Cu and Cu/oxide surfaces under CO_2-containing gas environments.

Table 1-1 The binding energies of surface oxygen and carbon species formed on various Cu-based catalytic surfaces under CO_2 containing environments.

Sample	Gas	C 1s and O 1s Binding Energies (eV)					Ref.
	CO_2	$CO_2^{\delta-}$	$HCOO^-$	CO_3^{2-}	OH^-	$-OCH_3$	
Cu(111)	CO_2	288.4	-	-	-	-	93
Cu (111)	CO_2, H_2O	288.4	287.3	289.4	286.3	-	101
$Cu_{x=1.5}O$	CO_2, H_2O	288.4	287.3	289.4	286.3	-	101
Cu (foil)	CO_2	288.4	-	289.3	530.8	-	104
Zn/Cu	CO_2	-	-	289.3	530.8		104
Cu (foil)	CO_2, H_2O	288.4	287.3	289.3	530.8	285.2	104
Zn/Cu	CO_2, H_2O	-	287.3	289.3	530.8	285.2	104
Cu_2O	CO_2	-	-	531.9	531.1	-	104
CuO_x/Cu	CO_2, H_2	288.4	-	-	-	-	105
ZnO/CuO	CO_2, H_2	288.4	289.2	-	-	-	105
Cu (100)	CO_2	531.1	-	-	-	-	94
CeOx/Cu	CO_2, H_2	288.4	289.2	-	-	-	109
CeO_2/Cu	CO_2, H_2	289.3	289.9	-	531.5	-	110

1.3.1.2 CO_2 dissociation and hydrogenation on Ni, Co and Fe surfaces

Besides copper catalysts, nickel and cobalt are also very promising for CO_2 transformation reactions, which motivated several NAP-XPS studies of CO_2 interaction with Ni and Co surfaces. CO_2 chemisorbs strongly and dissociates to CO and AO on the Ni(110) surface even under UHV.[111] On the contrary, density functional theory (DFT) calculations predicted that on Ni (111) surfaces the adsorption of CO_2 is not energetically favoured, especially under low pressure and temperature conditions.[112] M. Salmeron's group used NAP-XPS to investigate the evolution of Ni (111) surface composition in the presence of CO_2 and CO_2+H_2 atmospheres.[113] First of all the authors showed that the so called pressure gap plays an important role in the adsorption/dissociation and methanation of CO_2 on Ni(111). In particular, CO_2 is activated over Ni (111) at mbar pressure but not under UHV conditions. As it is evident by the O 1s spectra shown in **Figure 1-7a**, at 200 mTorr CO_2 dissociates to CO

and AO forming CO_3^{2-} and NiO (characteristic O 1s components around 531.2 and 529.3 eV respectively). In CO_2 + H_2 mixtures (**Figure 1-7b**) NiO is reduced back to metallic Ni^0 (at 160 °C) followed by elimination of the CO_3^{2-} adsorbed species. A weak O 1s peak at 531.1 eV **(Figure 1-7**c) was attributed to OH and CO adsorbents and was used as an evidence to suggest that the RWGS is taking place under these conditions. Furthermore, the presence of atomic carbon at 283.3 eV (**Figure 1-7d**) indicates that the methanation reaction mechanism on the Ni(111) surface involves the reduction of CO to atomic carbon, which in a subsequent step is hydrogenated to methane. More recently, a NAP-XPS study of zeolite supported Ni catalysts reported that the coexistence of Ni and NiO on the surface facilitates the adsorption and conversion of CO_2.[114] These findings need to be interpreted with caution though, since the quality of the Ni $2p_{3/2}$ spectra and the deconvolution procedure applied in this work[114] leave also space for other interpretations.

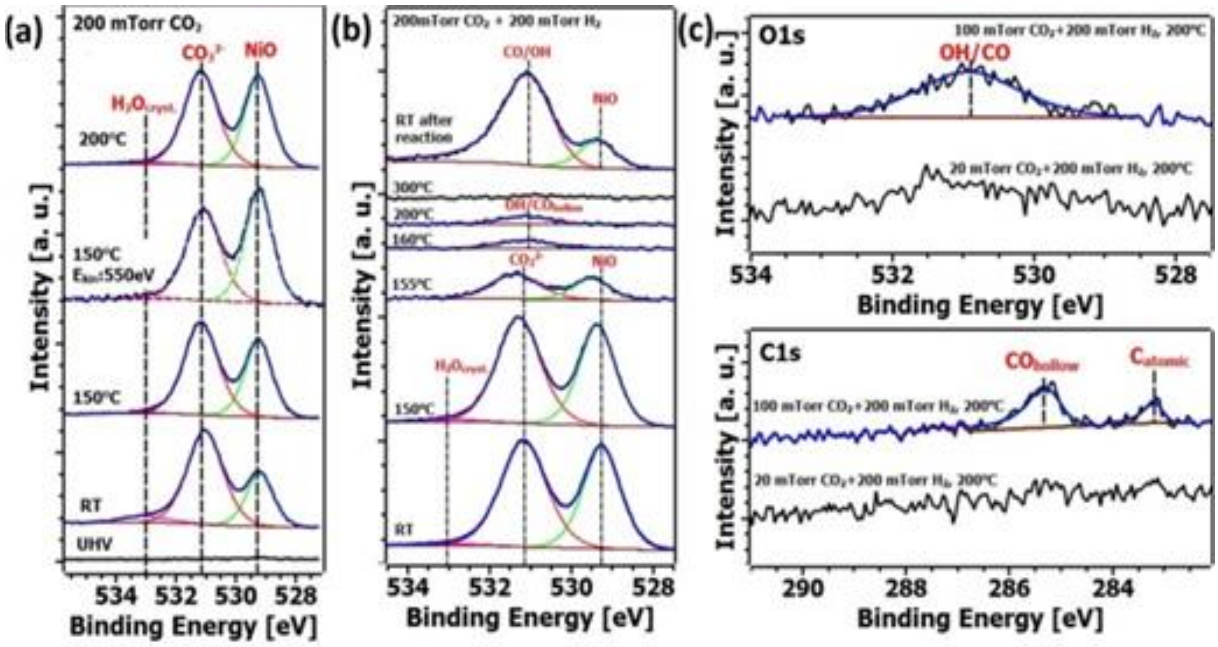

Figure 1-7. NAP-XPS spectra recorded on a Ni(111) model catalyst (a) O1s in 200 mTorr CO_2 in the temperature range from RT to 200 ºC; (b) O1s spectra in 200 mTorr CO_2 and 200 mTorr H_2 in the temperature range from RT to 300 °C. (c) O 1s and C 1s spectra in 20 mTorr CO_2 + 200 mTorr H_2 and in 100 mTorr CO_2 + 200 mTorr H_2. From ref.[113]

Detailed experimental studies focusing on the mechanism of CO_2 dissociation on well-defined cobalt surfaces are less frequent as compared to copper and nickel. Co/MnO_2 catalysts exhibited high activity and selectivity to methanol at low-pressure conditions.[115] Very recently, Liu et al. reported on the CO_2 activation over Co polycrystalline foils in the

presence of H_2O using NAP-XPS.[116] They found that the Co surface was partially oxidized, predominantly by the carbonates left by the CO_2 dissociative adsorption. Upon the co-adsorption of CO_2 with H_2O methoxy, formate and bulk carbonate species were formed, with a surprisingly high methoxy/formate coverage ratio, in line with the observation of similar studies on Cu.[104] This work gives hints that cobalt and copper might interact with CO_2:H_2O mixtures in a very similar way and can be used for future development of highly selective Co-based catalysts for CO_2 reduction.

Besides heterogeneous catalysis, the NAP-XPS approach was applied to the investigation of photocatalytic and electrocatalytic CO_2 conversion on Co and Fe. The photocatalytic hydrogenation of CO_2 was examined over cobalt/carbon composite catalysts promoted with Na and revealed the effect of light irradiation on the surface intermediate species during CO_2 hydrogenation reaction.[117] The electrochemical CO_2 reduction reaction over iron oxyhydroxide nanostructures (i.e. FeOOH) supported on O- and N-doped graphite has been studied by applying a combined experimental and theoretical approach.[118] NAP-XPS showed that a chemical interaction occurs between Fe sites and the pyridine N species on the carbon surface, which leads to the formation of Fe(II) species. The latter are important for the CO_2 reduction since their formation dictates the potential of the electrochemical reaction.[118]

1.3.1.3 Interaction of Co, Fe and Cu with CO/H_2 atmospheres

Cobalt and iron oxides catalysts are used in commercial Fischer–Tropsch (FT) reactors to convert H_2 + CO mixtures into liquid hydrocarbons.[119,120] The advances of using Co-based catalysts for FT reaction has been extensively reviewed in the past.[121–123] However, most commonly *ex situ* characterization was used to reveal the chemical and structural features of the catalysts. Following the development of NAP-XPS, a growing number of *in situ* studies appeared focusing on the description of the catalysts' chemical state and the nature of adsorbed species. Certainly one should be extremely cautious when evaluate the results of NAP-XPS studies of FT reaction due to the significant pressure gap between the spectroscopic studies, performed in few mbar, and the realistic FT reaction conditions, extending to several tens of atmospheres. Although it is rather unlikely to observe any meaningful catalytic turnover of the FT reaction in a NAP-XPS cell, the results can serve as a basis to understand the modification of catalytic surfaces in contact with the FT reactants.

Salmeron's group used NAP-XPS to investigate the evolution of the chemical state of a cobalt foil in equilibrium with pure CO, H_2 and their mixture,[124] with the aim to understand better their influence on the cobalt surface state. It was found that at low temperature the surface of cobalt is oxidized even in a reducing mixture of 100 mTorr CO + H_2, but eventually it is rapidly reduced back to metallic Co^0 at higher temperatures. The partial pressure of H_2 in the mixture affects the reduction temperature. Formation of cobalt carbides was detected when cobalt surfaces were annealed at high temperatures and are correlated to the reduction of cobalt oxides from CO.

Monodispersed 10 nm Co particles on TiO_2 and SiO_2 supports were examined in CO/H_2 and CO_2/H_2 mixtures.[125] The authors noticed that in both reactions, the Co/TiO_2 catalyst performs better when Co is partially oxidized as compared to the fully reduced cobalt state. On the contrary, the Co/SiO_2 catalyst has higher activity when cobalt is metallic. NAP-XPS helped to reveal partial encapsulation of metallic Co by TiO_{2-x} which eventually is related with the poor performance of this sample.[125]

Similar studies were also performed over nanosized and bulk iron oxide catalysts under $CO+H_2$ reaction mixture and temperatures up to 350 °C.[126] By combining NAP-XPS and DFT calculations the authors explained the relation between the formation of surface, subsurface, and carbide carbon species. Nanosized iron oxide catalysts change their surface state more readily as compared to their bulk equivalent, with the latter being more susceptible to oxidation and carbon deposition.[126] Very recently Niemantsverdriet and co-workers studied in detail carbon deposition on iron using Fe particles on planar supports (Si or SiO_2) in 1 mbar CO.[127] CO adsorbs stronger on Fe/Si as compared to Fe/SiO_2, which leads to lower onset temperature for carbidization. The authors found that carbidization is hampered by oxygen remained on Fe after CO dissociation. The abundance of the oxygen species on Fe is controlled by the type of the support. In particular, oxygen readily spill over from Fe to Si but not to SiO_2 support and as a consequence in the latter case Fe carbidization is hindered.[127]

NAP-XPS was used to investigate the surface composition of industrial $Cu/ZnO/Al_2O_3$ catalysts during methanol synthesis from synthesis gas mixtures ($H_2/CO_2/CO$). During activation the Cu to Zn NAP-XPS intensity ratio drops significantly, signifying spillover of ZnO_x on the Cu surface. With the aid of other analytical methods and DFT calculations the authors concluded that the active sites of the reaction consists of Cu steps decorated with Zn

atoms, which are stabilized with the aid of bulk defects.[128]

1.3.2 Catalytic oxidation reactions

Transition metal oxides have been widely used for catalytic oxidation reactions due to their ability to readily interchange among their various oxidation states under oxygen-containing atmospheres. In this section we considered oxidation reactions in the formal way i.e. increase in the formal oxidation number of the carbon atoms. Accordingly, reactions such as water-gas shift are also included in the discussion.

1.3.2.1 CO oxidation, preferential oxidation, and water gas shift

CO oxidation is maybe the most well-investigated catalytic reaction in surface chemistry, due to its presumed simplicity and of course in view of its great commercial interest.[129,130] Catalysts containing noble metals, such as Pt, Au and Pd, have shown excellent performance for CO oxidation and they are also selective for CO oxidation in the presence of H_2 (preferential oxidation).[1,131] However, non-precious metal catalysts like copper and cobalt have been proposed as inexpensive alternatives of noble metals.[130] In this section, recent NAP-XPS studies of transition metal-based catalysts for CO oxidation and preferential CO oxidation in H_2 are discussed.

Copper-based catalysts

The nature of the most active catalytic surface state of transition metal-based catalysts is very often a matter of debate in the relevant literature and NAP-XPS might be useful to provide conclusive elements. The active surface state of cobalt and copper during CO oxidation has been explored by NAP-XPS in combination with other techniques. Svintsitskiy et al. studied CO oxidation over oxygen deficient CuO NPs (NPs).[132] This study was performed in one of the first laboratory NAP-XPS apparatuses, therefore the reaction pressure during the in situ experiments was limited to 10^{-5} mbar. Nevertheless, based on Cu LMM and Cu 2p spectral analysis the authors' detected surface reduction of Cu^{2+} to Cu^{+}, suggesting that CuO is transformed to Cu_4O_3 under certain reaction conditions. They defined also O^{-} as the most active oxygen species on the surface of copper suboxides during the reaction.

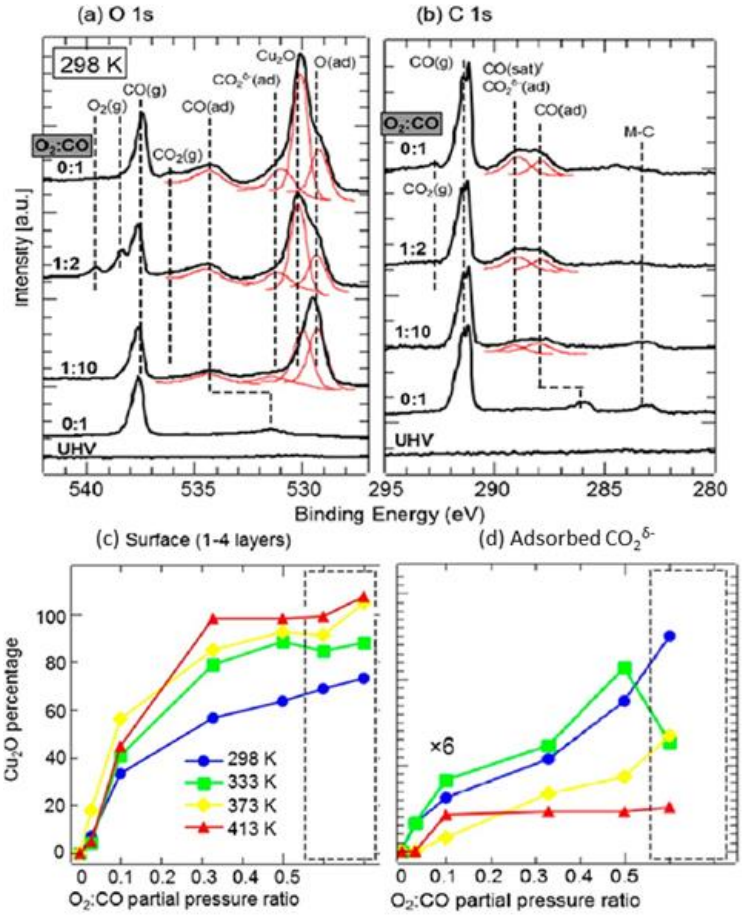

Figure 1-8 The O 1s (a) and C 1s (b) NAP-XPS spectra from a Cu (111) sample at 298 K in UHV and under various CO: O_2 reaction mixtures. The evolution of (c) the Cu_2O coverage and (d) the adsorbed $CO_2^{\delta-}$ species as a function of O_2/CO pressure ratio at different reaction temperatures obtained by analysis of NAP-XPS spectra. Reproduced from[133].

Later, Eren's et al. compared the reactivity of CO with oxygen chemisorbed on three different low-index surface planes of copper single crystals.[134] In order to determine the reaction rates, the O 1s NAP-XPS peak intensity was measured as a function of time, pressure, and temperature. Eventually, it was found that Cu (111) is the most active surface plane for CO reaction followed by Cu (100), while Cu (110) is the less active crystallographic plane. Although STM image analysis indicated reconstruction of Cu surfaces during reaction, no indications of copper surface oxidation were given in this work. In a subsequent report by the same group,[133] the CO oxidation was examined in detail over the most active Cu crystallographic plane, i.e. the Cu(111) surface. In this study NEXAFS was used to distinguish the oxidation state of copper catalyst, since Cu_2O and Cu have practically the same Cu 2p NAP-XPS spectra.[135] It was shown that the copper surface oxidation state

depends on the $CO:O_2$ partial pressure ratio. In particular, below 3:1 of $CO:O_2$, the surface contains chemisorbed O over a 1 nm thick Cu_2O layer. In O_2 mixtures the thickness of the copper oxide layer increases (>4 nm), however the oxidation state of copper remains as Cu_2O. Interestingly, further oxidation of Cu_2O to CuO was not observed to any stage of the reaction. As shown in **Figure 1-8**a and b, adsorbed $CO_2^{\delta-}$ was the main reaction intermediate observed during CO oxidation. In addition, the authors noticed that the coverage of $CO_2^{\delta-}$ is proportional to the amount of Cu_2O, which accordingly suggests that the Cu_2O phase is more active than metallic Cu for CO oxidation. The $CO_2^{\delta-}$ species seems to play a key role also for the water-gas shift (WGS) reaction over CeO_x/Cu(111) inverse catalyst.[136] In this case the precursor for $CO_2^{\delta-}$species formation is a carboxy (HCOO) intermediate on the metal–oxide interface.[136]

The important role of Cu_2O for CO oxidation was indicated also in reference[137] by investigating titanium-copper mixed oxide films. The incorporation of titanium cations into Cu_2O leads to the formation of a stable mixed-metal oxide with the Cu^+ terminated surface being highly active for CO oxidation. The presence of titanium prevents the facile oxidation and reduction of the Cu_2O films under the reaction conditions, thereby enhancing the robustness of the catalyst. Recently, Shao-Horn's group investigated CO oxidation over copper-substituted ceria NPs.[138] Based on the analysis of NAP-XPS and *in situ* infrared spectroscopy, it was suggested that CO_3^{2-} is formed on these surfaces in the absence of O_2 and can be desorbed only in oxygen-rich conditions. Moreover, there is a dramatic and reversible reduction of copper cations in the NPs lattice under reaction conditions.[138]

Cobalt and iron-based catalysts

Apart from copper, cobalt is another promising catalyst for CO oxidation at low temperature or in the presence of H_2 (preferential CO oxidation reaction).[5] It has been reported that Co_3O_4 (110) surfaces can convert CO into CO_2 at temperature as low as -77ºC.[51] However, the active state of cobalt for CO oxidation is controversial and several NAP-XPS studies attempted to resolve this issue. For example, in the study of CO preferential oxidation using Co_3O_4 nanopowder, the NAP-XPS results indicated that in hydrogen-rich reaction mixtures cobalt is maintained as Co_3O_4 from room temperature up to 300 ºC, implying that Co_3O_4 is the active surface species.[6] However, an earlier NAP-XPS report from Tao's group,[9] recommended the nonstoichiometric Co_3O_4 as the active catalytic state during CO

preferential oxidation. In addition, in a third NAP-XPS work examining CO oxidation over PtCo catalysts, it was suggested that the CoO/Pt interface formed in situ during the CO oxidation reaction is the active state.[8] Besides, more recent evidences provided again by Tao and co-workers found that above 140 ºC the CoO surface is oxidized into Co_3O_4 during CO oxidation reaction and this is followed by an increase in the reactivity.[139]

G. Rupprechter's group in collaboration with researchers from the Fritz-Haber institute in Berlin, used several *in situ* methods to monitor CO oxidation over Co_3O_4 surfaces.[140] The Mars-van-Krevelen mechanism was found to be the reaction pathway under steady state and dynamic conditions above 100 °C. The mechanism involves the Co^{3+}/Co^{2+} redox couple and oxygen vacancy formation, but under steady state conditions the Co_3O_4 surface appeared completely oxidized and CoO was not detected. Carbonate formation was noticed in the course of the reaction, but these species were considered mostly as spectators rather than active intermediates.[140] On the contrary in an earlier NAP-XPS work it was suggested that above 100 °C carbonates are not inhibitors but intermediates of CO oxidation on Co_3O_4.[141] In the same study it was shown that CO oxidation depends not only on Co^{3+} concentration but it is also influenced by the Co^{3+}/Co^{2+} ratio measured on the catalyst surface.[141] Overall, the review of the above studies suggests that there are no conclusive and converging literature arguments regarding the most active state of cobalt for CO oxidation or preferential oxidation in the presence of H_2.

The high temperature WGS reaction ($CO+H_2O \rightarrow CO_2+H_2$) was investigated on Cr and Cu-promoted bulk α-Fe_2O_3 (hematite) catalysts using several in situ methods including NAP-XPS, by Wachs and co-workers.[142,143] In Cr-promoted Fe_2O_3 catalysts, surface analysis under working WGS reaction conditions revealed that the α-Fe_2O_3 phase becomes partially reduced to Fe_3O_4 (magnetite). In parallel the Cr^{6+} promoter is reduced to Cr^{3+} and dissolves into the bulk of iron oxide forming a solid solution. Similarly, in Cu-promoter Fe_2O_3, Cu^{2+} cations are reduced to metallic Cu during WGS reaction. However contrary to chromium, during the WGS reaction copper is still present at the surface as nanosized-particles over iron oxide. The authors concluded that iron oxide is the catalytic active sites for WGS/RWGS and Cr mainly acts as a structural stabilizer in the bulk of iron oxide, while Cu is a chemical promoter by providing new catalytic active sites at the surface.[142,143]

1.3.2.2 Catalytic oxidation of methane and ethylene

Transition metals catalysts are used in other important oxidation reactions, such as oxidation of methane and ethylene. The investigation of these reactions using NAP-XPS provides important atomic-level information and assists to the comprehension of the reaction mechanisms. NAP-XPS studies of methane oxidation ($CH_4+O_2 \rightarrow CO_2+H_2O$) have been performed over $NiFe_2O_4$,[144] Ni-ZrO_2[145] and Co/CeO_2[146] catalysts. In case of the $NiFe_2O_4$ catalyst Ni and Fe were found in mixed Ni^{2+}/Ni^{3+} and Fe^{2+}/Fe^{3+} oxidation states. These states were stable in the CH_4:O_2 (1:5) reaction mixture at temperatures varying from 25 to 400 °C. The evolution of C 1s photoemission features and the calculated C/(Ni+Fe) atomic ratios suggested that formate-like intermediates are transformed to CO_2 and H_2O products.[144]

In another work the reactivity of Ni and NiCu alloy catalysts supported on ZrO_2 for methane decomposition was examined at temperatures up to 450 °C.[145] The formation of reduced Ni species on the surface due to the interaction with CH_4, promotes the catalytic activity. The addition of Cu lowers the amount of coke and improves the desired resistance of Ni against carbon deposition. However, the stability of NiCu alloy catalysts is limited in a narrow temperature window (up to 430 °C). This was ascribed to carbon-induced surface segregation of Ni over Cu, which boosts the methane decomposition reaction path and consequently carbon deposition.[145]

In the case of Co_3O_4/CeO_2 composite catalyst, the active surface phase during methane oxidation is a mixture of Co_3O_4 and CeO_2, while a CH_3-like intermediate specie was detected.[146] Interestingly, when the same Co_3O_4/CeO_2 composite catalyst was tested in methane reforming reaction ($CH_4+CO_2 \rightarrow 2CO+3H_2$) a clear transition of Co_3O_4 to metallic Co and Ce^{4+} to Ce^{3+} was found above 400 °C.[147] This difference in the oxidation state of the Co_3O_4/CeO_2 composite in the two reaction environments is a clear consequence of O_2 replacement by CH_4, which transforms the reaction mixture from oxidizing (CH_4+O_2) to reducing (CH_4+CO_2) environment for the cobalt catalyst.

Ethylene epoxidation ($7C_2H_4+6O_2 \rightarrow 6C_2H_4O+2CO_2+2H_2O$) over Ag, Cu and bimetallic AgCu catalysts has been studied by *Schlögl's* group using NAP-XPS for more than a decade now.[148–154] As mentioned above, Cu_2O and metallic Cu^0 have almost identical Cu 2p photoemission spectra,[135,155] therefore in most cases the Cu LVV Auger peak or the Cu

$L_{3,2}$-edge NEXAFS spectrum was alternatively used to distinguish between these two copper oxidation states. *In situ* photoemission spectroscopy showed that the oxidation selectivity of ethylene to ethylene epoxide over unsupported copper oxide powders is boosted when the catalyst surface is in the Cu_2O-CuO transition phase.[153] DFT results explained that the increase in the ethylene epoxide selectivity is caused by the formation of metastable O precursors created during the Cu_2O-CuO phase transition.[153] The *in situ* Cu-L_3 edge NEXAFS spectra measured under a mixture of C_2H_4:O_2 (1:1) and the corresponding catalytic activity measured *on line* is shown in Fig.5a. Analysis of these curves revealed that as the reaction temperature increases a CuO to Cu_2O phase transition takes place at about 200 °C. On line gas phase analysis showed that at this particular temperature the selectivity to ethylene epoxide was optimized (**Figure 1-9**b). On the contrary, when the surface state was stabilized to Cu_2O or fully oxidized CuO states, the reaction is less selective to ethylene epoxide. In a more recent study of the same group over AgCu alloy catalysts it was proposed that several forms of oxidic Cu coexist simultaneously on the active catalyst's surface, namely CuO, Cu_2O and some previously unreported form of oxidized Cu, referred as Cu_xO_y.[152]

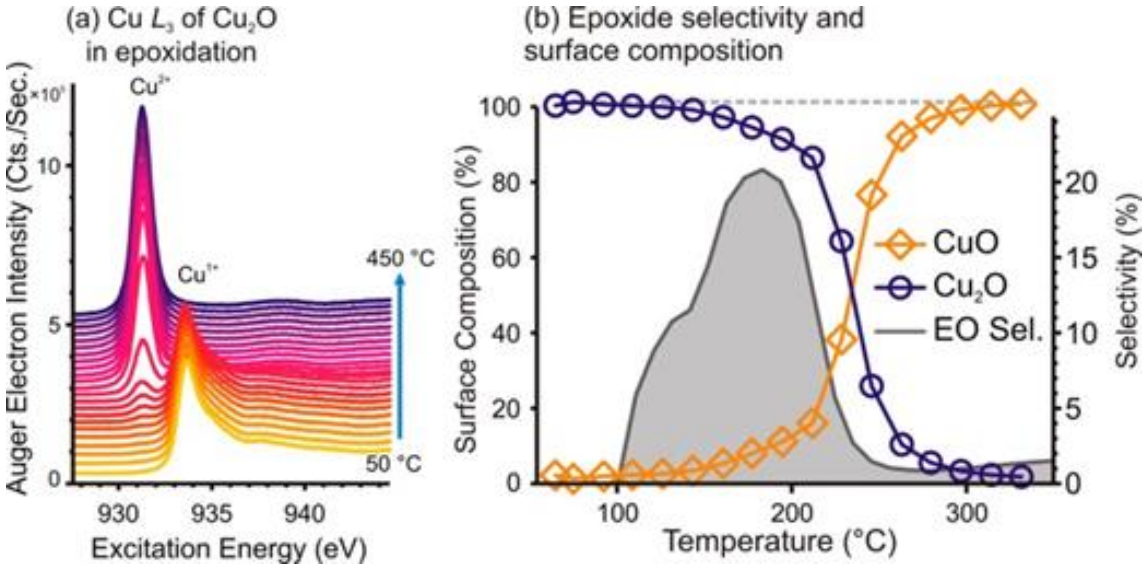

Figure 1-9. (a) In situ Cu L_3-edge spectra measured while heating Cu_2O in 0.3 mbar of O_2:C_2H_4. (b) Ethylene epoxide selectivity measured using gas chromatography during the temperature ramp, with the corresponding proportions of Cu_2O and CuO on the surface, as determined from the spectra in (a). Reproduced from[153]

1.3.3 Conversion and reforming of alcohols

Conversion of alcohols to other demanding chemicals has been the subject of a large numbers of studies focusing to understand the chemistry of the catalysts.[156] Several alcohols including, methanol, ethanol, 1-propanol, and 2-propanol, react with transition metal surfaces forming alkoxy hydroxyl species.[157] The active oxidation state of certain transition metals was investigated using model catalysts via NAP-XPS.

1.3.3.1 Partial oxidation and steam reforming of alcohols

Catalytic oxidation of methanol over transition metal catalysts is used to convert methanol to more valuable chemical compounds. Actually there are two main reaction paths of methanol oxidation: total ($CH_3OH+3/2O_2 \rightarrow CO_2+2H_2O$) and partial ($CH_3OH+1/2O_2 \rightarrow CH_2O+H_2O$) oxidation, with the latter being of particular importance since it is directly applied in industry for formaldehyde production.[158] Previous NAP-XPS studies of methanol oxidation have been mainly focused on the effect of the catalyst's surface on the dissociation of methanol. Cu-based catalysts are very active in methanol oxidation and therefore Cu was one of the first elements studied by NAP-XPS for this reaction. A key factor of the reactivity is the nature of the oxygen species on copper.

In 2003, Bukhtiyarov's group used a laboratory-based NAP-XPS to study methanol oxidation on a polycrystalline copper foil. It was proposed that when the Cu surface is covered with methoxy species it becomes inactive for formaldehyde production, while the catalyst turns again active when a copper sub-oxide is formed, detected at 531.2 eV in the O 1s spectrum.[157,159] More detailed information about the sub-oxide oxygen species on copper was given in a following publication in collaboration with *Schlögl's* group,[100] using a synchrotron-based NAP-XPS spectrometer (at this time still a prototype) at BESSY II facility in Berlin.[100] Synchrotron radiation gave the opportunity to perform photon-energy-dependent depth-profiling and describe in detail the "sub-oxide oxygen species" reported before. Analysis of the O 1s peak recorded during methanol oxidation revealed the presence of at least 3 oxygen species: *lattice* oxygen of Cu_2O at 530.3 eV, *subsurface* oxygen at 530.4 eV and *surface* oxygen at 532 eV. The subsurface oxygen was clearly correlated to the enchantment of the catalytic activity which was the first direct proof not only for its existence, but also about its important role in catalysis. Interestingly, sub-surface oxygen vanish when

the reaction is terminated and can be only observed by following an *in situ* surface sensitive approach.[100] Please note that there is a considerable shift in the reported O 1s binding energies between "sub-oxide" at 531.2 eV [159] and "sub-surface" oxygen species at 530.4 eV,[100] which allows one to suppose that the nature of these two types of oxygen species might be considerably influenced by the conditions.

Almost 15 years later from the work of Bukhtiyarov and *Schlögl*, the interaction of methanol with clean and oxygen-coved Cu (100) single crystal surfaces was investigated by NAP-XPS and high pressure scanning tunnelling microscopy at room temperature.[160] It was shown that methanol adsorbs dissociatively over clean Cu (100), to form methoxy species. When AO is pre-absorbed on Cu (100), methanol reacts with it to produce adsorbed methoxy and formate species, and consequently formaldehyde that desorbs to the gas phase. The authors proposed that the surface oxygen originates from segregation of O previously dissolved in the subsurface region of the Cu crystal,[160] but one should not confused it with oxygen dissolved in the bulk, since the latter is kinetically trapped and needs much higher temperatures to diffuse on the surface. [99]

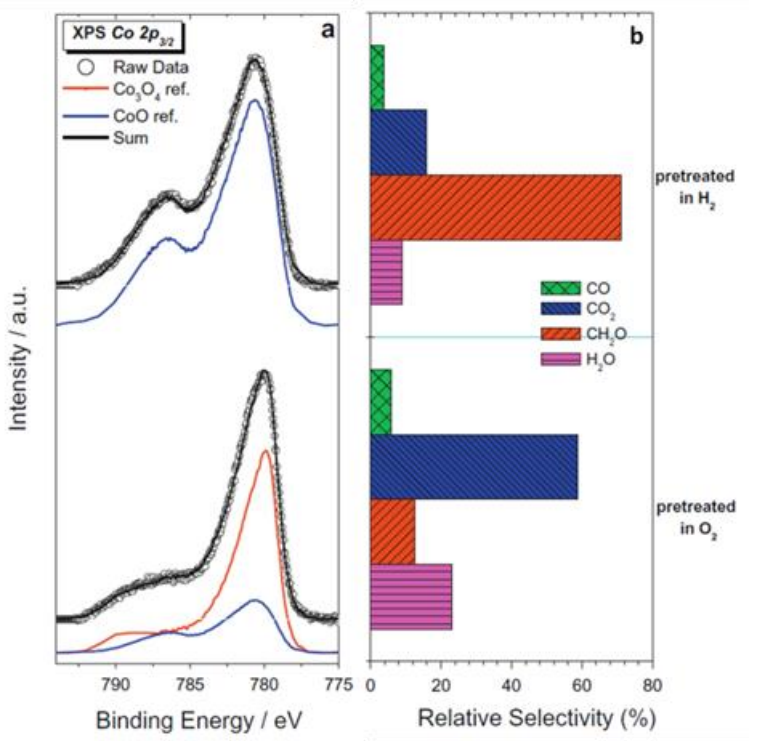

Figure 1-10. a) Co 2p3/2 XPS (hv = 965 eV), b) relative product selectivity of H_2 and O_2 pre-treated Co(0001) measured by *on line* mass spectroscopy during NAP-XPS. (250 C, in 0.3 mbar $CH_3OH:O_2$ = 1:5). From ref. [161]

Similar to copper, cobalt also reacts with methanol via the formation of surface methoxy species. However, the surface coverage of those species was not proportional to the catalytic activity, indicating that instead of intermediates, they might also act as reaction inhibitors.[161] The composition of the $CH_3OH:O_2$ reaction mixture influences the surface oxidation state of cobalt. As shown in **Figure 1-10**, CoO surfaces favour the partial oxidation of methanol to formaldehyde, while mixed CoO/Co_3O_4 the total oxidation to CO_2. In the absence of oxygen in the mixture, methanol effectively reduces cobalt to the metallic state, promoting H_2 and CO production.[161]

The intermetallic compound ZnNi has been tested in methanol steam reforming, showing considerable performance changes during the catalytic process.[162] NAP-XPS experiments proved that ZnNi surface is modified under the reaction mixture as a function of time and temperature. Based on both surface and bulk analysis of the ZnNi compound, the substitutional $Ni_{70}Zn_{30}$ alloy was proposed as a possible candidate for improved methanol steam reforming catalysts.

1.3.3.2 Ethanol steam reforming over Co/CeO_2 catalysts

The ethanol steam reforming reaction, abbreviated as ESR, ($C_2H_5OH+3H_2O\rightarrow6H_2+2CO_2$,) is a well-known catalytic process used for hydrogen generation from bio-sources.[163] Among the various ESR catalysts, cobalt-based catalyst has shown an exceptionally good performance at relatively low temperature.[164,165] **Figure 1-11** compares the NAP-XPS and NEXAFS spectra of cobalt recorded over different cobalt-based catalysts in H_2 and ESR reaction conditions.[164] The Co/ZnO maintains the CoO phase during ESR reaction, while in case of unsupported or CeO_2-supported catalysts cobalt is totally reduced to the metallic state.

The surface chemistry of Co/CeO_2 catalysts during ESR has been studied using both realistic[165] and model[166] catalysts. Using Co deposited on CeO_2 (111) support, Óvári et al. showed that cobalt promotes partial reduction of ceria. During the ESR reaction reduction of Co^{2+} to metallic Co^0 and Ce^{4+} to Ce^{3+} occurs up to 600 ^oC, accompanied by carbon deposition on the surface.[166] Similar results also found on realistic powder Co/CeO_2 catalysts by combining NAP-XPS with post mortem XPS analysis in a wide reaction pressure range (0.2–20 mbar).[165] This study revealed that the active surface state is formed primarily under the ESR reaction mixture and the catalytic pretreatment has a limited effect on the surface

characteristics. In the presence of metallic cobalt and reduced ceria, CO production is favoured, while the ionic cobalt species promotes higher CO_2 and acetaldehyde (CH_3CHO) yields. Correlation was found between the population of adsorbed hydroxyl groups and the reduction degree of ceria; however, under the examined low-pressure conditions, hydroxyl groups act more as inhibitors than as promoters of the ESR reaction rate. Remarkably, more oxidized ceria supports are in favour of the ESR reaction. Reduction of ceria support is facilitated by cobalt particles through hydrogen spillover, while reduced CeO_x has a higher number of oxygen vacancies as compared to CeO_2 enhancing in this way the oxygen mobility under ESR conditions.[167] Among others, the oxidation state of ceria during ESR reaction is influenced by the size of the ceria grains. Particularly, more Ce^{3+} was formed on nanosized Co/CeO_2 as compared to micro-sized Co/CeO_2, while as expected the reduction degree of ceria and cobalt during ESR reaction increases with temperature.[167,168] .

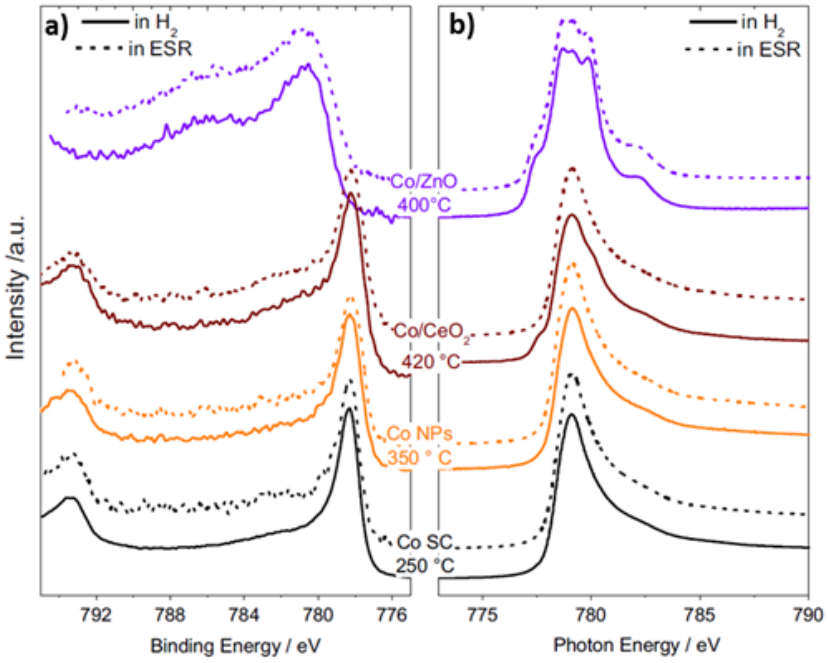

Figure 1-11. (a) The Co2p NAP-XPS spectra and (b) Co-L_3 edge in situ NEXAFS spectra of different cobalt-based catalysts under 0.2 mbar H_2 and 0.3 mbar of C_2H_6O: H_2O =1:3 (ESR) atmospheres. Reproduced from [164].

The above NAP-XPS studies of Co/CeO_2 agree that both cobalt and ceria in Co/CeO_2 catalysts undergo a reduction process during the ESR reaction, which is enhanced with temperature. Llorca's group explore the effect of Co oxidation state on the ESR reactivity by examining three different cobalt-based catalysts under the same ESR reaction conditions.[169]

These tests highlighted that the degree of metallic cobalt during ESR reaction is different in each case, with the catalysts prepared from $[Co_2Mg_4Al_2(OH)_{16}]CO_3 \cdot 4H_2O$ remaining oxidized both at the surface and in the bulk, in contrast to the other two catalysts. According to the authors, the absence of metallic cobalt formation under ESR reaction conditions enhances the stability of the catalyst, since metallic Co induces carbon deposition that provokes deactivation during ESR.

1.3.4 Studies of bimetallic catalysts composed of non-noble, late transition metals

The replacement of monometallic catalysts by bimetallic NPs (NP) has emerged as an attractive approach in the attempt to control their catalytic properties and develop better performing materials. This is because, bimetallic particles (or as sometimes referred "alloyed particles") not only combine the properties of the two individual metals, but also may possess new properties due to their synergy.[170] Several NAP-XPS studies exists over bimetallics composed of transition and noble metal elements,[44,171,180,181,172–179] however since noble metals are out of the scope of this review we will not discussed them here and some relevant information can be found elsewhere.[182] **Table** 1-2 provides an overview of NAP-XPS studies on bimetallic catalysts composed by late transition metals.

The NAP-XPS technique permits to distinguish between the outermost surface (shell) and the inner part (core) of the NPs, contributing to our understanding of surface segregation phenomena during catalytic reactions. Segregation at the near surface region is probed typically by depth-dependent NAP-XPS measurements, consisting of recording the same photoelectron peak by using various photon energies. In this way the inelastic mean free path of the photoelectrons is modified, so as the analysis depth of the technique. Finally, the evolution of photoelectron peaks intensity ratios is combined with the analysis depth and in this way segregation phenomena are identified.[183]

Mixed CuO/Fe_3O_4 catalysts in $CO+H_2$ mixtures were investigated by NAP-XPS in order to understand better the role of copper promoters on iron-based FT catalysts. For unsupported catalysts the reduction of CuO to Cu^0 above 180 °C marks the onset of Fe_3O_4 reduction to α-Fe. When CuO/Fe_3O_4 is supported on SiO_2, Cu and Fe oxides are only partially reduced, even after treatment at 350 °C. XPS showed that after reduction, Cu enhances oxygen and

carbon surface species on the catalysts, which is taken as an indication that Cu modifies the surface chemistry of Fe-based FT catalysts.[184]

Table 1-2 Reported NAP-XPS studies of non-noble late transition metals bimetallic systems.

Bimetallic System	Form	NAP-XPS tested Conditions	References
Cu-Fe	CuO/Fe_3O_4 mixed oxide	CO_2+H_2 up to 350 °C	184
CoNi	25-45 nm CoNi NPs on Au foil	O_2, H_2, CO_2+H_2 up to 270 °C	185,186
NiCu	NiCu on ZrO_2	O_2, H_2, CH_4 up to 500 °C	145,187
	11 nm NPs on SiO_2	O_2, H_2, CO+H_2 up to 450 °C	188
	5 nm NPs on SiO_2	O_2, H_2, CO_2+H_2, CO_2 up to 400 °C	189
	15 nm NiCu NPs on graphite	H_2 at 250°C	190
CoCu	11 nm NPs on SiO_2	O_2, H_2, CO_2+H_2, CO+H_2 up to 450 °C	188,191, 192
	Co deposition on Cu(110) (surface alloy)	CO at 127 °C	193

CoNi NPs with sizes ranging from 25-45 nm were dropped casted on an Au foil and heated up to 270 °C in O_2, H_2 and CO_2+H_2 mixture.[186,194] After each gas treatment the sample was cooled down, gases were pumped out and XPS spectra were collected. Although the authors referred to these measurements as (N)AP-XPS,[186,194] the way the experiment was done resembles more to ex situ analysis rather than operando. In addition, the fitting procedure of the NAP-XPS peaks shown in ref.[186] is debatable due to the high number of peaks used and the ill-defined fitting parameters (i.e. background, peaks shape and width, unfortunate choice of Au support due to overlapping with Au 5p region etc.). Still, by combining NAP-XPS with microscopy, the authors claimed that Ni enriches the surface of the CoNi NPs for both O_2 and H_2 atmospheres, but in H_2 the surface was slightly richer in nickel than in O_2.[186] This result agrees with a previous *ex-situ* XPS study of CoNi polycrystalline foils which proposed that in oxidative atmosphere Co segregates over Ni.[195] Under CO_2+H_2 the outer surface layer of the

CoNi NPs forms a metallic alloy with 1:1 Co:Ni ratio.[186,194] An important finding of this work (which actually does not require an operando approach) is that due to the synthesis procedure phosphorus, was incorporated in the NPs and segregated to the surface during reaction. It is almost certain that the presence of phosphorus will influence the reactivity of CoNi during hydrogenation of CO_2 but this was not discussed in detail.

NiCu has been studied by 4 groups the last 5 years, using both synchrotron and laboratory based NAP-XPS. NiCu on ZrO_2 was synthesized by impregnation and investigated for methane decomposition up to 500 °C, in order to understand why Cu rich bimetallic systems show improved coke resistance. The analysis indicated that the surface of NiCu is enriched with Cu in H_2, while in CH_4 the onset of CH_4 decomposition coincides with the segregation of Ni on the surface. By combining operando spectroscopy with DFT calculations the authors argue that independent of the initial Cu:Ni ratio under CH_4 reaction conditions the NiCu-ZrO_2 catalyst adopts a specific Ni rich surface.[187]

Somorjai's group investigated 11 nm NiCu and CoCu NPs supported on a planar SiO_2 support under O_2, H_2, CO and CO_2+H_2 (only for CoCu) environments up to 450 °C by using NAP-XPS.[188,191] The as prepared NiCu and CoCu have Ni and Co enriched shells respectively, and Cu rich core. In H_2 atmosphere Ni segregates on the surface of NiCu NPs which opposes the finding of ref.[187] In O_2 Ni is replaced by Cu (oxide). In case of CoCu NPs the surface remains rich in Cu both O_2 and H_2 atmospheres. NEXAFS measurements under CO_2+H_2 reaction conditions (2.7 bar, 1:3 CO_2:H_2, 260 °C) show that both Co and Cu exist in a fully reduced state. This is probably related to the CO_2+H_2 reaction mixture which is a highly reductive environment for the catalysts. It is worth noting that these findings are different of reports on bulk single crystals in vacuum and theoretical predictions based on the surface free energies and enthalpies of oxide formation, implying that bulk thermodynamics are not applied in nanoscale objects.[188] More recently, members of the same group, followed the near surface composition of bimetallic Co-M (M = Mn, Cu, Ru, Rh, Re) NPs during oxidation and reduction treatments by NAP-XPS. The effect of the second transition metal on the Co reduction and Co surface concentration was studied, with Re being the most effective for Co reduction.[192]

Size selected NiCu NPs supported on SiO_2 were investigated in various reactive atmospheres and temperatures.[189] The atomic percentage of Ni and Cu, calculated for 2

information depths are given in **Figure 1-12.** Evidently in O_2 atmosphere Ni is segregated over Cu, while in the subsequent H_2 and CO_2+H_2 atmospheres the structure remains practically the same. When the atmosphere turns to CO_2, Ni diffuses in the interior of the NPs and Cu goes back to the surface (see graphic representation in **Figure 1-12**). NiCu is almost totally reduced to the metallic state at 400 °C in H_2, confirming similar results reported for bigger NPs.[190] The authors noticed that the segregation trends observed in their study might be not directly applicable for other NiCu alloys since is mainly determined by the pretreatment and the degree of Ni and Cu oxidation.[189] This can explain why it is difficult to provide a universal trend about which element of the bimetallic NP will segregate at the surface under reducing and oxidizing conditions.

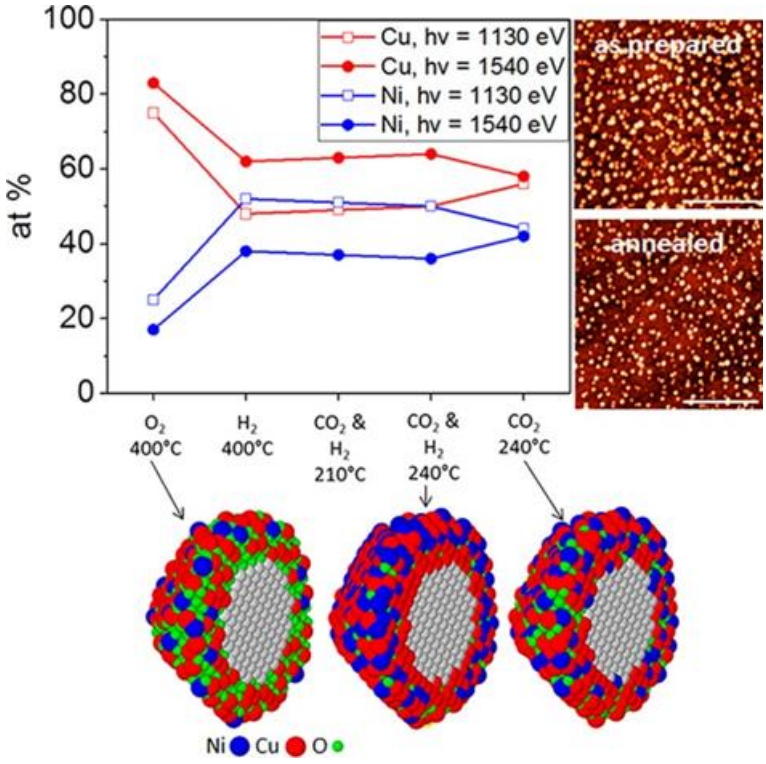

Figure 1-12. Cu (red) and Ni (blue) atomic percentages extracted from NAP-XPS measurements in the conditions indicated on the graphs. The insets show AFM images of the sample before and after the annealing (scale bar: 400 nm), as well as atomic models of the NPs, where the variation of the elemental composition with the distance from the surface, as determined by NAP-XPS, is depicted. From ref.[189]

Physical preparation methods (for example deposition of clusters from the gas phase[196]) usually provide a better control of the particle size and distribution than chemical synthesis, while do not involve organometallic reagents and protective surfactant layers, traces of which

might influence the reactivity.[189,195] On the other hand, chemical synthesis methods are typically employed to synthesize catalysts therefore is definitely a more realistic preparation method when it comes to catalytic applications. Well defined surface alloys can be also formed by vapour deposition of a metal on a single crystal surface in UHV. A CoCu surface alloy was formed by Co deposition on Cu (110) and examined in equilibrium with CO. In vacuum the Co atoms occupy preferentially the second layer sites, but in the presence of CO cobalt atoms move to the top surface layer forming structures in which multiple CO molecules attach to one Co atom. The observed BE shift of the Co 2p core level peaks due to the interaction with CO, suggests that the CoCu surface might have different catalytic properties than that of Cu or Co and in particular could reduce the probability C−O bond scission.[193]

1.4 Motivation and objectives of the thesis

The NAP-XPS studies over transition metal catalysts presented above, made clear that catalysts are not static but dynamic and the interaction with the gasses involved in the reaction (both reactants and products) can dramatically affect their chemical composition and consequently their catalytic properties. For this reason, studies of catalysts under working conditions using *in situ* and *operando* spectroscopies are imperative to understand the relationship between the surface chemical state and the reactivity. The gained knowledge of such studies can be used, in combination to approaches based on high-throughput synthesis and reaction kinetic studies, in order to design new catalysts or optimize those already existing in industry.

The literature review included in paragraph 1.2.2 suggested that cobalt oxide is the sole non-noble metal catalyst which can obtain a performance for CO oxidation comparable, if not better, to that of the noble metal-based catalysts. In spite the considerable amount of studies on the effect of morphology, structure and type of support of Co-based COPrOx catalysts, few works have focus on the identification of the active sites on cobalt surfaces during COPrOx. In the past some reaction models for CO oxidation over cobalt oxides (competing or not with H_2 oxidation, as it occurs under COPrOx conditions) have been proposed.[197198] These models are based on indirect analysis of redox or catalytic data. However, systematic studies on redox changes taking place in the cobalt catalyst surface under the reactant

atmosphere are scarce. For that reason there is not a general consensus about the nature of the active sites and in particular the active cobalt oxidation state during the reaction.

In literature the nature of cobalt active phase is mainly discussed in terms of bulk phase, neglecting the possibility of dynamic surface changes in the reaction environment, which typically are not detectable by "bulk" analysis methods.[199] In the context of the dynamic nature of the catalytic surfaces discussed above, this approach not only limits, but maybe even misleading, our current understanding of cobalt active phase for PrOx. This can also explain contradicting results concerning the activity of Co^{2+} and Co^{3+} appearing in the literature.[7,9,12,200] Inspired with the developments of the various *operando* or *in situ* analytical techniques, particularly sensitive to the surface such as XPS, NEXAFs and DRIFTs, this thesis aims to design an efficient cobalt-based COPrOx catalyst using a rational design approach. The work is divided into parts. In the first part of the thesis it is intended to identify the most active cobalt phase for the reaction. In the second part this thesis attempts to stabilize this (active) phase under reaction conditions in order to optimize the catalytic performance. In a more general context this work examines the relation between cobalt oxidation state and its reactivity to CO and H_2 oxidation, as well as the interaction between cobalt and two typical oxide promoters, namely V and Mn.

Chapter 2

Materials and Methods

2.1 Introduction

In this chapter, the materials, methodologies, and experimental techniques used in this thesis are overviewed. The studied cobalt catalysts in this thesis were commercially purchased and either used as is, or properly modified by vanadium and manganese promoters using standard synthesis methods. Catalytic evaluation has been performed on different setups equipped with Gas chromatography (GC) and/or mass spectrometry (MS). Routine characterization of fresh and post-mortem catalysts, was performed using standard laboratory methods such as X-ray diffraction (XRD), measurement of the surface area using the Brunauer–Emmett–Teller (BET) method, electron microscopies *etc*.. Advanced surface characterization based on *in situ* applied spectroscopies has been performed in collaborating research institutes and synchrotron-based laboratories. Soft X-ray adsorption spectroscopy has been used to check the coordination environment of metal atoms on the catalysts' surface. X-ray photoelectron spectroscopy (XPS), either laboratory or synchrotron based, is the primary technique used to study the surface composition and the chemical/oxidation state in this work. The principles and instrumentation of the various characterization techniques will be described in detail in the following paragraphs of this chapter.

2.2 Catalysts Preparation

2.2.1 Preparation of PreH_2-Co and PreO_2-Co catalysts

Various nanopowders of cobalt oxides were purchased from different chemicals reagents suppliers and used as precursors of cobalt-based catalysts. The basic information regarding the type of the commercial cobalt oxide used in each experiment is provided in the detailed experimental part included in every chapter. Notably, the specimens studied in chapter 3 are prepared by in situ pretreatment of commercial Co_3O_4 oxides. For the PreH_2-Co sample (abbreviation of the pre-reduced cobalt catalysts), before each measurement or analysis, the sample was reduced in pure H_2 for at least 30 min and subsequently the COPrOx mixture was introduced, thereby avoiding exposure into air. For the PreO_2-Co sample (abbreviation of the pre-oxidized cobalt catalysts), the sample was pre-oxidized in O_2 for 30 min to obtain the Co_3O_4 surface.

2.2.2 Synthesis of promoted cobalt-based catalysts

The incipient wetness impregnation (also called capillary impregnation or dry impregnation) is one of the easiest and inexpensive methods for heterogeneous catalyst synthesis. In this thesis, the loading content of the promoter (Mn or V) to the active phase (Co) is kept less than 15 at.%. The promoter precursors were firstly dissolved in a certain amount of water, the volume of which was calculated according to the water adsorption capacity of the cobalt oxide powder. Then the corresponding amount of commercial cobalt particles was impregnated into the aqueous solution of Mn or V precursor. The mixture was first let dry for 12 h at 100 ^{o}C in air and consequently calcined at 400^{o}C in air for 3h. The purity of the as-synthesized catalysts was confirmed by the XPS survey spectra.

2.3 Catalytic evaluation on fixed-bed reactor at 1 bar

The evaluation of the activity over pure CoO and promoted CoO catalysts for preferential oxidation of CO by O_2 in the presence of H_2 (PrOx) was performed in a fully automated fixed-bed flow reactor (CETRIB SARL, Andlau, France).[201] A schematic representation of the basic parts of the reactor is given in **Figure 2-1**.

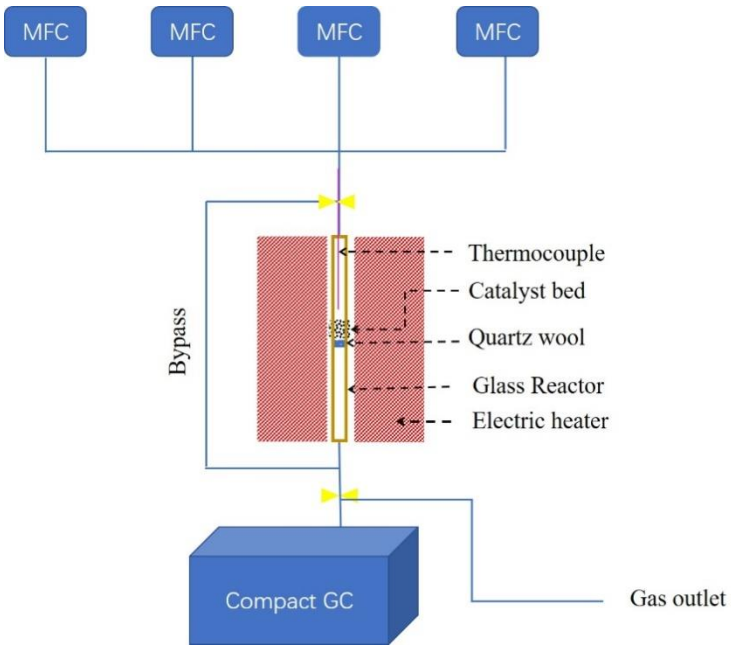

Figure 2-1. The scheme of the catalytic fix-bed reactor in ICPEES used in this thesis

A certain amount of catalyst was introduced in a Pyrex glass tube (i.d. 10 mm) and dispersed evenly on a P_3 glass frit (16-40 µm). The average thickness of the catalytic bed was

about 1 mm. The glass reactor was then introduced in a tubular oven with the catalyst bed located in the isothermal zone. The gas mixtures were generated using calibrated (Serv'Instrumentation) mass flow controllers (MFCs) from Bronkhorst. The catalyst was submitted to various temperature programs. The temperature was monitored by a type K-type thermocouple plunging inside the catalytic bed. The product analysis was performed using the back channel of a tailor-made on-line compact Gas Chromatograph (referred to as GC) (Interscience, Belgium), which allows to monitor the reaction progress. The back channel was equipped with Rt-Q-Bond (3m*0.32mm ID) and ShinCarbon (2m*0.53mm ID) columns (Restek) mounted in series and a thermal conductivity (TC) detector (Helium as a carrier gas), which allowed separation and detection of H_2, O_2/N_2, CO, CH_4 and CO_2 within 320 s using a backflush system. The response factor (concentration to surface area of GC peaks) of the corresponding gases is obtained by external calibration.

2.4 Structural and morphological characterization methods

2.4.1 BET surface area analysis

The specific surface area, which is defined as the total surface area of the catalyst per unit of mass, (with units m^2/g), is obtained by the Brunauer, Emmett and Teller (BET) method developed back in 1938. After several assumptions, the main of which being that adsorbed N_2 forms a monolayer over the catalyst, the BET-calculated surface area is deduced according to the following simplified relation:

$$S_{BET} = \frac{V \times б \times N_a}{V_m \times m} \qquad \textbf{Eq. 2-1}$$

where:

S_{BET} : specific surface (in $m^2.g^{-1}$),

V : volume of adsorbed (mL),

Na: Avogadro number ($6.023x10^{23}$. mol^{-1}),

б: surface area occupied by a molecule of gas,

V_m : molar volume ($mL.mol^{-1}$),

m: mass of the sample analyzed (g).

This formula is valid for low relative pressure values.

In this thesis, N_2-adsoprtion and Kr-adsorption (krypton) were both used for the

determination of the specific area of the analyzed materials. It is known that Kr-adsorption is more precise for small surface area due to its lower saturated vapor pressure at 77 K.[202] For material with a surface area more than 5 m^2/g, N_2 was used as the adsorbate, whereas Kr gas was used for the nonporous samples with a surface area around 1 m^2/g. The N_2-adsorption measurement was performed on a Micromeritics ASAP 2010 apparatus.

First, the sample is degassed at 250 ° C for 6 h under primary vacuum, in order to remove the adsorbed species, mainly water. Nitrogen adsorption isotherms are then measured at -196 ° C. To do this, known quantities of N_2 are successively injected into the tube containing the material. After each injection, the equilibrium pressure is measured. The amount of nitrogen adsorbed is calculated for each equilibrium pressure, which allows the establishment of an absorption isotherm. A desorption isotherm is also collected by following the decrease of the relative pressure of N_2 in the tube. Based on the isotherm plots, the BET surface area, pore volume and average pore size can be obtained. Krypton-adsorption measurements were carried out over a Quantachrome Autosorb-6B surface area analyzer in the Inorganic chemistry (AC) department AC in the *Fritz-Haber-Institute*, Berlin, Germany. Samples were degassed at 120 °C for about 5 h prior to Kr adsorption at 77 K and the specific surface areas were calculated according to the BET method using 11 data points in the relative pressure (p/p0) range of 0.05−0.3.

2.4.2 X-ray diffraction (XRD)

The three-dimensional structure of non-amorphous materials can be considered as regular, repeating planes of atoms that form the crystal lattice. When a focused X-ray beam interacts with these planes of atoms several processes take place. A part of the X-ray beam will be transmitted while another part will be absorbed by the sample. If the X-rays are considered as waves of electromagnetic radiation and the atoms of the sample as the scatterer points, then a regular array of secondary spherical waves will be produced by the interaction of the two. Like any scattering process, in most of the directions these waves interference destructively and cancel one another, but in specific directions their interference is constructive. In this case the relation between the spacing of the diffraction planes and the incident angle is determined by applying Bragg's Law, shown in **Figure 2-2**:

$$\lambda = 2d_{hkl} \sin\theta$$

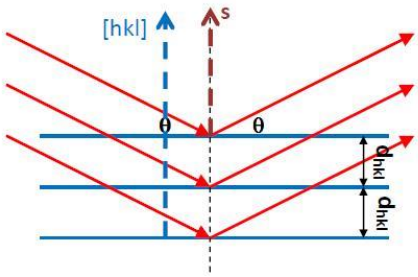

Figure 2-2. Equation (left) and scheme of Bragg's Law (Right).

The distance between the atomic planes (d_{hkl}) is a function of the wavelength (λ) of X-rays and the angle (θ) between the atomic plane and the sample. For parallel planes of atoms, with a space d_{hkl} between the planes, constructive interference only occurs when Bragg's law is satisfied.[203] For common lab-based X-ray diffraction, the wavelength of X-rays is fixed. Consequently, a family of planes produces a diffraction peak only at a specific angle 2θ. The characteristic set of d-spacing generated in a typical X-ray scan provides a unique "fingerprint" of the unit cell present in the sample. When properly interpreted, by comparison with standard reference patterns and measurements, this "fingerprint" allows for identification of the material structure.

In this work the X-ray diffraction (XRD) patterns were recorded on a Bruker D8 advanced diffractometer equipped with a Cu Ka radiation source (0.15418 nm) and a Lynxieye detector operating at 40 kV and 40 mA. A continuous mode was used to collect data in the angle range from 20 to 80 degrees at a scanning speed of 0.01 or 0.005 s. The average sizes of nanoparticles were calculated according to the Scherrer equation:[203]

$$D = \frac{K\lambda}{BCOS\theta} \times \frac{180}{\pi}$$

D is the mean size of the ordered (crystalline) domains, λ is the wavelength of the incident X-ray beam, B is the full width at half maximum of spectrum domains, θ is the Bragg's angle of the peak position and finally K is a dimensionless shape factor, with a value close to unity. The shape factor has a typical value of about 0.9 but varies with the actual shape of the crystallite. In this thesis, K value was taken 0.9, which corresponds to spherical crystals with cubic unit cells.[204]

2.4.3 Electron Microscopy techniques

Microscopy techniques provide the ability to observe the morphological characteristics of the catalysts and thus are often the tools of choice in analysis of the surface morphology before and after the catalytic reaction. In electron microscopy, high-energy electrons, with consequent short wavelengths, form an electron beam which focuses on the sample and used for the analysis. Typically, small objects in the size range down to 0.1 nm can be detected. Many different types of electron microscopes are available today and can be used depending on the type of necessary analysis, the nature of the sample and of course the availability. The most widely used microscopy techniques in catalysis research are scanning electron microscopy (SEM) and transmission electron microscopy (TEM). In case of planar/model catalytic systems, scanning tunneling microscopy (STM) and photoemission electron microscopy (PEEM) are also very informative. Due to the nature of the catalysts studied in this thesis, i.e. powder samples, only SEM and TEM have been employed.

In SEM, a focused electron beam is scanned over the surface of the sample. These electrons (primary electrons) interact with the material and are either backscattered or produce secondary electrons and X-rays. The benefit of SEM is that it can be applied to a wide range of materials, including both conductive and, with some restrictions, insulating materials. In case of very low electrical conductivity, a thin gold or carbon layer coating can provide sufficient conductivity to avoid charge accumulation on the surface. The samples analyzed by SEM in this thesis do not have particular charging problems, therefore they were measured without applying a coating.

The images provided by collecting the secondary and backscattered electrons in SEM represent primarily the sample morphology, but also other type of information can be gained. In this thesis the detection of backscattered electrons for morphological analysis and the detection of characteristic X-rays in energy dispersive X-ray spectroscopy (EDX), which provides chemical information on the studied surface, have been primarily used. Please note that since in the EDX technique X-rays are detected, the surface sensitivity is inferior as compared to XPS (some μm for EDX instead of few nm in XPS). However, the technique is useful to identify specific features on the samples, with relatively high spatial resolution. The high-resolution SEM analysis was applied to image the catalysts before and after the reaction or pretreatment. All SEM images and EDX spectra included in this work were obtained by a

Zeiss GeminiSEM 500 SEM microscope installed in ICPEES. A photograph of the instrument is shown in **Figure 2-3**.

Figure 2-3. The SEM apparatus Zeiss in ICPEES

TEM is an important high-resolution microscopy technique for the analysis of nanostructures and nanostructured materials. In TEM the image is produced by electrons transmitted through the sample. This requires very thin specimens, or in case of bulk samples e very thin cross sections are cut from the main specimen. In case of powders, like in the case here, a small amount of the sample is dispersed in a volatile solvent and subsequently is deposited on the sample holder grid. If the powder particles size is not in the nanoscale range, then the TEM beam is focused on the very near surface of the particles. Information about the particle size, morphology of particles, crystalline structure (using electron beam diffraction patterns) and chemical composition of the sample can be obtained. TEM has a number of advantages such as: high spatial resolution below one nm, powerful magnification potentially over one million times, which gives to the technique the ability to provide insight of shape, size and structure of the specimen. The main disadvantage of TEM is its high acquisition and operation cost and the requirement of a proper infrastructure assuring a vibration-isolated building free from strong magnetic fields. In addition, it requires complex sample preparation, and in case of soft mater the high energy electron beam can cause damage to the specimen and complicates the interpretation of TEM images.[205] All the TEM images of this thesis were obtained by collaborating with colleagues in ICPMS, Strasbourg. The measurements were

carried out in scanning mode (STEM) using bright field (BF) and annular dark field (ADF) detectors on a JEOL 2100F microscope working at 200 kV.

2.4.4 Temperature Programmed Reduction

Temperature programmed reduction (TPR) is usually used in heterogeneous catalysis to find the most effective reduction conditions. The reduction gas passes through the catalyst layer and the catalyst is reduced according to a certain heating program. The signal of hydrogen concentration detected by a thermal conductivity cell or a mass spectrometer as a function of temperature provides the TPR profile of the catalyst. The reduction temperature depends on the properties of the material including the oxidation state, particle size and morphology *etc*.. In the case of mixed phases, due to the interaction between the different phases, the properties of the original oxide might change and the reduction temperature will change accordingly. On the contrary, the interaction between the components can be inferred according to the degree of the mixture reduction compared to the reduction temperature of the pure compound.

In this thesis, H_2-TPR was used to monitor the optimum reduction temperature of pure cobalt oxide as well as the promoted cobalt oxide catalysts. All the tests were performed on a Micromeritics Auto Chem I 2920 analyzer, a schematic representation of which can been seen in **Figure 2-4**. Each sample was loaded in a quartz U-tube and heated with suitable heating program and gas conditions. A trap cooled with acetone/liquid-nitrogen slurry was placed before the TCD detector to retain the water produced. The quantification of H_2-consumption is performed by calibrating the H_2-concertration to TCD signal.

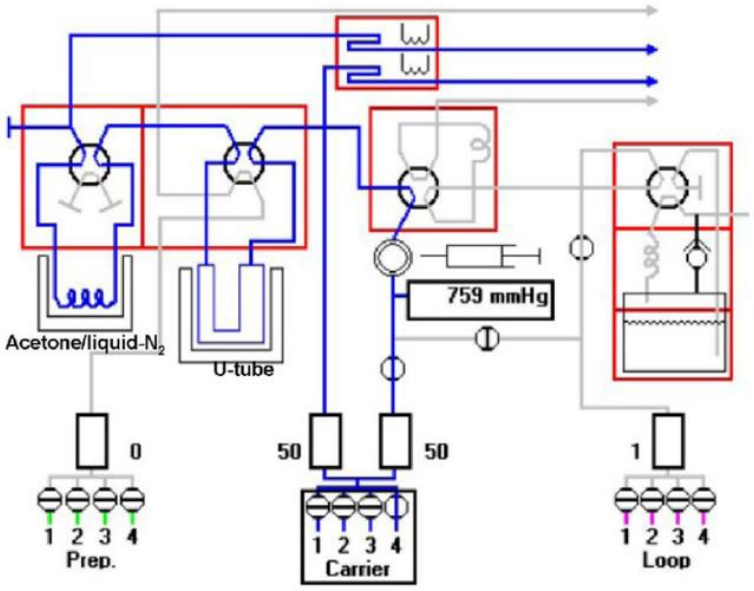

Figure 2-4. The instrumental scheme of TPR system at ICPEES, ECPM, Strasbourg.

2.5 X-ray Photoelectron Spectroscopy

X-ray photoelectron spectroscopy (XPS) is the principal technique used in order to study the surface state of catalysts in this thesis. It provides information of the composition and oxidation state of the elements on the catalysts' surface. Moreover, XPS can provide depth-selective information by varying the angle between sample surface and analyzer (in case of planar samples) or by changing the excitation photon energy within synchrotron-based X-ray sources. In this section, the theory behind XPS is briefly described, and then the instrumentation of different XPS setups used in this thesis, are discussed.

2.5.1 Theoretical background

The XPS technique is based on the photoelectric effect which was discovered by Heinrich Hertz in 1887 and latterly explained by Einstein's famous publication in 1905. Based on these two principles, half a century later, Siegbahn's group in Sweden developed several apparatuses and established a new analytical method at this time, which he called *electron spectroscopy for chemical analysis* (ESCA), or XPS as commonly referred nowadays. The development of XPS is based on the observation that when an atom absorbs a photon of fixed energy, hν, it ejects a core or valence electron (so called photoelectrons) with kinetic energy E_k. The measured kinetic energy can be used to calculate the binding energy E_b that the ejected photoelectron had inside the atom, according to Einstein's equation:

$$E_k = h\nu - E_b - \varphi \qquad \textbf{Eq. 2-2}$$

where

E_k is the kinetic energy of the photoelectron

h is Planck′is Planck′s constant

E_b is the binding energy of the photoelectron with respect to the Fermi level of the element

φ is the work function of the spectrometer

A typical XPS system is composed of an X-ray source and an electron detector, referred to as the *electron analyzer*. Laboratory-based XPS are using either monochromatic or non-monochromatic dual X-ray sources which typically produce photons with one or maximum two energies (typically Al or Mg Kα lines). Besides, synchrotron-based XPS use synchrotron radiation as a source of X-rays which can provide a wide and easily tunable photon energy range (typically from few up to several thousand eV). An XPS spectrum is obtained by collecting the photoelectrons with an electron analyzer equipped with a detector. A photoelectron spectrum represents the number of photoelectrons versus their kinetic energy E_k (or binding energy, E_b) distribution. The E_b is informative not only for elemental analysis but also for the local chemical environment around the ionized atom. For example, the different oxidation state of cobalt can be differentiated in the XPS spectra of Co 2p (**Figure 2-5**). The Co 2p spectra show two main peaks resulting from the spin-orbit splitting: Co $2p_{3/2}$ and Co $2p_{1/2}$. The theoretical ratio between the two peaks is 2:1. Compared to metallic Co, the two peaks of CoO and Co_3O_4 shift to higher binding energy. The difference between CoO and Co_3O_4 oxidation state is mainly indicated by the shake-up satellite localized at the high BE side of the main peak. In particular, CoO has sharper and stronger satellite peaks while Co_3O_4 show broad and weak satellite peaks located at ~780eV and 803~ eV.

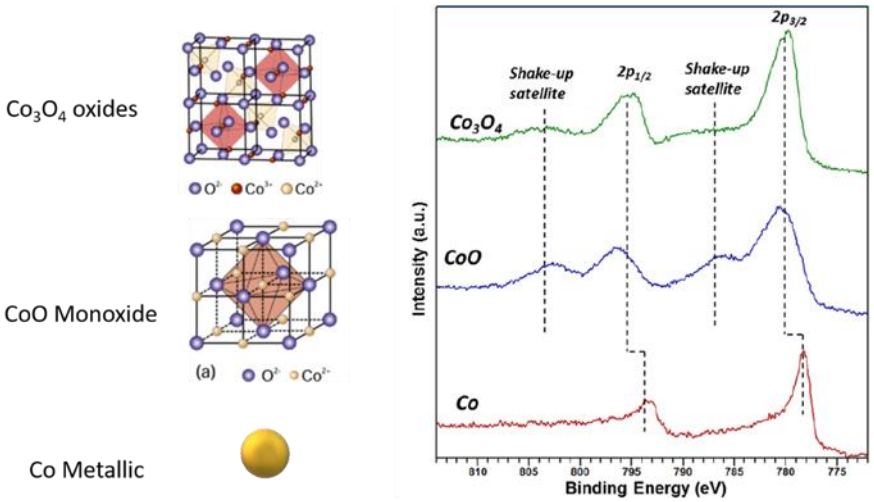

Figure 2-5. Different cobalt phases and their XPS spectra. Taken from literature.[206]

2.5.2 Near ambient pressure X-ray photoelectron spectroscopy

X-ray photoelectron spectroscopy (XPS) has been established as one of the best analytical methods to probe the composition and electronic structure of solid surfaces and interfaces.[207] However, conventional XPS spectrometers operate under ultra-high vacuum (UHV) conditions, which imposes evident limitations when it comes to studies of materials involved in catalytic reactions.[208] Therefore in the past, most of the XPS characterization in catalysis was performed before and after the reaction. The recent development of XPS spectrometers able to operate at the mbar pressure range allows surface studies of catalysts under reaction conditions and helps to describe *in situ* and *in real time* the interactions between the catalyst and the gases or vapours involved in the reaction. Since XPS operation with the sample in gas atmosphere is more recent and less known than standard vacuum XPS, we provide here a short introduction to the technique.

In the emerging years of XPS in the mbar pressure range, these kind of studies were usually referred to as "*in situ XPS*"[209,210] or "*high-pressure* XPS".[211,212] However, in order to avoid confusion with UHV works measuring catalysts transferred from a high-pressure reaction cell, which is also referred to as "*in situ"*,[213–216] the terms "*operando* XPS"[217] and "*near-ambient pressure* XPS" (NAP-XPS)[218] were introduced. It must be noted that the term "*in situ*" refers usually to XPS studies where the catalyst is analysed in reactive gas atmospheres and under relevant temperature and pressure conditions, while the term "*operando*" is used when *in situ* measurements are correlated with simultaneous *on line* gas

phase analysis of the NAP-XPS cell atmosphere via gas chromatography (GC) or quadrupole mass spectrometry (QMS).[219–221] In order to keep the consistency of the text the method is referred as NAP-XPS throughout this thesis. Whichever is the terminology in use, the potential of this technique to reveal the active surface during the catalytic processes and eventually to describe the reaction mechanism, was fast recognized.[222] Both laboratory and synchrotron-based X-ray sources can be used for NAP-XPS,[223] but synchrotron light sources have several advantages, including tunability that allows to investigate the elemental distribution in various depths (depth profiling).[183,224–226] Very often NAP-XPS is combined with calculations or other *in situ* techniques so as to gain improved understanding of the catalytic materials in reactive environments.[227]

In a typical XPS experiment the sample is irradiated by soft X-ray photons and the kinetic energy of the emitted photoelectrons is measured by an electron energy analyser. As mentioned above, the binding energy of the photoelectrons prior to photoionization is calculated by the Einstein's Photoelectric Equation. Due to the relatively low kinetic energy of the photoelectrons (tens or hundreds eV) only those emitted from the outer atomic layers are detected without energy losses, making XPS a surface sensitive method. However, this is also a main reason that limits the operation of conventional XPS spectrometers in UHV conditions, so as to avoid scattering of the photoelectrons with gas phase molecules in their way between the sample and the electron detector.[228]

In the 70's Siegbahn's group reported about an XPS spectrometer able to operate under gas atmosphere,[229] however it took almost 30 years before the development of the first modern NAP-XPS instrument with a differentially pumped electrostatic lens system,[230,231] similar to the one schematically shown in **Figure 2-6**.[231] The last few years NAP-XPS spectrometers are commercialized and to date more than 30 synchrotron and laboratory based instruments of this kind are in operation globally.[219,223,232] Several designs of NAP-XPS spectrometers are available, including backfilling of the sample cell with gas or using miniature gas cells,[233] but the unique element of the NAP instruments as compared to UHV, is the long, differentially pumped electron lenses, which separate the sample cell from the electron analyser. Typically the operating pressure of a NAP-XPS instrument is few mbar, while with further optimization, it can reach up to 130 mbar.[232,234–236] Special cell designs using graphene membranes or high energy X-rays photons, allow performing NAP-XPS experiments at real ambient pressure (1

bar).[237–240] Up to now, studies in such instruments involve liquids and electrochemical reactions that won't be discussed here.

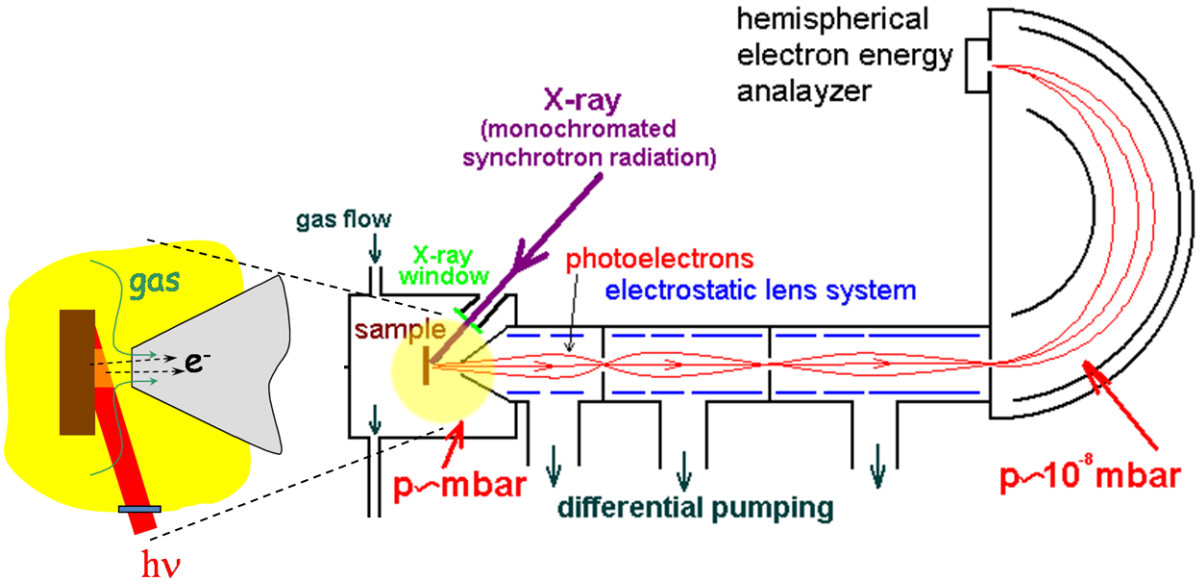

Figure 2-6 Schematic representation of a NAP-XPS set up and close up of the analyser nozzle-sample area (from ref.[231])

In a typical NAP-XPS experiment the incident X-ray beam irradiates not only the sample, but also part of the gas phase between the sample surface and the electron analyzer aperture (**Figure 2-6**). Therefore, in addition to the core-level and valence band photoemission peaks, the gas phase can be also measured by NAP-XPS. Gas-phase spectra have been exploited as a direct probe to measure changes of the sample work function.[241–244] This is because the gas-phase spectra are referred to the vacuum energy level and not to the Fermi level of the sample as the core-level peaks.[241] However, apart from the sample work function, the position (binding energy) of a gas-phase peak is affected by several other factors such as the geometrical arrangement between sample/ aperture/incident beam and the composition of the gas phase.[245] Besides, as explained by Schnadt and co-workers, the binding energy shift measured using gas-phase molecules is smaller than the real work function changes. All these reasons complicate the analysis of gas phase peaks and increase the uncertainty in the calculation of the work function.[233] Therefore some end-stations (e.g. ISISS, HZB/BESSY II Berlin) intentionally suppress the gas phase signal in the recorded spectra by applying a bias to the entrance aperture of the NAP-XPS spectrometer.[164] To the best of our knowledge there aren't any NAP-XPS studies where the gas-phase peaks were employed to estimate the work

function of late-transition metals under working catalytic conditions. However, this approach has been used to measure the work function changes during the oxidation of FeO(111) layers grown on Pt(111) and gave a good correlation with the calculated values.[243]

2.5.3 The laboratory-based XPS setup in ICPEES

Preliminary studies of catalysts' surface evolution were performed in a homemade Variable Pressure Reactor (VPR) which is attached to the ultra-high vacuum UHV-XPS setup in ICPEES. The general scheme of this system is described in **Figure 2-7**. As displayed in the scheme, the apparatus is composed of 4 UHV-chambers, which are nominated as **Load-lock chamber**, **Preparation chamber**, **VPR chamber** and **XPS analysis chamber**, respectively. Three gate valves are used to separate each chamber and to allow the transfer of the sample between the different chambers, when necessary. Each chamber is equipped with a pumping system, composed by a turbomolecular pump connected to a primary pump. With an exception of the VPR chamber, the pressure in all the other chambers can routinely attain pressures below 10^{-7}mbar. The working pressure in the VPR chamber can vary from 10^{-3} mbar to 1 bar. The VPR chamber is equipped with a gas dosing system with 4 mass flow controllers and a quadrupole mass spectrometer connected to the reactor through a leak valve. After the sample was treated under gas environment in the VPR chamber, the gas could be pump down to 10^{-7} mbar and the sample was transported under vacuum to the XPS analysis chamber.

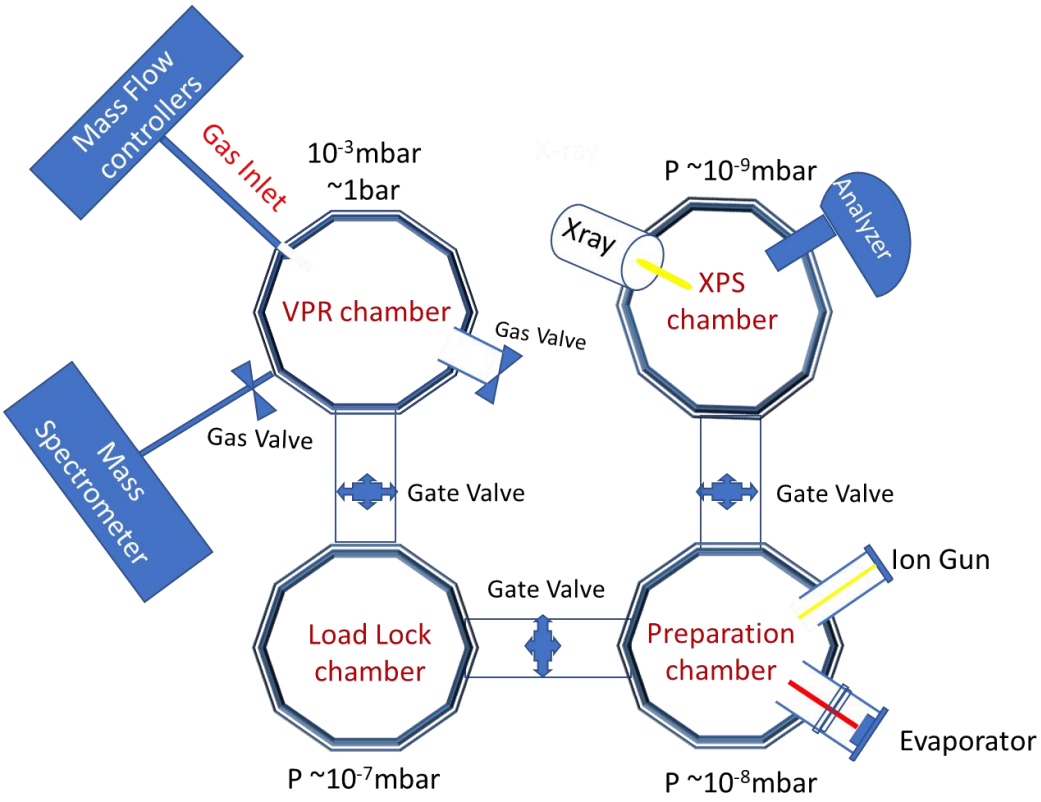

Figure 2-7. Schematic representation of the UHV-XPS setup equipped with a Variable-Pressure Reactor for catalytic studies.

The sample is loaded into the system through the Load-lock chamber by mounting onto a sample holder shown in **Figure 2-8**. As can be seen in the picture, the sample pellet (for powder samples) or crystal is mounted between two stainless steel plates and placed on a boron nitrate heater. The temperature of sample is measured by a K-type thermocouple, spot welded underneath the top stainless steel plate. The sample is grounded by a wire attached to it. A stainless-steel mask with one or two open holes (windows) is used for fixing the sample. Notably, the mask with two windows allows to simultaneously monitoring with XPS two samples treated under the same conditions. With three transferring arms, the sample holder can be transferred among different chambers under ultra-high vacuum.

Sample preparation and cleaning can be done in the preparation chamber. An evaporator allows preparing thin films of metals, while an ion gun can produce a variable energy ion beam for sputter cleaning the sample surfaces in UHV. The XPS analysis chamber is equipped with an ultraviolet source for UPS, an IQE 11/35 (SPECS) ion source for LEIS, a VSW Class WA hemispherical electron analyzer (150 mm radius) with a multi-channeltron detector and two X-ray sources for XPS. One of the X-ray sources is a non-monochromatic

dual anode (Al Kα and Mg Kα) X-ray source and the other one is a monochromatic Al Kα source. In this work, the monochromatic Al source (hv=1486.6 eV; anode operating at 240 W) is chosen for recording spectra with higher resolution. The X-ray incident angle is 45 degrees with respect to the sample and the collecting angle of the analyzer was 0 degrees to the surface normal. The photoelectrons were detected by using pass energy of 44 eV or 22 eV for high-resolution spectra and 90 eV for the survey scan.

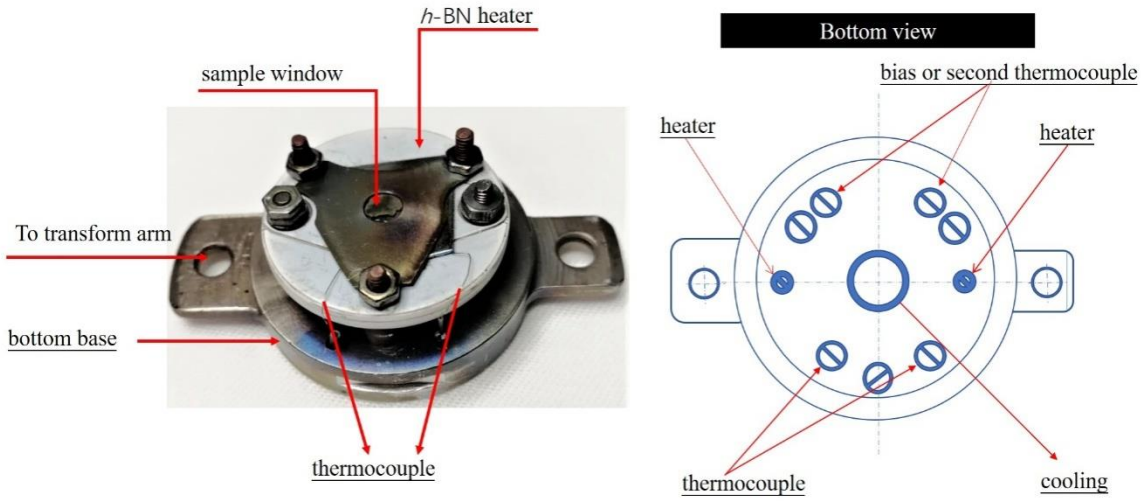

Figure 2-8. Sample holder used on UHV-VPR-XPS system in this thesis.

2.5.4 Laboratory-based NAP-XPS setup in Charles University, Prague

Part of the *in situ* NAP-XPS studies, in particular those of the Co-Mn based catalysts under COPrOx reaction conditions, were performed at the Charles University in Prague, Czech Republic. The experiments were carried out using a photoelectron spectrometer (SPECS Surface Nano Analysis GmbH, Germany) which is equipped with a PHOIBOS-150 multichannel hemispherical electron energy analyzer coupled with a differentially pumped electrostatic pre-lens system (**Figure 2-9**). A DeviSim reaction cell[246] installed in the analytic chamber allows obtaining in situ core-level spectra of the catalyst surface directly under the gas mixture flow at pressures up to several mbar in a wide temperature range. Spectra were obtained using the monochromatized Al Kα X-ray source (1486.6 eV). The powder catalysts were pressed to pellets and fixed on the sample holder using spot welding of Ta foil stripes.

The sample holder contained a K-type thermocouple welded near the sample pellet for temperature control. Heating was performed by electron bombardment of the rear side of the NAP cell stage, which was in contact with the sample holder. XPS experiments were complemented with simultaneous analysis of the gas mixture by mass spectrometry (Prisma Pro, Pfeiffer Vacuum, Germany) to follow the change of concentrations of the reagents and products with temperature increase.

(a)

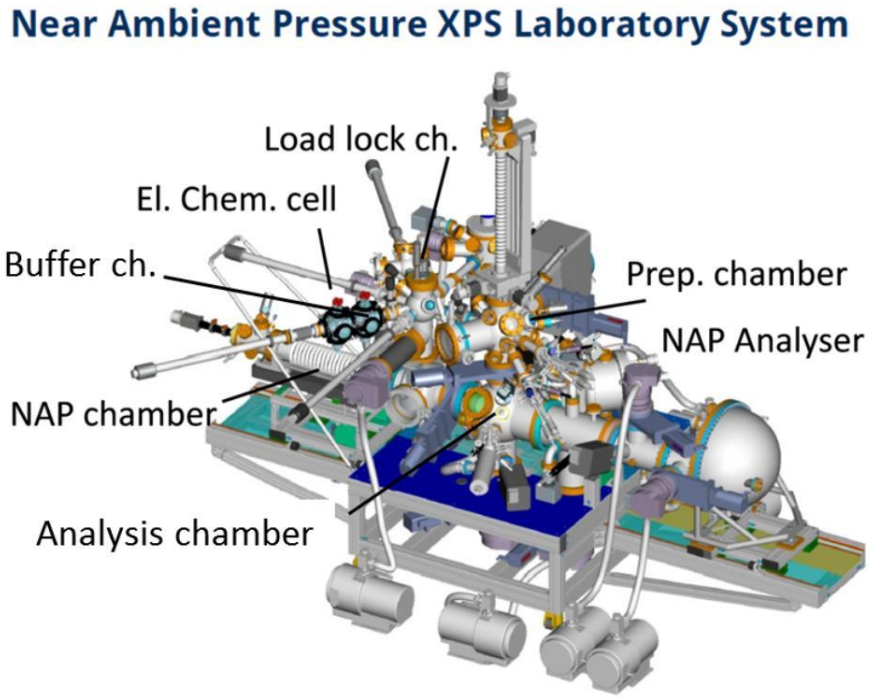

(b)

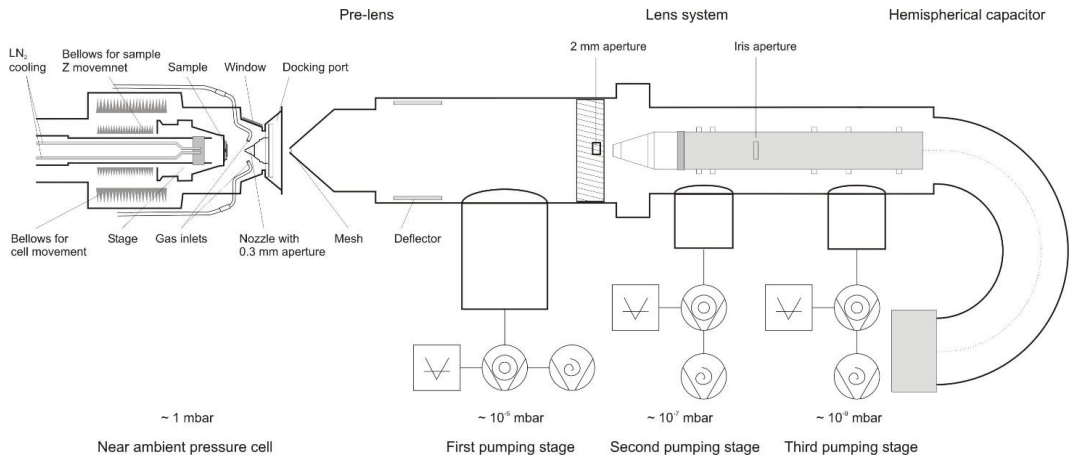

Figure 2-9. The overview of lab-based NAP-XPS system (a) and the scheme of the analysis part (b) in Charles University in Prague. The picture is provided by Charles University.

2.5.5 In situ synchrotron-based NAP-XPS and NEXAFS apparatuses

In this thesis, in-situ near ambient pressure XPS and NEXAFS measurements of cobalt-based catalysts were performed at the third generation synchrotron HZB/BESSY II (Berlin, Germany). For this purpose, two different beamlines, namely ISISS[247] and CAT@EMIL[248], with very similar experimental stations were used. Both beamlines and end-stations were built and administrated by Fritz-Haber-Institut of the MPG (FHI-MPG)/ Inorganic chemistry department. The ISISS beamline was used for pure cobalt catalyst study. The experimental station is equipped with a hemispherical electron analyser (Phoibos 150 /SPECS) with a 2D Delay Line detector from Surface Concept. The analyzer is connected to the analysis chamber through an electrostatic lens system with 3 stages differential pumping as described above. The gases were introduced into the NAP-XPS chamber using the mass flow controllers (Bronkhorst). The evolution of gases in the NAP-XPS cell is constantly monitored by an on-line quadrupole mass spectrometer (QMS Prisma, Pfeiffer Vacuum, Inc, Germany) and a micro gas-chromatograp with 3 columns. The wide-energy tunability of monochromated soft X-ray synchrotron radiation validates the depth-profiling analysis of the catalyst. The photoelectrons produced in the gas ambient of the NAP-XPS chamber introduce lines in the corresponding spectrum from the material surface, particularly in the O ls and C 1s spectra.

The in situ NEXAFs spectra were collected at the same experimental setup in between the NAP-XPS spectra, therefore the two experiments were performed under identical reaction conditions. Spectra were measured both in the Auger electron yield (AEY) and total electron yield (TEY) modes, but only the TEY-NEXAFS spectra are included in this thesis. The TEY-NEXAFS spectra were collected via a Faraday cup via the first aperture of the differential pumping system with an applied accelerating voltage.

The CAT@EMIL beamline in HZB/BESSY II was used for the in situ spectroscopic study over promoted-cobalt catalysts. As said above, the experimental station is very similar in the two, however there are some differences in the photon flux. In particular, CAT@EMIL beamline has higher photon flux (since it is an undulator beamline) than ISISS (a bending magnet beamline) especially at the higher excitation energies.

The in situ-NEXAFs study of promoted-cobalt catalysts at 1 bar was performed in collaboration with Dr. Elisa Borfecchia, department of Chemistry, University of Turin at the

APE-HE beamline at Elettra, Trieste, Italy. The details of the setup and experimental methods can be found in reference [249].

2.5.6 Analysis of the XPS spectra

In this thesis, all XP spectra were analyzed, i.e. peak fitting or peak deconvolution by using the CasaXPS vs 2.3.23 software. The analysis of the Co 2p region is complicate due to the complex peak shape and the overlap between Co_3O_4, CoO and Co photoemission peaks and requires at least 8 individual peaks for the Co_3O_4 peak fitting (Figure 2-10a and b).[250] Alternatively, the contribution of each species oxidation state in the overall spectrum was estimated here by a linear combination of pure Co^0, CoO and Co_3O_4 spectra measured at the same spectrometer over standard reference samples.[195] An example of fitting of the Co 2p spectra by reference spectra typically used in this thesis is shown in Figure 2-10(c, d).

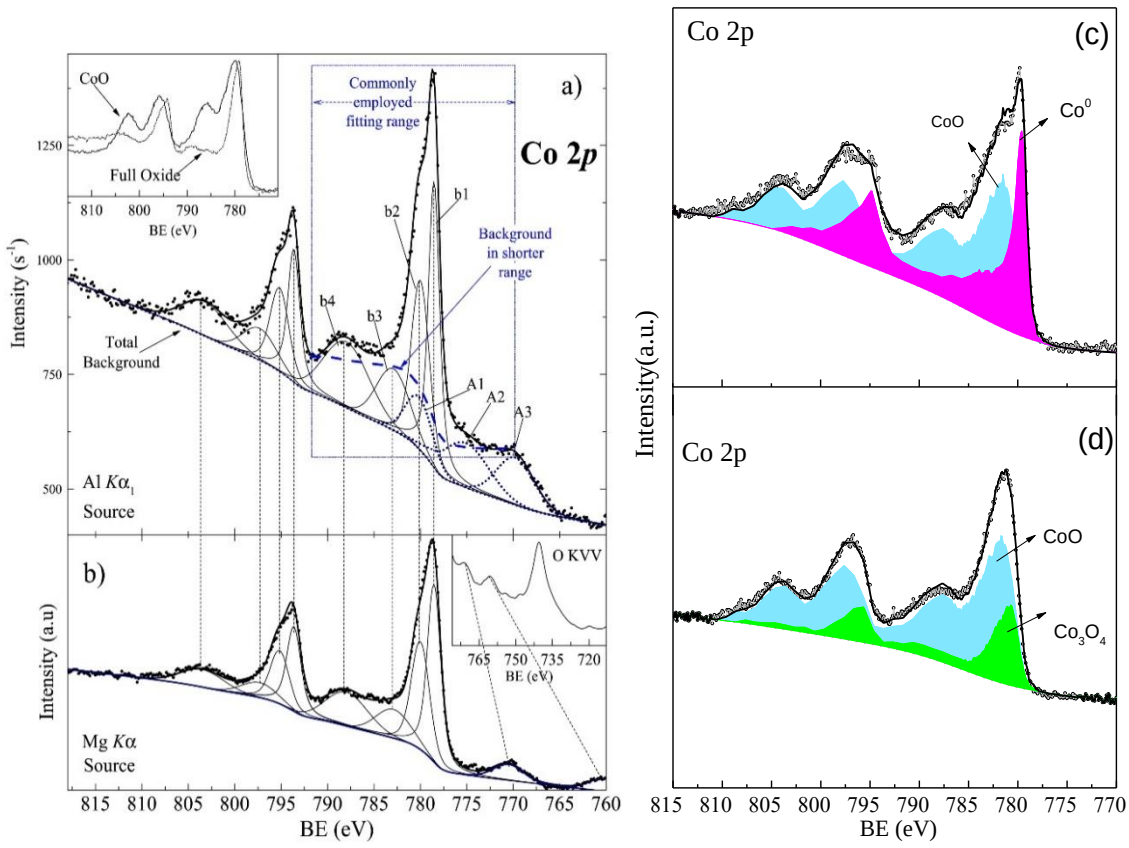

Figure 2-10. The fitting of Co 2p spectra reported in the literature (a, b), taken from [250]; The deconvolution of Co 2p spectra by using Co 2p spectra of Co, CoO and Co_3O_4 in this thesis(c, d).

The relative ratio of different cobalt phases was then calculated based on their peak area. The deconvolution and assignment of C1s, O1s, Mn 2p and V 2p is based on literature reports.

The atomic ratio of different elements on the surface is determined by the following formula:

$$\frac{X_A}{X_B} = \frac{I_A/(f_A \times n_A)}{I_B/(f_B \times n_B)}$$

where,

X is the atomic ratio of elements; (A) or (B) :

I is the spectral intensities obtained at the same kinetic energies of the emitted photoelectrons

f (only in case of spectra recorded in synchrotron) is the energy dependent incident photon flux, measured using a gold foil with known quantum efficiency at each beamline.

n is the photoelectric cross-section for the interested atomic orbital taken from[251] .

The incident photon fluxes recorded at synchrotrons were directly provided by scientists at each beamline.

2.6 Operando Fourier diffraction infrared spectroscopy

Diffuse reflectance infrared Fourier transform spectroscopy (DRIFTS) experiments were performed on a Bruker Vertex 70 FTIR spectrometer with a Praying Mantis diffuse reflectance accessory and a reaction cell equipped with ZnSe windows. The scheme of the apparatus is shown in **Figure 2-11**. The experiments can be performed from -20°C to 800°C under different pressure conditions by controlling the heating and cooling system. The obtained spectra were analyzed based on OPUS software from Bruker.

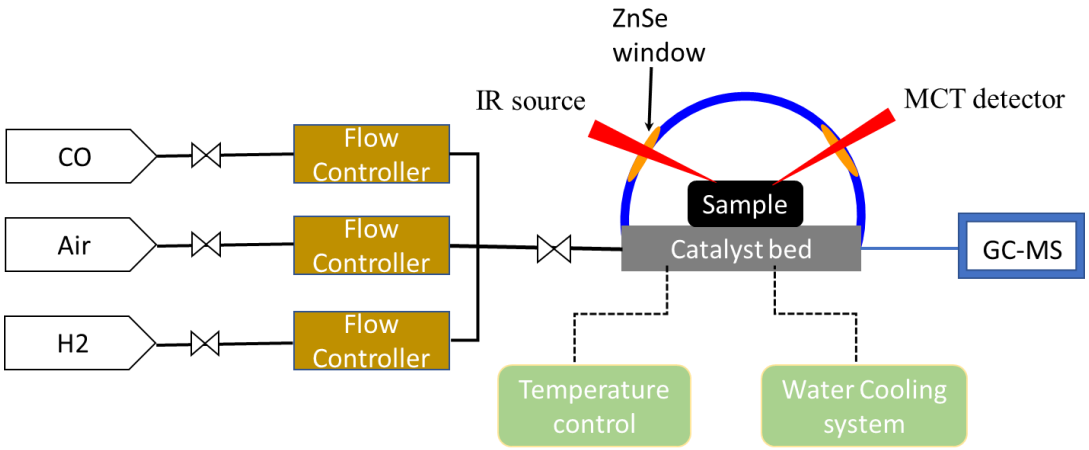

Figure 2-11 The scheme of operando DRIFT setup in ICPEES, ECPM, Strasbourg.

For each experiment, certain amount of catalyst was loaded in a sample cup of the reaction cell and after relevant treatment (oxidation and reduction), the sample was subsequently heated to 200 ^{o}C in helium (10ml/min) for 30 min to remove the adsorbed water and carbon species. A spectrum collected after the helium flush was used as the reference spectrum of each measurement under different gas conditions. Notably, the CO adsorption experiment below room temperature was performed by cooling with liquid nitrogen.

Chapter 3

Correlation Between Reactivity and Oxidation State of Cobalt Catalysts for CO Preferential Oxidation

3.1 **Introduction**

It has been proposed that CO oxidation over cobalt oxide catalysts follows the Mars-van-Krevelen reaction mechanism.[1,227] In particular, the CO species react with the oxygen atoms around cobalt ions to produce CO_2, which leads to the reduction of Co^{3+} to Co^{2+}. Consequently, the reduced Co^{2+} ions are reoxidized to Co^{3+} by gas phase O_2. To be able to design efficient cobalt-based catalysts, it is essential to identify the most active phase of cobalt during COPrOx. Although most literature reports agree that cobalt remains oxidized during COPrOx reaction, there are contradicting accounts regarding the role of Co^{3+} and Co^{2+} ions. In the majority of studies, Co_3O_4 is considered as the active oxidation state of cobalt-based catalysts during COPrOx.[5,10,80,252–258] This is supported by recent *in situ* surface studies which showed that Co_3O_4 is stable under the reducible COPrOx reaction environment.[6,259] Theoretical modeling of CO oxidation, a key step of COPrOx, over Co_3O_4 proposed that octahedrally coordinated Co^{3+} in Co_3O_4 (111) is much more active than tetrahedrally coordinated Co^{2+} for CO oxidation.[260–262] Quite the contrary, other studies found that reduced Co_3O_4 or cobalt monoxide (CoO) has higher reactivity than that of Co_3O_4 for CO oxidation.[7,8,263] CoO is a lower valence cobalt oxide, where Co^{2+} ions are octahedrally coordinated to lattice oxygen.[196,264] Besides, *in situ* investigations showed that the active surface state of cobalt in the reaction is nonstoichiometric Co_3O_{4-x}.[9] A recent density functional theory (DFT) study supported this idea by demonstrating that Co^{2+}_{Oh} in CoO has the best oxidation activity as compared to Co^{3+}_{Oh} and Co^{2+}_{Td}.[265]

The controversy on the reports about the active state of cobalt oxide might be partially explained by the difficulty to define the surface oxidation state of the catalyst during the COPrOx reaction conditions. This is a quite challenging task since, as has been shown in several previous studies, the surface of the catalysts is dynamic and can be transformed under reaction conditions.[182] An additional factor is the substantial effect of the catalysts preparation method and the support, which can lead to drastically different activities of cobalt.[266] For an unambiguous reply to this scientific challenge, CoO and Co_3O_4 should emerge from the same original material and compared under the same COPrOx reaction following an *operando* analysis approach with high surface specificity.

In this chapter we directly compare CoO and Co_3O_4 for COPrOx by using the same unsupported cobalt oxide powder after oxidative and reductive gas pretreatments. In this way,

we focus on the intrinsic activity of cobalt oxides and circumvent the effects of the support and the catalyst morphology. To elucidate the influence of material properties on the activity, we combine standard characterization with advanced *operando* spectroscopy and first principle calculations, performed in collaboration with the group of Computational Surface Science and Catalysis (CSSC) of Prof. M. Mavrikakis at the University of Wisconsin at Madison, USA .

3.2 Experimental methods

3.2.1 Synthesis of materials and catalytic tests

3.2.1.1 Catalyst Preparation

Commercial high-purity Co_3O_4 nanopowders, 99% (metals basis, Alfa Aesar) was used as a precursor for the preparation of oxidized and reduced cobalt catalysts in the experiments presented in this work. In addition, catalytic tests were also performed over cobalt(II) oxide (99.995%) from Alfa Aesar and cobalt(II, III) oxide (99.99%) from Sigma-Aldrich with qualitatively similar results with the aforementioned Co_3O_4 nanopowders (the data are not complete and are not included in this thesis). The surface purity of Co_3O_4 nanopowders was confirmed by the survey XPS spectra. The sample referred as "oxidized cobalt" was obtained by oxidation of the Co_3O_4 nanopowders in O_2 at 350^{o}C for 30 min, while the one called "reduced cobalt" via reduction of Co_3O_4 nanopowders in pure H_2 at 400^{o}C for 60 min.

3.2.1.2 Activity tests

Preferential oxidation of CO on oxidized and reduced cobalt catalysts was performed in a continuous-flow fixed-bed reactor under atmospheric pressure. 0.15 g of the sample was loaded into the reactor and pretreated with synthetic air (10ml min^{-1}) at 350 ^{o}C for 30 min (heating rate 10 ℃ min^{-1}) to remove water and carbon. For the reduced cobalt, the sample was exposed in pure hydrogen (10ml min^{-1}) at 400℃ for 1 hour, which according to TPR-H_2 profile reduces Co_3O_4 to metallic Co. Consequently, the sample was cooled down at 20 ^{o}C where the gas mixture switched to 1% CO, 2% O_2, 40% H_2 in helium. The qualification and quantitation of reactants and products was done by gas chromatography–mass spectrometry (GC-MS) with 3 different GC columns followed by a mass spectrometer. The sample was maintained at each temperature for 30 min while gas was injected constantly to the GC to obtain an average concentration. The CO conversion (X_{CO}), the O_2 selectivity to CO_2 (S_{CO2}) and the surface specific activity (SSA) were calculated based on Equations 1 to 3 respectively:

$$X_{CO}(\%) = \frac{[CO]_{in} - [CO]_{out}}{[CO]_{in}} \times 100$$ **Eq. 3-1**

$$S_{CO2}(\%) = \frac{1}{2} \times \frac{[CO]_{in} - [CO]_{out}}{[O_2]_{in} - [O_2]_{out}} \times 100$$ **Eq. 3-2**

$$SSA = \frac{[CO]_{in} \cdot X_{CO}}{m_{Co} \times BET_{Co}}$$ **Eq. 3-3**

In these equations, $[CO]in/[O_2]in$ and $[CO]out/[O_2]out$ are the flows of CO/O_2 into and out of the reactor respectively, m_{Co} the mass of cobalt in the reactor and BET_{Co} the cobalt specific surface area as obtained by Kr-BET after each pretreatment.

3.2.2 Structural and morphological characterization methods

The surface area of cobalt powders after oxidation and reduction pretreatments were determined with a Quantachrome Autosorb-6B surface area analyzer using krypton (Kr) as adsorbate gas. Due to the relatively low surface area of unsupported cobalt powders, Kr offers higher precision than Ar or N_2. Samples were degassed at 120 °C for about 5 h prior to Kr adsorption at 77 K and the specific surface areas were calculated according to the Brunauer−Emmett−Teller (BET) method using 11 data points in the relative pressure (p/p0) range of 0.05−0.3. The specific surface area of cobalt samples pretreated in different conditions is given in **Table 3-1**. Temperature-programmed reduction with hydrogen (TPR-H_2) of Co_3O_4 powder was performed by means of an automated catalyst characterization system (Micromeritics, model AutoChem II), which incorporates a thermal conductivity detector (TCD). The surface morphology of cobalt was inspected by a Zeiss GeminiSEM 500 SEM microscope, while TEM was carried out in scanning mode (STEM) using bright field (BF) and annular dark field (ADF) detectors on a JEOL 2100F microscope working at 200 kV. X-ray patterns were measured with a Bruker D8 advance diffractometer using Cu Kα radiation. The ex-situ laboratory-based XPS measurements were carried out in an ultrahigh-vacuum (UHV) setup coupled with a variable-pressure reactor (VPR) described in more detail in chapter 2 and in reference.[165] The VPR was connected via a leak valve to a differentially pumped Pfeiffer QMS 200 mass spectrometer allowing on line gas phase analysis. About 120 mg of cobalt oxide powder was pressed into pellet and mounted on the sample holder equipped with a boron

nitride heater and a temperature sensor. Reduced cobalt was pre-treated in 7 mbar hydrogen at 400 ^{o}C for 1 h and then exposed to the reaction mixture (1% CO, 2% O_2 and 97% H_2) at 4 different total pressures (10, 100, 600 and 1000 mbar). The reaction was performed at 210 ± 10 °C where CoO is the dominant oxidation state as suggested by NAP-XPS experiments. After reaction the VPR was evacuated and the sample was rapidly transferred under vacuum to the analysis chamber for XPS characterization.

3.2.3 Characterization methods for catalysts' surface

3.2.3.1 Synchrotron-based experiments

The *in situ* synchrotron-based near ambient pressure X-ray photoelectron (NAP–XPS) and near edge X-ray absorption fine structure (NEXAFs) spectroscopies were performed at the *ISISS beamline* at the synchrotron radiation facility BESSY II of the *Helmholtz* Zentrum Berlin, in a setup described in chapter 2 and in details in reference.[44] The gas phase composition was monitored on line by a differentially pumped quadrupole mass spectrometer (QMS), which was connected to the experimental cell through a leak valve. The Co $L_{3,2}$-edge NEXAFS spectra were obtained by recording in the total electron yield (TEY) mode. The fresh cobalt oxide powder was pressed into pellets and placed on a stainless steel plate which could be heated at the back side by an IR laser beam. Prior to the catalytic tests, cobalt was pretreated at 0.5 mbar in O_2 (300 ^{o}C) in the NAP-XPS cell for about 1 hour in order to remove adventitious carbon. Co_3O_4 is formed after this procedure as concluded by the NAP-XPS and NEXAFS spectra. The reduced cobalt was firstly pretreated in 1 mbar H_2 at 400 ^{o}C until the cobalt surface became metallic (Co^0), as confirmed by the characteristic Co 2p peak at 778.3 eV.[165] After each pre-treatment the reactant gas mixture of 1%CO, 2%O_2 and 97%H_2 was introduced at room temperature and the catalyst was annealed by a ramping rate of 5 ^{o}C/min. The XPS spectra of Co $2p_{3/2}$, O1s and C1s were collected during the reaction using two photon energies. The NAP-XPS and NEXAFS spectra were fitted using standard reference curves of metallic Co, CoO and Co_3O_4 recorded at the same spectrometer using the same analyzer conditions (i.e. pass energy, step size and excitation photon energy).

3.2.3.2 *In situ* DRIFT experiments

Diffuse reflectance infrared Fourier transform spectroscopy (DRIFTS) experiments were performed on a Bruker Vertex 70 FTIR spectrometer with a Praying Mantis diffuse reflectance accessory and a reaction cell equipped with ZnSe windows (more details are given in chapter 2).

150 mg of Co_3O_4 powder was loaded in a sample cup of the reaction cell and after relevant treatment (oxidation and reduction) and the sample was subsequently heated to 200 ^oC in helium (10ml/min) for 30 min to remove the water and adsorbed carbon species. After cooling down at 25^oC in helium, the reaction mixture was switched into the reactor. The spectra of each sample collected in helium at 25^oC after flushing at 200^oC have been used as the reference spectra for those in COPrOx reaction. All spectra were recorded at atmospheric pressure with an accumulation of 20 scans at a resolution of 4 cm^{-1}. The COPrOx gas mixture was identical to the one used in the catalytic tests (1%CO, 2%O_2 and 40% H_2 in He). The temperature was increased stepwise from room temperature with a ramping rate of 10 ^oC/min up to 300 ^oC and for each measured temperature the sample stayed for 30 min for gas stabilization and spectra collection. The FTIR spectra presented here were smoothed and the background was removed to facilitate the comparison.

3.3 **Results**

3.3.1 The intrinsic activity of PreH_2-Co and PreO_2-Co

The COPrOx activity and selectivity of cobalt powder after pre-treatment in H_2 or O_2 (for brevity hereafter referred as *PreH_2-Co* and *PreO_2-Co*, respectively) were evaluated at atmospheric pressure using identical reaction conditions for both samples. To compare the intrinsic catalytic activity of cobalt after H_2 and O_2 pretreatments the surface-specific activity, that is, the amount of CO converted per cobalt surface area measured by Kr-BET, is shown in **Figure 3-1**a. As expected, CO conversion increases with temperature for both catalysts, but there is a remarkably higher specific activity on PreH_2-Co as compared to PreO_2-Co. The differences in the overall % CO conversion are even higher if one normalizes the data to the mass of the catalyst as shown in **Figure 3-2**. Going back to **Figure 3-1**a, at 200 ^oC the specific activity for PreH_2-Co is about 8 times higher than that measured for PreO_2-Co. Notably, when the reaction temperature increases above 250 °C the activity of PreH_2-Co is stabilized causing similar specific activities for the two catalysts. Concerning their O_2 selectivity, both samples display a similar profile (**Figure 3-1**b), which decreases with temperature due to the boost of H_2 conversion.[87]

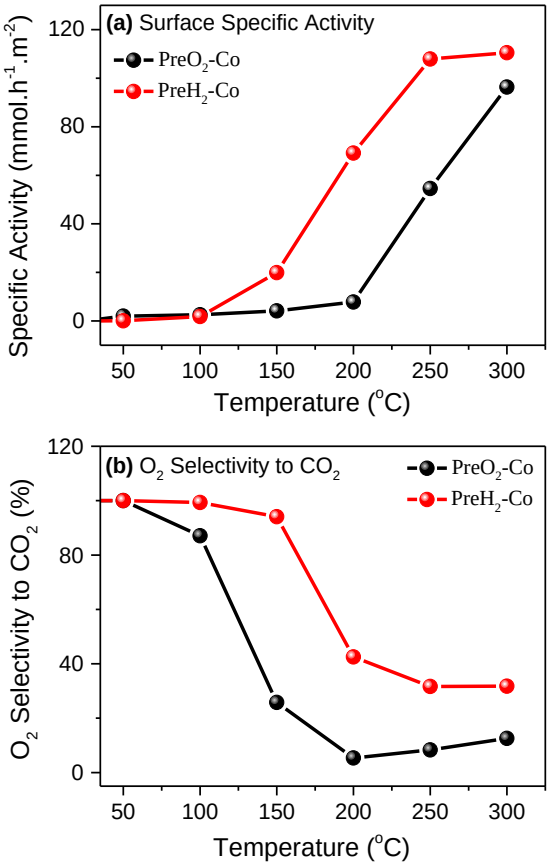

Figure 3-1. Surface specific activity or the amount of CO converted per surface area in mmol·h^{-1}·m^{-2} and b) O_2 selectivity to CO_2 for $PreO_2$-Co and $PreH_2$-Co as a function of temperature-based gas chromatography (GC) measurements. Experimental Conditions: 1%CO, 2%O_2 and 40% H_2 in He-balanced flow; 0.15 g catalysts; 10ml/min of total flow; atmospheric pressure (1 bar). Every point was recorded after remaining for 30 min at each temperature.

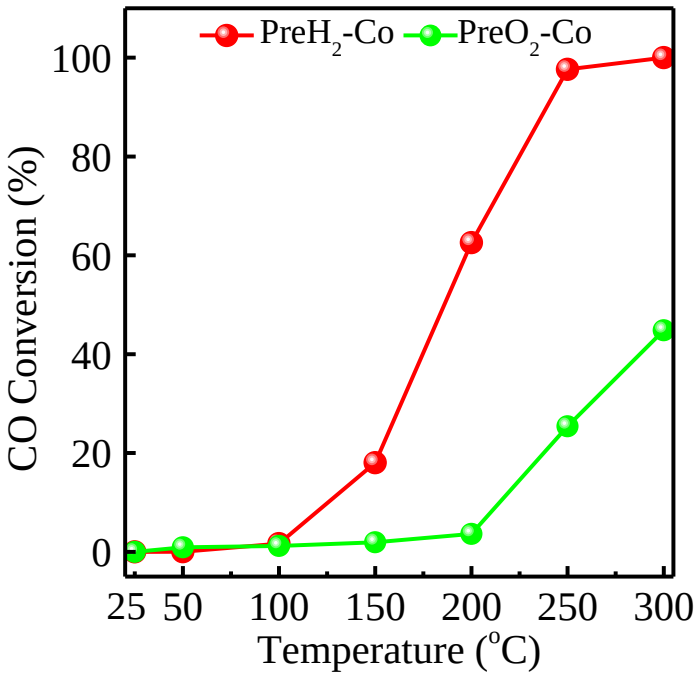

Figure 3-2. CO conversion for $PreO_2$-Co and $PreH_2$-Co as a function of temperature-based gas chromatography (GC) measurements. Experimental Conditions: 1%CO, 2%O_2 and 40% H_2 in He-balanced flow; 0.15 g catalysts; 10ml/min of total flow; atmospheric pressure (1 bar). Every point was recorded after remaining for 30 min at each temperature.

The GC signals of the main carbon products (CO_2 and CH_4) are shown in **Figure 3-3**. Up to 200 °C the production of CO_2 increases for both samples (although as mentioned above the increase for $PreO_2$-Co is marginal), but above this temperature in case of $PreH_2$-Co the CO_2 production decreases steadily with a consequent increase of the methane signal. This suggests that on the $PreH_2$-Co, CO methanation is promoted above 200 °C, while CO oxidation is suppressed, in accordance with previous COPrOx studies showing that CO methanation reaction is enhanced with temperature.[267] In some of the previous COPrOx studies on cobalt, the formation of CH_4 has been attributed to the presence of reduced cobalt species (CoO_x or metallic Co).[3,7,26,268] Besides cobalt oxidation state, methane formation has been associated to the interaction of CO with surface adsorbed OH groups.[269,270] As will be discussed next, significantly higher population of adsorbed OH groups is observed in the case of $PreH_2$-Co as compared to $PreO_2$-Co, which might be linked to the higher methane production over $PreH_2$-Co catalyst. Overall, the catalytic results indicate that $PreH_2$-Co has significantly enhanced COPrOx reactivity as compared to $PreO_2$-Co, while at least for temperatures up to 200 °C, both samples exhibit similar carbon product selectivity.

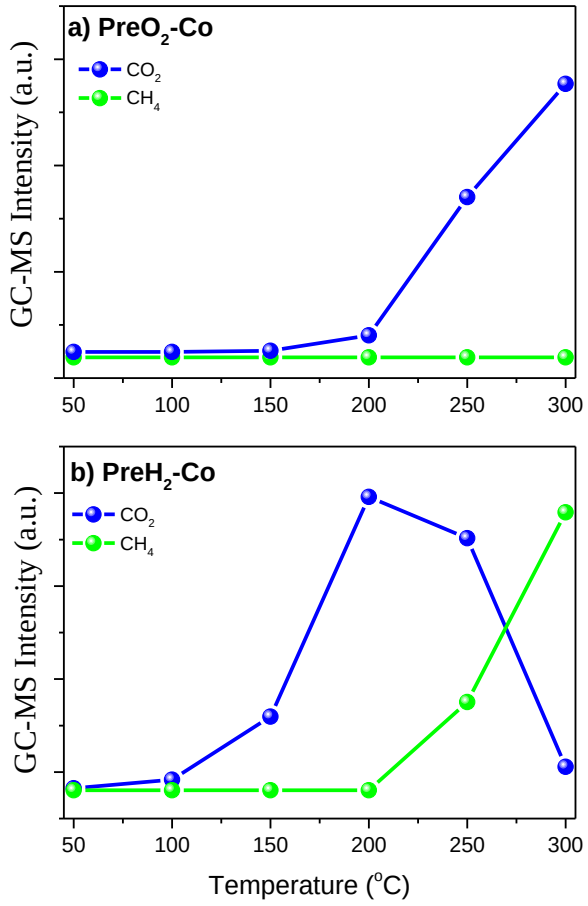

Figure 3-3. The evolution of CO_2 and CH_4 GC signals of the COPrOx reaction as a function of temperature for (a) $PreO_2$-Co and (b) $PreH_2$-Co catalysts. Experimental conditions: 1%CO, 2%O_2 and 40% H_2 in He-balanced flow; 0.15g catalysts; 10ml/min of total flow; atmospheric pressure (1bar) and after remaining for 30 min at each temperature.

3.3.2 Structure and morphology characterization

The X-ray diffraction (XRD) patterns of both fresh and spent $PreO_2$-Co (**Figure 3-4**) correspond to the Co_3O_4 cubic structure. The strong and sharp Bragg diffraction peaks suggest a high degree of crystallinity, while the absence of secondary phases in the XRD patterns confirms the high phase purity of Co_3O_4 powder. In the case of $PreH_2$-Co, the XRD pattern before reaction is dominated by the diffraction peaks of metallic Co, while after COPrOx the peaks of metallic Co disappear and the diffractogram is composed exclusively of CoO and Co_3O_4 diffraction peaks,[14] suggesting that the bulk crystallite structure of cobalt is affected by the H_2 pretreatment and remains partially reduced also during COPrOx reaction.

Table 3-1 The structural properties of cobalt catalysts after different pretreatment

Cobalt Catalysts	Crystallite size (nm)	Kr-BET surface area (m^2/g)
$PreH_2$ Co	**42.8^{CoO}**	**1.616**
$PreO_2$ Co	**58.9^{Co3O4}**	**0.831**

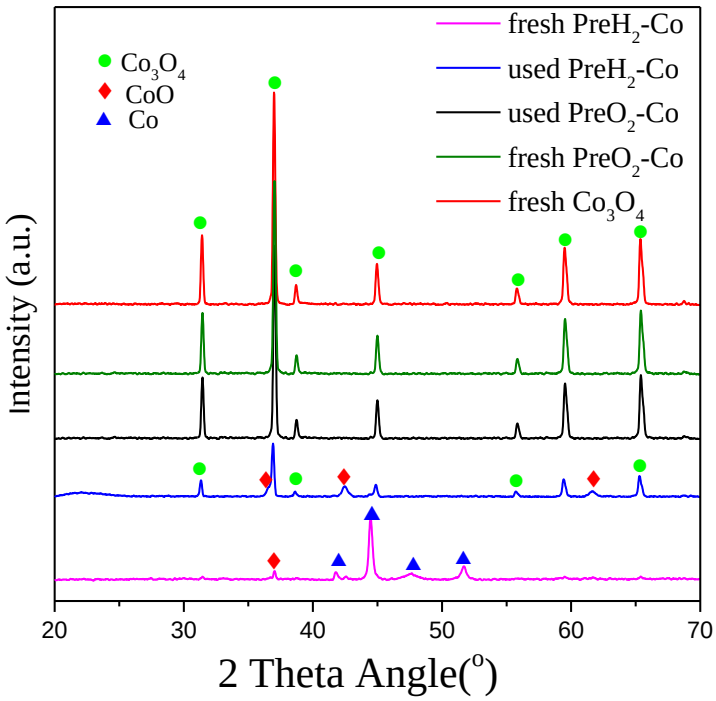

Figure 3-4. The XRD patterns of fresh cobalt catalyst, as well as $PreO_2$-Co and $PreH_2$-Co catalysts just before (*fresh*) and after (*used*) the COPrOx reaction at 1bar for 2 hours.

Figure 3-5 shows some representative scanning transmission electron microscopy (STEM) images of the spent $PreO_2$-Co and $PreH_2$-Co catalysts. The $PreO_2$-Co catalyst display a well crystallized structure with only the characteristic lattice fringes of Co_3O_4 (**Figure 3-5**), while the $PreH_2$-Co was found to display a porous "opened" structure with the presence of the lattice fringes of CoO (200), (220) and (111) planes (**Figure 3-5**e) in accordance with the XRD results. The scanning electron microscopy (SEM) images of the two spent catalysts are shown in **Figure 3-5c,f**. The micrographs indicate aggregated cobalt particles but with similar sizes for both samples. Notably, in both TEM and SEM images formation of pores at the

exterior of some cobalt particles can be seen in the case of spent $PreH_2$-Co but not for $PreO_2$-Co catalysts. Pore formation after reduction could be explained by a Kirkendall-type effect as has been reported previously.[271,272]

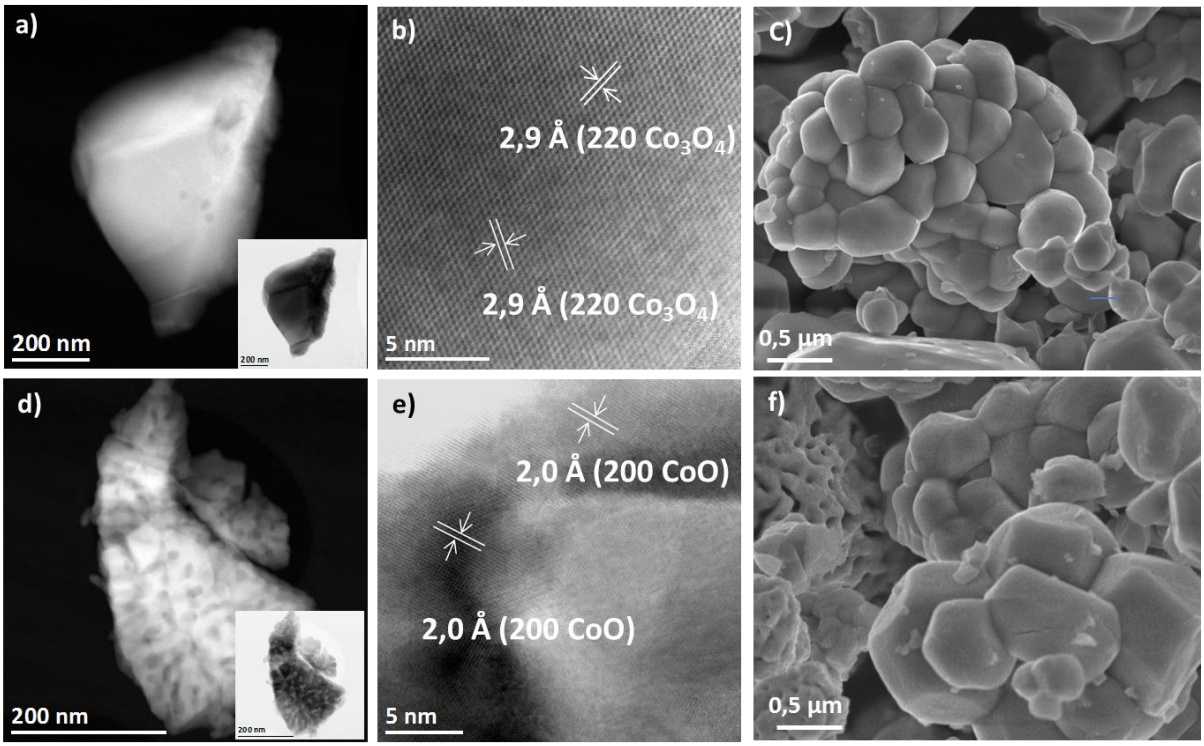

Figure 3-5. ADF-STEM images (inset, the corresponding BF-STEM images) (a,d) and high resolution BF-STEM images (b,e) of the spent $PreO_2$-Co (a, b) and $PreH_2$-Co catalysts (d, e) SEM micrographs of the spent $PreO_2$-Co (c) and $PreH_2$-Co catalysts (f). In all cases the images were recorded after COPrOx reaction up to 200 °C for 1 hour.

3.3.3 Surface state of cobalt under reaction conditions monitored by in situ XPS and NEXAFS

Synchrotron-based near-ambient-pressure X-ray photoelectron spectroscopy (*NAP-XPS) was used to* shed light on the surface oxidation state of cobalt under working COPrOx conditions. **Figure 3-6** presents the evolution of Co 2p spectra of $PreO_2$-Co sample with the reaction temperature. The Co 2p peak appears at 780 eV and is accompanied by a broad satellite at the high binding energy side, which are typical spectra characteristics of spinel Co_3O_4 compound.[164] The Co 2p peak remains identical from 25 ^oC to 300 ^oC, suggesting that the Co_3O_4 phase is sustained during COPrOx reaction on $PreO_2$-Co, confirming previous results over calcined cobalt catalysts.[6] These findings are further supported by the Co L_3-edge NEXAFS spectra presented below.

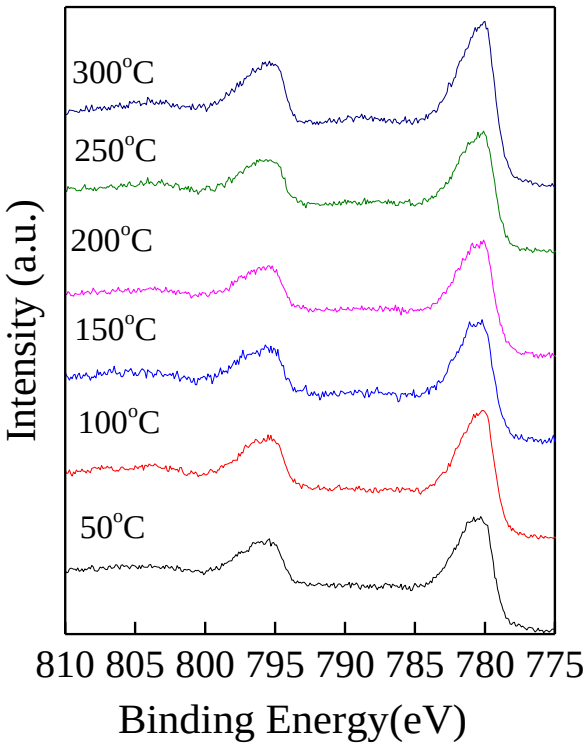

Figure 3-6. The Co2p spectra of $PreO_2$-Co measured in different COPrOx reaction temperatures. *Reaction conditions*: 1%CO, 2%O_2 and 97%H_2 at 0.5mbar with a temperature ramping rate of 5°C/min; prior to the reaction cobalt was reduced in 1 mbar O_2 at 300 °C for 30 min.

In the case of $PreH_2$-Co, the Co 2p photoemission spectra during COPrOx are shown in **Figure 3-7a**. At 50 °C the Co 2p peak contains the contribution of both metallic Co at 778.8 eV and Co^{2+} clearly evident by the characteristic peak around 781 eV and the intense satellite shifted by 6 eV at higher binding energy.[273] By increasing the COPrOx reaction temperature the metallic Co feature of the Co 2p spectra disappears and CoO dominates the spectrum up to 250 °C. At 300 °C the Co 2p spectrum of $PreH_2$-Co resembles the one of $PreO_2$-Co suggesting further oxidation to Co_3O_4. A peak deconvolution procedure using Co 2p profiles recorded over reference Co, CoO and Co_3O_4 samples was used to assess quantitatively the oxidation state evolution as a function of temperature. As shown in the inset of **Figure 3-7**a in the COPrOx temperature window between 75 and 250 °C, CoO is the dominant oxidation state of $PreH_2$-Co, while metallic Co and Co_3O_4 appear at low and high reaction temperatures, respectively.

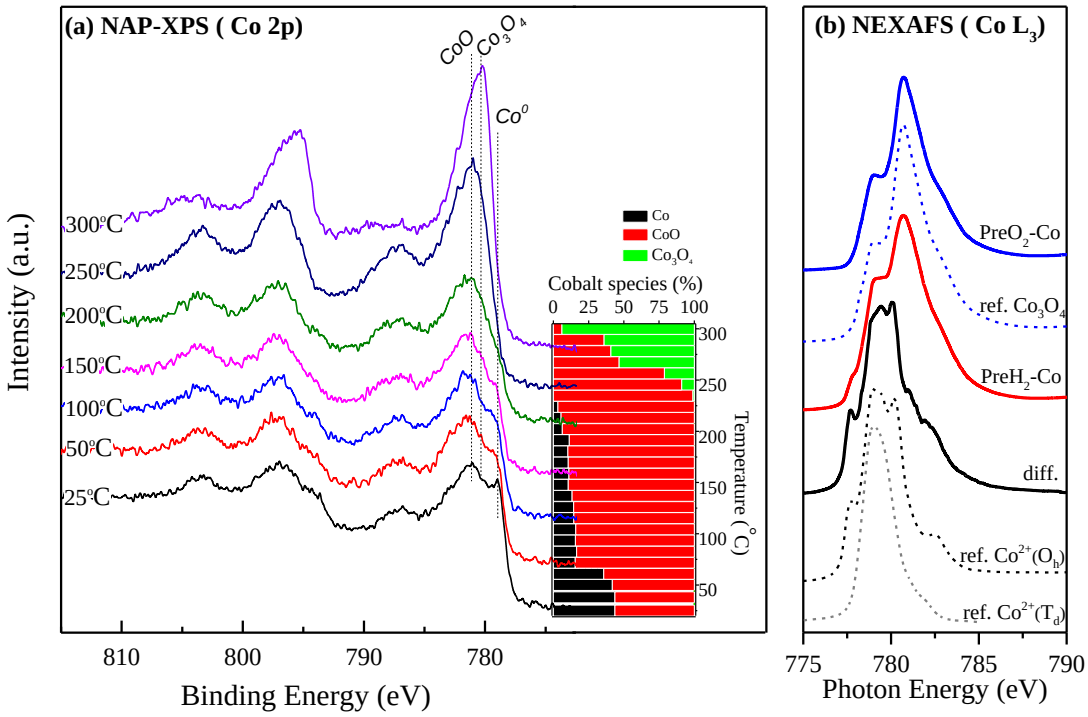

Figure 3-7. a) In-situ NAP-XPS spectra of Co 2p on $PreH_2$-Co during COPrOx at various temperatures. The inset shows the distribution of cobalt phases obtained by Co 2p peak deconvolution. *Reaction conditions*: 1%CO, 2%O_2 and 97%H_2 at 0.5mbar with a temperature ramping rate of 5ºC/min; prior to the reaction cobalt was reduced in 1 mbar H_2 at 400 ºC for 30 min. b). *In situ* NEXAFS spectra of $PreO_2$-Co and $PreH_2$-Co recorded at 300ºC at the aforementioned reaction conditions.

The depth distribution of CoO and metallic Co over the first few atomic layers was investigated by non-destructive depth profile measurements, in order to distinguish which of the two phases is located at the outermost surface layers during the dramatic enchantment of the COPrOx activity. The Co 2p spectra of $PreH_2$-Co recorded at 200 °C in COPrOx mixture with two different photon energies are shown in **Figure 3-8a**. As the photon energy increases (deeper layers are probed) the contribution of the metallic Co components in the Co 2p spectrum increases, suggesting that metallic cobalt is buried under a CoO surface layer, in a CoO-shell/Co-core like arrangement. Quantitative calculations based on the intensity ratio between CoO and Co species in the Co 2p spectrum,[274] indicate that the average thickness of the CoO layer at 200 °C is 1.1±0.1 nm, or about 3 to 4 CoO atomic layers. This result implies that the dramatic increase of the $PreH_2$-Co catalytic activity is associated with the formation of an ultrathin CoO layer on the surface of the cobalt catalyst.

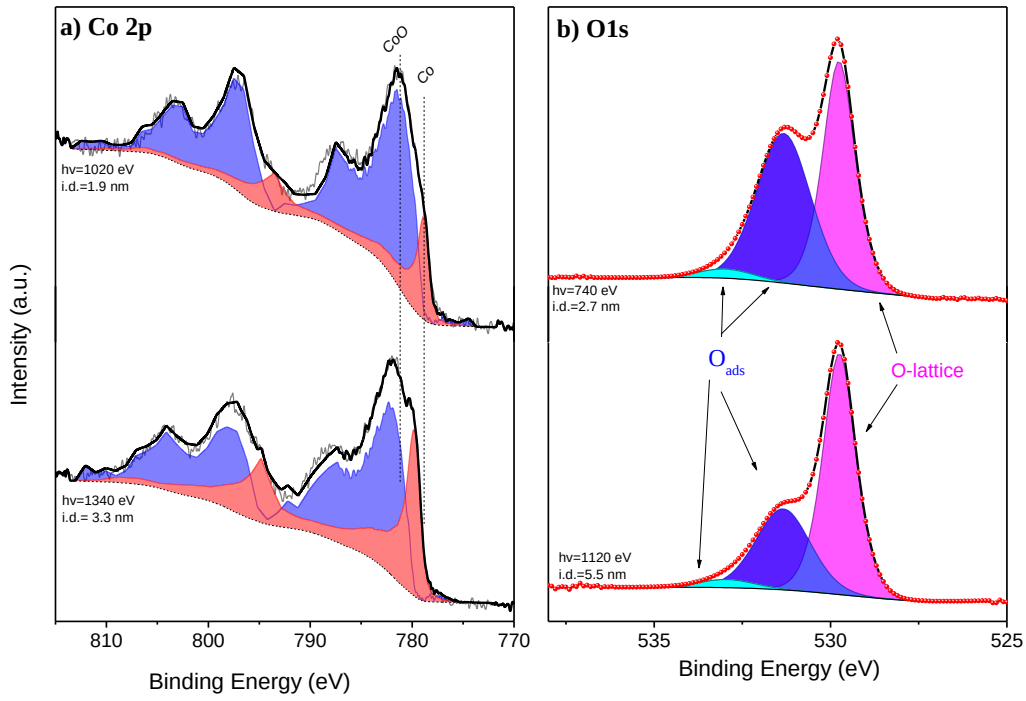

Figure 3-8. a) The Co 2p peak obtained on PreH$_2$-Co catalyst in CO-PrOx at 200ºC. b) The O 1s peak obtained on PreO$_2$-Co catalyst in CO-PrOx at 250ºC. CO-PrOx conditions: 1%CO, 2%O$_2$ and 97%H$_2$, 0.5 mbar. Spectra are recorded using two different excitation energies (hv), resulting in two electron kinetic energies (KE) and information depths (i.d.). The mean thickness of CoO estimated by the two spectra in figure is 1.1±0.1 nm.

To clarify the atomic structure of the cobalt oxides, NEXAFS was used as a sensitive local structure probe.[275] The Co L_3-edge absorption spectra of PreO$_2$-Co and PreH$_2$-Co under COPrOx at 300 ℃, as well as reference spectra of various cobalt oxides are summarized in **Figure 3-7b**. The Co-L_3 adsorption peak in case of PreO$_2$-Co is matching the reference Co_3O_4 spectrum indicating a Co_3O_4 spinel structure with an octahedral Co^{3+} and a tetrahedral Co^{2+} coordinated to oxygen,[196] in accordance with the NAP-XPS spectra shown in **Figure 3-6**. In the case of PreH$_2$-Co the Co L_3-edge peak differs from those of the reference Co_3O_4 and CoO samples. The curve obtained by subtraction of Co_3O_4 reference spectrum (indicated as diff. in **Figure 3-7b** corresponds to that of the standard CoO reference.[164] In addition, the resemblance of the difference spectrum with that of the octahedrally (Oh) coordinated CoO reference, suggests formation of the cubic rocksalt CoO phase, instead of the tetrahedral (Td) wurtzite CoO previously observed over oxidized cobalt nanoparticles.[177,196]

Figure 3-9 compares the C 1s and O 1s core level spectra of the PreO$_2$-Co and PreH$_2$-Co

catalysts recorded under identical COPrOx reaction conditions. In the C 1s region of $PreO_2$-Co shown in **Figure 3-9**, three carbon components can be clearly identified. The peak around 284.6 eV is due to C-H and C-C bonds, while those at 286.4 eV and 288.4 eV are induced by oxygenated carbon species (abbreviated as CO_x).[276] Similar carbon species are also detected over $PreH_2$-Co, however in a considerably lower amount than $PreO_2$-Co, as it is reflected by the evolution of the carbonate species (CO_x) inserted in **Figure 3-9**. As can be seen, the population of CO_x in the case of $PreO_2$-Co is systematically higher as compared to $PreH_2$-Co. Furthermore, the decrease of carbonates population on $PreO_2$-Co above 200 °C is correlated with the enhancement of the catalytic activity on this sample found in **Figure 3-1.** This result suggests that the population of carbonates over Co_3O_4 is inversely proportional to the catalytic activity of this sample, as will be discussed in detail later.

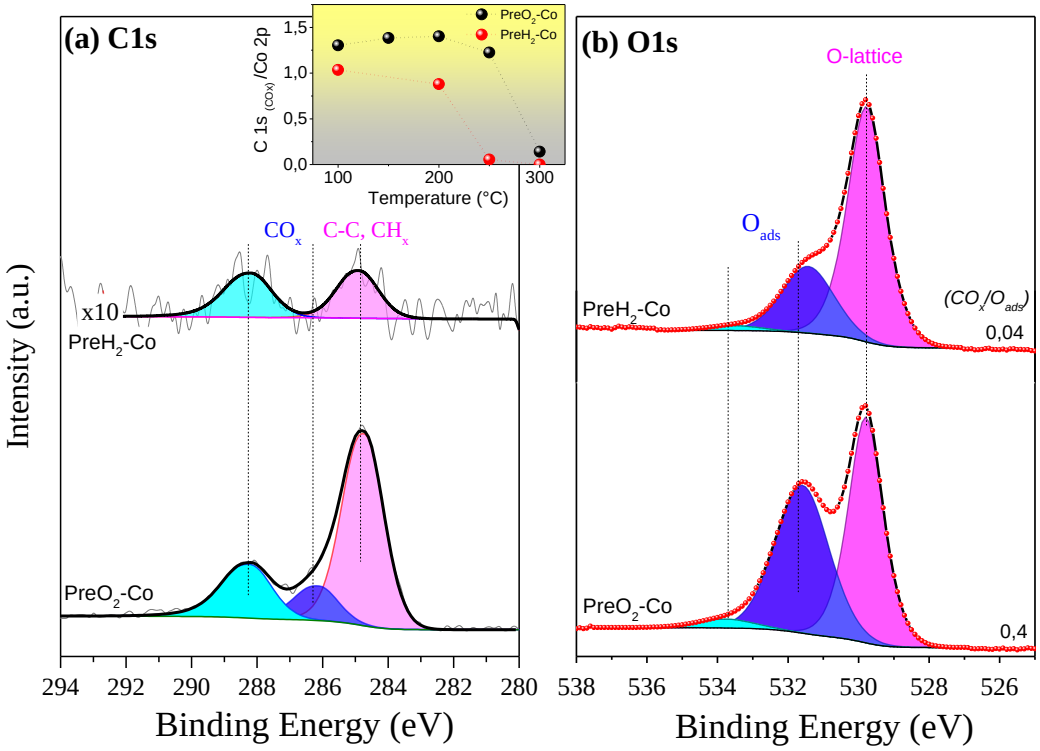

Figure 3-9. The NAP-XPS spectra of C1s (a) and O1s (b) on $PreO_2$-Co and $PreH_2$-Co recorded during COPrOx. Experimental Conditions: 1%CO, 2%O_2 and 97%H_2 at 250ºC in 0.5mbar. The Co 2p peak analysis shows that at these conditions the surface oxidation state is 100% Co_3O_4 and 95% CoO for $PreO_2$-Co and $PreH_2$-Co catalysts, respectively. The inset graph shows the evolution of the carbonate species (COx) as a function of the COPrOx reaction temperature calculated by the C 1s and Co 2p NAP-XPS spectra. The intensity of COx in the C 1s spectrum was determined by deconvolution of the C 1s peak similar to the one shown in figure 3-7a. Spectra were properly normalized to the photon flux and the photoemission cross section.

The O1s spectra shown in **Figure 3-9b** indicate the presence of multiple oxygen species. The peak at 529.8 eV is assigned to lattice oxygen of cobalt oxides, while the two O 1s components at 531.5 and 533.5±0.1 eV are typical for oxygenated carbon species and/or hydroxyl groups (abbreviated as O_{ads}).[103,175,254,277,278] *Depth-dependent NAP-XPS* spectra (see **Figure 3-8b** confirmed that O_{ads} components are mainly surface located over the lattice oxygen. Comparison of the O 1s spectra between the two samples indicates a notable enhancement of the O_{ads} in the case of PreO_2-Co catalysts. In particular, the O_{ads}/Co ratio increases from 0.53 for PreH_2-Co to 1.14 for PreO_2-Co. Since oxygenated carbon and hydroxyl groups have very similar binding energies in the O 1s region, it is not straightforward to compare their relative abundance on the two samples based on the O_{ads}/Co. In order to do so, we include in the **Figure 3-9b** the peak area ratio between the C 1s and O 1s components associated exclusively to CO_x and O_{ads} species respectively. The CO_x/O_{ads} ratio for PreO_2-Co is found 0.4 which is in fair agreement with the expected stoichiometry of carboxyl species (0.33). On the contrary, the corresponding CO_x/O_{ads} ratio for PreH_2-Co is 10 times lower (0.04), which suggests that the oxygenated carbon species are accountable of a very small fraction of the O 1s peak at 531.5 eV. Therefore, one can assume that the PreH_2-Co contains a significant contribution of adsorbed OH groups, at least as compared to the PreO_2-Co.

3.3.4 The influence of the pressure gap on the cobalt oxidation state during COPrOx

In order to examine the effect of the pressure gap between the spectroscopic and catalytic experiments (0.5 mbar instead of 1 bar) on the stability of CoO, the COPrOx reaction over PreH_2-Co was performed at various pressure regimes using a variable-pressure reactor. The Co $2p_{3/2}$ spectra (**Figure 3-10**) recorded after reaction reveal that CoO is the main cobalt oxidation state with minor contribution of metallic Co (<12%) in the entire pressure range, with an exception the experiment at 10 mbar, where metallic Co is not observed. Since XPS measurements were not performed in situ, it is difficult to verify the cause of complete cobalt oxidation at this pressure. However metallic Co is not expected to significantly influence the reaction, since according to depth dependent measurements (**Figure 3-8a**), the surface is dominated by CoO. Variable pressure experiments provide strong evidence that for PreH_2-Co the CoO can be maintained during COPrOx reaction at temperatures around 200 °C and realistic reaction pressures. We note that when variable pressure experiments were performed

over $PreO_2$-Co, the Co_3O_4 phase was the only one detected after reaction (data not shown).

The evolution of the reactants and products as a function of temperature at the two extreme pressure regimes, namely $0.5x10^{-3}$ and 1 bar, are shown in the mass spectrometry results inserted in **Figure 3-10**. The reactivity profiles are comparable in both pressure regimes indicating a qualitatively similar catalytic performance of CoO. Mass spectrometry profiles are also very much alike the GC results discussed in **Figure 3-3**. Please note that during the combined catalytic and XPS experiments the H_2 concentration in the PrOx mixture was 97%, which is considerably higher than the one used for the catalytic tests and the DRIFTS experiments discussed next (40% H_2).

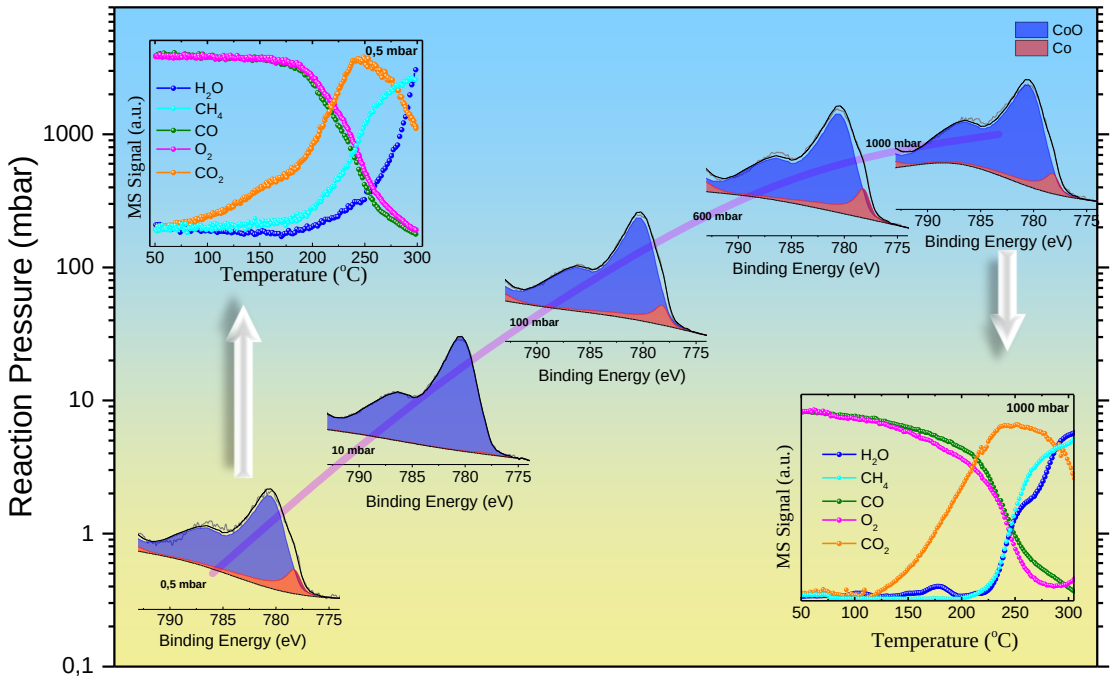

Figure 3-10. The XPS $Co2p_{3/2}$ spectra of $PreH_2$-Co measured after COPrOx reaction at 210 °C at various total pressures. The $Co2p_{3/2}$ spectrum at 0.5 mbar is in situ NAP-XPS, while higher pressures Co $2p_{3/2}$ spectra were recorded ex situ after 30 min reaction followed by reactants evacuation and transfer under vacuum to the XPS spectrometer. The inset graphs show the corresponding QMS data of the consumption of reactants and yields of products as a function of the reaction temperature recorded at 0.5 and 1000 mbar (the reaction temperature in these experiments was expanded up to 300 °C).

The influence of H_2 concentration on COPrOx catalytic performance has been previously studied over Ru and Au catalysts.[279,280] These studies have shown that at low concentrations H_2 promotes CO oxidation reaction, but above 20 % H_2 the influence of H_2 concentration in the CO conversion activity fades. According to these reports it is expected that the high H_2

concentration used during the NAP-XPS and VPR XPS experiments should not significantly influence the catalytic behaviour. Overall, both ex situ and in situ spectroscopic results confirm that CoO can be stabilized during COPrOx in a quite broad pressure range.

3.3.5 Operando DRIFTs Study

Diffuse reflectance infrared Fourier transform spectroscopy (DRIFTS) was used to evaluate in situ the formation of adsorbed species. The DRIFTS peaks related to CO adsorbed species after careful subtraction of the contribution of the gas phase bands are shown in **Figure 3-11**a and b, for $PreO_2$ and $PreH_2$-Co respectively. The absorption band around 2058 cm^{-1} observed at low temperatures on both samples is assigned to the linearly adsorbed CO (CO_{ads}) on cobalt.[281] The CO_{ads} peak disappears at higher temperature due to the weak interaction of CO with the surface. The band at 2018 cm^{-1} corresponds to C=O species and it is stable on $PreH_2$-Co but is practically absent on $PreO_2$-Co. This type of adsorbed species is known to strongly adsorb on reduced cobalt phases,[282,283] confirming the in situ XPS results of **Figure 3-7.** The band at 2040 cm^{-1} which is enhanced with temperature could be assigned to CO adsorbed on ionic cobalt species,[284] *e.g.* Co^{2+} of CoO, the presence of which is expected according to the photoemission results. This is in agreement with the CoO distribution as a function of reaction temperature and the fact that the cobalt with higher valence has a CO absorption band at higher wavenumber region.[281]

On the $PreO_2$-Co the absorption bands in the range between 2030 and 2090 cm^{-1} have been previously attributed to CO absorption on Co^{3+} and Co^{2+} sites of Co_3O_4.[283] However, apart from CO_{ads} at 2058 cm^{-1} and a weak absorption peak at 2081 cm^{-1}, it is difficult to consistently identify the CO absorption bands in this region. This is partially due to the weak FTIR signal induced by multiple absorptions on the dark Co_3O_4 powder in this case. Nevertheless, the in situ DRIFTS results support the fact that $PreH_2$-Co may contain metallic Co and CoO under atmospheric pressure reaction conditions.

The absorption bands in the region from 3200 to 4000 cm^{-1} (**Figure 3-11b**) are due to adsorbed hydroxyl groups (-OH_{ads}) and water molecules.[283] A broad band around 3530 cm^{-1} appears in both $PreO_2$-Co and $PreH_2$-Co and its intensity is notably increased with the reaction temperature. This peak is induced by the stretching modes of H-bonded OH- groups of water molecules[285,286] and it is consistent with the water formation due to hydrogen oxidation shown by the mass spectrometry at high temperatures. Besides, at low temperatures

an additional absorption band is observed around 3745 cm^{-1} mainly on the $PreH_2$-Co. This band was previously ascribed to non-H-bonded OH- species,[287] formed on the surface of CoO via surface hydrogenation. Above 250 ºC an additional narrow band at 3015 cm^{-1} related to the methyl ($-CH_3$) species[288,289] is observed on $PreH_2$-Co, complying with the production of methane at higher temperatures observed in the gas phase.[7,26,268,290]

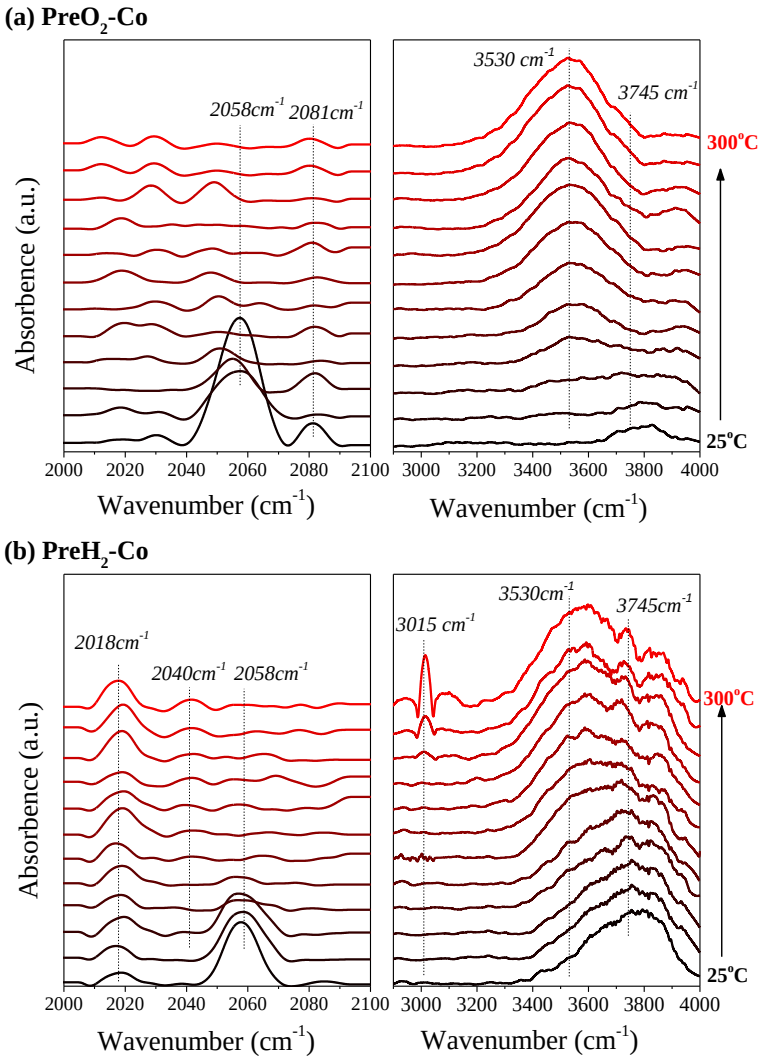

Figure 3-11. *In situ* DRIFTS spectra recorded under COPrOx reaction at various temperatures over a) $PreO_2$-Co and b) $PreH_2$-Co. *Reaction conditions*: 1%CO, 2%O_2 and 97%H_2 at 1 bar with a temperature ramping rate of 5ºC/min.

The main frequency region of carbonate vibrations is shown in **Figure 3-12**. In this region the absorption bands of several carbonate species, such as bidentate and monodentate, appear together with other carbon species such as formate and acetates.[291–293] Comparison between $PreH_2$-Co and $PreO_2$-Co samples reveals that 3 particular peaks are relatively more intense in

the case of $PreO_2$-Co. These peaks are centered at frequencies of about 1230, 1340 and 1465 cm^{-1}. Based on previous results the band at 1230 cm^{-1} can be assigned to bicarbonate and/or carbonate species,[291] the one at 1340 cm^{-1} to formate and/or bidentate carbonates,[227,291,294,295] while the peak around 1465 cm^{-1} is due to mono- or poly-dentate carbonates species.[227,294–296]

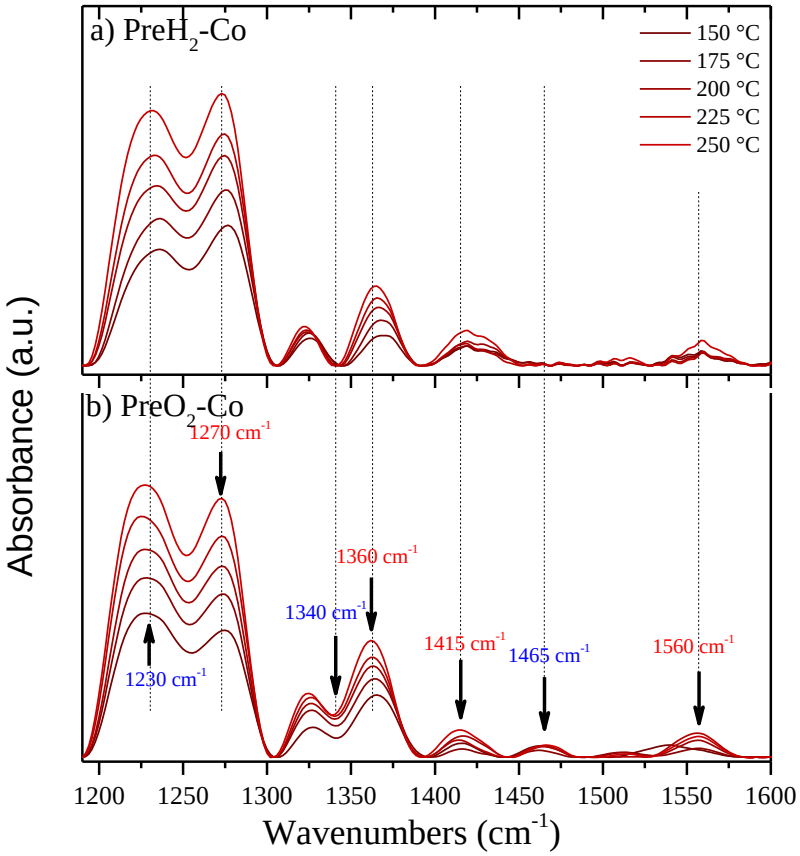

Figure 3-12. The in situ DRIFTS spectra over $PreH_2$-Co (a) and $PreO_2$-Co (b) under COPrOx reaction condition from 150 to 250ºC. Conditions:1%CO, 2%O_2, 40%H_2 in He balance. The broad peak of absorbed water around 1600 cm^{-1} has been subtracted to facilitate the detection of carbon-based species.

Quantitative comparison of carbonate coverage between the two samples is not straightforward since the DRIFTS signal is influenced by the penetration depth of the infrared beam into the powder sample which is a strong function of the particle size and packing density.[297] However, DRIFTS results reveal key differences in the adsorbed species between the two surfaces during COPrOx.

3.4 **Correlation between cobalt oxidation state and COPrOx reactivity**

The COPrOx catalytic tests showed that pre-reduced cobalt oxide catalysts can maintain a significantly higher specific activity as compared to their oxidized counterparts, at least for intermediate reaction temperatures. The reduction pretreatment induces pore formation (**Figure 3-5**) and increases the BET surface area of cobalt powders (**Table 3-1**), which can partially explain the dramatic enhancement of the overall % CO conversion observed on this sample. However, comparison of the surface specific activities between 150 and 250 °C (**Figure 3-1a**) manifests that the higher activity of PreH_2-Co cannot be entirely justified by invoking the differences in the surface areas. The *in situ* NAP-XPS and NEXAFS experiments (**Figure 3-7**) demonstrated that CoO is maintained on the surface of PreH_2-Co during COPrOx at least up to 250 °C, while PreO_2-Co remains as Co_3O_4. The higher surface specific activity at identical COPrOx reaction conditions (up to 8 times) is associated with CoO surfaces. When the reaction temperature increases to 300 °C, the CoO phase of the PreH_2-Co sample is transformed into Co_3O_4, and correspondingly the difference between the surface specific activities between the two catalysts fades (**Figure 3-1a**). In spite of that, the overall % CO conversion remains higher on the PreH_2-Co catalysts due to their porous morphology induced by the pretreatment (seen in SEM and TEM images). The findings of NAP-XPS results regarding the stability of CoO during COPrOx can be at least qualitative, extrapolated also in 1 bar reaction conditions (**Figure 3-10**), which represents an important confirmation of the dominant effect of the surface oxidation state on the COPrOx reactivity.

The in situ DRIFTS spectra (**Figure 3-11**) advocated formation of several carbon and oxygen-bearing adsorbed species, which are transformed during the reaction. Along with that, the analysis of the C 1s and O 1s in situ photoemission spectra (**Figure 3-9**) suggested that the surface oxidation state of cobalt catalyst can directly affect the concentration of surface-adsorbed species during COPrOx and consequently the reaction kinetics. With the aid of first principles DFT calculations we could explain why more carbon species were detected on the pre-oxidized catalyst as compared to the pre-reduced one at the same temperature. The calculation of CO adsorption suggests that CO oxidation is significantly less exothermic (-35 kJ/mol) on Co_3O_4 than on CoO (-67kJ/mol), which actually cannot explain why CoO performs better in the reaction. However, the calculated barriers for CO_2 desorption is

significantly lower for CoO (41 kJ/mol) than for Co_3O_4 (71 kJ/mol), which practically means an increased residence time of CO_X-type species on the more coordinatively unsaturated Co_3O_4. The increase in carbon coverage translates into a higher number of blocked sites on Co_3O_4, which would rationalize the higher CO oxidation activity of CoO under the same conditions. The DFT predictions are in accordance with the experimental data shown in **Figure 3-9a,** where a net increase of carbonate species under COPrOx was observed in the case of surface Co_3O_4 formation.

3.5 Effect of the reactants flow on the cobalt oxidation state

The above presented results established the relation between cobalt oxidation state and reactivity. In this paragraph we examine how the flow of the reactants (the inverse of the weight hourly space velocity, WHSV) affects the oxidation state of cobalt and consequently its reactivity. The experiments were performed in the variable pressure reactor (VPR, 0.6L volume) attached to the UHV setup with a monochromatic XPS spectrometer, described in the experimental part and in reference [298]. Prior to the reaction the Co_3O_4 powder catalyst was reduced *in situ* in the VPR reactor at 400 °C in 1 mbar of H_2 for 30 min. Consequently, it was cooled down in H_2 and the COPrOx reaction mixture (composition: 1% CO, 1% O_2 %, 50% H_2 in He, total pressure of 10 mbar) was introduced at 30 °C. The temperature was raised at 300 °C with a ramp rate of 10 °C/min and the catalysts maintained at this temperature for 30 min. Finally, the sample was cooled down in the COPrOx mixture, the reactor was evacuated to 10^{-7} mbar and the sample was transferred under vacuum to the XPS chamber for analysis. This procedure was repeated for 5 different gas inlet flows using calibrated mass flow controllers. In all cases, the total pressure of the reaction was kept constant at 10 mbar by regulating the exit flow of the reactor using a motorized gas regulating valve (EVR 116, Pfeiffer). The reactor residence time (τ_r) is calculated based on the formula given below.

$$\text{Reactor residence time}, \tau_r\ (\text{s}) = \frac{\text{volume of reactor}(\text{cm}^3)}{\text{output volumetric flow rate}\ (\text{cm}^3\ \text{s}^{-1})} \qquad \textbf{Eq. 3-4}$$

The applied flows and the corresponding residence times used in the experiment are given in **Table 3-2**:

Table 3-2 The content of different Co species on spent pure Co under different gas flows corresponding to different residence time.

Reactants flow (cm^3/min)	**Reactor residence time** (sec)	**Co^0** *from Co 2p* (%)	**CoO** *from Co 2p* (%)	**Co_3O_4** *from Co 2p* (%)
8	4500	55.9	44.1	0
10	3600	39.5	60.5	0
25	1440	0	100	0
50	720	19.5	0	80.5
100	360	8.5	12.2	79.3

Figure 3-13 shows the Co 2p spectra recorded after COPrOx reaction for the different gas inlet flows shown in **Table 3-2.** The percentage of the 3 different oxidation states of cobalt (Co^0, CoO and Co_3O_4) included in **Table 3-2**, was estimated by deconvolution of the Co 2p peak using reference spectra. The mean valence state of cobalt as a function of τ_r is shown in the inlet graph of **Figure 3-13**. From these results it becomes clear that the flow of the reactants has a dramatic effect on the oxidation state of cobalt catalyst. In particular, the higher the flow (*i.e.* the lower the reactor residence time of the gases) the more oxidized the cobalt catalyst.

The catalytic response of each experiment as a function of the reactor residence time (i.e. gas flow) is given in **Figure 3-13b**. The O_2 conversion (X_{O2}) is influenced dramatically by the residence time, with higher τ_r contributing to equally higher X_{O2}. On the contrary, the conversion of CO (X_{CO}) is stable up to τ_r = 1440 sec (flow 25 cm^3/min), but drops almost 3 times for τ_r < 1440 sec. According to the discussion in the previous paragraphs, the drop of the CO conversion it is most probably caused by the high concentration of Co_3O_4 on the surface of the catalyst reveled by the post-mortem XPS analysis (**Figure 3-13a**). The selectivity of CO to CO_2 (S_{CO2}) between the higher the lower τ_r increases of about 2 times, in agreement with the observations of the X_{O2} (please note that the S_{CO2} is calculated here as the X_{CO} / 2*X_{O2} ratio).

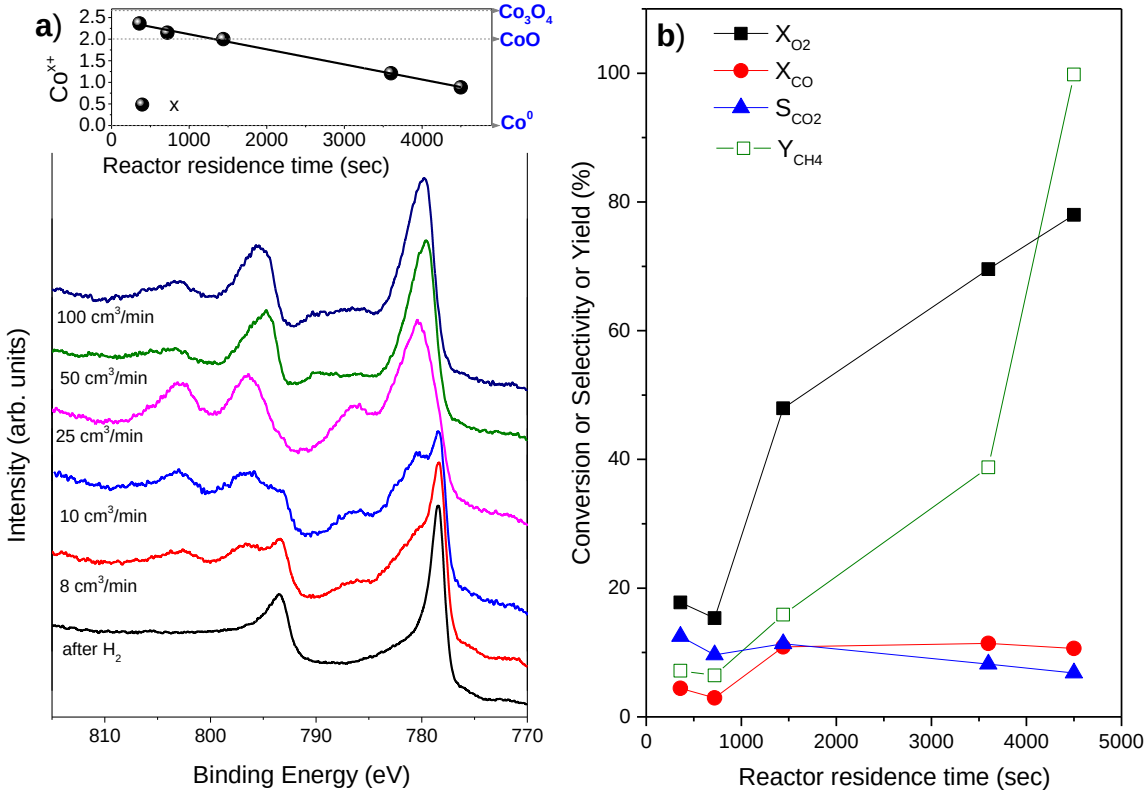

Figure 3-13. (a) XPS spectra of Co 2p after reaction under different flow corresponding to different reactor residence time and (b) the% conversion of O_2 and CO, the CO_2 selectivity and the CH_4 yield calculated based on the QMS date recorded during COPrOx reaction with different residence time. The inset of figure a, shows the mean cobalt oxidation state as a function of the reactor residence time. Reaction conditions: 1%CO, 1%O_2, 50%H_2 in He, total pressure of 10mbar, heating from 30°C-300°C with a ramping rate of 10°C/min.

It is extremely interesting to note the dramatic differences observed in the CH_4 production (represent as the yield, Y_{CH4}, normalized to the maximum CH_4 signal increase observed by the QMS) as a function of the residence time. The higher CH_4 yields are observed in flow conditions where high amounts of metallic cobalt are noted by XPS (i.e. high τ_r). This correlation is in agreement with the well-known property of metallic cobalt to catalyze the CO and CO_2 methanation reactions[7,26,268,290] and provides another indication that reactivity and surface oxidation state of cobalt are closely associated.

The catalytic tests performed in the VPR are in agreement with previous studies suggesting that the residence time has an influence over the performance of the catalysts for COPrOx. In particular, it has been reported that the CO conversion increases with the increase in the residence time, while the CO selectivity slightly decreases[299] similar to the results in **Figure 3-13b**. However, here we provide new evidences about this behavior by combining catalytic

results with XPS analysis. It is shown clearly that the effect of the residence time might be directly correlated with the changes in the surface state of the catalyst.

Describing in detail the influence of the residence time of the reactants in the reactivity is a complex task that requires detail kinetic studies, using a conventional catalytic reactor. Although, such analysis is out of the scope of this thesis, it is interesting to attempt to qualitatively explain why high COPrOx reactants flows oxidize cobalt catalysts in a greater extent than the low flows. The gas phase O_2 in the COPrOx mixture is not only used for the CO oxidation reaction, but it is also an oxygen source for cobalt oxidation. It is evident that the higher the abundance of O_2 in the COPrOx gas mixture the more extended the cobalt oxidation would be. For a fixed COPrOx mixture composition, the abundance of O_2 in the gas phase above the catalyst depends of 2 main factors: i) the O_2 conversion either to CO_2 or to H_2O formation and ii) to the flow of the reactants in the sense that higher flows means decrease of contact time and the amount of the adsorbed reactants on the surface of the catalyst. The gas phase analysis in **Figure 3-13b** shows that the O_2 conversion increases considerably with the increase of the residence time, which indicates that in this case there is less available oxygen for the oxidation of cobalt. This can explain why the cobalt catalyst appears more reduced in the post-mortem XPS analysis under low flow reaction conditions.

Here should be noted that the explanation provided above takes into account only one of the factors that affect cobalt oxidation, i.e. the oxygen concentration in the gas phase. Definitely, other parameters such as the temperature, the intrinsic reactivity, the redox effect of the other gases in the mixture (e.g. H_2O), *etc.* are affecting the redox behavior of the catalysts. However, these results indicate that changes in the surface oxidation state of cobalt, and probably for other transition metals as well, is the rule rather than the exception during COPrOx. Therefore, it should be considered also for other types COPrOx studies, as for example in kinetic studies targeting to describe the reaction mechanism.

3.6 **Conclusions**

In this chapter, CoO and Co_3O_4 surfaces were formed over unsupported cobalt powder by gas pretreatments and their COPrOx reaction performance was compared. Notably, the oxidation state of cobalt has a remarkable effect on the COPrOx activity, suggesting that octahedrally coordinated Co^{2+} in the CoO form is considerably more active for this reaction as compared to Co_3O_4. DFT calculations made by colleagues in University of

Wisconsin–Madison suggest that a possible origin of the activity differences is the blocking of surface sites by carbonates which are favored on Co_3O_4 (001) but not on CoO(001) surfaces.

Overall, this chapter provides solid arguments about the most active state of cobalt oxide catalysts for COPrOx reaction and concludes a lasting debate on this topic. The insights into the high CoO activity for COPrOx reaction provided here not only shed light on a long standing debate, but also provided an important step towards new design strategies of high-performance COPrOx catalysts. Moreover, these results might be also extended to emphasize on the crucial role that the near-surface region has on the catalytic performance. Although this role has been made apparent since the early surface chemistry studies, determination of the more active catalytic state has been always challenging due to the so called material and pressure gaps. Here we were able to correlate surface state and catalytic performance over complex catalytic materials and under realistic reaction conditions, following an approach that can be employed in the future for other catalytic reactions.

An additional important point found in this chapter is that at certain reaction conditions the cobalt deactivates fast and this is clearly related to the oxidation of CoO to Co_3O_4. As it will be shown, this information will be used in the next chapters as a guide to synthesize a cobalt catalyst, which is not only active, but also much more stable.

Chapter 4

Influence of Manganese in the Catalytic Performance of Cobalt during COPrOx

4.1 Introduction

In the previous chapter it was shown that formation of CoO-type surface oxide is beneficial for the COPrOx activity, but unfortunately this face is metastable and is transformed fast to the less active Co_3O_4. In an attempt to stabilize CoO on the surface for longer time and in a wider range of reaction conditions, cobalt oxide catalyst was modified by the addition of transition metals. In general, this approach is quite common in the research of new catalytic materials and has been partly exploited also in the case cobalt-based COPrOx catalyst. However, this thesis is not interested to scan the effect of various metal additives on cobalt, hereafter called a promoter, in order propose the best combination. This type of research requires combinatorial tests of maybe hundreds cobalt based catalysts, which focus exclusively to evaluate the catalytic performance and consider the catalyst as a "black box". As mentioned in the introduction part, this thesis focus on the effect of the surface state of the catalyst and therefore the role of the promoter will be considered in anticipation of its effect on cobalt oxidation state. This is a new approach to deal with the effect of metal promoters and it made possible only after the research described in the previous chapter which reveal the desired cobalt oxidation state for the reaction.

Among the reported cobalt-based catalysts for COPrOx, cobalt modified via addition of MnO_x and CeO_2 have shown the most promising catalytic performance.[10,12,300,301] Since the effect of ceria as a source or sink of mobile oxygen is well described and extensively studied in the literature, it was decided to focus on the effect of the less studied manganese oxide promoter on cobalt. Several groups have reported that the addition of Mn has a positive effect on the performance of cobalt catalysts, which is superior to that of other metal promoters for both CO oxidation[10,83,307,308,256,300–306] and COPrOx reactions.[83,309,310] The positive effect of manganese is not well understood, but several authors speculate that the existence of MnO_x in Co_3O_4 stabilizes the Co^{3+} species on the catalyst surface by facilitating oxidation of Co^{2+} to Co^{3+}.[300,308] However, this hypothesis assumes that Co^{3+} sites inside Co_3O_4 are the active sites for CO oxidation in the presence of H_2, which according to the findings shown in *Chapter 3* is inaccurate.[311] This evident contradiction between the spectroscopic findings supported by DFT calculations presented in *Chapter 3*, and the common perception in literature, was the

driving force to investigate the promotional effect of Mn over cobalt for COPrOx in this chapter. One has to keep also in mind that pure nanostructured MnO_x was proposed to be a highly active catalysts for CO oxidation.[312] The following trend for the CO oxidation activity of various manganese oxidation states oxides (at 523 K) has been reported by Ramesh et al.[313] and Wang et al.[314] : $MnO<MnO_2<Mn_2O_3$. This indicates that the oxidation state of manganese may also play an essential role for CO conversion.

Understanding the interaction of elements in a hybrid catalyst is of importance for the catalyst's development. As discussed in *Chapter 1* the oxidation state of manganese and cobalt during COPrOx is dynamic and their evolution needs to be studied by *in situ* and *operando* analytical techniques. However, to the best of the authors' knowledge the evolution of Mn oxidation state in Co-Mn system during the COPrOx has never been studied in detail. This provides an additional motive for the study of Co-Mn using *in situ* surface sensitive methods.

According to literature a certain ratio between Co and Mn seems to be the optimal composition for CO PrOx. [83,310] Therefore in this work we did not try to optimize the Co-Mn catalyst composition, but we were focus on the study of the known ratio which has shown the best activity based in previous reports. [83,310] In this chapter, in addition to the conventional *ex situ* structural characterization (H_2-TPR, XRD, SEM, BET), operando and *in situ* NAP-XPS and NEXAFs were applied to investigate the active phase of MnO_x-CoO_x for COPrOx, emphasizing to the oxidation state of each component at various reaction conditions. Moreover, this chapter reports the first study on the evolution of manganese oxidation state during COPrOx and its effect on CO conversion and selectivity.

4.2 Experimental Methods

4.2.1 Catalysts preparation

In the attempt to study the promotional effect of Mn on CoO phase, commercially available cobalt monoxide nanoparticles (CoO, 99.99%, Sigma Aldrich CAS# 1307-96-6) are used in this chapter. These particles were used as catalysts in their in pure form (CoO_x), or as a support for the synthesis of Co-Mn catalysts (Co_8MnO_x). The Co_8MnO_x catalyst was synthesized by incipient wetness impregnation method. In details, 0.5025g of Manganese(II) nitrate tetrahydrate ($Mn(NO_3)_2.4H_2O$) was dissolved in 0.317g of water. The obtained

solution was added into 1.2 g of the commercial CoO nanoparticles and the obtained mixture was dried in air at 120 ºC for 12 h. The dry product was subsequently calcined in air at 400ºC for 3h. The chosen atomic ratio of Co/Mn was 8/1, which, as mentioned above, has been reported to be the best atomic ratio for a Co-Mn PrOx catalyst.[300] The same synthesis method was also used for the preparation of the $CoMn_8O_x$ catalyst (the atomic ratio of Co/Mn was 1/8 in this case). However, in this catalyst the Mn_3O_4 particles were acting as support and were impregnated with cobalt-containing solution. In particular, 1.83 g of commercial Mn_3O_4 was impregnated with an aqueous solution of 0.582g of $Co(NO_3)_2.6H_2O$ solved in 0.144 g of water. Then the mixture was firstly dried for 12 h at 120 ºC and subsequently calcined in air for 3 h at 400 ºC. The calculated atomic ratio of Co/Mn is 1/8.

4.2.2 Catalytic evaluation

The catalytic oxidation of CO in the presence of H_2 (COPrOx) was performed in a fully automated fixed-bed flow reactor (CETRIB SARL, Andlau, France).[201] 50 mg of the catalytic powder was introduced in a Pyrex glass tube (i.d. 10 mm) and dispersed evenly on a P3 glass frit (16-40 µm). Average thickness of the catalytic bed was about 1 mm. The glass reactor was then introduced in a tubular oven with the catalyst bed located in the isothermal zone. Gas mixtures were generated using calibrated (Serv's Instrumentation) mass flow controllers from Bronkhorst. The COPrOx gas mixture was composed of 1% CO, 1% O_2, 50% H_2 balanced in helium. Please note that the concentration of O_2 in the mixture is half as compared to the experiments described in Chapter 3. The reactants feed was introduced in reactor at a total flow rate of 50 mL/min (1 atm, GHSV ~ 7,500 h^{-1}). The temperature (reaction temperature) was monitored by a type K thermocouple plunged inside the catalytic bed.

Prior to each test, the pre-reduced catalyst was reduced once again this time *in situ*, by using the following protocol: heating at 400°C for 30 min in 100% H_2 (50 mL/min) with a ramping rate of 10°C/min and cooling back down to 30°C . The residual oxygen content of the gas phase was below 100 ppm. For light-off tests, the catalyst was heated under the COPrOx mixture at 50, 100, 150, 200, 250, 300 and 350°C using a ramp of 10°C/min and dwells of 30 min at each temperature. For COPrOx stability tests, the catalyst was heated at 250°C then 300°C (10°C/min) and finally back to 250°C again. The catalyst was held at each temperature for 2.5 h.

The CO and O_2 conversions (X_{CO}(%)) and O_2 (X_{O2}(%)) are calculated as follows:

$$X_{CO,T}\ (\%) = \frac{A_{CO,30°C} - A_{CO,T}}{A_{CO,30°C}} \times 100$$

$$X_{O2,T}\ (\%) = \frac{A_{O2,30°C} - A_{O2,T}}{A_{O2,30°C}} \times 100$$

Where

$A_{CO,30°C}$ and $A_{O2,30°C}$ are the areas of the corresponding GC peaks at 30°C (no reaction, hence proportional to the concentration of each gas in the unreacted feed). $A_{CO,T}$ and $A_{O2,T}$ are the areas of the corresponding GC peaks at a given reaction temperature (proportional to the concentration of each gas at the outlet).

Selectivity of O_2 towards CO conversion (S_{CO2}) is calculated as follows:

$$S_{CO2,T}\ (\%) = \frac{1}{2} \times \frac{A_{CO,30°C} - A_{CO,T}}{A_{O2,30°C} - A_{O2,T}} \times 100$$

where RF_{CO}, RF_{O2} are the response factors of the corresponding gases determined by external calibration.

4.2.3 Structural and morphological characterization

Temperature-programmed reduction with hydrogen (TPR-H_2) of catalyst was performed by means of an automated catalyst characterization system (Micromeritics, model AutoChem II), which incorporates a thermal conductivity detector (TCD). 50 mg of sample was loaded in a U tube and heated by 5 °C/min under 10ml/min of 10% H_2 in Ar. Ex situ XRD patterns were collected on a Bruker D8 advance diffractometer using Cu Kα radiation. The crystallite size of cobalt phase was calculated according to the line broadening of the most intense reflections using the Scherrer equation.[315] The BET surface area of each sample was monitored by physical adsorption of N_2 method. Samples were degassed at 200 °C for 5 h before launching the adsorption-desorption of N_2. The specific surface areas were calculated according to the Brunauer−Emmett−Teller (BET) method using data points in the relative pressure (p/p0) range of 0.05−0.35. The morphology of spent and fresh catalysts was

examined by a Zeiss GeminiSEM 500 SEM microscope, combining with energy dispersive X-ray spectroscopy (EDX) to study the distribution of elements on surface.

4.2.4 Synchrotron-based *in situ* spectroscopic study

In order to investigate the interaction among Co, Mn and the reaction environment, synchrotron-based *in situ* spectroscopy of NAP-XPS and NEXAFs were performed on CAT beamline based on BESSY II synchrotron facility in Berlin, Germany. Two catalysts (pure CoO_x and Co_8MnO_x) were examined under identical conditions in a comparative basis. The powder catalysts were pressed into pellets and mounted on the sample holder using a stainless steel mask. The heating was done from the back side by an IR laser. The temperature was measured by a K-type thermocouple contacted on the sample surface. The gas flow was monitored via 4 calibrated mass flow controllers. The total flow rate for these experiments was kept constant at 15 ml/min. Please note that this flow is half of the one used in the synchrotron experiments related to cobalt-vanadium catalyst which will be discussed in *Chapter 5* below (30 ml/min in this case). The NAP-XPS spectra of Co 2p, Mn 2p, O 1s and C 1s were collected under gas environment at 0.5 mbar total pressure. Quantitative analysis of elements was performed using normalized intensities, taking into account the photon flux and the photon-energy dependence of the atomic subshell photoionization cross sections.[251] The deconvolution of spectra was based on the literature reference and experimental reference spectra. The adsorption spectra of Co L_3-edge and Mn L_3-edge were measured on total electron yield mode.

4.2.5 Operando NAP-XPS study using a conventional X-ray source

An *operando* NAP-XPS study of pure CoO_x, Co_8MnO_x and $CoMn_8O_x$ catalysts under the reaction conditions was performed at Charles University in Prague, Czech Republic. The experiments were carried out on a photoelectron spectrometer (SPECS Surface Nano Analysis GmbH, Germany) which is equipped with a PHOIBOS-150 multichannel hemispherical electron energy analyzer coupled with a differentially pumped electrostatic pre-lens system. Spectra were obtained using the monochromatized Al Kα X-ray source (1486.6 eV). The powder of fresh as-synthesized catalysts was pressed to pellets and fixed on the sample holder using a stainless-steel mask with a window. The thermocouple was welded on the mask at the side which was in contact with the sample surface. The catalyst was

investigated in flows of pure CO, pure O_2 and H_2 with the $CO:O_2:H_2$ molar ratios of 1: 1: 98. Before introduction of the COPrOx gases, the sample was pre-reduced in 1 mbar of hydrogen at 400°C for about 2 hours. After cooling down to 50 °C, 1 mbar of the aforementioned COPrOx mixture was introduced into the NAP-XPS cell. During the pretreatment and reaction, after arriving at certain target temperature and stabilizing at least 30 min, the XPS spectra were collected. To follow the change of concentrations of the reagents and products with temperature increase the gas mixture in the cell was simultaneously monitored by mass spectrometry (Prisma Pro, Pfeiffer Vacuum, Germany).

4.3 Experimental Results

4.3.1 Textural and morphological properties of CoO_x/MnO_x

Prior to the *operando* experiments, the three catalysts were characterized through standard analytical methods. The BET specific surface area of the materials was determined by N_2 physisorption measurements. As suggested by the results presented in **Table 4-1**, the parent CoO nanoparticles have relatively low surface area of about 10 m^2/g, which further decreased to extreme low surface area of 1.4 m^2/g due to severe agglomeration caused by the reduction at 400°C. The addition of Mn to pure Co (Co_8MnO_x) led to a small decrease of the surface area after calcination of about 10%, however, it limits the agglomeration degree of cobalt particles during reduction pretreatment. In particular the surface area decreases from 9 to $6m^2/g$ in case of Co_8MnO_x which is considerably better as compared to the decrease in pure cobalt from 10 to 1.4 m^2/g. In the case of the $CoMn_8O_x$ catalyst, the surface area is significantly lower than that of other two catalysts, which is due to the low porosity of parental manganese oxide (Mn_3O_4) used for the sample preparation. Surprisingly, contrary to the other samples the surface area of $CoMn_8O_x$ increased from 3 to 8 m^2/g after the reduction pretreatment. The reason of this increase is not clear yet, but it might be ascribed to introduction of cobalt from the solution into the grain boundaries of the agglomerated parent Mn_3O_4 particles during the H_2 pretreatment which changes the $CoMn_8O_x$ particles size.

The crystalline nature of the three catalysts was assessed by X-Ray Diffraction. The diffractions patterns of the catalysts recorded before (fresh) and after reduction are presented in **Figure 4-1**. The XRD patterns of fresh CoOx correspond to the single CoO phase (JCPDS 03-065-2902), while two types of the metallic cobalt phases including the cubic phase with

the strong diffraction peaks (face-centered cubic (FCC); JCPDS 15-0806) and the hexagonal phase with the weak diffraction peaks (hexagonal close-packed (HCP);JCPDS 05-0727) were observed after reduction.[316]

Table 4-1. Textural parameters of fresh and reduced Co-based catalysts.

Catalyst	S_{BET} ($m^2 g^{-1}$)	*Crystallite size*[a] *(nm)*
	Reduced	***Reduced***
CoO_x	1.4	32.7 (Co^0)
Co_8MnO_x	6.5	26.8 (Co^0), 23.2 (MnO)
$CoMn_8O_x$	8.5	23.0 (MnO)

a. The crystallite size of each dominated phase was estimated from the Scherrer's equation applied to the most intense diffraction peak.

The increase of crystallite size of metallic cobalt may be attributed to the migration and growth of cobalt during the heating at 400 ^oC. The growth of metallic cobalt nanoparticles is limited by the addition of Mn, thus leading a smaller crystallite size of Co^0 in Co_8MnO_x sample. This could be responsible for the higher surface area of Co_8MnO_x than that of pure CoO_x after reduction pretreatment.

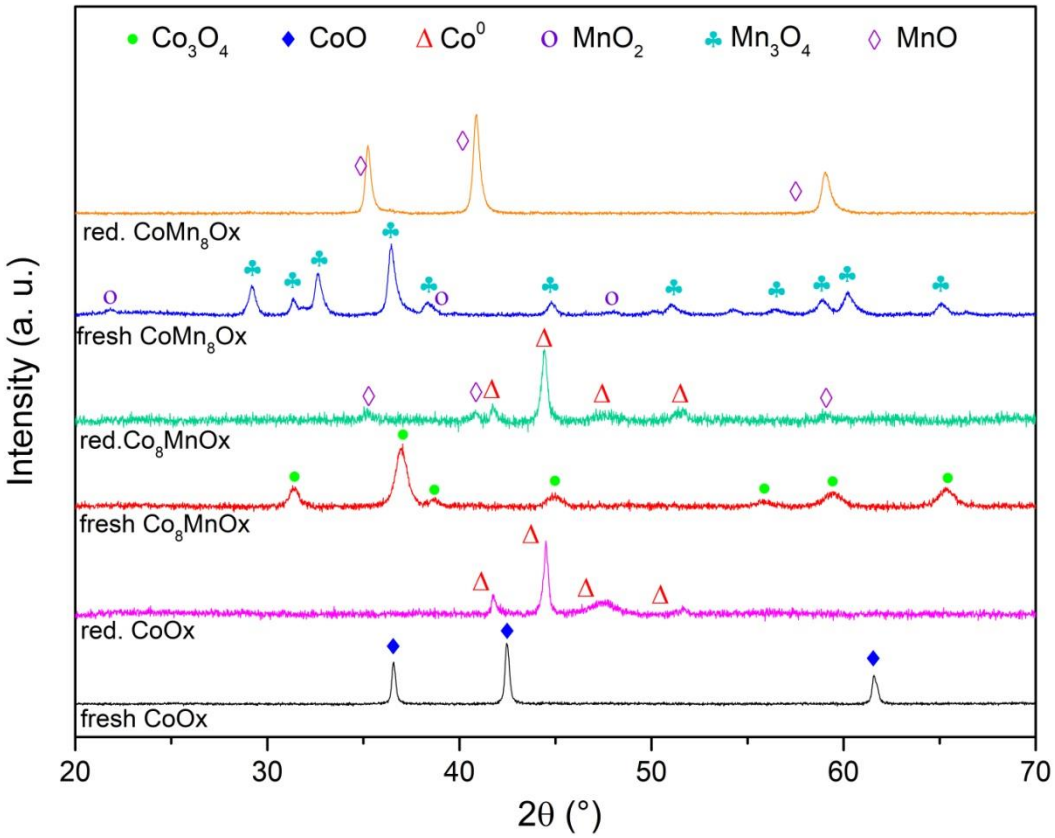

Figure 4-1. XRD profiles of the fresh and reduced CoO_x, Co_8MnO_x and $CoMn_8O_x$ catalysts.

As far as the fresh Co_8MnO_x is concerned, all the observed peaks are attributed to Co_3O_4 (JCPDS 03-065-3103). No traces of Mn-containing phases are distinguished in the fresh Co_8MnO_x sample, which can be due to various factors, such as low crystallinity, low content, or high dispersion. However, after reduction, the diffraction patterns confirm the presence of small amounts of MnO in addition to metallic cobalt. On the as-synthesized $CoMn_8O_x$ sample, the most intense peaks are characteristic of hausmannite phase (Mn_3O_4, JCPDS 01-089-4837) while small peaks indicate the presence of ramsdellite (MnO_2, JCPDS 01-073-1539). No traces of Co-containing phases are clearly observed, as the peaks resulting from the probable presence of Co_3O_4-like phases are of low intensity and close in position to the peaks from Mn_3O_4. After reduction, only characteristic peaks of MnO phase (JCPDS) are observed, which implies a total reduction of MnO_2 and Mn_3O_4 phases.

Pure Co, Co_8MnO_x and $CoMn_8O_x$ catalysts were further examined by SEM (**Figure 4-2**). Both fresh catalysts display particles ranged between 50 and 200 nm wide (**Figure 4-2a and b**). A Mn/Co ratio of around 1/10 is observed by EDS to the overall surface (see example in **Figure 4-3a**), which is close to the nominal value (0.125) used during synthesis. After

reduction at 400 °C (**Figure 4-2c and d**), the particle size of both catalysts significantly increased. The images recorded after reduction of Co_8MnO_x clearly evidence a sintering process, with a rougher surface as compared to its previous form.

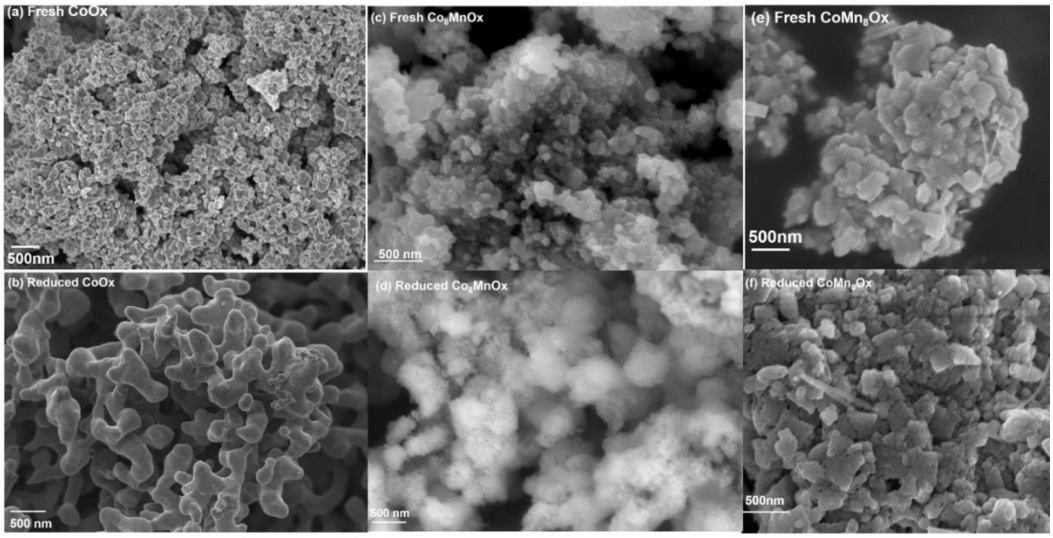

Figure 4-2. SEM micrographs of the fresh CoOx (a), reduced CoOx(b), Co_8MnOx (c), reduced Co_8MnOx (d), CoMn$_8$Ox(e) and reduced CoMn$_8$Ox(f).

Interestingly, EDS analysis of several spots of the catalyst particles revealed important differences in the surface composition with Mn/Co ratios not only close to the nominal value but also significantly higher, up to 1/1.4 **(Figure 4-3b**). This implies the formation of Mn-rich areas on several parts of the surface. In addition, these high ratios are always accompanied by an important oxygen content. Regarding these results, it is assumed that isolated MnO_x areas are present on the surface of the reduced Co_8MnO_x sample.

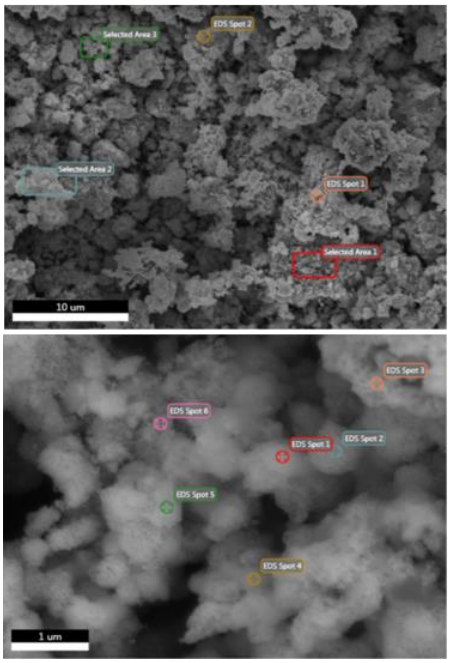

(a) Fresh Co_8MnOx

	Area 1	Area 2	Area 3	Spot 1	Spot 2
O K	29.7	53	13.7	55.1	56.2
MnK	6.5	4.5	7.7	3.3	3.3
CoK	63.8	41.4	78.2	39	39.7
Mn/Co	0.10	0.11	0.10	0.08	0.08
O/(Co+Mn)	0.4	1.2	0.2	1.3	1.3

(b) reduced Co_8MnOx

	Spot 1	Spot 2	Spot 3	Spot 4	Spot 5	Spot 6
O K	35.3	13.6	12.5	32.1	23.2	25
MnK	21.2	8.6	10	19.6	7.9	7.2
CoK	30.1	75.3	76.7	41.3	63.2	60.7
Mn/Co	0.70	0.11	0.13	0.47	0.13	0.12
O/(Co+Mn)	0.7	0.2	0.1	0.5	0.3	0.4

Figure 4-3. EDS analyses of several spots and areas of the surface of (a) fresh and (b) reduced Co_8MnO_x

H_2-TPR measurements were conducted with the aim to compare the reducibility in the bulk of each catalyst. **Figure 4-4** shows the corresponding TPR profiles of the pure Co and the two Co-Mn catalysts. On calcined pure CoO_x sample two main peaks are observed: one relatively sharp at 275 ^oC and a broader one centered around 365 °C. The two peaks are usually attributed to the progressive reduction of Co_3O_4 *via* a two-step reduction process (**Eq. 4-1 and 4-2**):

$$Co_3O_4 + H_2 \rightarrow 3CoO + H_2O \qquad \textbf{Eq. 4-1}$$

$$CoO + H_2 \rightarrow Co + H_2O \qquad \textbf{Eq. 4-2}$$

The TPR profiles of Co-Mn catalysts are more complex. On the Mn-rich catalyst ($CoMn_8O_x$) the TPR profile is dominated by progressive reduction of manganese oxide ($MnO_2 \rightarrow Mn_3O_4 \rightarrow MnO$) in accordance with literature reports.[317,318] In particular, the peaks at 270 °C and 440 °C correspond to MnO_2 and Mn_3O_4 reduction respectively. Note that the reduction peaks of cobalt oxides are not clearly evidenced due to the relatively low amount of cobalt and the strong overlapping between its reduction peaks with these of the manganese oxides. However, a broad peak is observed at the high temperature region (near 550 °C) which cannot be attributed to neither of the single MnO_x or CoO_x phases and may be caused

by synergetic interactions between Mn and Co species.

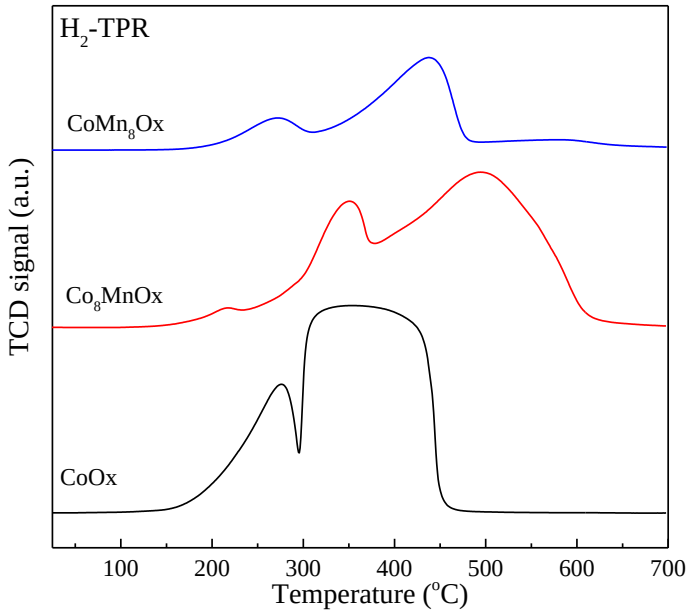

Figure 4-4. H_2-TPR profiles of calcined pure CoOx (—), Co_8MnO_x (—) and$CoMn_8O_x$ (—).

This assignment is also supported by the TPR profile of the Co_8MnO_x catalyst showing a clear shift of the reduction peaks to the high-temperature region, the more intense of which is being centered at around 500 °C. As stated in the literature,[318–321] this shift can be caused by the formation of a $Co_{3-x}Mn_xO_4$-type solid solution upon calcination. This statement is supported by the fact that, according to the phase diagram of Co-Mn-O system,[322] binary Co-Mn oxides, such as Co_2MnO_4 for example, can be formed at temperatures as low as 300 °C. Indeed, Co-Mn oxides of different compositions can be prepared at this temperature, by several methods such as by thermal decomposition of Mn and Co nitrate salts,[323,324] or carbonates.[325] The thermal conditions leading to these binary oxides are similar to the conditions in which the Co-Mn catalysts has been treated in this study, suggesting that formation of a mixed $Co_xMn_yO_z$ phase in the bulk is feasible. However, the low concentration of Mn as compared to Co (1:8) and the absence of any relevant diffraction lines in the XRD data do not provide any indication to support the formation of an extended mixed Co-Mn phase out the catalysts.

4.3.2 The COPrOx reactivity of reduced CoOx/MnOx at atmospheric pressure

The COPrOx reactivity of the three catalysts was evaluated after a H_2 reducing

pretreatment. The CO conversion and the selectivity towards CO_2 are shown in **Figure 4-5 a** and **b** respectively. As expected, the CO conversion (X_{CO}) increases with temperature, with the Co_8MnO_x catalyst showing a systematically higher activity at all temperatures than the other two samples. Notably, at low temperature the Co_8MnO_x catalyst is significantly more active than the other two. For instance, 80% of CO was converted over Co_8MnO_x at 200 °C while only 50 and 20% were reached over pure CoO_x and $CoMn_8O_x$, respectively.

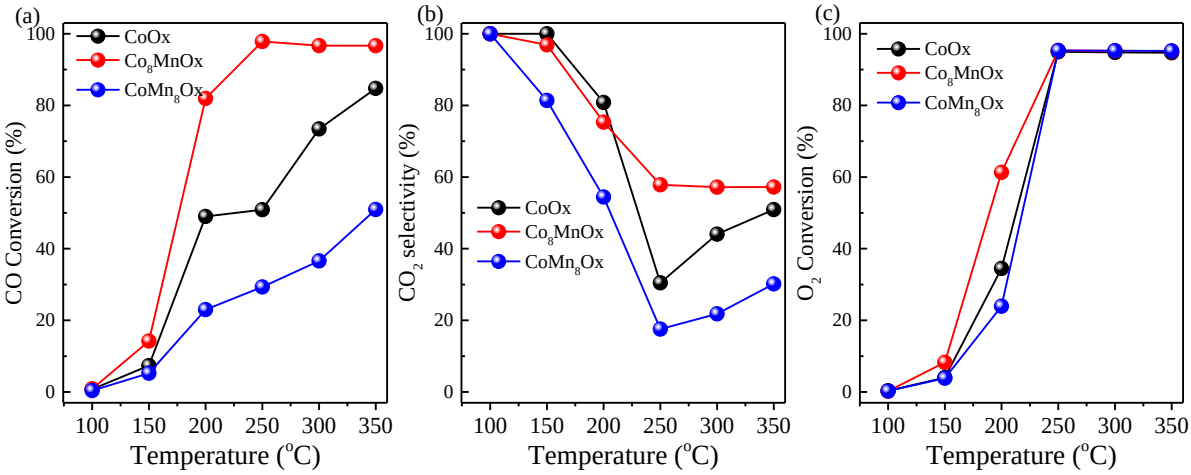

Figure 4-5. COPrOx activity tests. (a) CO conversion, (b) CO_2 selectivity and (c) O_2 conversion vs temperature, over pure Co (●), Co_8MnO_x (●) and $CoMn_8O_x$ (●) catalysts. Experimental conditions: 1% CO, 1% O_2, and 50% H_2 in He-balanced flow; 0.05 g of catalyst; 50 mL min^{-1} of total flow; atmospheric pressure (1 bar). Every point was recorded after remaining for 30 min at each temperature.

The CO_2 selectivity demonstrates the O_2 consumption for CO oxidation to CO_2, while the O_2 conversion represents the consumption of O_2 for both CO and H_2 oxidation. As shown in **Figure 4-5**(c), the O_2 conversion starts below 100 °C over cobalt-rich catalysts, with almost no CO conversion (**Figure 4-5**c) at this temperature range, and therefore lower CO_2 selectivity. However, from 150 °C, CO conversion and CO_2 selectivity increase over these two catalysts which implies that at this temperature the conditions are optimal for conversion of CO to CO_2. However, as the temperature increase to 200 °C and above the CO_2 selectivity decrease again which signifies that a large part of O_2 consumption is used for reactions other than CO oxidation.

CO oxidation: $CO + O_2 \rightarrow CO_2$ **Eq.4-5**

H_2 oxidation: $H_2 + O_2 \rightarrow H_2O$ **Eq. 4-6**

The O_2 consumption below 150^{o}C indicated that except from the CO oxidation (**Eq. 4-5**) other oxidation reactions were carrying on at this temperature region. The possible oxidation reactions can be ascribed to catalytic H_2 oxidation (**Eq. 4-6**) and the oxidation of pre-reduced cobalt catalyst to cobalt oxide, as revealed by in situ measurements in *Chapter 3*. Interestingly, both CO and O_2 conversions were almost zero for Mn-rich catalyst until 100^{o}C. Therefore, its CO_2 selectivity is equal to 100% below 150 ^{o}C. However, CO_2 selectively over the Mn-rich catalyst is up to three times lower than on the Co-rich catalysts while O_2 is 100% consumed above 200^{o}C, indicating more O_2 was consumed by H_2 oxidation and/or oxidation of catalyst over Mn-rich catalyst. Unfortunately, the H_2 oxidation was not able to be quantified based on GC analysis. Thus, to further understand the role of Mn for COPrOx, operando experiments which can simultaneously analyse all the reactions products (especially H_2O) and catalyst oxidation behaviour were performed.

4.3.3 In situ surface characterization of the Co-Mn interaction by NAP-XPS and NEXAFS

The section above shows that Mn addition improves the activity and CO_2 selectivity for COPrOx reaction. It was also evident that Mn acts as a promoter of cobalt in this reaction and it is not a good COPrOx catalyst itself, since high Mn loading (i.e. the $CoMn_8O_x$ catalyst) reduces the activity and the selectivity of the reaction. The H_2-TPR profiles shown in **Figure 4-4** suggest that the addition of Mn shift the reduction of catalyst at higher temperature. According to the findings of *Chapter 3* the oxidation state of cobalt has a dominant effect on the catalytic performance, providing in this way a link between the TPR profiles and the catalytic tests. However, H_2-TPR provides information regarding the reducibility of the catalyst in the bulk which is not straightforwardly related to the catalytic performance. Therefore, this paragraph attempts to *in situ* characterize by NAP-XPS and NEXAFs the oxidation state and composition at the surface of the Mn promoted cobalt catalyst under conditions resembling those of the catalytic tests. Since the Co_8MnO_x catalyst showed clearly a much better performance than the $CoMn_8O_x$ it is selected for the *in situ* characterization. In order to take into account of the possible effect of pressure gap between NAP experiments and catalytic tests, the in situ results over Co_8MnO_x will be presented in comparison with pure CoO_x catalyst. Please note here that the in situ NAP results over pure CoO_x catalyst presented in this chapter may have certain quantitative differences as compared the results

included in *Chapter 3*. This should be expected since different bulk cobalt powders and reaction conditions were employed in the two chapters (please refer to the experimental section of the two chapters for details). However as will been shown below the response of the pure CoO_x catalyst in the reaction conditions is qualitatively the same in the two chapters which is an additional evidence of that the conclusions of chapter 3 describe an intrinsic characteristic of cobalt surfaces which is independent of the cobalt bulk structure and the COPrOx reaction conditions.

In order the synchrotron-based NAP-XPS and NEXAFs experiments to be consistent with the conditions used in the fixed-bed flow reactor catalytic tests shown in the paragraph above, the gas composition was kept the same in the two experiments (COPrOx feed gas (1% CO, 1%O_2, 50% H_2 in He). These reaction conditions are different from those employed in chapter 3 (no He gas in that case) and notably are not the optimal in order to detect changes in the gas atmosphere of the NAP-XPS cell/reactor. In other words, even if the CO, CO_2 H_2O and O_2 signals were monitored by MS and GC during these experiments not significantly changes could be detected in the gas phase under reaction conditions. Therefore, gas phase analysis results from NAP-XPS chamber will not further discussed and the results of the catalytic tests will be used as indicator of the reactivity at each temperature. The stability of Co and Mn phases and the segregation between two components under COPrOx environment is predominantly discussed in this section.

4.3.3.1 Comparative analysis of cobalt oxidation state in the two catalysts

Figure 4-6a and **b** display the Co $2p_{3/2}$ and the Co L_3-edge spectra respectively, recorded on pure CoO_x during the pretreatment in H_2 and at various COPrOx reaction temperatures. As presented in **Figure 4-6a** the catalyst surface was fully reduced to metallic cobalt during the H_2 pretreatment, but as the temperature rises in the COPrOx reaction mixture the Co^0 phase undergoes progressive oxidation. The evolution of cobalt oxidation state was calculated by deconvolution of the Co 2p peak using reference spectra and is presented below **Figure 4-6a.** When the temperature of the reaction reach 250 °C more than 80% of cobalt is covered to CoO phase. Then, within a short period of time at 250 °C, CoO undergoes further oxidation to Co_3O_4 and remains practically stable afterwards to a Co_3O_4 and CoO mixture approximately 70/30 ratio.

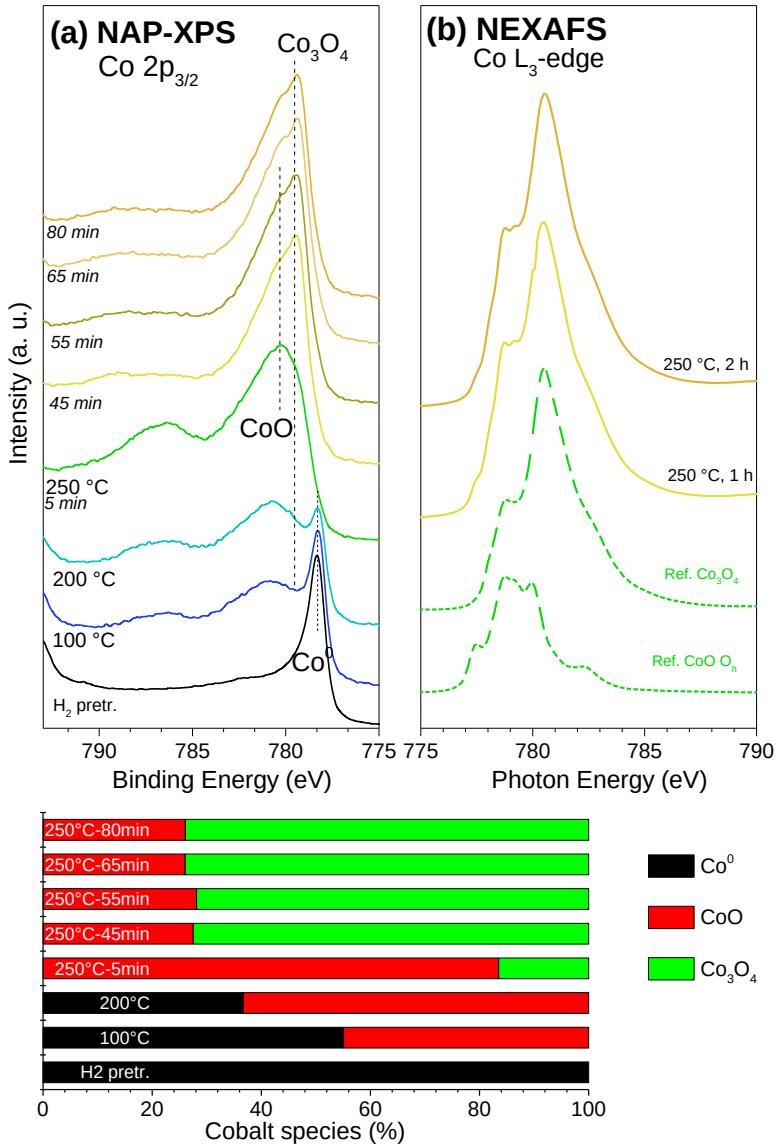

Figure 4-6. In situ NAP-XPS and NEXAFS spectra of a) Co $2p_{3/2}$ (hν = 1020 eV) and b) Co L_3-edge recorded on pure Co after H_2 pretreatment and during COPrOx at various temperatures. Operating conditions: 0.5 mbar of 1% CO, 1% O_2, 50% H_2 and He, from room temperature to 250 °C. The bar graph at the represents the percentage of each cobalt oxidation state calculated by deconvolution of the Co 2p peaks shown in figure a.

The Co L_3-edge NEXAFS spectra recorded after 1 and 2 h at 250 °C in the COPrOx conditions are presented together with reference CoO and Co_3O_4 spectra (in green dotted line)[326] in **Figure 4-6**b. The Co L_3-edge recorded during COPrOx resembles very much the Co_3O_4 reference spectrum displaying a maximum at the photon energy of 780.5 eV and a shoulder located at 778.5 eV. However, it is noticed that the intensity ratio between these two peaks is different in comparison to the reference profile. Moreover, a small peak is observed

at 777.5 eV and overlaps the peak at 778.5 eV. This peak is attributed to the presence of the cubic rock salt CoO phase with Co^{2+} in octahedral position (O_h, see the reference in green dotted line).[311] Consequently, NAP-XPS and NEXAFS lead to similar conclusions, which is to say that at 250 °C in the COPrOx mixture the surface of pure CoO_x catalyst is composed of a mixture between Co_3O_4 and CoO species.

Relevant in situ spectroscopic measurements were also performed in the case of Co_8MnO_x catalyst. The evolution of the Co $2p_{3/2}$ peaks during heating in the COPrOx mixture at 250 °C and 350 °C as well as the cobalt oxidation state derived by spectra deconvolution are shown in **Figure 4-7**a. The Co_8MnO_x catalyst oxidation state is similar to that of the CoO_x presented above, however comparison between the bar graphs in **Figure 4-7** and **Figure 4-6** indicates some evident differences. In particular, at 250 °C higher amount of the CoO phase is observed for Co_8MnO_x catalyst as compared to CoO_x. In addition, it is more difficult to reduce Co_8MnO_x in H_2 (a small amount of CoO persists even if the H_2 treatment for this catalyst even if the duration of the reduction treatment was 2 hours instead of 1 hour for CoO_x) while during the temperature ramping in COPrOx mixture relatively higher amount of CoO is found for Co_8MnO_x.

Similar conclusions can be also drawn by the NEXAFS spectra shown in **Figure 4-7**b. A simple comparison with the reference NEXAFS spectra included in the figure shows that at 250 °C the Co L_3-edge of Co_8MnO_x resemble the characteristic peak profile of Co_3O_4, while at 350 °C the peak shape is modified indicating a mixture of CoO-Co_3O_4, in full accordance with the NAP-XPS results.

After reaction at 250 °C, the COPrOx reaction temperature of Co_8MnO_x catalyst was raised to 350 °C and the surface stability was examined. As shown in **Figure 4-7**, heating at 350 °C led to significant modifications in the cobalt oxidation state. In particular, after 30 min at this temperature the metallic Co reappears in the spectrum in the expense of Co_3O_4, while longer reaction times at 350 °C (about 1 h) favors progressive re-oxidation to Co_3O_4. Notably, the CoO is not considerably influenced by the reaction temperature and remains around 50% at 350 °C which is very similar to what was observed for the reaction at 250 °C.

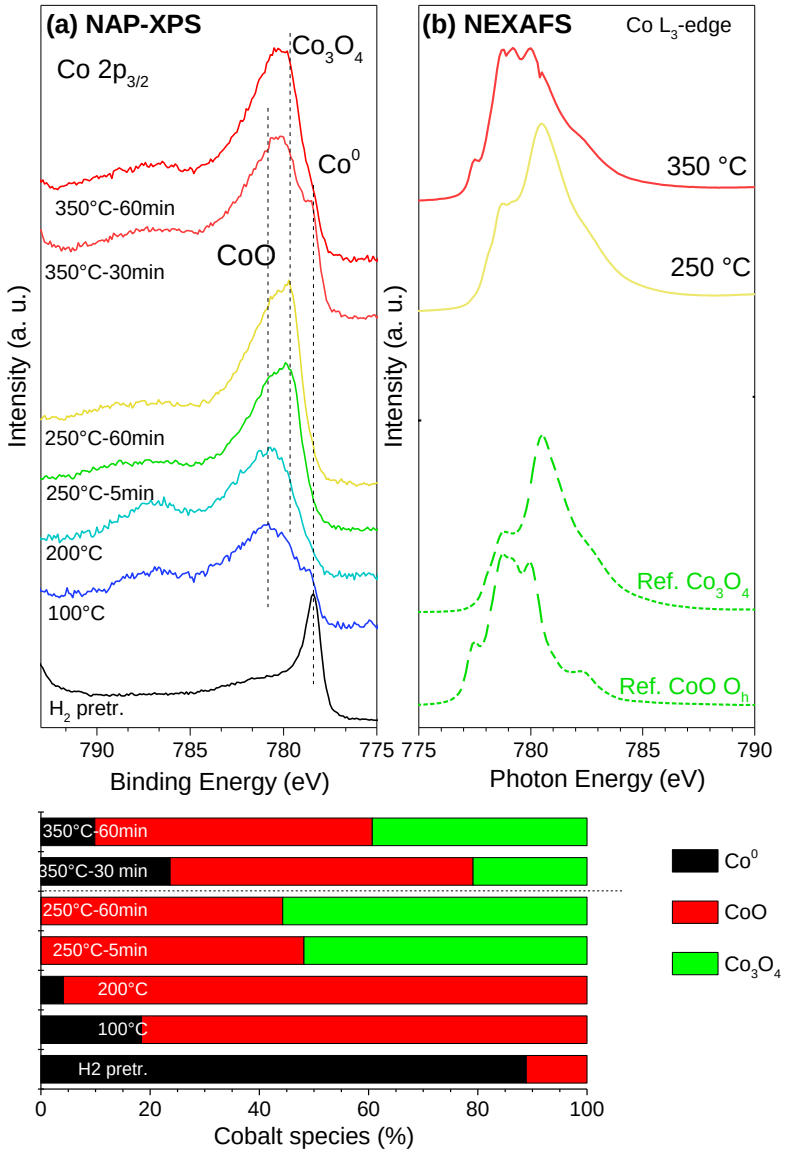

Figure 4-7. In situ NAP-XPS and NEXAFS spectra of a) Co $2p_{3/2}$ (hv = 1020 eV) and b)Co L_3-edge recorded on Co_8MnO_x at room temperature, in H_2 pretreatment and during COPrOx at various temperatures. Operating conditions: 0.5 mbar of 1% CO, 1% O_2, 50% H_2 and He, from room temperature to 250 °C and 350 °C. The bar graph at the represents the percentage of each cobalt oxidation state calculated by deconvolution of the Co 2p peaks shown in figure a.

Interestingly, comparison of the Co $2p_{3/2}$ spectra of Co_8MnO_x and CoO_x samples in the case that Co^{2+} is the dominant oxidation state (see **Figure 4-8**) do not show any evident difference in the shake-up satellite position (peak around 786.8 eV). According to previous studies the shift of the Co 2p satellite is an indicator of mixed Mn-Co oxide formation. Besides, no clear differences are observed on the Co L-edge NEXAFS spectra of the two samples. Therefore the spectroscopic results do not provide any evidence for the formation of

a mixed Co-Mn oxide phase on the surface of the catalyst. Of course mixed Co-Mn oxides can have very similar Co_8MnO_x spectra to pure cobalt oxides, as already observed elsewhere for $Co_xMn_{3-x}O_4$ [327] Of course on should take into account that numerous cobalt oxide phases may co-exist having possibly spectra which overlap to each other. This hampers the observation of small differences in the Co 2p peaks, therefore one cannot completely exclude their presence on the surface of the Co_8MnO_x. However, it is clear that in the present study both XPS and XRD results fail to give any evidence in this direction.

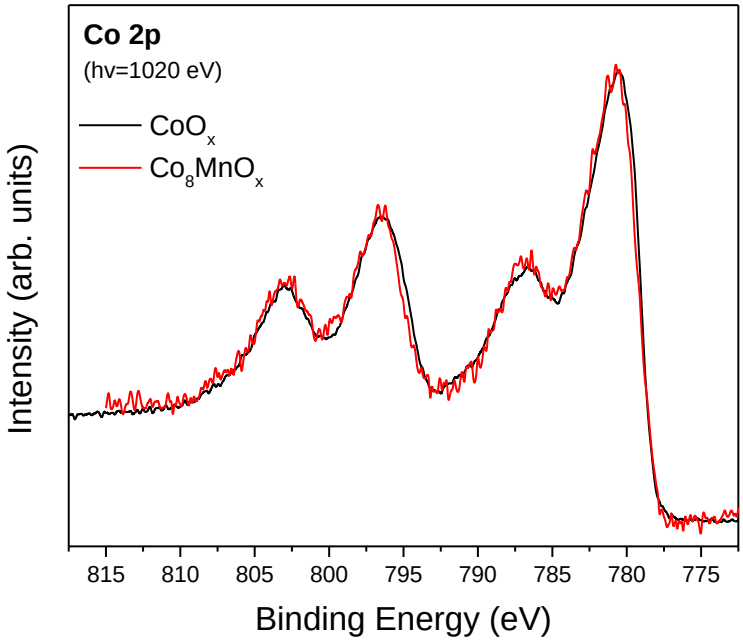

Figure 4-8. Comparison of NAP-XPS Co 2p spectra recorded over CoO_x and Co_8MnO_x catalysts (hv=1020 eV) under conditions where CoO is dominant. The almost identical peak profiles do not support the possibility of a mixed Co-Mn phase formation over Co_8MnO_x catalysts.

4.3.3.2 Analysis of the Mn surface oxidation state and composition

The modification of manganese oxidation state at the different stages of the reaction is discussed next. The NAP-XPS Mn $2p_{3/2}$ (a) and NEXAFS Mn L_3-edge (b) spectra are shown in **Figure 4-9**. Since Mn possess numerous oxidation states having binding energies possibly overlapping, the deconvolution of the Mn $2p_{3/2}$ spectrum turns out to be very complex. In accordance with several works devoted to Mn curve fitting,[328–330] two different chemical states were noticed on both Mn-promoted Co catalysts in these operating conditions. An asymmetric peak at 640.5 eV is attributed to Mn^{2+} in MnO phase, while a second at 641.5 eV

is attributed to Mn^{3+} in Mn_2O_3. Although the variation of their binding energies is too narrow, an intense shake-up satellite at 647.5 eV attributed to MnO allows to deconvolute the peaks, with quite high certainty. Note that, when possible, these attributions were also confirmed by the comparison between XPS and NEXAFS profiles.

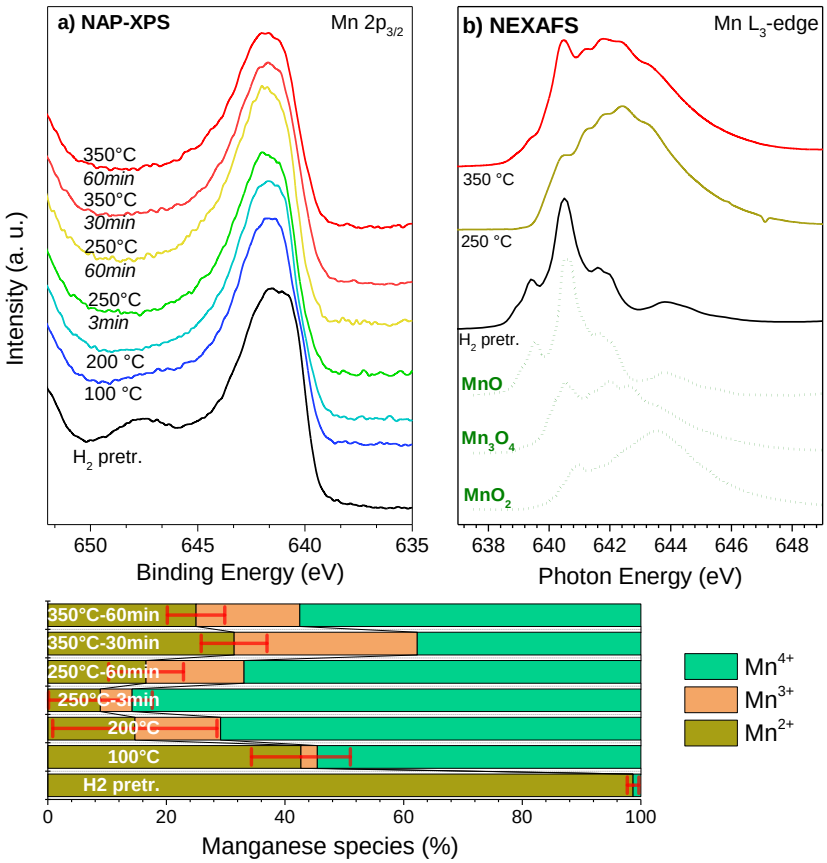

Figure 4-9. In situ NAP-XPS and NEXAFS spectra of a) Mn $2p_{3/2}$ (hv = 880 eV) and b) Mn L_3-edge recorded on Co_8MnOx at room temperature, after H_2 pretreatment and during COPrOx at various temperatures. Operating conditions: 0.5 mbar of 1% CO, 1% O_2, 50% H_2 and He, from room temperature to 250 °C and 350 °C. The bar graph at the represents the percentage of each Mn oxidation state calculated by deconvolution of the Mn 2p peaks shown in figure a.

The Mn $2p_{3/2}$ spectrum of the fresh Co_8MnO_x sample, corresponds to Mn in the 3+ and 4+ oxidation states (Mn_2O_3 and MnO_2, respectively). The presence of the MnO_2 phase is characterized by a shift of the Mn $2p_{3/2}$ peak to the higher BE, with the presence of an asymmetric peak located at 642.5 eV.[313] This presence was comforted to the analysis of the NEXAFS spectrum of the fresh sample, with a maximum situated at the 643.7 eV photon energy.[331] After the pretreatment under H_2, the surface was fully covered by Mn^{2+}, as

evidenced by the similarities between the NEXAFS spectrum and the MnO reference (green dotted line). Mn^{2+} was progressively oxidized to Mn^{3+} during the heating step to 250 °C. At 350 °C, the surface was composed of a mixture of MnO and Mn_2O_3, confirmed by the appearance of a peak at the photon energy of 640.5 eV on the corresponding NEXAFS spectrum.

It is worth noting that given the possibility that Mn oxides might be reduced by the synchrotron radiation, two NEXAFS spectra have been recorded at 250 °C at different time scale of the experiment (not shown). The spectra were identical, which implies that the degree of oxidation of Mn was not affected by the continuous exposure to the powerful X-ray beam.

Overall, the analysis of the Mn spectra shows that MnO is formed on the catalyst during the initial reduction step, but this is gradually oxidized in COPrOx reaction conditions. The Mn_2O_3 is the dominant oxidation state of manganese for at 250 °C, while at 350 °C undergoes partial reduction back to Mn_2O_3. Please note that this redox behavior is similar to the one observed for cobalt (oxidation up to 250 °C and partial reduction at higher temperature).

4.3.3.3 Investigation of spatial distribution of Mn over Co

The Mn/(Mn+Co) atomic ratio (at. %Mn) was calculated based on Mn 2p and Co 2p spectra recorded using different photon energies so as the information depth to be the same in each set of Mn 2p and Co 2p spectra. Four excitation photon energies, corresponding to two analysis depths (or information depths) were used in these measurements. Al the values can be found in **Table 4-2**.

Table 4-2. Measurements conditions of Co 2p and Mn 2p spectra used for the depth dependent NAP-XPS measurements.

Photon energy (eV)	Spectrum recorded	Photoelectron kinetic energy (eV)	IMFP[a] (nm)	Information depth (nm)[b]
1340	Co 2p	550	1.23 (*for Co_3O_4*)	3.7
1200	Mn 2p	550	1.33 (*for Mn_2O_3*)	4.0
1020	Co 2p	230	0.71	2.1
880	Mn 2p	230	0.77	2.3

a. IMFP refers to the Inelastic Mean Free Path and its calculation was done by using the QUASES-IMFP-TPP2M software. [332]

b. Calculated as 3 times of the IMFP

The evolution of at. %Mn at various reaction conditions is shown in the bar graph of **Figure 4-10**. It is clear that at for all the examined temperatures the surface concentration of Mn is much higher of the nominal one (about 11%) which indicates that Mn is located primarily on the surface of cobalt and the two materials do not form an extensive mixed oxide phase, in agreement with the XRD results shown in **Figure 4-1**. A significant drop of %Mn is observed at 250 °C in the COPrOx, while at 350 °C the %Mn increases again close to the initial values. Comparison of %Mn with the Mn oxidation state shown in **Figure 4-9** suggests that the higher surface dispersion of Mn (i.e. higher %Mn) is correlated with the appearance of MnO phase and vice versa for the Mn_2O_3. Finally, the %Mn is systematically lower at the most surface sensitive analysis depth (around 2.2 nm) which confirms that Mn is mainly segregated on the surface over cobalt and the two materials do not form an extensive mixed oxide.

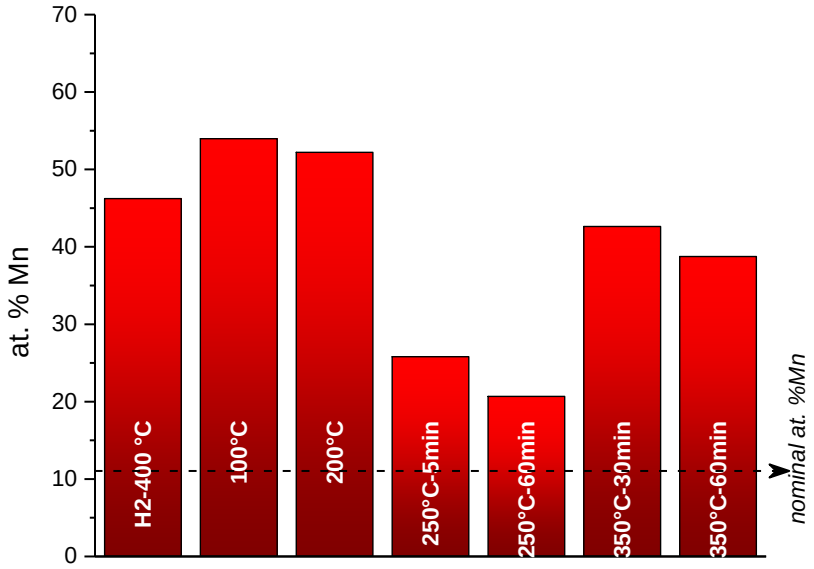

Figure 4-10. The evolution of at. % Mn at various reaction conditions calculated by the Mn 2p and Co 2p NAP-XPS spectra. The analysis depth is estimated 2.2 ±0.1 nm

The discussion about %Mn surface distribution makes evident that surface composition may adapt to the reaction conditions. It also gives a lead that Mn oxidation state might be the driving force for the observed changes in the composition. In addition to that, the EDX analysis showed in **Figure 4-3** implies that the surface of the Co_8MnO_x catalyst is not homogenous but there are areas on the surface where Mn concentration is higher than others. The surface area analyzed by the employed NAP-XPS instrument is largely defined by the spot size of the incident X-ray beam. Under the employed measurement conditions the X-ray spot on the sample is a parallelogram with dimensions 180x10 μm^2 (as we have worked with the 1 mm nozzle on the analyzer lenses, the spot intensity profile in the horizontal dimension is smeared out so not all parts of the spot contribute the overall XPS signal, therefore the 180 μm is probably overestimated and the real size is even smaller).

Here we use the surface inhomogeneity of the catalyst in order to obtain detail information about the effect of Mn on the oxidation state of cobalt. In particular, the NAP-XPS spectra were collected in two different spots of the same catalyst pellet while keeping the sample at the same reaction conditions (250 °C in COPrOx). This is possible by shifting the sample lateral position in respect to the analyzer. In this way we could directly correlate the oxidation state of cobalt in areas that are rich and poor in Mn and draw conclusions about possible effect of Mn in the redox stability of cobalt oxides. We chose two characteristic analysis spots on the surface, one

with high Mn concentration (*spot 1*) and a second with low Mn concentration (*spot 2*), depicted schematically in **Figure 4-11**. As mentioned, both measurements were performed at 250 °C in COPrOx mixture.

As shown in **Figure 4-11** the Co 2p peaks in the two cases are different. After the Co 2p peak deconvolution it becomes evident that CoO is more pronounced in areas that contain more Mn *(spot 1)*, while Co_3O_4 prevails in areas dominated by cobalt *(spot 2)*. In particular the CoO:Co_3O_4 from 44:56 in Mn-rich areas drops to 30:70 in Co-rich areas of the catalyst. Please note that the 30:70 is very close to what was observed for the parent pure Co catalyst. The CoO:Co_3O_4 ratio in the two spots is practically the same for the two analysis depths, which means that there is no depth distribution between CoO and Co_3O_4 and the two oxides.

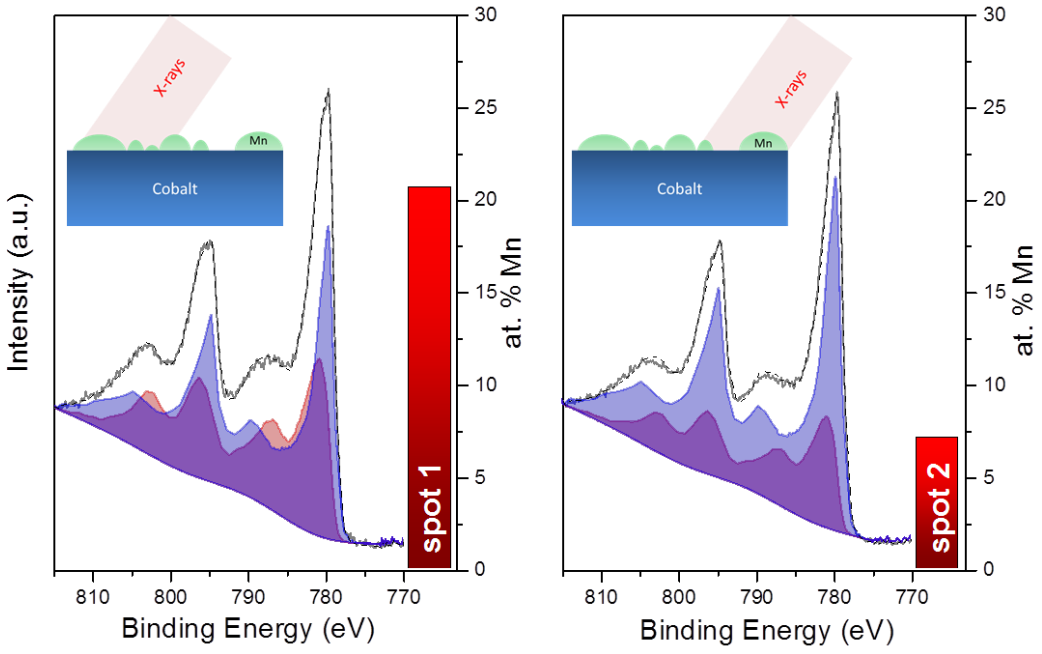

Figure 4-11. The Co 2p spectra recorded over two different areas (spots) of Co_8MnO_x catalyst under identical COPrOx reaction conditions. Each Co 2p peak was deconvoluted into CoO (dark purple peak) and Co (light purple peak) components. The bar in the right part of each figure shows the at. % Mn calculated by the Mn 2p and Co 2p peaks recorded at each spot. A schematic representation of the expected morphology in each spot based on the % Mn is included at the top-left of each figure.

The correlation between Mn and high CoO concentration indicates that the addition of Mn stabilizes the CoO phase at conditions that the pure cobalt catalysts tents to oxidize to Co_3O_4 (see also **Figure 4-6**). This is also confirmed when the sample is heated at higher temperature

(350 °C). In this case the part of the catalyst which is not in contact with Mn is transformed to Co and Co_3O_4, while the part in contact with Mn remains as CoO. As it will be shown in *Chapter 5*, at similar reaction conditions (i.e. at 350 °C) pure cobalt catalysts form a mixture of Co^0 and Co_3O_4 without being able to preserve the CoO phase.

The effect of Mn to stabilize the CoO phase can be used to explain the higher activity of the Co_8MnO_x catalyst as compared to pure cobalt. Taking into account the results presented in *Chapter 3* the stability of the CoO phase should give more active COPrOx catalysts. However, the evident inhomogeneity on the surface concerning the Mn distribution means that there are areas on the surface that cobalt is most probably not in contact with Mn. These areas are expected to preserve the redox properties of the parent material, in other words of pure cobalt particles (i.e. CoO_x), therefore at low COPrOx reaction temperature are prone to oxidation to Co_3O_4 and at higher to reduction towards Co^0.

4.3.4 Operando NAP-XPS measurements to reveal the effect of Mn on the selectivity

We have shown above that Mn can help to stabilize the CoO phase, at least partially, with beneficial effect on the *catalytic activity*. Unfortunately, since cobalt for both pure CoO_x and Co_8MnO_x catalysts was in a mixed CoO/Co_3O_4 oxidation state, it is difficult to draw conclusions about the effect of Mn in the selectivity. We recall here that the desired product of COPrOx reaction is CO_2, but there are two other byproducts of the reaction, namely H_2O and CH_4, which should be avoided since consume valuable H_2. Therefore, a highly selective COPrOx catalyst should boost the production of CO_2 and minimize those of H_2O and CH_4.

In *Chapter 3* it was shown that the flow of the COPrOx gas mixture can influence the cobalt oxidation state in a way that the higher the flow of the reactants the more oxidized the cobalt surfaces will be. This observation implies that by carefully controlling the flow one can maintain the CoO phase over pure CoO_x catalyst during reaction, at least for time periods long enough to obtain spectroscopic and catalytic data. In this paragraph the reaction conditions were adapted in order to maintain the CoO phase for longer periods and to be able to study the material by *in situ* spectroscopy. In particular, the flow of the reactants was lower (the exact value was unfortunately not possible to define) and inert gas wasn't inserted in the feed, so H_2 was 98% instead of 50% in the previous experiment discussed in paragraph 4.3.3. These two

modifications gave a relatively stable CoO phase for both catalysts during NAP-XPS tests as will be shown below. In addition to that, as discussed above, in the H_2 pretreatment the reduction of Co_8MnO_x is not complete therefore this catalyst was more oxidized already from the initially reaction temperatures.

Spectroscopic results

The three catalysts (Co, Co_8MnO_x and $CoMn_8O_x$) that were evaluated for their catalytic activity in paragraph 4.3.2, are analyzed here by NAP-XPS under COPrOx reaction conditions. Prior to the activity tests, the samples were reduced in the NAP-XPS chamber under 1 mbar of H_2 at 400 °C for 1 h. The reaction conditions were: i) reaction mixture: 1% CO, 1% O_2 and 98% H_2, ii) temperature range: 50 and 300 °C, iii) heating rate: 10 °C.min^{-1} and iv) total pressure 1 mbar. **Figure 4-12** displays the Co $2p_{3/2}$ peaks of the three catalysts recorded in COPrOx conditions at 3 characteristic temperatures. Please note, that after a reducing pretreatment at 400 °C the surface of pure CoO_x was fully reduced to Co^0 as was evident by the intense peak at 778.4 eV[333] while the Mn-based catalysts remained as CoO indicated by the broad peak at 780.6 eV and a shake-up satellite at 786.3 eV, characteristic of Co^{2+} [164] (for brevity these data were not included in **Figure 4-12**). This difference is consistent with the findings of TPR and synchrotron-based NAP-XPS experiments showing that the addition of Mn prevents the reduction of CoO at conditions where pure CoO_x is promptly reduced.

Under COPrOx mixture the pure CoO_x undergoes progressive oxidation, while over Co_8MnO_x and $CoMn_8O_x$ catalysts the CoO phase remains stable. It is worth noting that under the employed reaction conditions cobalt it is not oxidized to Co_3O_4 phase even up to 300ºC. As mentioned above, the oxidation of CoO to Co_3O_4 might be inhibited by the high consumption of O_2 at higher temperature and/or the highly reductive feed gas composition we used here, which is 1%CO, 1%O_2 and 98%H_2. This assumption will confirmed later in the text, in the presentation of the *on line* mass spectrometry data from the cell.

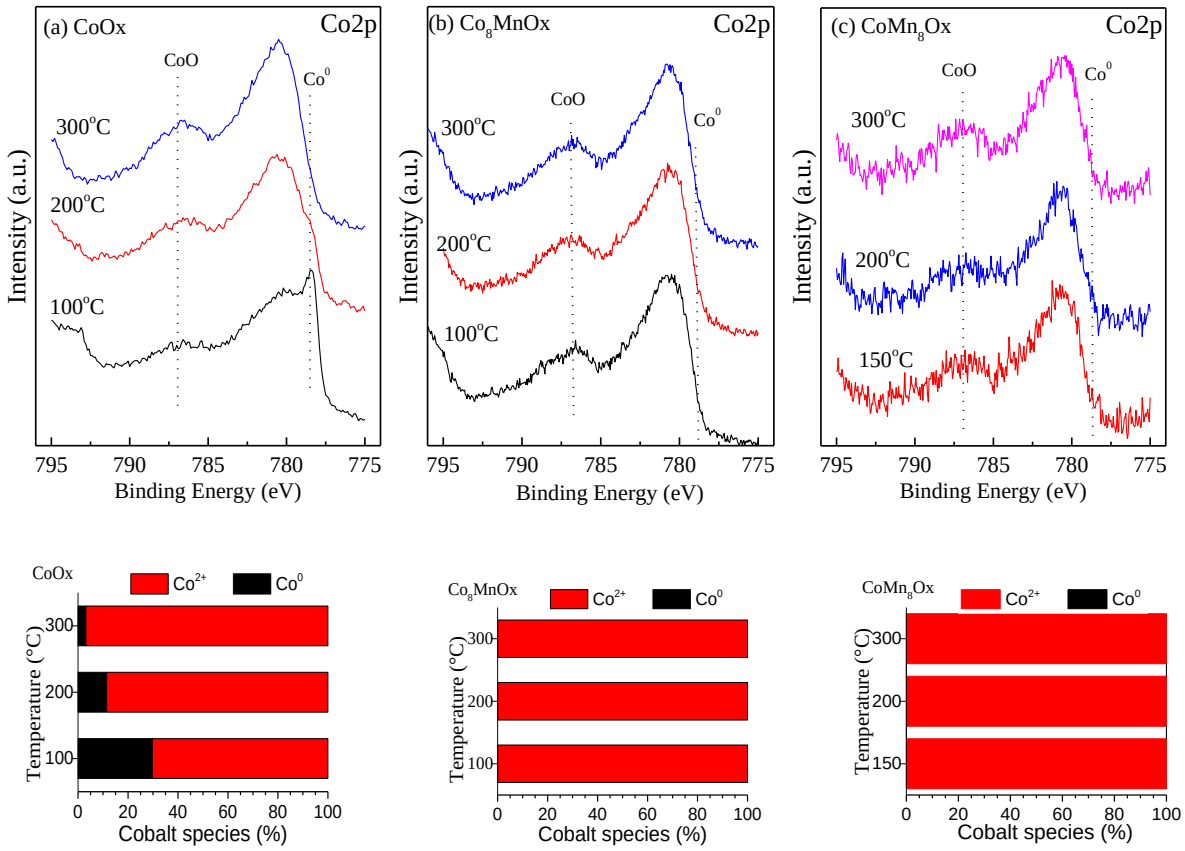

Figure 4-12. In situ NAP-XPS spectra of Co $2p_{3/2}$ on (a) pure CoOx, (b) Co_8MnOx and(c) $CoMn_8Ox$ recorded during COPrOx at various temperatures. Distribution of cobalt species resulting from Co $2p_{3/2}$ deconvolution. Operating conditions: 1 mbar of 1% CO, 1% O_2 and 98% H_2, from room temperature to 300 °C.

The evolution of the Mn oxidation was studied by analysis of the Mn $2p_{3/2}$ peak **(Figure 4-13)**. Note that owing to the superimposition of the peaks corresponding to each Mn phase it is challenging to distinguish minor differences in the oxidation state. However, by superimposing two Mn $2p_{3/2}$ spectra small differences can be distinguished due to the differences in the position and the width (of about 0.2-0.3 eV) of the various manganese oxidation state peaks.[317] After the H_2 pretreatment, manganese is in a mixed Mn^{2+}/Mn^{3+} state for both samples, while in COPrOx mixture Mn^{2+} is gradually oxidized to Mn^{3+} phase. In comparison, manganese is more oxidized in the Mn-richer catalyst as shown by the relatively higher amount of Mn^{3+} over $CoMn_8O_x$. Overall, for both samples, the results evidenced a progressive oxidation of manganese ($2MnO + 1/2O_2 \rightarrow Mn_2O_3$) between 200 and 300 °C.

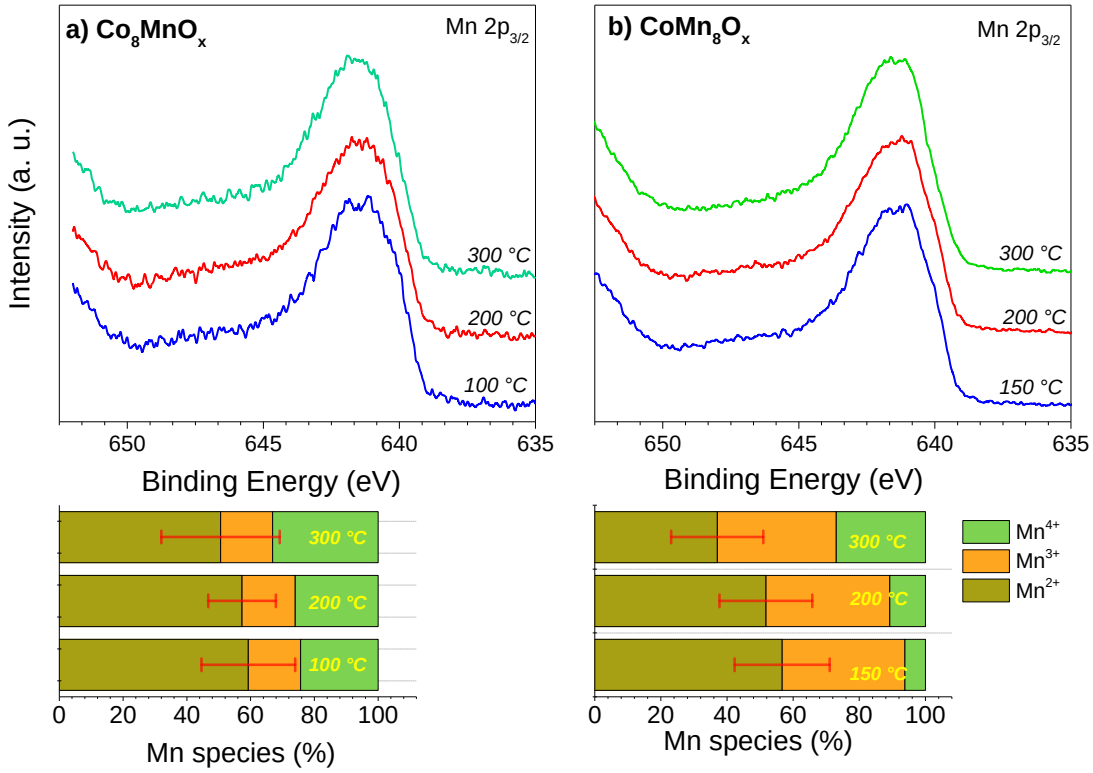

Figure 4-13. In situ NAP-XPS spectra of Mn $2p_{3/2}$ on (a) Co_8MnOx and (b) $CoMn_8Ox$ recorded after H_2 pretreatment during COPrOx at various temperatures. Distribution of manganese species resulting from Mn $2p_{3/2}$ deconvolution. Operating conditions: 1 mbar of 1% CO, 1% O_2 and 98% H_2, from room temperature to 300 °C.

The Mn 2p peak profile between synchrotron and laboratory based NAP-XPS apparatuses was very similar (see **Figure 4-14**) which validate the utilization of the same deconvolution procedure of the Mn $2p_{3/2}$ spectra in the two experiments. In this way, any error in the estimation of the relative amount of the Mn^{2+} and Mn^{3+} derived by the employed Mn 2p peak profiles of two oxides, should be systematic and the same in the two experiments.

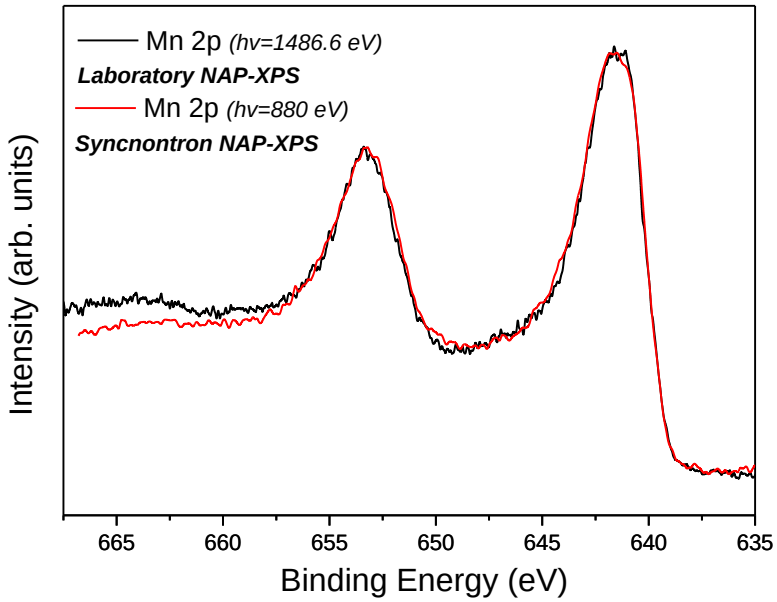

Figure 4-14. Comparison of NAP-XPS Mn 2p spectra recorded over Co_8MnO_x catalysts using synchrotron radiation (hv=880 eV) and a laboratory monochromatic AlKα X-ray source (hv=1486.6 eV). The two Mn 2p peak have almost identical peak profiles. Please note that the intensity of the two spectra is normalized in order to compare their peak shapes. In reality the spectrum of the synchrotron-based instrument has 35 times higher intensity than the laboratory source under the conditions employed for the two measurements.

Online mass spectrometry results

After the examination of the oxidation state of the catalysts, the discussion is now focused on the comparison of the catalytic response between the three samples in the NAP-XPS cell/reactor. The distribution of the reactants and products was monitored by a quadrupole mass spectrometer (QMS) fitted in the 1st pumping stage of the pre-lens of the analyzer. One should also note here that the response of MS signal in the laboratory-based experiments described in this paragraph is much better as compared to the synchrotron-based data described in the previous paragraph. The reason of this is not absolutely clear but most probably is related to the different COPrOx reaction conditions applied in the two NAP-XPS spectrometers. This includes the higher pressure (0.5 against 1 mbar), the contact time between the catalyst and the gas phase (linked with the setup design, the size of the pellet, the flow rate, the exit slit *etc.*) and finally the installation position of the QM spectrometer in the two instruments.

The evolution with time of the reactants and main products as recorded by QMS, as well as the temperature profile, are presented in **Figure 4-15**. In the same figure it is included the CO

and O_2 conversion (X_{CO} and X_{O2} respectively), the selectivity of O_2 to CO_2 (S_{CO2}), and the yields of CO_2, H_2O and CH_4 (Y_{CO2}, Y_{H2O} and X_{CH4} respectively) normalized to the maximum signal recorded with the QMS for each mass. For all samples the CO and O_2 conversion appears from around 100 °C and step up at higher temperatures with parallel increase of the CO_2, CH_4 and H_2O signals. The Co_8MnO_x catalyst shows the highest CO conversion (up to 250°C) and the $CoMn_8O_x$ the lowest in accordance with the catalytic results at 1 bar shown in **Figure 4-5.** A notable difference between the pure and Mn-promoted CoO_x catalysts is in their relative H_2O and CH_4 production (shown as a yield). In particular on Mn-promoted CoO_x the H_2O production is enhanced, while that of CH_4 is suppressed as compared to the pure CoO_x.

The calculated X_{O2} is in accordance with the observations in the CO_2 and H_2O yields. For example at 200 °C, although the Co_8MnO_x catalyst has significant higher X_{O2} than CoO_x (60% instead of 45%), the S_{CO2} of the two catalysts is about the same (around 30%), which can be explained by the almost 3 times higher Y_{H2O} observed for Co_8MnO_x. In the catalyst with the higher amount of Mn these differences are magnified with $CoMn_8O_x$ to have almost 2 times higher X_{O2} and 5 times higher Y_{H2O} in comparison to CoO_x at 200 °C. This implies that Mn catalyses the undesired H_2 oxidation reaction (**Eq. 4-6**) leading to the formation of water and more importantly the loss of H_2.

However, Mn has not only negative effects on the COPrOx selectivity, but it can be beneficial to suppress CH_4 formation, especially at higher temperature. Focusing at 300 °C, the Y_{CH4} of both Mn-containing catalysts are negligible as compared to CoO_x. The CH_4 is produced by the methanation of CO and/or CO_2 according to the **Eq. 4-7 and Eq.4-8**. CO methanation reaction can explain also that CoO_x maintains higher X_{CO} than Co_8MnO_x at 300 °C since at the former CO continues to consumed by this reaction, while as expected at this temperature region the reaction is more selective to H_2O. As for $CoMn_8O_x$, the decline of CO conversion observed at 300 °C is mainly related to the over-consumption of O_2 for H_2 oxidation, which seems to be predominant in these operating conditions.

CO methanation: $CO + 3H_2 \rightarrow CH_4 + H_2O$ **Eq. 4-7**

CO_2 methanation: $CO_2 + 4H_2 \rightarrow CH_4 + 2H_2O$ **Eq. 4-8**

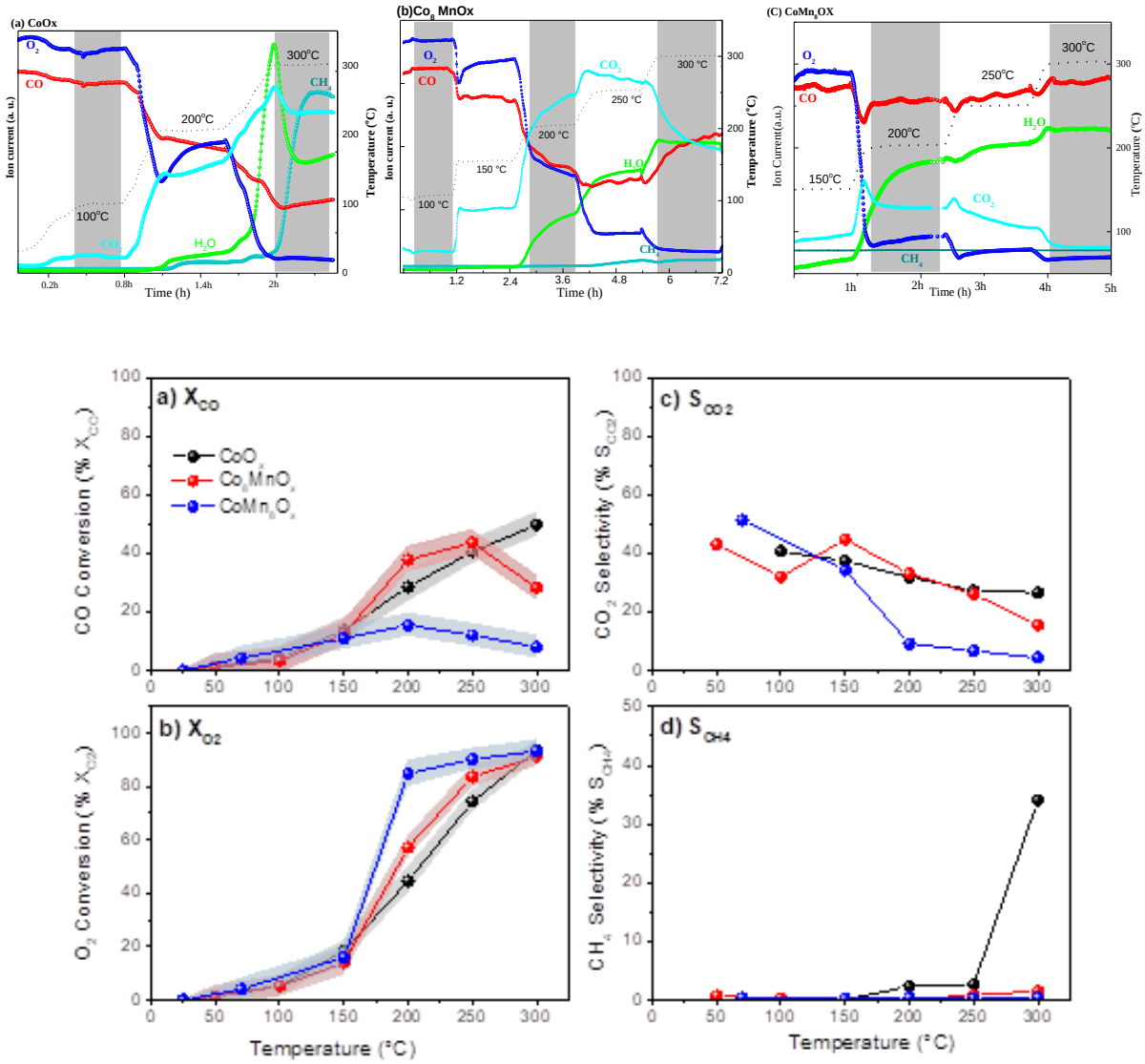

Figure 4-15. On line MS data recorded on (a) Co_8MnO_x, (b) $CoMn_8O_x$ and (c) pure CoO_x during NAP-XPS measurements under COPrOx conditions. Operating conditions: 1 mbar of 1% CO, 1% O_2 and 98% H_2, temperature range between 50 and 300 °C with a heating rate of 10 °C/min between each temperature stage. Prior to the activity tests, the samples were pretreated in the XPS chamber under 1 mbar of H_2 at 400 °C for 1 h.

One should comment here on the differences observed here with methanation reaction at the catalytic tests performed in 1 bar (paragraph 4.3.2). It is difficult to define with certainty the exact reason of the difference between the two experiments, but a plausible reason might be the oxidation state of cobalt. All the experimental results suggest that above 250 °C cobalt is mainly in the Co_3O_4 state on CoO_x catalyst at the 1 bar experiment. As mentioned, in laboratory NAP-XPS tests the conditions were such that CoO phase prevails up to 300 °C. It is known that methanation reactions are enhanced at high temperatures and they are promoted

by the presence of reduced cobalt (Co or CoO) as compared to Co_3O_4.[7] This can rationalize that CH_4 is particularly present in the conditions of laboratory based experiments since this is practically the only case in this thesis that cobalt remains as CoO during high temperature COPrOx reaction. The above presented catalytic results suggest that Mn influences both the activity and selectivity of the COPrOx reaction in a complex way. Since water production is significant on the Mn-promoted Co catalysts (**Figure 4-15**), it is proposed that the Mn_2O_3 phase is very active to catalyze the oxidation of H_2 into H_2O, thus inhibiting CO oxidation. As a result, the increase in Mn_2O_3 concentration is thought to be the main cause of the decrease in COPrOx selectivity.

The effect of oxygen and carbon species

In **Table 4-3** are presented the atomic ratios between the light elements (O, C) and the transition metals derived from the NAP-XPS results for the two most active catalysts discussed above.

Table 4-3. Atomic ratios of the elements on the surface of Co and Co8MnOx and binding energies of the peaks extracted from the C 1s and O 1s photoelectron lines.

Sample	T (°C)	O 1s (eV)	$[O_{ads}]/[O_{latt}]$	C 1s (eV)	[C]/[Co+*Mn*]
CoO_x	100	529.8 531.5[b]	0.8	284.4	0.7
	200		0.5	284.7	0.5
	300		0.3	286.2	0.4
Co_8MnO_x	100	530.1 531.6[b]	0.3	284.8	1.0
	200		0.3	286.3	1.0
	300		0.3	288.5	1.0

Interestingly, the presence of CO_x species at 288.5 and 286.3 eV[276] was evidenced from the C 1s spectra (**Figure 4-16**), with a maximum of population at 300 °C. Yet, these species were not observed in the C 1s spectra of pure CoO_x. In addition, CO_x species were observed on the surface of the Mn-rich catalyst ($CoMn_8O_x$), with a higher proportion in comparison to the peaks attributed to C-H and C-C bonds at 284.7-284.8 eV. As a result, it appears that the observed CO_x species are preferentially located on manganese. This confirms the

observations realized by Jiang *et al.* in a FTIR study of the Co-Mn interactions.[283] More precisely, since the CO_x species gain in population with the temperature along with the Mn_2O_3 population on the surface (**Figure 4-13**), the CO_x are thus probably located on this specific Mn phase known to provide effective adsorption sites for CO.[334]

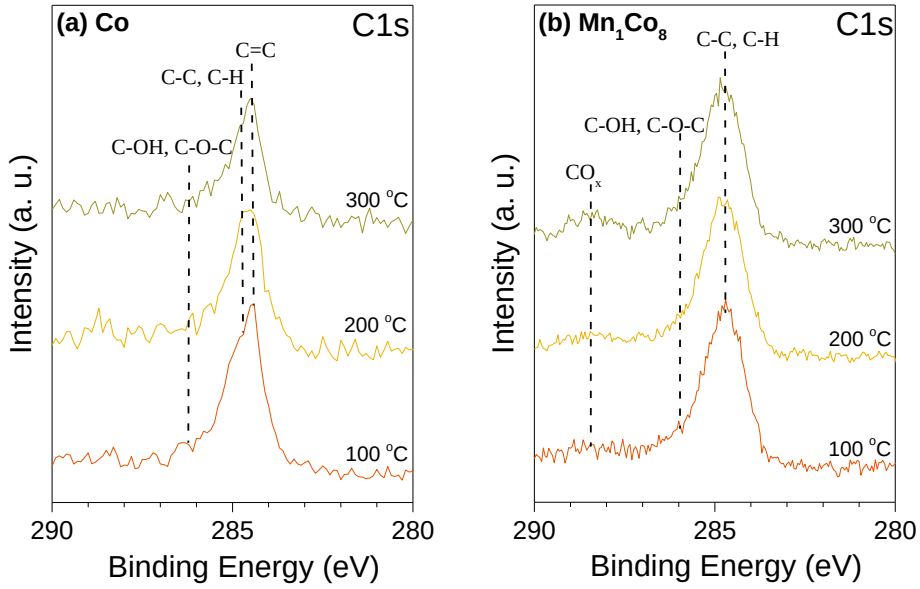

Figure 4-16. In situ NAP-XPS spectra of C 1s over Co and Co8MnOx catalysts, recorded after H_2 pretreatment and during COPrOx at 100, 200 and 300 °C. Operating conditions: 1 mbar of 1%CO, 1%O_2 and 98%H_2.

As previously stated, no peaks attributed to CO_x species were observed on pure Co. However, it was noticed that the peak at 284.8 eV corresponding to C-C and C-H bonds was overlapped by a second peak at lower BE (284.4 eV). This latter is attributed to sp2 hybridized C=C carbon. Thus, their presence underlines the ability of pure Co to reduce the carbonaceous species, probably owing to the presence of metallic cobalt on the surface. This hydrogenating/dehydrogenating character may explain why methane is significantly formed on pure Co.

One should also notice here the absence of a C 1s component due to carbonates species, typically observed around 290 eV. This is a confirmation of the interpretation of the role of carbonate species in the catalytic activity given in the previous chapter. In particular, carbonate species are related to the presence of Co_3O_4 which is not formed in the employed conditions of NAP-XPS experiment (see **Figure 4-12**). The absence of Co_3O_4 and the related

carbonates justifies the high activity (i.e. X_{CO}) of CoO_x catalyst relative to Co_8MnO_x at 300 °C. This result confirms that the reactivity and the oxidation state of cobalt are interrelated and changes in the surface state are followed by different catalytic behavior.

4.4 Discussion

The catalytic tests at 1 bar showed that Mn promotion of Co (Co_8MnO_x) leads to an important increase of the COPrOx activity and improvement of CO_2 selectivity. The promotional effect is related to the synergy of the two elements since the Mn-rich catalyst ($CoMn_8O_x$) is significantly less active. On the Mn-rich catalyst ($CoMn_8O_x$) high O_2 conversion was observed owing to a promotion of Mn towards H_2 oxidation. BET measurements show that the dispersion of Mn into cobalt particles can prevent severe agglomeration, therefore maintaining a higher surface area of Co_8MnO_x than that of pure CoO_x after reducing pretreatment. *Operando* NAP-XPS measurements revealed that the addition of Mn influences the reduction of cobalt surface in H_2, preventing reduction of CoO to Co^0 at certain reaction conditions.

The addition of manganese does not only promote the activity, but depending on its oxidation state, can also have negative effects on the S_{CO2}. The *operando* NAP-XPS results suggest that manganese is in a mixed MnO/Mn_2O_3 (i.e. Mn^{2+}/Mn^{3+}) and in conditions that the Mn_2O_3 phase is dominant (please compare **Figure 4-9** with **Figure 4-13** at 250 °C) the catalyst is less selective to H_2 oxidation. This, in addition to the differences in the oxidation state of cobalt, is hypothesized to be the reason for the important differences in the S_{CO2} between **Figure 4-5** and **Figure 4-15** especially observed at higher reaction temperatures.

Overall, the experimental results lead to the fact that Mn-promotion does not have a net positive effect on the cobalt reactivity for COPrOx. The addition of Mn may help to stabilize the CoO phase and, in this way, enhance the catalytic activity, but the interaction of Co and Mn is rather weak leading to facile separation of two elements either during pre-treatment or under reaction conditions. A direct effect of this, is that the areas of the catalyst that Mn and Co are not in contact Co_3O_4 and MnO are formed with negative effect on the CO conversion and S_{CO2} selectivity. Most probably, more complex catalyst synthesis methods could be elaborated to enhance the distribution of Mn on Co so as to stabilize better and in larger extent the CoO phase, targeting to an even more active catalyst. However, the significant evolution of the %Mn as a

function of the reaction conditions (**Figure 4-10**) at the same catalyst spot, suggests that in long term the stability of such a Co-Mn catalyst might be an issue. In addition to that, a commercially viable cobalt-based COPrOx catalyst should employ relatively simple synthesis methods which can scale up easily, like those used in this work. Therefore, in *Chapter 5* the effort to discover a promising cobalt-based COPrOx catalyst will be pursuit.

4.5 Conclusions

In this chapter Mn-Co catalysts were synthesized and their performance in COPrOx reaction was evaluated. Under continuous-flow conditions, Mn addition to Co (Co_8MnO_x) led to a significant increase of the catalyst performance. Operando NAP-XPS combined with gas phase analysis indicates that the CoO, found to be the more active cobalt phase for COPrOx in the previous chapter, was partially stabilized in presence of Mn. Interestingly, the Mn oxidation state is also dynamic and transformed during the COPrOx reaction. Depending on the operating conditions (time, T, gas mixture), MnO can be progressively oxidized into Mn_2O_3 and reduce back to MnO again. Excess of MnO phase on catalyst's surface was correlated with high O_2 consumption through the unwanted H_2 oxidation. Although, the optimum surface phases of CoO and Mn_2O_3 were identified here, it was also evident that the surface of the Co-Mn catalyst is dynamic and difficult to stabilize during COPrOx reaction. Thus, further efforts needed in order to stabilize the CoO phase on the surface of cobalt-based catalyst during COPrOx reaction.

Chapter 5

Improving the Catalytic Performance of Cobalt for CO Preferential Oxidation by Stabilizing the Active Phase through Vanadium Promotion

5.1 Introduction

In *Chapter 3* was discussed the correlation between the cobalt oxidation state of the COPrOx reactivity. It was concluded that CoO has a higher activity than that of Co_3O_4 for COPrOx, validating some of the earlier proposals on this debate.[7,263] However, in situ XPS made clear that CoO is not stable in COPrOx reaction conditions and at certain temperature can be readily oxidized to Co_3O_4, causing deactivation. The COPrOx reaction temperature seems to be critical for the oxidation state of cobalt, since recent studies report that at higher temperatures Co_3O_4 is rapidly reduced to metallic Co.[6,88] Metallic Co is not active for CO oxidation and has the tendency to catalyze methanation and hydrogen combustion reactions.[258] In fact, these reports have revealed that cobalt oxidation state is extremely dynamic during COPrOx reaction and the reactivity is closely related to the redox effect of the gas phase. A good durability or stability is indispensable for an efficient catalyst. Thus, stabilizing the optimum surface oxidation state of cobalt-based COPrOX catalyst is essential.

The redox ability of cobalt, which is related to the stability of a certain oxidation state, can be modulated by several factors. This includes the particle size and morphology[326,335,336] as well as the choice of the catalytic carrier/support.[88] The admixture of another metal or oxide, usually referred as promoter or doping agent, may also be used to influence the redox ability of cobalt.[337] For example, CoO may be stabilized in an oxidative atmosphere by the presence of Pt,[44,338] but needless to say that its high price limits its application of platinum as a promoter. In the previous chapter it was shown that Mn might be a good alternative, but several issues related to its stability might limit its application. Given that variable-valence metal ions have been regarded as active modifiers able to tune the chemical bond or surface state of metal oxides, we became interested in vanadium-modified cobalt catalysts. Vanadium can easily exchange between various oxidation states,[13] while it is known to promote CO oxidation[339] and Fischer–Tropsch synthesis[340] reactions on cobalt. In order to keep the complexity of the catalyst to the minimum possible, vanadium was loaded directly onto commercial CoO nanoparticles, without using a catalytic carrier/support. In this chapter, the catalytic behavior of Co-V and the effect of V promotion on cobalt will be discussed. The interaction between Co and V, is addressed in detail for the first time in this study, hopefully opening a path for future applications of vanadium-cobalt mixed oxides.

5.2 Experimental Methods

5.2.1 Catalyst Preparation

Commercial highly pure cobalt oxide nanoparticles: CoO nanoparticles (99.99%, Sigma Aldrich) were used as precursors. V-modified cobalt oxides were synthesized by incipient wetness impregnation method. Pure CoO or Co_3O_4 were post-impregnated in the solution of NH_4VO_3, respectively. The mixture was dried at 120^{o}C for 12h. The dry product was subsequently calcined in air at 400^{o}C for 3h. The nominal atomic ratio of V/Co is kept at 8 ($V_{0.125}Co$). The ratio of 1:8 between promoter and cobalt is reported as an optimum content for many promoted-Co systems for COPrOx, for example Ce-Co and Mn-Co systems.[83,341] For this reason, this ratio was chosen at first to prepare a V-Co catalyst. Since the catalytic results demonstrated an excellent performance and stability of a $V_{0.125}Co$ catalyst as compared to pure cobalt, we did not attempt to further optimize this ratio, but we picked this system for a detailed mechanistic study to understand the role of surface vanadia promotion on cobalt. The surface purity of the catalysts after synthesis was confirmed by the survey XPS spectra.

5.2.2 Catalytic tests

COPrOx catalytic tests on CoO and vanadium modified CoO catalysts were performed in a continuous-flow fixed-bed reactor under atmospheric pressure. 50 mg of the catalyst was loaded into the quartz tube and pretreated in H_2 (30 ml/min) at 400 ^{o}C for 30 min (heating rate 10 ℃ min^{-1}), which according to TPR-H_2 profile (**Figure 5-5**) reduces CoO to metallic Co. Consequently, the sample was cooled down at 50 ^{o}C while the gas mixture switched to 1% CO, 1% O_2, 50% H_2 in He (50 ml/min). The qualification and quantification of reactants and products was monitored by a gas chromatograph (GC) equipped with TCD detector. The sample was maintained at each temperature for 30 min while gas was injected constantly to the GC to obtain an average concentration of reactants and products. The steady-state test was carried out after each light-off test using the same catalyst. Before the steady state tests the catalysts was pretreatedt in H_2 for 30 min, the COPrOx gases were introduced and then heated with a ramping rate of 10°C/min to 250 ^{o}C. CO conversion (X_{CO}) and CO selectivity to CO_2 (S_{CO2}) were calculated based on Equations 1 and 2 respectively:[342,343]

$$X_{CO}(\%) = \frac{[CO]_{in} - [CO]_{out}}{[CO]_{in}} \times 100 \qquad \textbf{Eq. 5-1}$$

$$S_{CO2}(\%) = \frac{1}{2} \times \frac{[CO]_{in} - [CO]_{out}}{[O_2]_{in} - [O_2]_{out}} \times 100 \qquad \textbf{Eq. 5-2}$$

In these equations, $[CO]_{in}/[O_2]_{in}$ and $[CO]_{out}/[O_2]_{out}$ are the concentration of gases into and out of the reactor, respectively.

5.2.3 Characterization of bulk structure and morphology

X-ray diffractograms (XRD) were performed on a Bruker D8 Advance diffractometer, using Cu Kα radiation (λ = 0.15418 nm) between 20 and 90° (2θ), with a step of 0.02° and a time of 1s per step. Hydrogen temperature-programmed reduction (TPR-H_2) was performed by means of an automated characterization system (Micromeritics, model AutoChem II), which incorporates a thermal conductivity detector (TCD). The surface morphology of cobalt was inspected by a Zeiss GeminiSEM 500 SEM microscope. TEM was carried out in scanning mode (STEM) using bright field (BF) and annular dark field (ADF) detectors on a JEOL 2100F microscope working at 200 kV.

5.2.4 Operando Near ambient XPS and NEXAFs

The *in situ* synchrotron-based near ambient pressure X-ray photoelectron (NAP–XPS) and near edge X-ray absorption fine structure spectroscopies (NEXAFS) were performed at CAT beamline at the synchrotron radiation facility BESSY II of the Helmholtz Zentrum Berlin. The catalysts powders ware pressed into pellets and placed on a stainless steel plate which could be heated at the back side by an IR laser. The pellets were initially pretreated in 0.5 mbar H_2 at 400 ^oC for 30 min. After the pre-treatment the catalyst was cooled at room temperature and the reactant gas mixture of 1%CO, 1%O_2 and 50%H_2 in He of 0.5mbar was introduced via 4 calibrated mass flow controllers at a total mass flow of 30 sccm. The catalysts were initially measured at different temperatures by stepwise annealing for about 1 hour in each temperature. In addition, fresh catalysts after pre-reduction step were measured by directly annealing at 250 °C for about 2 hours, to resemble the conditions of the steady-state catalytic tests. The gas phase composition was monitored online by a differentially pumped quadrupole mass spectrometer (QMS), which was connected to the experimental cell through a leak valve. XPS spectra of Co 2p, V 2p, O1s and C1s as well as NEXAFS Co L_3 and V L_3-edges were collected during the reaction. The Co and V L_3-edges NEXAFS spectra were recorded in the total electron yield (TEY) mode. The NAP-XPS and NEXAFS spectra were fitted using standard

reference curves of metallic Co, CoO and Co_3O_4 recorded at the same spectrometer.

The V L_3-edges were simulated using the charge-transfer multiple (CTM) approach in order to obtain qualitative information from the absorption spectra.[344,345] The calculations have been performed using the CTM4XAS v5.23 program.[346] The tetrahedral symmetry is chosen for the calculations of V^{5+} in the $Co_3V_2O_8$[347] and $CoVO_x$ while the octahedral one for V^{5+} in the V_2O_5.[348] The crystal field value (10Dq) and the charge transfer energy value (Δ) were the main parameters adjusted in the simulation to obtain the best accordance with the experimental spectra. The other parameters were: i) for $CoVO_x$, slater integrals (F_{dd}, F_{pd}, G_{pd})=0.8, spin-orbit spitting parameter SO=1, optical parameters Dt=Ds=-0.1 eV, core hole potential U_{pd} and the 3d-3d repulsion energy U_{pd}=U_{dd}=0.5, and the hopping parameters e_g =1eV and t_{2g}=0.7 eV ii) for V_2O_5 reference, (F_{dd}, F_{pd}, G_{pd})=1, SO=1.05, U_{pd}-U_{dd}=2.5, e_g =1.2 eV and t_{2g}=0.6 eV, iii) for $Co_3V_2O_8$ reference, (F_{dd}, F_{pd}, G_{pd})=0.75, SO=1, the Dt=Ds=-0.1 eV, U_{pd}=0, U_{dd}=1.2, e_g =1.6 eV and t_{2g}=0.

5.2.5 In situ NEXAFS in 1bar

In situ NEXAFS experiments at 1 bar of H_2 or O_2 were performed at the APE-HE beamline of the Elettra synchrotron radiation facility (Trieste, Italy), exploiting a dedicated setup based on a reaction cell with Si_3N_4 membrane, as described in detail elsewhere.[249] The NEXAFS signal was detected in TEY mode, by probing the drain current from the sample with a picoammeter. The catalyst powder was loaded in the in situ cell, installed in the APE-HE instrument and interfaced with gas delivery and temperature control systems. For all the experiments a total gas flow of 50 cm^3/min was used. NEXAFS data were acquired after 15 min at each selected temperature point. After the reduction step in H_2, the sample was cooled down to room temperature in He gas flow prior to the oxidation step in 10%O_2/He.

5.3 Results

5.3.1 Catalytic performance in COPrOx reaction

Figure 5-1 compares the COPrOx catalytic performance of pure CoO (hereafter referred as CoO_x) and V-modified CoO (hereafter referred as $CoVO_x$) catalysts. Prior to the reaction the samples were reduced according to the conditions reported in the experimental part. As shown in **Figure 5-1a**, for both catalysts the CO conversion increases with reaction temperature.

However, at a given temperature the conversion of CO over *CoVO$_x$* is much higher than pure *CoO$_x$*. At the same time, the O_2 selectivity to CO_2 (S_{CO2}) is on average higher on *CoVO$_x$*, while a significant variation of S_{CO2} is found on *CoO$_x$* in the temperature range between 100 and 250 °C. This instability should be attributed to O_2 consumption for CoO oxidation as will be explained later in the text based on the spectroscopic results.

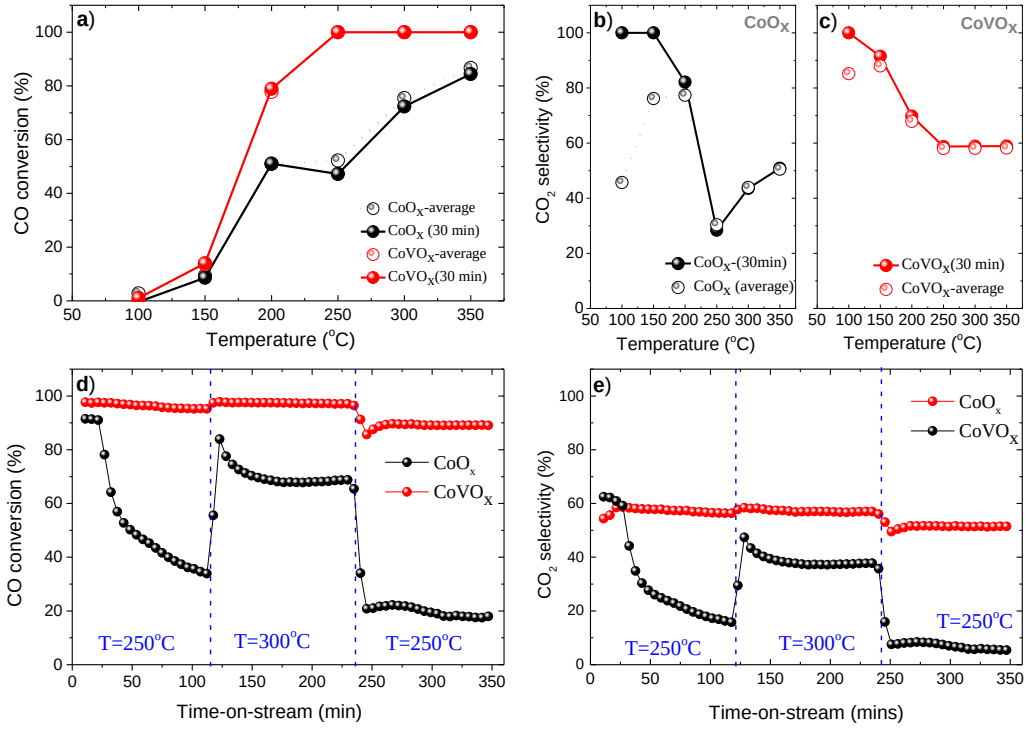

Figure 5-1. Fixed bed reactor catalytic tests of CoO_x and $CoVO_x$ catalysts. (a) CO conversion and (b) CO_2 selectivity as a function of the COPrOx reaction temperature. (c) CO conversion and (d) CO_2 selectivity as a function of the time-on-stream at 2 characteristic temperatures. Experimental conditions: 1%CO, 1%O_2 and 50%H_2 in He-balanced flow; 50 mg of catalyst; 50ml/min of total flow at atmospheric pressure.

To evaluate their stability, the two catalysts were monitored during COPrOx at 250 °C and 300°C for about 4 h on stream. As shown by the evolution of the CO conversion and CO_2 selectivity in **Figure 5-1** c and d, the catalytic performance is maintained in the case of *CoVO$_x$*, in contrast to *CoO$_x$* which undergoes rapid deactivation especially at 250 °C. As shown in **Figure 5-1c**, the activity of *CoO$_x$* at 250°C rapidly decreased from 90% to 35% within 1 hour. The CO conversion increases for both catalysts when the temperature rises to 300 °C, with *CoVO$_x$* being almost 30% more active than *CoO$_x$*. Finally, when the temperature goes back to 250 °C there is a slight deactivation of *CoVO$_x$* as compared to the one initially observed, but the catalysts remain about 60% more active than the pure one. Moreover, for both spent

cobalt-based catalysts, the reductive pretreatment after each COPrOx test recovered the high activity in repeated cycles, which makes the loss of surface area due to cobalt sintering as the cause of deactivation highly unlikely.

The superior performance of *CoVO$_x$* also expands in terms of the CO_2 selectivity which is significantly higher (up to 10 times) in both examined temperatures. Overall, the addition of vanadium into cobalt oxide has significantly enhanced the COPrOx reactivity of the catalyst both in term of activity and in a lower extent in CO_2 selectivity as well. Pure vanadium oxide is practically inactive for COPrOx; therefore, the dramatic improvement of reactivity can be only ascribed to a synergetic/promotional effect between cobalt and vanadium.

5.3.2 *Ex situ* characterization

5.3.2.1 Structure and morphology

The X-ray diffraction (XRD) patterns of fresh *CoO$_x$* and *CoVO$_x$* catalysts, as well as after reduction pretreatment and COPrOx reaction referred to **Figure 5-1**c, are shown in **Figure 5-2**. The characteristic diffraction peaks of the pristine *CoO$_x$* are clearly observed at 2θ= 36.54, 42.44, 61.53, 73.82 and 77.66^o which correspond to the crystalline planes of (111), (200), (220), (311) and (222) of face-centered cubic (fcc) CoO phase.[293,349]

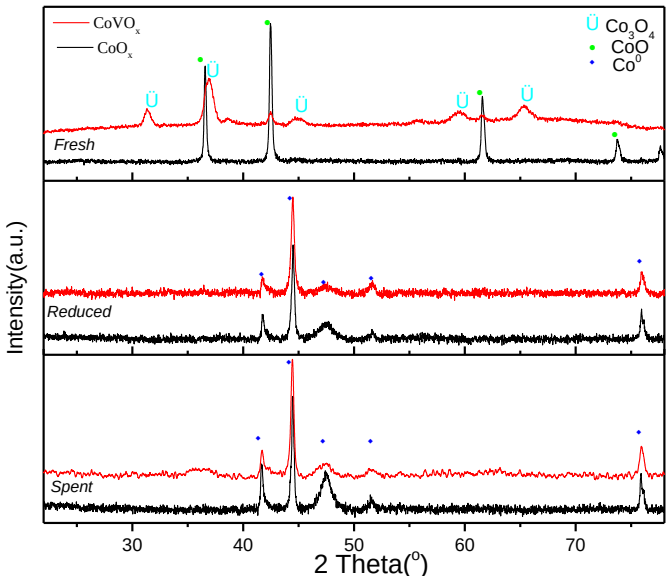

Figure 5-2. The ex situ XRD patterns of catalysts after different treatment, the spent samples were used for COPrOx test under atmospheric pressure.

Different diffraction peaks appear in the XRD pattern of the as-prepared *CoVO$_x$*, which are

well assigned to the crystallographic planes of Co_3O_4 cubic spinel structure (PDF#76-1802 of the JCPDCS). The Co_3O_4 phase formation over *$CoVO_x$* is the result of air calcination at 400 °C according to the preparation protocol of this catalyst. After reduction in H_2, the XRD patterns of both *CoO_x* and *$CoVO_x$* have the same diffraction peaks, which characterize the metallic Co phase. This proves that both catalysts are fully reduced in their bulk during the reduction treatment presenting the COPrOx. The XRD patterns after reaction (spent catalyst) are very similar to those after H_2 treatment, suggesting that metallic Co is preserved in the bulk of the catalysts also under COPrOx. Notably, no additional peaks associated to vanadium compounds are observed in the XRD pattern of V-modified CoO sample. The absence of vanadium phase suggests that the vanadium atoms either form an amorphous oxide, or are highly dispersed on the surface of cobalt, or even inter diffused in the lattice of cobalt oxide.

The morphology of fresh and spent catalysts was examined by scanning electron microscopy (SEM). The typical images of fresh and spent samples after several hours of reaction COPrOx at 250°C as well as Energy Dispersive X-Ray Analysis (EDX) micrographs of the fresh *$CoVO_x$*, are shown in **Figure 5-3**. SEM images reveal that both fresh *CoO_x* and *$CoVO_x$* consist of similar nanoparticles with sizes between 30 nm and 60 nm. The typical images of spent catalysts demonstrate the agglomeration of the particles, which should be expected for unsupported metal particles after the long-term stability test above 250^{o}C. The EDS mapping of as-synthesized CoVOx shows that vanadium is homogeneously distributed over cobalt powders with certain V-rich clusters. The atomic ratio of V/Co is close to the nominal ratio of 1/8.

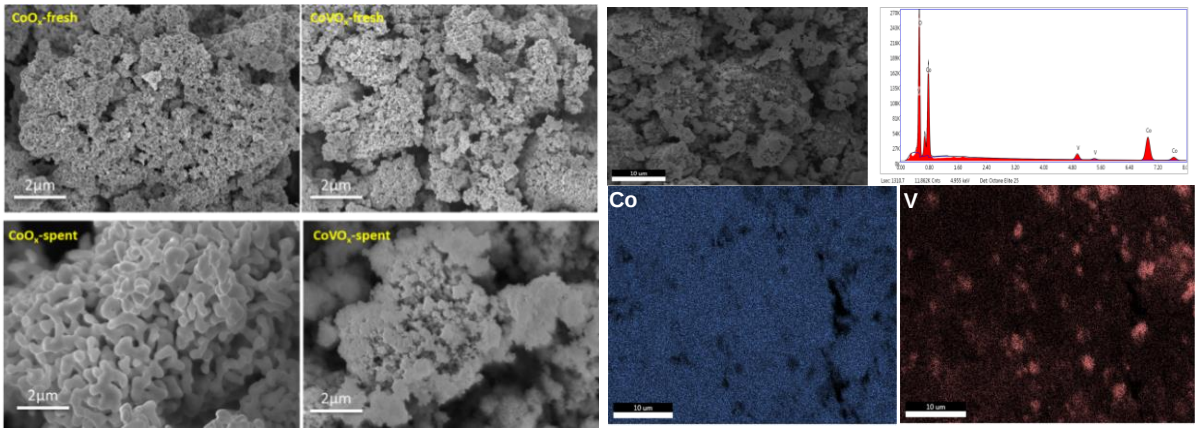

Figure 5-3. SEM micrographs of fresh and spent CoO_x and $CoVO_x$ catalysts (left) and EDS mapping (right) of fresh $CoVO_x$ along with elemental analysis spectrum.

The scanning TEM (STEM)-EDS elemental mapping images of spent CoVOx sample (**Figure 5-4**) confirmed that the V was uniformly distributed throughout the cobalt nanoparticles. Moreover, a V-rich thin layer is seen on the out-most edge/surface of large cobalt particles (**Figure 5-4b**), indicating the V-containing phase exists mostly on the surface of cobalt particles. Interestingly, the XRD patterns of spent CoVOx demonstrated the absence of O-containing and V-containing phase in the bulk, but in **Figure 5-4e**, it is shown that O is highly distributed through the particles. This might be attributed to the possibility that O is only existed in an amorphous oxide of vanadium, or dispersed on the surface cobalt oxides, suggesting that the V probably exists on the cobalt surface as an oxide. This assumption is confirmed by XPS measurement with V 2p spectra.

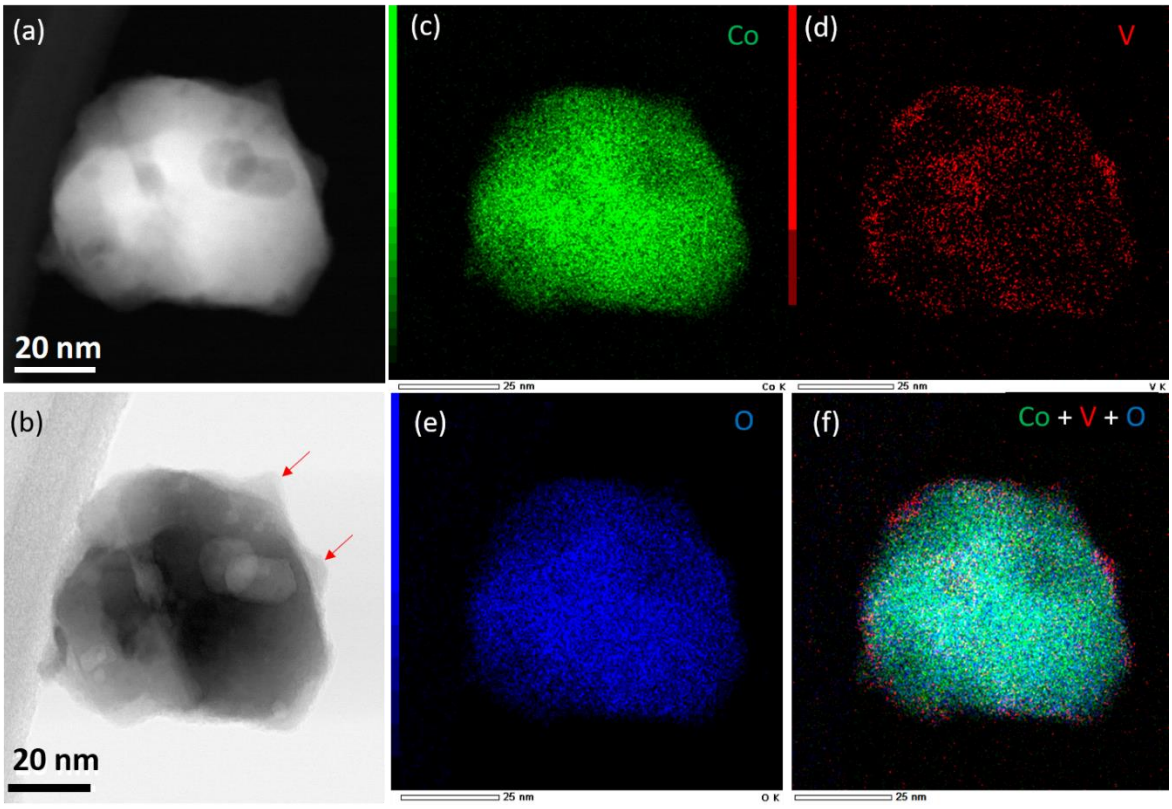

Figure 5-4. STEM-EDS mapping images of spent CoVOx sample after reaction in atmospheric pressure.

5.3.2.2 BET and TPR

Temperature programmed reduction (TPR), was used to investigate the effect of V addition to cobalt oxide reducibility. The TPR profile (see **Figure 5-5**) of pure CoO_x after calcinations in air is characterized by two main features (peaks), which represent a two-stage reduction

process $Co_3O_4 \rightarrow CoO \rightarrow Co$, in good agreement with previous reports.[339,350] The TPR profile of the $CoVO_x$ catalyst shows a number of additional peaks shifted to higher temperatures as compared to CoO_x. Although the attribution of each feature in the TPR profile of *$CoVO_x$* is not straightforward since it involves reduction of both V and Co oxide species as well as their interfaces, the higher reduction temperature implies a strong interaction between cobalt and vanadium, resulting in a material that is more difficult to reduce.[351] The TPR profiles are related to bulk reduction and therefore it is hard to correlate them with the catalytic performance. The differences in the reducibility of the surfaces of the two catalysts will be defined in more detail based on the operando spectroscopic results presented below.

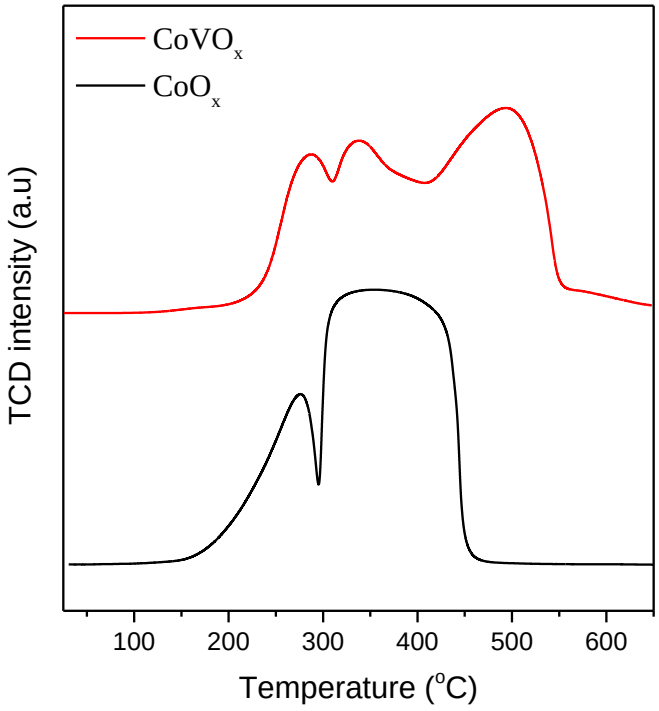

Figure 5-5. H_2-TPR profiles of $CoVO_x$ and CoO catalysts after calcination in air 400ºC 3h.

5.3.3 Comparative *operando* NAP-XPS and NEXAFS at 0.5 mbar

5.3.3.1 The oxidation state of cobalt

In the previous chapters it was demonstrated that the surface oxidation state of cobalt plays a key role for COPrOx reactivity, in agreement with literature reports.[9,10,311] At low temperature the COPrOx mixture can oxidize metallic cobalt, whereas at relatively high temperature cobalt oxides could be reduced back to metal.[6,86,88] Thus, depending on the COPrOx reaction

conditions, cobalt may easily swap between different oxidation states. Herein, synchrotron-based NAP-XPS and NEXAFS were used to monitor, in a comparative basis, the surface oxidation state of CoO_x and $CoVO_x$ during COPrOx reaction. Experiments were performed both in temperature ramping and quasi steady state conditions following an experimental protocol similar to the catalytic tests shown in **Figure 5-1**. Fresh samples, retrieved from the same synthesis batch, were used in each case. Prior to the reaction the samples were pre-reduced at 400°C in 0.5 mbar H_2 for 30 min.

Figure 5-6 shows the evolution of Co $2p_{3/2}$ spectra as a function of COPrOx reaction temperature, for CoO_x (**Figure 5-6a**) and $CoVO_x$ (**Figure 5-6b**) catalysts. Deconvolution of the spectra using reference peaks, was used to quantify the various oxidation states of cobalt. At 50 °C the main Co $2p_{3/2}$ peak of the CoO_x catalyst (**Figure 5-6a**) is centered at 780.5 eV with a satellite peak around 786.7eV characteristic of Co^{2+} species.[147,293,326,335] The shoulder around 778.6 eV is induced by metallic Co,[139,264,293,352] indicating that cobalt forms a mixed Co^0/CoO phase in the COPrOx mixture, in accordance with our previous findings.[311] As the reaction temperature rises, cobalt is further oxidized into Co_3O_4 (herein referred as $Co^{2.67+}$) identified by a broad satellite at 789.5 eV clearly indexed at 300 °C. However, when temperature reaches 350 °C, the low binding energy (BE) peak appears again in the Co $2p_{3/2}$ spectrum, indicating that part of Co_3O_4 is reduced back to metallic Co. This is an intriguing observation showing that the redox effect of COPrOx mixture on cobalt surface is controlled by the reaction temperature.

In the case of $CoVO_x$ (**Figure 5-6b**), a mixed Co^0/Co^{2+} oxidation state is found at 50 °C, while at 150°C the surface is dominated by Co^{2+}, likewise to CoO_x sample. However, above this temperature the stability of Co^{2+} species is distinctly different between the two catalysts. In particular, as clearly shown in the bar graphs, over $CoVO_x$ the Co^{2+} phase is stabilized up to 250 °C, while partial oxidation to $Co^{2.67+}$ is observed only above 300 °C. Contrary to CoO_x, the sample is not reduced to metallic Co^0 at 350 °C. Notably, Co^{2+} is a dominant $CoVO_x$ surface phase at intermediate reaction temperatures (ca. 250°C), which are actually of main interest for COPrOx since higher temperatures promotes water formation.[311]

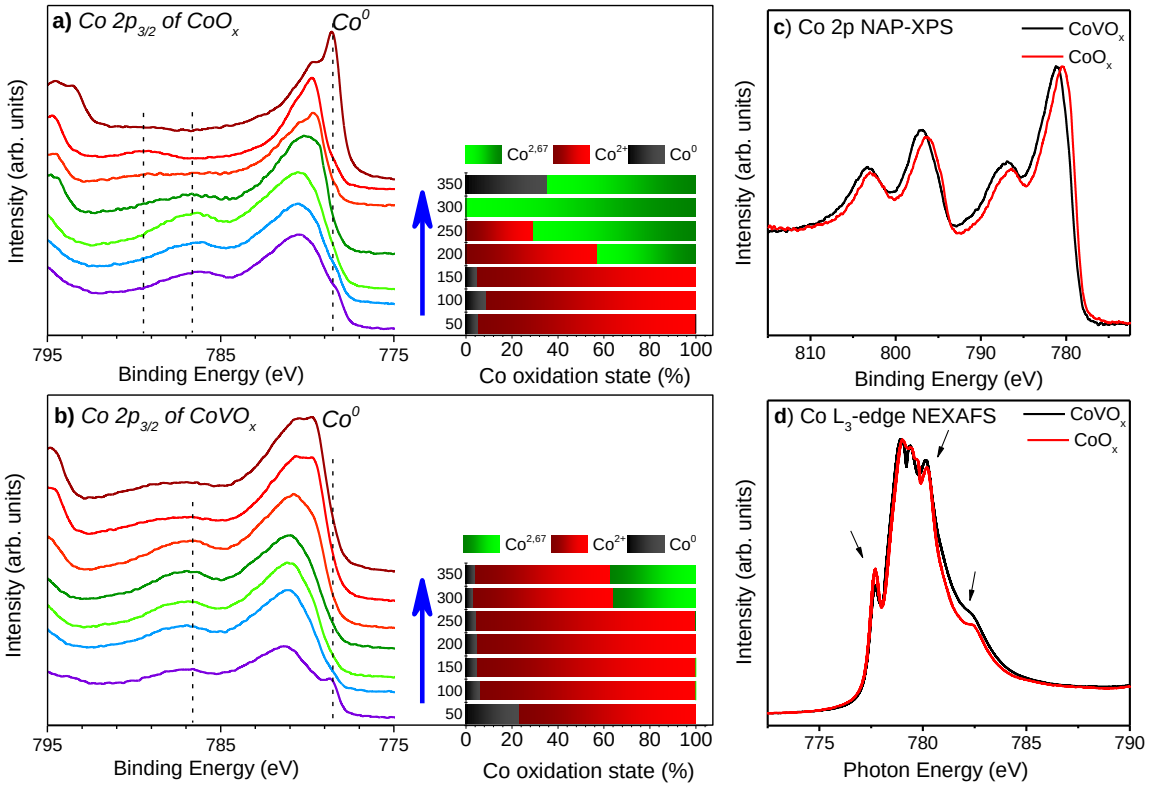

Figure 5-6. Operando NAP-XPS spectra of Co 2p over *CoO_x* *(a)* and *$CoVO_x$* *(b)* catalysts recorded at different temperature during COPrOx reaction: 1%CO, 1%O_2 and 50%H_2 in He, at 0.5 mbar total pressure. Each spectrum was recorded after about 10 min in the reaction. The distribution of cobalt species obtained by Co 2p peak deconvolution is shown in the inserted bar graphs. (c) Co 2p NAP-XPS and (d) Co L_3-edge NEXAFS spectra of *CoO_X* and *$CoVO_x$* catalysts in conditions that favour the formation of Co^{2+} state, i.e. at 150 °C in COPrOx mixture.

NEXAFS is a powerful technique to study the electronic and geometric structure of materials in an element specific fashion.[353] Moreover, contrary to XRD, it is surface sensitive and can detect both crystalline and amorphous phases.[354–356] *Operando* NEXAFS spectra, presented in **Figure 5-7**, confirm the higher stability of Co^{2+} species over *$CoVO_X$* catalyst. In addition to that, the characteristic line shape of octahedrally coordinated Co^{2+} can be easily distinguished at intermediate temperatures in both samples. This result suggests that the octahedral symmetry of Co^{2+} ions does not change by V addition, in contrast to other promoters, e.g. Zn, with stabilizes tetrahedral Co^{2+} species.[164]

In an attempt to identify minor differences in the electronic structure of Co^{2+} species in the two cases, we compare in **Figure 5-6c** the Co 2p spectra of the two catalysts at conditions where the Co^{2+} species dominate. Despite the similar peak profiles, the spectrum of *$CoVO_X$* is shifted about 0.6 eV in respect to *CoO_X*. This shift is also observed for Co 2p spectra recorded

at different photon flux conditions and cannot be induced by electrostatic charging, considering the identical position of the C 1s peak of the two samples (see below). Besides, the shift between the spectra is also visible in partially reduced CoO_x and $CoVO_x$ where the sharp photoelectron peak of Co^0 was used as an internal reference. The $Co2p_{3/2}$ shift to higher binding energies is consistent with previous studies of cobalt vanadates,[357–360] however the magnitude of 0.6 eV observed here is lower than the one previously for cobalt-vanadates.

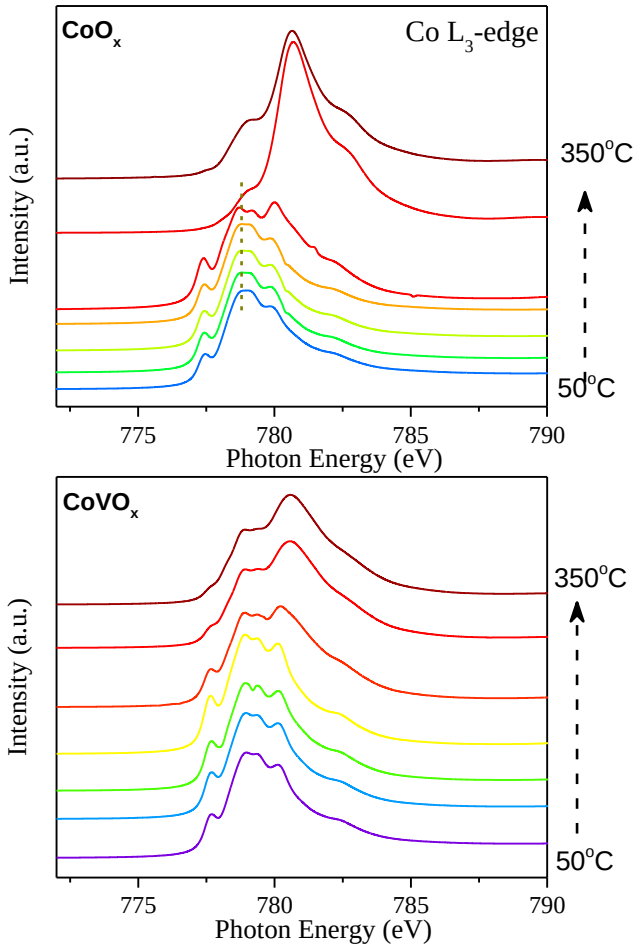

Figure 5-7. Operando NEXAFS spectra of Co L_3-edge over CoO_x *(a)* and $CoVO_x$ *(b)* catalysts recorded at different temperature during COPrOx reaction: 1%CO, 1%O_2 and 50%H_2 in He, at 0.5mbar total pressure. The spectra are recorded on the Total Electron Yield (TEY) mode. Each spectrum was recorded after about 30 min in the reaction conditions.

The Co L_3-edges corresponding to the photoelectron peaks (**Figure 5-6**) are characteristic of octahedrally coordinated Co^{2+} species[44,254] as mentioned above. Although the spectral line shapes closely overlap to each other, in the case of $CoVO_x$ there is relatively lower intensity of the peak at 777.7 eV and higher at the features around 780.1 and 781.8 eV (pointed out by

arrows). Changes in the NEXAFS spectra indicate deviation in the ligand-field-related Co 3d electronic states in the two catalysts, despite the same symmetry. This can be caused by differences in the Co-O bond length, angle and strength, as well as the interaction of cobalt ions with V heteroatoms.[361,362] Similar changes in the Co L_3-edge of cobalt-halogen compounds have been attributed to the increase of cobalt ion electronegativity.[361]

Short-term stability tests were performed at 250 °C, in order to explicate the dramatic differences in the durability of the two catalysts found in **Figure 5-1d**. The evolution of the % CoO, derived by deconvolution of Co 2p peaks, as a function of the time on stream is shown in **Figure 5-8a**. Initially, the surface of both catalysts was dominated by Co^{2+} which decreases with time in favor of $Co^{2.67+}$ formation. However, significant differences can be observed in the % fraction of Co^{2+} between the two samples. In particular, for CoO_x the Co^{2+} amount rapidly drops to 30% due to $Co^{2.67+}$ formation, while for $CoVO_x$ this value drops only up to 78% in the time scale of the experiment.

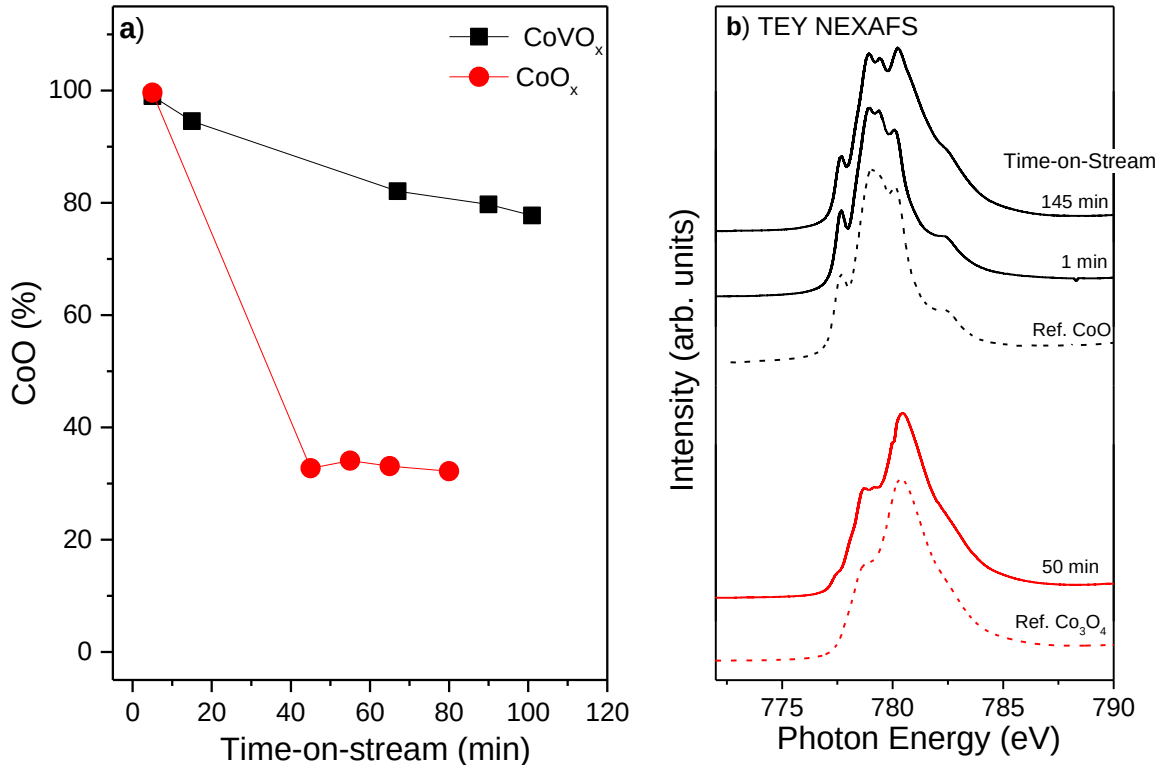

Figure 5-8 a) The % CoO in the overall CoO and Co_3O_4 oxide layer quantified from NAP-XPS Co 2p peak deconvolution as a function of time on stream. b) Characteristic Co L_3-edge NEXAFS spectra recorded at various steps in the COPrOx reaction. The spectra of reference CoO and Co_3O_4 oxides are included for comparison. The spectra for both CoO_x and $CoVO_x$ catalysts were recorded at 250 °C in 1%CO, 1%O_2 and 50%H_2 in He, at 0.5mbar total pressure.

Depth dependent measurements of the Co 2p peak were used to distinguish the distribution of the two oxides on the $CoVO_x$ surface. As shown in **Figure 5-9**, there is no evident depth dependency between the two Co 2p components, which indicates that Co^{2+} and $Co^{2.67+}$ phases do not overlap significantly but are arranged separately on the $CoVO_x$ surface. Comparison of the Co L_3-edges in **Figure 5-8b** confirms the significant differences in the oxidation state of the two catalysts in consistence with NAP-XPS.

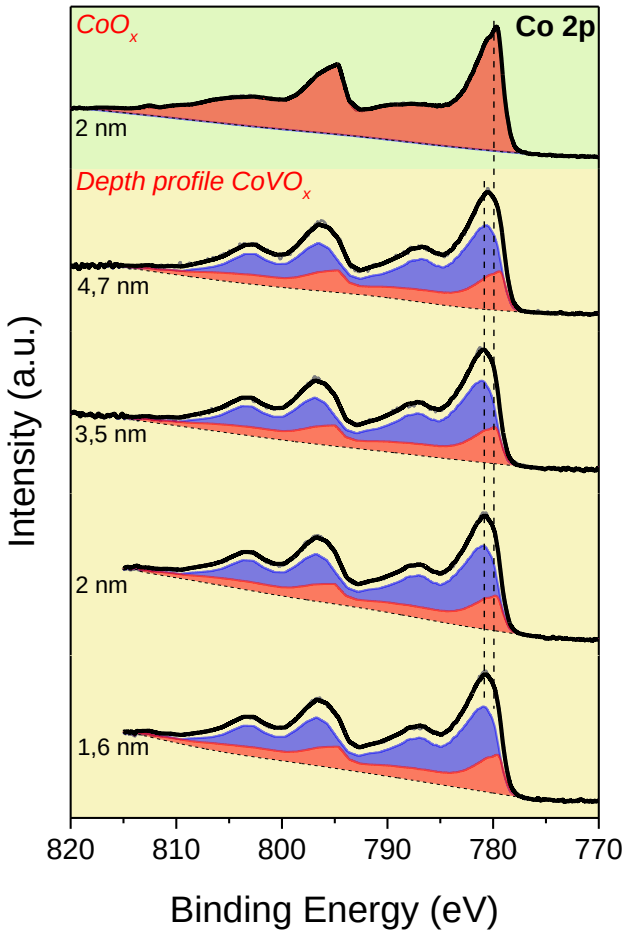

Figure 5-9. (*bottom part in yellow background*) *Orerando* NAP-XPS Co 2p spectra collected over $CoVO_x$ catalyst using four different photon excitation energies (960, 1020, 1340 and 1620 eV). The analysis depth of each photon energy was estimated as 3 times the inelastic mean free path. The latter was calculated using the QUASES-IMFP-TPP2M Ver.3.0 software. (*top part in green background*) *Orerando* NAP-XPS Co 2p spectra of CoO_x catalyst recorded using excitation photons of 1020 eV. All spectra were recorded at 250 °C in COPrOx reaction conditions.

Overall, from the above presented results it can be claimed that the thermal stability of octahedral Co^{2+} species in COPrOx conditions is improved by V addition. The observed differences in the Co $2p_{3/2}$ BEs and the Co L-edge NEXAFS features between the two catalysts,

evoke that V interfere with Co^{2+} ions, implying the formation of a mixed cobalt-vanadium oxide. Nonetheless, the spectra of *$CoVO_x$* do not exactly match these of known octahedral cobalt vanadate compounds (e.g. $Co_3V_2O_8$)[347,362] and do not allow the direct identification of the mixed oxide formed in our case. Further details on the nature of *$CoVO_x$* are provided by the analysis of vanadium peaks.

5.3.3.2 The oxidation state of Vanadium

To understand better the behavior of *$CoVO_x$* catalyst, it is important to determine the oxidation state and the stability of vanadium. Vanadium can take several oxidation states that can be easily distinguished in photoemission experiments. A complete list of the V 2p and L-edge XPS and NEXAFS spectra for all reaction temperatures can be found in **Figure 5-10**.

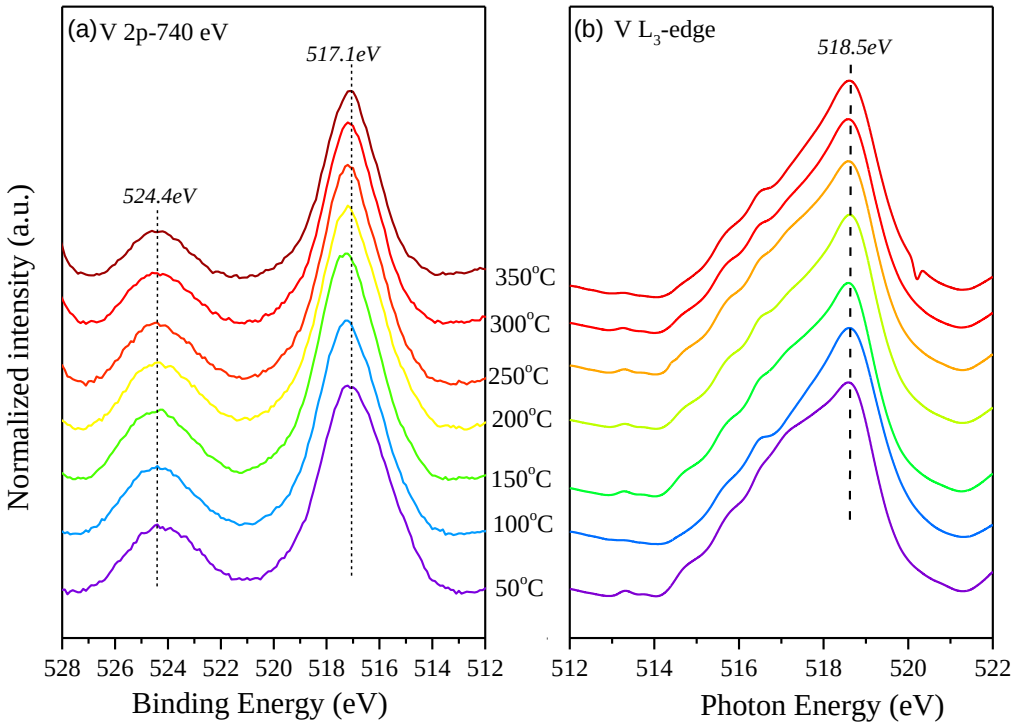

Figure 5-10: (a) Operando V 2p NAP-XPS and (b) V L_3-edge NEXAFS spectra of CoVOx catalysts recorded at various temperatures during COPrOx reaction: 1%CO, 1%O_2 and 50%H_2 in He, at 0.5mbar total pressure. Each spectrum was recorded after about 10 min in the reaction. All spectra recorded above 100°C look quite similar, with several small features visible and the dominant spectra peak positioned at ~518 eV. No shifts are observed with V L_3 edge spectra of CoVOx at different temperature, confirming the XPS results which show that V^{5+} is the dominant oxidation state of vanadium during COPrOx.

In order to facilitate the discussion **Figure 5-11a** shows the selected V 2p spectra recorded at some characteristic COPrOx reaction conditions. As shown in **Figure 5-11a**, at 50 °C the V

$2p_{3/2}$ peak can be deconvoluted in two components at 515.8 eV and 517.1eV which correspond to V^{4+} and V^{5+}species respectively,[363–366] while at 350 ºC the V^{5+} peak dominates the spectrum in the expense of the V^{4+} component. Depth dependent V 2p measurements (not shown) suggested that both vanadium oxidation states co-exist on the surface without evident depth distribution. The increase of the % V^{5+} with reaction temperature (**Figure 5-11b**) implies progressive oxidation of V^{4+} to V^{5+}. The % of Co^{2+} included in the same graph is practically stable between 100-250 °C, suggesting that the oxidation behavior of the two elements of $CoVO_x$ is different. This is also supported in the stability experiments, where after about 30 min in the stream, all vanadium was converted to V^{5+} and remained stable at this oxidation state onwards (**Figure 5-11a**).

In **Figure 5-11c** the V L_3 edge of $CoVO_x$ recorded at 250 °C during COPrOx stability tests is compared with spectra of $Co_3V_2O_8$ and V_2O_5 reference compounds. For the evolution of $CoVO_x$ V L_3 edge as a function of the reaction temperature please refer to **Figure 5-10**b. The reference oxides were selected because of their different coordination geometry with the oxygen ligands: tetrahedral (T_d) for $Co_3V_2O_8$ [347] and octahedral (O_h) for V_2O_5,[348] albeit they are both composed of V^{5+} cations similar to $CoVO_x$. According to literature, the various V oxidation states are differentiated by the shift of all discernible spectral features of V L-edge spectra. For example, the NEXAFS peak maximum of V^{5+} in V_2O_5 oxide is centered at around 518.8 eV and is shifted by approximately 1 eV from that of V^{4+}.[13,356,367–370] The alignment of the peak maximum for all NEXAFS spectra in **Figure 5-11c** confirms the XPS results, which show that V^{5+} is the dominant oxidation state of vanadium during COPrOx. The $CoVO_x$ peak profile does not contain the features around 517 and 519.5 eV resembling more to the $Co_3V_2O_8$ than V_2O_5 reference oxide. This suggests that V^{5+} in our catalyst is in T_d coordination with O^{2-} anions and does not form V_2O_5 particles separated from cobalt, but most probably Co and V ions interact to each other to form a mixed oxide. However, there are some clear differences in the NEXAFS line shapes between $CoVO_x$ and $Co_3V_2O_8$, with the most prominent being the increased intensity of the former at around 517.5 eV. This cannot be induced by lower vanadium oxidation states, since these states should have been also visible in the V 2p spectra. This observation suggests a distortion of V-O symmetry as compared to the reference oxide.

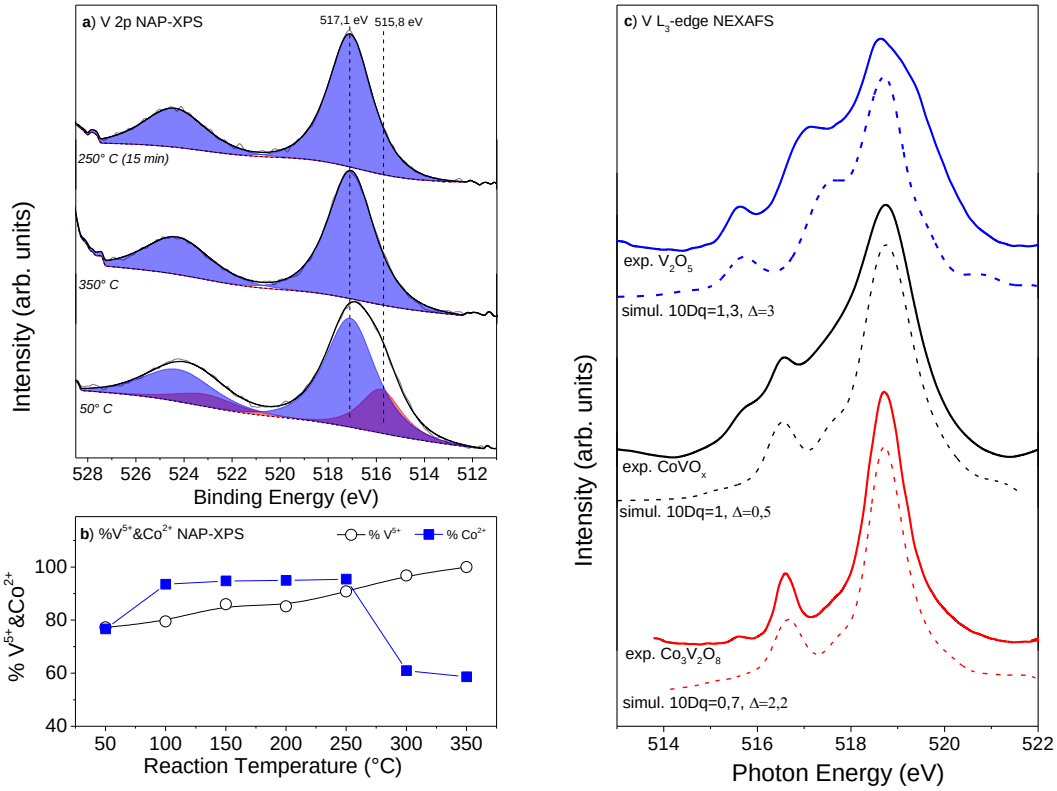

Figure 5-11. (a) *Opreando* NAP-XPS V 2p spectra of $CoVO_x$ catalyst recorded during temperature-dependent and stability COPrOx tests. (b) The % evolution of V^{5+} and Co^{2+} species with temperature calculated based on V 2p peak deconvolution shown in (a) and Co 2p spectra shown in figure 4-5b. (c) *Operando* V L_3 edge NEXAFS spectra of $CoVO_x$ catalyst (solid black line) at 250 °C in the COPrOx reaction. Reference V L_3 edge spectra of V_2O_5 and $Co_3V_2O_8$ (solid blue and red lines respectively) extracted from literature[347,367] are included for comparison. Theoretically simulated V L_3 edges (*dashed lines*) for the same V oxidation state (+5) but different crystal field geometries (Td, Oh) and 10Dq and Δ values are included under each experimental spectrum.

The spectral shape of the NEXAFS V L_3-edge is strongly correlated to the coordination environment and number of 3d electrons of the metal center.[344] Therefore it may be used to provide interesting insights about the local geometry around the V^{5+} cation,[368] as has been shown previously for other transition metal oxides.[177,371] Theoretical simulation of the V L_3-edge using the charge-transfer multiplet (CTM) approach can help to estimate the variations in the V-O interaction that are accountable for the differences in the line shapes.[344,345] The two key parameters affecting the shape of the calculated XAS curves are 10Dq (crystal field splitting) and Δ (charge transfer energy). The 10Dq parameter determines the splitting in the crystal field and depends mainly on the metal-ligand distance, in a way that an increase in the value of 10Dq corresponds to a decrease in V-O distance. The charge transfer energy term Δ

describes the interaction of V 2p ions with delocalized electrons from the O 2p orbital.[196] An increase in Δ value corresponds to weaker interaction between V 2p and O 2p orbitals. The theoretically simulated V L_3-edges that give the best accordance with the experimental spectra are included in **Figure 5-11c**, while the 10Dq and Δ parameters are shown in **Table 5-1**. The *$CoVO_x$* catalyst has higher 10Dq and lower Δ values as compared to $Co_3V_2O_8$. According to the assignment mentioned above, the distance between V and O ions is shorter and their interaction is stronger in *$CoVO_x$* as compared to $Co_3V_2O_8$. Assuming that Co and V ions share some of the oxygen atoms in the lattice, shorter V–O bonds induce correspondingly longer Co–O bonds. The net result of this change is that the cobalt 3d electrons are more localized on the cobalt atoms in $CoVO_x$ as compared to $Co_3V_2O_8$.[362]

Table 5-1. The symmetry, 10Dq (crystal field splitting) and Δ (charge transfer energy) parameters found by the multiplet calculation to give the best accordance with the experimental spectra shown in Figure 5-11c.

Sample	Symmetry	10Dq (eV)	Δ (eV)
V_2O_5	O_h	1.3	3
$Co_3V_2O_8$	T_d	0.7	2.2
$CoVO_x$	T_d	1	0.5

Overall, the analysis presented above suggests that the electronic structure of V^{5+} species on *$CoVO_x$* catalysts does not correspond to the octahedral coordination expected for V_2O_5 simple oxide, but to tetrahedral coordination, most probably by formation of a mixed oxide with the cobalt support. As also discussed above for Co^{2+}, the spectroscopic results do not allow attributing the cobalt-vanadate oxide formed on the *$CoVO_x$* surface to one of the already described bulk cobalt vanadates. However, it seems that V-Co interaction is the key of the high stability of Co^{2+} ions and increases the resistance of *CoVOx* to Co_3O_4 oxide formation.

5.3.3.3 Surface composition and evolution of the adsorbed species during COPrOx

Figure 5-12 presents the surface atomic percent (at. %) evolution of V on *$CoVO_x$* surface, as determined by the intensity of the V 2p and Co 2p NAP-XPS peaks. The as-synthesized $CoVO_x$ has considerably higher V concentration than the nominal one (23 instead of 11 at. % V), suggesting that vanadium was initially highly dispersed on the sample's surface. However, the V% concentration decreases rapidly with the COPrOx reaction temperature in favor of cobalt,

either due to agglomeration or subsurface segregation of V species. Recording Co 2p and V 2p peaks with increasing photon energies allowed calculating the %V concentration at different analysis depths. The results, included in the inset of **Figure 5-12**, make clear that V concentration decreases with the analysis depth. This indicates that V and Co are not homogenously mixed in the outermost 5 nm of the catalyst, but V is concentrated at the outermost surface while the inner layers are dominated by cobalt. This is an additional argument suggesting that surface and bulk parts of the $CoVO_x$ catalyst are distinctly different, validating our approach to use primarily surface sensitive methods for its analysis.

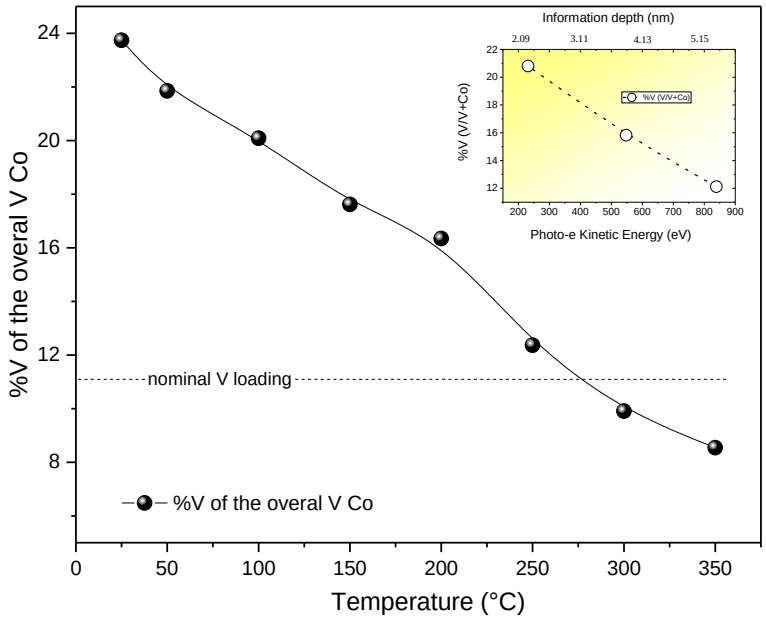

Figure 5-12. Surface atomic percent (at. %) of V as a function of COPrOx reaction temperature, calculated by V 2p and Co 2p NAP-XPS. The analysis depth is estimated around 2 nm. The inset shows the modification of the %at. V with the NAP-XPS analysis depth, calculated from measurements with increasing excitation photon energies. The latter measurements correspond to the long-term stability test experiment.

Operando NAP-XPS provides the necessary chemical and surface specificity to identify adsorbed carbon species during reaction. In **Figure 5-13** the C 1s spectra at characteristic reaction temperatures are shown together with the evolution of the surface concentration for CoO_x and $CoVO_x$ catalysts. The amount of adsorbed carbon over $CoVO_x$ is constant up to 200 °C, while above this temperature it shows a decreasing tendency. Carbon evolution over CoO_x is notably different, exhibiting a fast decrease of carbon population up to 200 °C and a steep rising above this temperature, which overwhelms almost 4 times the carbon observed

CoVO$_x$.

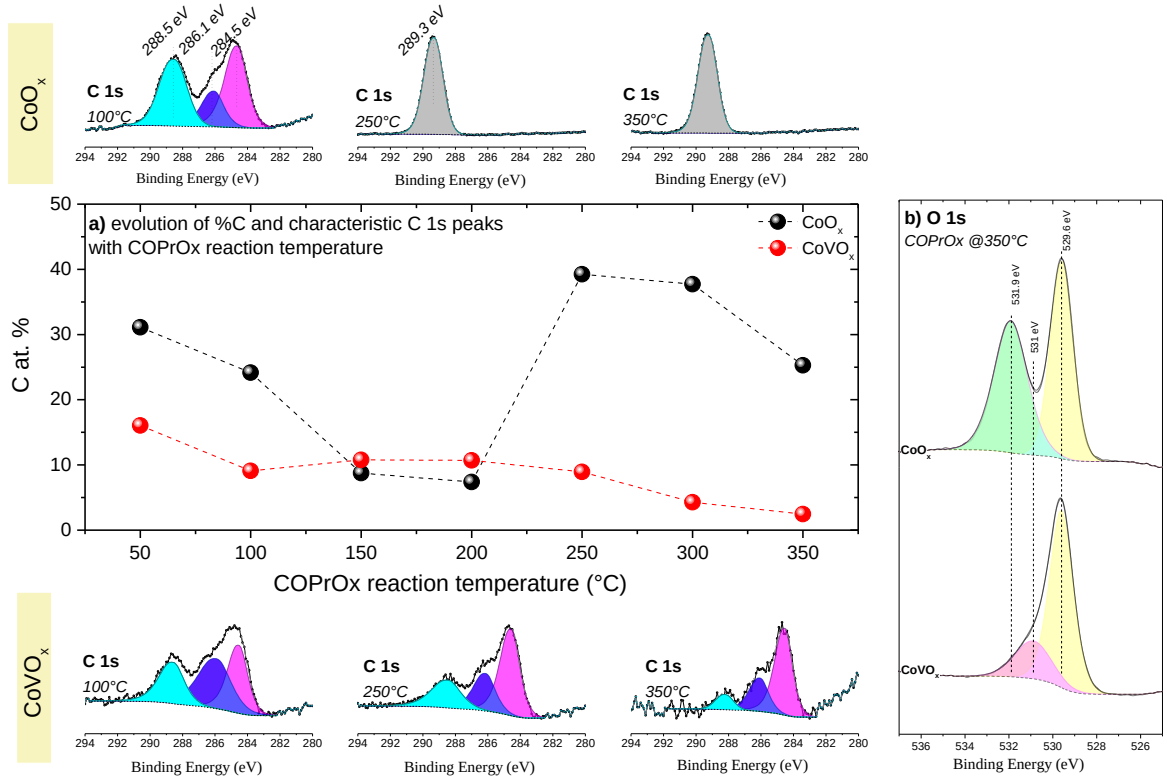

Figure 5-13 (a) *Operando* C 1s NAP-XPS spectra recorded at different COPrOx reaction temperatures over *CoO$_x$* (top) and *CoVO$_x$* catalysts. The middle graph shows the evolution of the carbon atomic percent (at. %) at the surface (2 nm) as a function of the COPrOx reaction temperature, calculated by the C 1s, Co 2p and V 2p peaks. (b) Comparison of the O 1s NAP-XPS spectra of the two catalysts recorded at 350 °C in COPrOx.

Deconvolution of the C 1s peak can help to distinguish the nature of adsorbed carbon. As shown in **Figure 5-13**a, four main carbon species coexist on the two surfaces. Based on previous reports, the peak at 284.5 eV is due to C−H and C−C bonds, while the two peaks at 286.4 and 288.4 eV are attributed to oxygenated carbon species like C-O-C and O-C=O respectively.[311] These species persist on the surface of *CoVO$_x$* catalysts at all reaction temperatures with small variations in their relative population. In the case of *CoO$_x$* the evolution of carbon species is remarkably different, with a new C 1s peak at 289.3 dominating the surface above 250 °C. The binding energy of this peaks is characteristic for carbonate (CO^{2-}) or oxalate ($(COO)^{2-}$) species as has been clearly shown before.[372,373]

This attribution is confirmed by the O 1s spectra recorded at 350 °C and shown in **Figure 5-13**b. The overall O 1s peak can be deconvoluted in two main oxygen species. The one around

529.6 eV is assigned to the lattice oxygen of the cobalt oxides (CoO and Co_3O_4 have very similar O 1s binding energies) [311]. The high binding energy components are located at 530 eV (*$CoVO_x$*) and 531.9 eV (*CoO_x*) and can be attributed to oxygenated carbon/hydroxyl species[175,277] and carbonate/oxalate species,[372,373] respectively. N. Kruse and *coworkers* showed that the binding energy difference between the O1s and C 1s peaks ΔBE(O1s–C1s) can be used to distinguish between carbonate and oxalate carbon species. Taking as an internal reference the position of the C-C peak, this difference is found in our case 242.1 eV which is in good agreement with the value of 242 ± 0.2 eV reported for carbonate species.[372,373] In *Chapter 3* the differences in the reactivity between CoO and Co_3O_4 were attributed to their different capacity to form carbonates under COPrOx reaction conditions. The NAP-XPS analysis presented here evidences that stabilization of the Co^{2+} oxidation state by V promoter controls the amount of adsorbed carbonates during the reaction, having direct benefits on the reactivity.

5.3.4 Reducibility of *$CoVO_x$* measured by *in situ*–NEXAFS at 1 bar

The operando NAP-XPS and NEXAFS results clearly demonstrated that Co^{2+} remains the dominant cobalt oxidation state during COPrOx over *$CoVO_x$*, in contrast to the pure *CoO_x* catalyst which forms a mixture of Co^{3+} and Co^0, at least above 200 °C. This finding provides clear evidence that the high catalytic activity and stability of *$CoVO_x$* demonstrated in the catalytic tests (**Figure 5-1**) is related to the enhanced redox stability of cobalt monoxide. However, before being able to directly correlate NAP-XPS with fix-bed reactor results, the effect of the pressure gap between the two experiments (0.1 mbar in NAP-XPS *vs.* of 1 bar in catalytic tests) should be considered. The XRD analysis of the spent catalysts showed that their bulk structure was not notably affected by COPrOx reaction, which contradicts the fast adjustment of the surface oxidation state and composition found in NAP-XPS. Therefore, in order to fulfill the requirements of surface sensitivity and atmospheric pressure operation, a recently developed experimental approach was selected which allows performing *in situ* NEXAFS under controlled gas atmosphere at 1 bar.[249] Since the designs of the NAP-XPS and 1 bar NEXAFS cells are considerably different, it is very challenging to obtain the same reaction conditions (reactants flow, gas space velocity, beam effects etc.) in the two experiments. Therefore, the stability of *$CoVO_x$* was investigated under 1 bar H_2 atmosphere (without CO and O_2 addition) and 10% O_2/He, which are much harsher reducing and oxidizing conditions respectively than those the catalyst faces in COPrOx reaction.

Figure 5-14a and b show the V and Co L_3-edges respectively, of pristine *$CoVO_x$* (calcined) upon annealing in H_2. Not surprisingly, just after calcination the V and Co L_3-edges correspond to V^{5+} and a mixture of Co^{3+} and Co^{2+} species, respectively. Annealing in H_2 partially reduces both V and Co, but not at the same temperature. V^{5+} readily reduces to V^{4+} already from 50 °C, and after this temperature the spectral shape remains similar up to 250 °C. In case of cobalt, the reduction of Co^{3+} appears above 200 °C, while at 315 °C the line shape of Co L_3-edge resembles that of Co^{2+}.

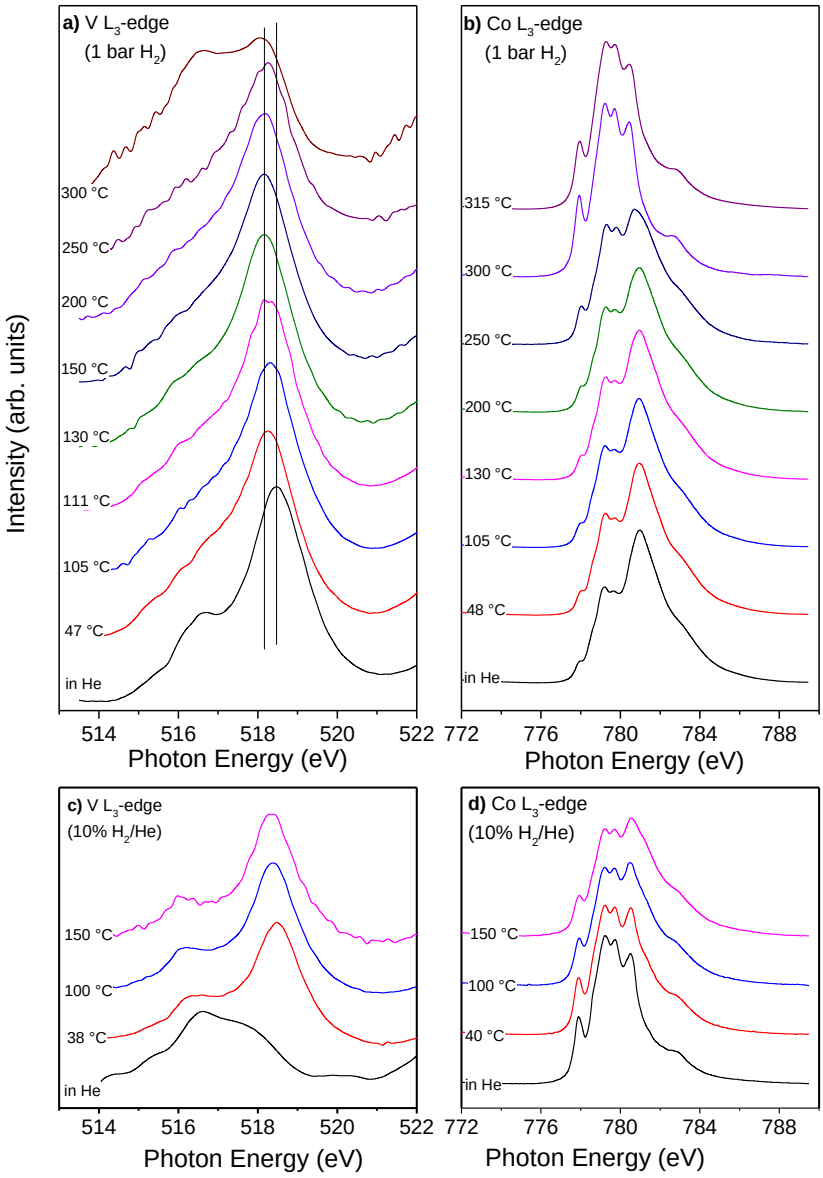

Figure 5-14. ***(a) In situ*** **V L_3-edge and** ***(b)*** **Co L_3-edge NEXAFS spectra of $CoVO_x$ catalysts recorded at 1 bar H_2 between 47-315°C.** ***(c) In situ*** **V L_3-edge and** ***(d)*** **Co L_3-edge NEXAFS spectra of $CoVO_x$ catalysts recorded at 1 bar 10%O_2 in He between 38-150°C.**

The oxidation behavior between vanadium and cobalt in 10%O_2 in He at 1 bar (**Figure 5-14c and d**) is also very different. When the pre-reduced catalyst is exposed to O_2 vanadium is readily oxidized to the V^{5+} state already at 38 °C and remains stable afterwards, while cobalt is much more resistant to oxidation. At the maximum annealing temperature of this experiment (150 °C) only a part of Co^{2+} has been oxidized to Co^{3+} as deduced by the Co L_3-edge line shape. Please note that in 10%O_2 in He, cobalt is more oxidized as compared to the COPrOx mixture shown in NAP-XPS, which is however expected due to the much higher oxidative effect of 10%O_2 atmosphere. However, this result clearly shows that cobalt and vanadium do not respond to the same manner in oxidative environments with the latter being much more resistant to oxidation than the former. Consequently, in situ NEXAFS confirms that the Co^{2+} state might be stable under atmospheric pressure conditions that closely resemble those of the catalytic tests. This result directly supports the idea that the higher activity and stability of *$CoVO_x$* should be a direct consequence of the redox stability of surface Co^{2+} species.

5.4 Discussion

Catalytic tests show that vanadium addition to cobalt oxide results in a material with a higher conversion in preferential CO oxidation in H_2 rich mixtures. There are two general paths in which promoters, V in our case, may influence the reactivity of the active catalytic sites, i.e. Co. The first is related to an electronic modification of the catalytic active sites and the second to structural stabilization that enhances their abundance during the reaction.[374] Our results show that the population of Co^{2+} on the surface of cobalt adjusts to the working conditions independent of the promotion. Nevertheless, under identical conditions *$CoVO_x$* has always higher abundance of Co^{2+} as compared to CoO_x. Therefore, the primary effect of V on cobalt is related to the structural stabilization of Co^{2+} sites and their resistance to Co^{3+} transformation. As we have shown previously, this affects the COPrOx reactivity since Co^{2+} surfaces are less susceptible to carbonate species formation,[311] which is one of the main reasons of cobalt catalysts deactivation.

To elucidate the stabilization effect of V on Co^{2+} we need first to describe the mechanism of CoO oxidation to Co_3O_4. Combining theory with experiment, Robinson and coworkers[271] showed that CoO oxidation proceeds by Co^{2+} ions diffusion to the outer surface through the oxide lattice and/or the grain boundaries. In this process the O lattice is not considerably affected and it is expected to remain rigid. [271] Our results showed that Co^{2+} and V^{5+} ions at

$CoVO_x$ surface share to a large extent the same lattice oxygen. The vanadium ions can exchange between 5+ and 4+ valences more easily than cobalt changes between the 2+ and 3+ ones, as shown in the NAP-XPS and the atmospheric pressure NEXFAS experiments. Therefore, since V has higher redox ability as compared to Co, it will be selectively oxidized by gas O_2 acting as a buffer for Co^{2+} oxidation. Taking into account that the COPrOx mixture contains only 1% O_2, this can slow down the kinetics of cobalt oxidation and increase the durability of the catalyst. Similarly, in reducing conditions V^{5+} will be the first ion to release oxygen and convert to V^{4+}, keeping Co^{2+} stable. An analogous stability mechanism has been previously proposed for Fe-doped Co_3O_4 catalyst.[375]

In addition to the clearly manifested stability of Co^{2+}, the analysis of absorption spectra gave evidence of a less pronounced, but still distinguishable, difference between the two catalysts. Namely, although V does not change the coordination symmetry of Co^{2+}, yet it affects the Co^{2+}-O anions distance in the *$CoVO_x$* oxide lattice as well as the Co^{2+} electronic state. Unfortunately, our analysis cannot quantify the electronic charge of cobalt ions, however, can qualitatively explain the electronic effects. As described above, the Co^{2+} electronegativity in *$CoVO_x$* is higher as compared to *CoO_x*, while the bond distance between Co^{2+} and O^{2-} increases. Theoretical models predict that higher metal electronegativity should be followed by lower interaction with oxygen, thus weaker metal-oxygen bond.[376] This can be related to enhanced oxygen mobility on the surface of the *$CoVO_x$* catalyst. The oxidation of CO on cobalt oxide follows a Mars−van Krevelen mechanism,[311] which implies that higher mobility of lattice oxygen ions will result to higher reaction rates [377]. This hypothesis is directly supported by the fact that *$CoVO_x$* has higher activity in the 150-200 °C temperature region (**Figure 5-1**), even if NAP-XPS analysis shows that the amount of adsorbed carbon species (**Figure 5-13**) is very similar in the two catalysts. Therefore V-addition has a dual function on cobalt, first it helps to stabilize the Co^{2+} phase and inhibit carbonate-induced deactivation and second modifies the electronic state of Co^{2+} increasing oxygen mobility and in this way enhancing the reaction kinetics.

5.5 Conclusions

The COPrOx activity of cobalt oxide is significantly improved by introduction of vanadium. Several *ex situ* and *operando* methods were applied to understand the promotion effect including NAP-XPS and atmospheric NEXAFS at 1 bar. The bulk structure and morphology of

V-modified catalysts is not significantly influenced as compared to pure cobalt. However, detailed spectroscopic analysis revealed the formation of a mixed cobalt vanadate phase on the surface, which does not resemble the known bulk mixed oxides. This phase is formed by tetrahedrally coordinated V^{5+} and octahedral Co^{2+} species. Both, electronic and structural effects must be considered to understand cobalt catalyst promotion by vanadium. In particular, V prevents the oxidation of CoO and provides stable active octahedral Co^{2+} sites for COPrOx, resistant to deactivation through carbonate species formation. In addition to that, we found evidences of modifications in the electronic state of Co^{2+} species induced by V promotion, in the direction that enhances the reaction kinetics. Furthermore, by using NEXAFS at atmospheric pressure we could show that Co^{2+} species are preserved on the $CoVO_x$ surface at temperature and pressure relevant to the catalytic tests. Overall, the study presented in this chapter shows that one can use insights from operando surface spectroscopy to design and produce better COPrOx catalysts. Considering the rising accessibility and availability of these methods this can be a sustainable strategy for the development of new generation catalysts.

Chapter 6

Conclusions and Perspectives

6.1 Summary and General conclusions

Cobalt can be found in three main oxidation states in nature (i.e. Co^0, CoO and Co_3O_4).[378] What makes cobalt a good catalyst for many heterogeneous reactions is its ability to undergo facile transitions between these oxidation states acting as a source/sink for electrons. In order to design an efficient cobalt-based COPrOx catalyst, it is essential to clarify fist the most active cobalt oxidation state for the reaction of interest. It is known that the surface of a catalyst under reaction conditions is dynamic and very sensitive to the gas phase environment and the temperature. For this reason this thesis identified foremost the optimum oxidation state of cobalt for CO conversion in H_2 feed stock. In a second step it was attempted to optimize the reactivity and stability of the most active phase via introduction of another component as a promoter. *In situ* and *operando* techniques, in combination with conventional structural and morphological characterization methods, were applied in order to identify the optimum active phase of the cobalt-based catalyst composites.

In *chapter 3*, pure cobalt oxide (Co_3O_4) nanoparticles (NPs) were used as a model system to investigate the most active oxidation state of cobalt for COPrOx. Although we were aware of the fact that NPs are far more complex "model systems", as compared to metal single crystals or foils, we intentionally made this choice in order to be able to combine the spectroscopic results with catalytic data recorded in parallel at most of the times. Preliminary studies in the frame of this thesis (not included in this manuscript) clearly showed that the catalytic response of planar samples was negligible under the employed conditions. Pure cobalt NPs after reduction and oxidation pretreatment have shown different catalytic reactivity for selective CO oxidation in H_2-rich feed gas. The spectroscopic analysis of their surfaces suggested that the pretreatment has a dominant effect on the oxidation state of cobalt during COPrOx. In particular, pre-reduced cobalt ($PreH_2$-Co) is much more active than its pre-oxidized equivalent ($PreO_2$-Co) for COPrOx. In order to compare the intrinsic activity of the different oxidation states of cobalt, the surface specific activity on two pretreated Co NPs was calculated based on the Kr-BET surface area measurements. Even after taking into account the surface area differences between the two catalysts, $PreH_2$-Co remains significantly more active than $PreO_2$-Co.

Ex situ XRD and TEM results indicate that the nanoparticles have comparable size but

different oxidation states. In particular, in case of the $PreH_2$-Co sample, the catalyst after COPrOx reaction contains mixture of CoO and Co_3O_4 in the bulk, suggesting oxidation either during COPrOx reaction or after exposure to air before the ex situ measurements. Synchrotron-based operando NAP-XPS and NEXAFs were used to monitor the active phase on the catalyst surface during COPrOx reaction. The Co 2p spectra and Co L_3 edge spectra demonstrate that the surface of $PreO_2$-Co NPs during COPrOx maintains the Co_3O_4 phase, while under the same reaction conditions CoO dominates on the surface of the $PreH_2$-Co sample. Considering the pressure gap between spectroscopic study (0.5 mbar) and real activity tests (1 bar), the effect of reaction pressure on the evolution of the surface cobalt oxidation state was clarified. The CoO phase on $PreH_2$-Co surface was proved to be able to sustain in a wide pressure range (from 0.5 mbar to 1 bar) along with comparable reaction products as a function of temperature. In situ DRIFTs and NAP-XPS results revealed that more carbonates are formed over Co_3O_4 as compared to CoO during reaction and DFT calculations elucidate their effect to act as site blockers of the active sites on cobalt. Although the CoO phase was clearly identified to be more active than Co_3O_4, it was found that it is exceedingly difficult to be stabilized under COPrOx gas environment. The direct effect of this is rapid deactivation in the course of the reaction, which is reversible when the catalyst is reduced again, but it is definitely a limit for the practical application of pure cobalt.

Thus, in *chapter 4*, efforts have been put to investigate the promotional effect of Mn to CoOx for COPrOx. The choice of Mn was based on literature results that proposed Mn-promoted Co catalysts as the one of the most promising combinations for active and stable CO oxidation cobalt catalysts.[83,310] In order to focus on the understanding of the reactivity and exclude complexities induced by elaborate synthesis methods, Mn has been simply loaded onto commercial CoO_x NPs by the incipient wetness impregnation method. The comparison of the activity among CoO_x, Co_8MnO_x and $CoMn_8O_x$ shows that the addition of small amount Mn into CoO_x improves the reactivity for COPrOx, while Mn-rich cobalt catalyst ($CoMn_8O_x$) has the lowest CO conversion towards CO oxidation among all studied materials. This is expected since pure MnO_x is reported to be less active than CoO_x for CO oxidation.[379]

BET, SEM and XRD characterization demonstrated that the addition of Mn into CoO_x inhibits the severe agglomeration of particles caused during pretreatment and reaction, therefore maintaining the larger surface area in contrast with pure CoO_x particles that undergo

severe agglomeration. NAP-XPS revealed that the CoO phase can be stabilized in the presence of Mn, but only partially. Besides, the oxidation state of Mn is also dynamic and changes during the COPrOx reaction. Indications that the transformation of Mn^{3+} to Mn^{2+} leads to high reactivity of the unwanted H_2 oxidation were found. Therefore, Mn might bring positive effects on cobalt by stabilization of the CoO phase, but at the same time it is itself a "good" hydrogen oxidation catalyst, which is not desired in this case since it consumes valuable H_2 from the COPrOx reaction feed.

The research described in *Chapter 4* revealed that Mn is not an ideal promoter of CoOx for CO oxidation in the presence of H_2 and it is worth looking for an alternative and better promoter to stabilize the CoO phase. After several unsuccessful and time consuming efforts to achieve this goal, following different approaches (not included in this manuscript), vanadium was identified as a promising promoter for cobalt-based COPrOx catalysts and the relevant research is described in *Chapter 5*. To the best of the author knowledge, vanadium-cobalt catalyst has not been reported before for this reaction. However, inspired by the property of vanadium to take various oxidation states, together with recent electrocatalytic studies reporting that cobalt in $CoVO_x$ mixed oxides is stabilized in the octahedral Co^{2+} state under different conditions,[359,380] we initiated the study of V-promoted cobalt. As explained before for Mn, the easiest possible method was followed to prepare the Co-V catalyst by simply loading V from a solution onto CoOx NPs.

The evaluation of the catalytic activity at 1 bar depicted that the addition of V not only improves the reactivity, but also the stability and notably the CO_2 selectivity of cobalt for COPrOx reaction. The XRD patterns indicated that the bulk structure of cobalt was not influenced by the addition of vanadium, neither after pretreatment, nor during COPrOx reaction. The vanadium phase was indistinctly observed with XRD, SEM and STEM-EDS mapping. Element analysis demonstrated that vanadium is well dispersed over cobalt and the two materials do not mix in the bulk. Definitely, due to the simple synthesis method employed, the preparation is not optimized and Co and V-rich areas still exist on the catalyst. H_2-TPR measurements inferred that the reduction temperature of cobalt oxide bulk is shifted to higher temperature, indicating the strong interaction between Co and V as has been also reported previously.[339] All the investigation on structure and morphology indicates that vanadium forms an amorphous rather than a crystalline phase on the surface.

In situ surface analysis reveals that the active surface phase of V-modified cobalt is composed of $Co^{2+}$and V^{5+} sites. Notably, the cobalt surface of reduced CoVOx is more stable as compared to pure CoOx, sustaining octahedral Co^{2+} as a dominant surface phase over CoVOx during COPrOx reactions at the mbar range. X-ray absorption spectroscopic analysis directly evidenced the formation of a mixed cobalt vanadate phase on the surface. This phase is formed by tetrahedrally coordinated V^{5+} and octahedral Co^{2+} species. In addition to that, simulation of the NEXAFS results using multiplet calculations demonstrated that the distance of Co^{2+}-O is modified by the V. This has a likely effect on the reaction kinetics by increasing the mobility of oxygen bonded to cobalt. In situ NAP-XPS O 1s and C 1s spectra illustrated that the formation of carbonates is limited on CoVOx surface due to stable active octahedral Co^{2+}, therefore preventing the deactivation of the catalyst as compared to Co_3O_4.

In *Chapter 3*, it was investigated the pressure gap between NAP-XPS study at ~mbar pressure and conventional catalytic activity tests (1bar) by performing pressure dependent XPS characterization in a reactor attached to a conventional XPS setup. In *Chapter 5* it was used a more direct approach by performing an *in situ* NEXAFS study at 1 bar. This study demonstrated that Co^{2+} species can be preserved on the $CoVO_x$ surface at temperature and pressure relevant to the catalytic tests. As a conclusion of this thesis, V is proposed as an ideal promoter of cobalt catalyst for COPrOx following a rational approach for catalyst development targeting to form, stabilize and maintain the Co^{2+} phase on the surface of the catalyst under COPrOx conditions.

6.2 **Perspectives**

In this thesis the optimum oxidation state of cobalt for a maximum COPrOx reaction activity has been identified. This state is the octahedral Co^{2+} phase in CoO oxide, which shows much better reactivity as compared to Co^{3+} in Co_3O_4. Evidence for this finding comes from *in situ* and *operando* studies and hopefully will give a conclusive answer to a debate maintained for years due to many contradicting results reported in the literature on this topic.[258,341] In line with most of the previous *in situ* surface sensitive studies, it was found that the surface of cobalt is dynamic and very sensitive to the reaction conditions. Several transformations in its oxidation state might occur during reaction and this can explain, at least partly, the controversy in the literature about this issue.

Although CoO phase is metastable and susceptible to further oxidation to Co_3O_4 during COPrOx testing, it can be stabilized in the presence of vanadium. This found to have an immediate effect on the performance of catalyst, in terms of stability with time and temperature. However, except from the addition of promoters on cobalt catalysts, there are other approaches that can be used to control the redox ability of cobalt NPs and avoid the oxidation of Co^{2+} to Co^{3+}.[206] One of them is to control the interaction between cobalt and the catalytic carrier (support). There are already literature reports that confirm the effect of the support to the redox ability of cobalt NPs.[88] In this thesis, unsupported cobalt particles have been used primarily to reveal the relationship between cobalt surface oxidation state and reactivity. This approach reduces the complexity of the catalyst and simplifies the interpretation of the experimental results, but unfortunately not without consequences in the catalytic tests. The major one is the low surface area and the fast agglomeration of the studied catalysts which limits their reactivity. However, most probably, the promoted CoO phase can be stabilized on a high surface area support and by carefully adjusting the interaction between Co atoms and support, high dispersion can be achieved. Further efforts can be devoted to search for a favorable catalytic support which can stabilize the active cobalt state for COPrOx reaction, maintaining at the same time a high surface area which is suitable for the applications.

The extraordinary performance of the CoVO*x* catalyst was ascribed to the stable octahedral Co^{2+} phase maintained during COPrOx reaction. This thesis demonstrates just the proof of concept for this catalyst. However, due to time limitations, the catalyst was not optimized. Evidently, further improvements of CoVOx catalyst's properties are possible, as for example an optimum loading of V and better distribution of V on cobalt. Moreover, octahedral Co^{2+} phase can exist in the bulk of various cobalt vanadates, by forming CoO_6 octahedrons coordinated to VOx unit.[357,359,381,382] However, the performance of different cobalt vanadates within octahedral Co^{2+} phase for CO oxidation in the absence and/or presence of H_2 has never been studied before. It is interesting to investigate the catalytic performance of these cobalt vanadates for COPrOx reaction, shedding light on the effect of electronic environment of Co^{2+}-O bond towards the CO oxidation reactivity.

Understanding of the reaction mechanism is known to be essential for catalysts design. In this thesis, based on a common conception in literature reports, it was assumed that the COPrOx reaction on cobalt follows a Mars–van Krevelen mechanism. However, more efforts

are required to clarify the COPrOx reaction mechanism on promoted and pure CoO catalysts. Some studies argue that the CO conversion is related to the concentration of OH^- groups.[19,383,384] In *Chapter 3*, the DFT, DRIFTs and XPS results converge to the fact that more OH^- groups are formed on reduced cobalt surfaces, suggesting that the OH^- groups are involved into the reaction mechanism. Thus, it is necessary to clarify if the reaction mechanism of CoO for COPrOx is following the traditional Mars–van Krevelen mechanism ($CO + O_2$) alone, or also combined with an OH^- involving mechanism ($CO + OH^-$), or even if the OH^- involving mechanism can be dominant in some cases. To do this, one can combine the *in situ* XPS and operando DRIFTs experiments to further study the water dissociation mechanism on CoO surface and build the correlation between concentration of OH^- groups and CO conversion. Another possibility could be to perform isotopic labeling experiments using for example ^{18}O isotopes[385]

Last but not least, although a new active phase of cobalt for COPrOx is discovered in this thesis, the temperature for 100% CO conversion is still too high as compared to noble metal catalysts and CuO_x-CeO_2 catalysts. The ideal catalyst should start working already at room temperature (RT) and have high activity and selectivity around 80–100 °C.[29] The main problem with high reaction temperatures in PrOx is the selectivity. Higher temperatures favor H_2 oxidation and methanation side reactions which cause an undesired consumption of H_2. Further work should be devoted to decrease the triggering temperature of the reaction by optimizing the reaction conditions and synthesis methods of the materials on the basis of the new findings of this thesis.

References

(1) Bion, N.; Epron, F.; Moreno, M.; Mariño, F.; Duprez, D. Preferential Oxidation of Carbon Monoxide in the Presence of Hydrogen (PROX) over Noble Metals and Transition Metal Oxides: Advantages and Drawbacks. *Top. Catal.* **2008**, *51* (1–4), 76–88.

(2) Xie, X.; Li, Y.; Liu, Z. Q.; Haruta, M.; Shen, W. Low-Temperature Oxidation of CO Catalysed by Co_3O_4 Nanorods. *Nature* **2009**, *458* (7239), 746–749.

(3) Khasu, M.; Nyathi, T.; Morgan, D. J.; Hutchings, G. J.; Claeys, M.; Fischer, N. Co3O4 Morphology in the Preferential Oxidation of CO. *Catal. Sci. Technol.* **2017**, *7* (20), 4806–4817.

(4) Ma, L.; Seo, C. Y.; Chen, X.; Sun, K.; Schwank, J. W. Indium-Doped Co3O4nanorods for Catalytic Oxidation of CO and C3H6towards Diesel Exhaust. *Appl. Catal. B Environ.* **2018**, *222* (September 2017), 44–58.

(5) Bao, T.; Zhao, Z.; Dai, Y.; Lin, X.; Jin, R.; Wang, G.; Muhammad, T. Supported Co_3O_4-CeO_2 Catalysts on Modified Activated Carbon for CO Preferential Oxidation in H_2-Rich Gases. *Appl. Catal. B Environ.* **2012**, *119–120*, 62–73.

(6) Lukashuk, L.; Föttinger, K.; Kolar, E.; Rameshan, C.; Teschner, D.; Hävecker, M.; Knop-Gericke, A.; Yigit, N.; Li, H.; McDermott, E.; et al. Operando XAS and NAP-XPS Studies of Preferential CO Oxidation on Co_3O_4 and CeO_2 -Co_3O_4 Catalysts. *J. Catal.* **2016**, *344*, 1–15.

(7) Teng, Y.; Sakurai, H.; Ueda, A.; Kobayashi, T. Oxidative Removal of Co Contained in Hydrogen by Using Metal Oxide Catalysts. *Int. J. Hydrogen Energy* **1999**, *24* (4), 355–358.

(8) An, K.; Alayoglu, S.; Musselwhite, N.; Plamthottam, S.; Melaet, G.; Lindeman, A. E.; Somorjai, G. A. Enhanced CO Oxidation Rates at the Interface of Mesoporous Oxides and Pt Nanoparticles. *J. Am. Chem. Soc.* **2013**, *135* (44), 16689–16696.

(9) Nguyen, L.; Zhang, S.; Yoon, S. J.; Tao, F. F. Preferential Oxidation of CO in H_2 on Pure Co_3O_{4-x} and Pt/Co_3O_{4-X}. *ChemCatChem* **2015**, *7* (15), 2346–2353.

(10) Guo, Q.; Liu, Y. MnOx Modified Co_3O_4-CeO_2 Catalysts for the Preferential Oxidation of CO in H_2-Rich Gases. *Appl. Catal. B Environ.* **2008**, *82* (1–2), 19–26.

(11) Gómez-Cuaspud, J. A.; Schmal, M. Nanostructured Metal Oxides Obtained by Means Polymerization-Combustion at Low Temperature for CO Selective Oxidation. *Int. J. Hydrogen Energy* **2013**, *38* (18), 7458–7468.

(12) Zhao, Z.; Bao, T.; Li, Y.; Min, X.; Zhao, D.; Muhammad, T. The Supported CeO_2/Co_3O_4-MnO_2/CeO_2 catalyst on Activated Carbon Prepared by a Successive-Loading

Approach with Superior Catalytic Activity and Selectivity for CO Preferential Oxidation in H_2-Rich Stream. *Catal. Commun.* **2014**, *48*, 24–28.

(13) Abbate, M.; Pen, H.; Czyzyk, M. T.; de Groot, F. M. F.; Fuggle, J. C.; Ma, Y. J.; Chen, C. T.; Sette, F.; Fujimori, A.; Ueda, Y.; et al. Soft X-Ray Absorption Spectroscopy of Vanadium Oxides. *J. Electron Spectros. Relat. Phenomena* **1993**, *62* (1–2), 185–195.

(14) Glaspell, G. P.; Jagodzinski, P. W.; Manivannan, A. Formation of Cobalt Nitrate Hydrate, Cobalt Oxide, and Cobalt Nanoparticles Using Laser Vaporization Controlled Condensation. *J. Phys. Chem. B* **2004**, *108* (28), 9604–9607.

(15) International Energy Agence. Data and statistics https://www.iea.org/data-and-statistics?country=WORLD&fuel=Energy Supply&indicator=TPESbySource.

(16) Bae, J.; Lee, S.; Kim, S.; Oh, J.; Choi, S.; Bae, M.; Kang, I.; Katikaneni, S. P. Liquid Fuel Processing for Hydrogen Production: A Review. *Int. J. Hydrogen Energy* **2016**, *41* (44), 19990–20022.

(17) Ghenciu, A. F. Review of Fuel Processing Catalysts for Hydrogen Production in PEM Fuel Cell Systems. *Curr. Opin. Solid State Mater. Sci.* **2002**, *6* (5), 389–399.

(18) Satyapal, S. Hydrogen and Fuel Cells Program Overview. In *US Department of Energy Annual Merit Review*; in Washington, D.C, 2018; p June 13-15.

(19) Jing, P.; Gong, X.; Liu, B.; Zhang, J. Recent Advances in Synergistic Effect Promoted Catalysts for Preferential Oxidation of Carbon Monoxide. *Catal. Sci. Technol.* **2020**, *10* (4), 919–934.

(20) Zhang, S.; Yuan, X.; Wang, H.; Mérida, W.; Zhu, H.; Shen, J.; Wu, S.; Zhang, J. A Review of Accelerated Stress Tests of MEA Durability in PEM Fuel Cells. *Int. J. Hydrogen Energy* **2009**, *34* (1), 388–404.

(21) Dawood, F.; Anda, M.; Shafiullah, G. M. Hydrogen Production for Energy: An Overview. *Int. J. Hydrogen Energy* **2020**, *45* (7), 3847–3869.

(22) Madej-Lachowska, M.; Kulawska, M.; Słoczyński, J. Methanol as a High Purity Hydrogen Source for Fuel Cells: A Brief Review of Catalysts and Rate Expressions. *Chem. Process Eng. - Inz. Chem. i Proces.* **2017**, *38* (1), 147–162.

(23) Baschuk, J. J.; Li, X. Carbon Monoxide Poisoning of Proton Exchange Membrane Fuel Cells. *Int. J. Energy Res.* **2001**, *25* (8), 695–713.

(24) Benesch, R.; Salman, S.; Jacksier, T. The Effect of Fuel and Oxidant Contaminants on the Performance of PEM Fuel Cells. In *In: WHEC 16*; Lyon, France, 2006.

(25) Besancon, B. M.; Hasanov, V.; Imbault-Lastapis, R.; Benesch, R.; Barrio, M.; Mølnvik, M. J. Hydrogen Quality from Decarbonized Fossil Fuels to Fuel Cells. *Int. J. Hydrogen Energy* **2009**, *34* (5), 2350–2360.

(26) Palmer, R. L.; Vroom, D. A. Mass-Spectrometric Measurements of Enhanced Methanation Activity over Cobalt and Nickel Foils. *J. Catal.* **1977**, *50* (2), 244–251.

(27) Trimm, D. L. Minimisation of Carbon Monoxide in a Hydrogen Stream for Fuel Cell Application. *Appl. Catal. A Gen.* **2005**, *296* (1), 1–11.

(28) Cao, L.; Liu, W.; Luo, Q.; Yin, R.; Wang, B.; Weissenrieder, J.; Soldemo, M.; Yan, H.; Lin, Y.; Sun, Z.; et al. Atomically Dispersed Iron Hydroxide Anchored on Pt for Preferential Oxidation of CO in H2. *Nature* **2019**, *565* (7741), 631–635.

(29) Mishra, A.; Prasad, R. A Review on Preferential Oxidation of Carbon Monoxide in Hydrogen Rich Gases. *Bull. Chem. React. Eng. Catal.* **2011**, *6* (1), 1–14.

(30) Bourane, A.; Bianchi, D. Oxidation of CO on a Pt/Al2O3 Catalyst: From the Surface Elementary Steps to Lighting-Off Tests: II. Kinetic Study of the Oxidation of Adsorbed CO Species Using Mass Spectroscopy. *J. Catal.* **2002**, *209* (1), 114–125.

(31) Gao, F.; Wang, Y.; Cai, Y.; Goodman, D. W. CO Oxidation on Pt-Group Metals from Ultrahigh Vacuum to Near Atmospheric Pressures. 2. Palladium and Platinum. *J. Phys. Chem. C* **2009**, *113* (1), 174–181.

(32) Gohn, G. Process for Selectively Removing Carbon Monoxide from H2-Containing Gases. 3216782, 1965.

(33) Vlastnik, V J, Armellini, F J, and Jordano, F. A. Carbon Monoxide Removal by Preferential Oxidation from Hydrogen-Rich Gas Streams, 1987.

(34) Son, I. H.; Shamsuzzoha, M.; Lane, A. M. Promotion of Pt/γ-Al2O3 by New Pretreatment for Low-Temperature Preferential Oxidation of CO in H2 for PEM Fuel Cells. *J. Catal.* **2002**, *210* (2), 460–465.

(35) Igarashi, H.; Uchida, H.; Suzuki, M.; Sasaki, Y.; Watanabe, M. Removal of Carbon Monoxide from Hydrogen-Rich Fuels by Selective Oxidation over Platinum Catalyst Supported on Zeolite. *Appl. Catal. A Gen.* **1997**, *159* (1), 159–169.

(36) Sebastian, V.; Irusta, S.; Mallada, R.; Santamaría, J. Selective Oxidation of CO in the Presence of H2, CO2 and H2O, on Different Zeolite-Supported Pt Catalysts. *Appl. Catal. A Gen.* **2009**, *366* (2), 242–251.

(37) Pozdnyakova, O.; Teschner, D.; Wootsch, A.; Krohnert, J.; Steinhauer, B.; Sauer, H.; Toth, L.; Jentoft, F. C.; Knop-Gericke, A.; Paal, Z.; et al. Preferential CO Oxidation in Hydrogen (PROX) on Ceria-Supported Catalysts, Part II: Oxidation States and Surface Species on Pd/CeO_2 under Reaction Conditions, Suggested Reaction Mechanism. *J. Catal.* **2006**, *237* (1), 17–28.

(38) Teschner, D.; Wootsch, A.; Pozdnyakova-Tellinger, O.; Kröhnert, J.; Vass, E. M.; Hävecker, M.; Zafeiratos, S.; Schnörch, P.; Jentoft, P. C.; Knop-Gericke, A.; et al. Partial Pressure Dependent in Situ Spectroscopic Study on the Preferential CO Oxidation in Hydrogen

(PROX) over Pt/Ceria Catalysts. *J. Catal.* **2007**, *249* (2).

(39) Avakyan, L. A.; Kolpacheva, N. A.; Paramonova, E. V.; Singh, J.; Hartfelder, U.; Van Bokhoven, J. A.; Bugaev, L. A. Evolution of the Atomic Structure of Ceria-Supported Platinum Nanocatalysts: Formation of Single Layer Platinum Oxide and Pt-O-Ce and Pt-Ce Linkages. *J. Phys. Chem. C* **2016**, *120* (49), 28057–28066.

(40) Liu, K.; Wang, A.; Zhang, T. Recent Advances in Preferential Oxidation of CO Reaction over Platinum Group Metal Catalysts. *ACS Catal.* **2012**, *2* (6), 1165–1178.

(41) Dey, S.; Dhal, G. C. Property and Structure of Various Platinum Catalysts for Low-Temperature Carbon Monoxide Oxidations. *Mater. Today Chem.* **2020**, *16*, 100228.

(42) Komatsu, T.; Tamura, A. Pt_3Co and PtCu Intermetallic Compounds: Promising Catalysts for Preferential Oxidation of CO in Excess Hydrogen. *J. Catal.* **2008**, *258* (2), 306–314.

(43) Nuñez, N. E.; Bideberripe, H. P.; Mizrahi, M.; Ramallo-López, J. M.; Casella, M. L.; Siri, G. J. CO Selective Oxidation Using Co-Promoted Pt/γ-Al_2O_3 catalysts. *Int. J. Hydrogen Energy* **2016**, *41* (42), 19005–19013.

(44) Papaefthimiou, V.; Dintzer, T.; Lebedeva, M.; Teschner, D.; Hävecker, M.; Knop-Gericke, A.; Schlögl, R.; Pierron-Bohnes, V.; Savinova, E.; Zafeiratos, S. Probing Metal-Support Interaction in Reactive Environments: An in Situ Study of PtCo Bimetallic Nanoparticles Supported on TiO2. *J. Phys. Chem. C* **2012**, *116* (27), 14342–14349.

(45) Ko, E.; Park, E. D.; Lee, H. C.; Lee, D.; Soonho Kim. Supported Pt–Co Catalysts for Selective CO Oxidation in a Hydrogen-Rich Stream. *Angew. Chemie - Int. Ed.* **2007**, *46* (5), 734–737.

(46) Kotobuki, M.; Watanabe, A.; Uchida, H.; Yamashita, H.; Watanabe, M. Reaction Mechanism of Preferential Oxidation of Carbon Monoxide on Pt, Fe, and Pt-Fe/Mordenite Catalysts. *J. Catal.* **2005**, *236* (2), 262–269.

(47) Li, H.; Yu, X.; Tu, S.-T.; Yan, J.; Wang, Z. Catalytic Performance and Characterization of Al_2O_3-Supported Pt–Co Catalyst Coatings for Preferential CO (1) Li, H.; Yu, X.; Tu, S.-T.; Yan, J.; Wang, Z. Catalytic Performance and Characterization of Al_2O_3-Supported Pt–Co Catalyst Coatings for Preferenti. *Appl. Catal. A Gen.* **2010**, *387* (1), 215–223.

(48) Wang, C.; Li, B.; Lin, H.; Yuan, Y. Carbon Nanotube-Supported Pt-Co Bimetallic Catalysts for Preferential Oxidation of CO in a H2-Rich Stream with CO2 and H2O Vapor. *J. Power Sources* **2012**, *202*, 200–208.

(49) Fu, Q.; Yao, Y. X.; Guo, X. G.; Wei, M. M.; Ning, Y. X.; Liu, H. Y.; Yang, F.; Liu, Z.; Bao, X. H. Reversible Structural Transformation of FeOx Nanostructures on Pt under Cycling Redox Conditions and Its Effect on Oxidation Catalysis. *Phys. Chem. Chem. Phys.* **2013**, *15* (35), 14708–14714.

(50) Environ, E. Energy & Environmental Science Highly Active Pt – Fe Bicomponent Catalysts for CO Oxidation in the Presence. **2012**, *2* (111), 6313–6320.

(51) Xie, X.; Li, Y.; Liu, Z. Q.; Haruta, M.; Shen, W. Low-Temperature Oxidation of CO Catalysed by Co_3O_4 Nanorods. *Nature* **2009**, *458*, 746–749.

(52) Haruta, M.; Yamada, N.; Kobayashi, T.; Iijima, S. Gold Catalysts Prepared by Coprecipitation for Low-Temperature Oxidation of Hydrogen and of Carbon Monoxide. *J. Catal.* **1989**, *115* (2), 301–309.

(53) Bauer, J. C.; Mullins, D.; Li, M.; Wu, Z.; Payzant, E. A.; Overbury, S. H.; Dai, S. Synthesis of Silica Supported AuCu Nanoparticle Catalysts and the Effects of Pretreatment Conditions for the CO Oxidation Reaction. *Phys. Chem. Chem. Phys.* **2011**, *13* (7), 2571–2581.

(54) Widmann, D.; Hocking, E.; Behm, R. J. On the Origin of the Selectivity in the Preferential CO Oxidation on Au/TiO_2 – Nature of the Active Oxygen Species for H2 Oxidation. *J. Catal.* **2014**, *317*, 272–276.

(55) Shodiya, T.; Schmidt, O.; Peng, W.; Hotz, N. Novel Nano-Scale Au/α-Fe_2O_3 Catalyst for the Preferential Oxidation of CO in Biofuel Reformate Gas. *J. Catal.* **2013**, *300*, 63–69.

(56) Khoudiakov, M.; Gupta, M. C.; Deevi, S. Au/Fe_2O_3 Nanocatalysts for CO Oxidation: A Comparative Study of Deposition–Precipitation and Coprecipitation Techniques. *Appl. Catal. A Gen.* **2005**, *291* (1), 151–161.

(57) Chang, L.-H.; Sasirekha, N.; Chen, Y.-W.; Wang, W.-J. Preferential Oxidation of CO in H2 Stream over $Au/MnO_2{-}CeO_2$ Catalysts. *Ind. Eng. Chem. Res.* **2006**, *45* (14), 4927–4935.

(58) Qiao, B.; Liu, J.; Wang, Y. G.; Lin, Q.; Liu, X.; Wang, A.; Li, J.; Zhang, T.; Liu, J. Highly Efficient Catalysis of Preferential Oxidation of CO in H2-Rich Stream by Gold Single-Atom Catalysts. *ACS Catal.* **2015**, *5* (11), 6249–6254.

(59) Qiu, Z.; Guo, X.; Mao, J.; Zhou, R. The Catalytic Performance of Isolated-Dispersed Au on Nanosized CeO_2 for CO Preferential Oxidation in H_2 -Rich Stream. *Appl. Surf. Sci.* **2019**, *481* (January), 1072–1079.

(60) Schubert, M. M.; Hackenberg, S.; van Veen, A. C.; Muhler, M.; Plzak, V.; Behm, R. J. CO Oxidation over Supported Gold Catalysts—"Inert" and "Active" Support Materials and Their Role for the Oxygen Supply during Reaction. *J. Catal.* **2001**, *197* (1), 113–122.

(61) Hernández, J. A.; Gómez, S. A.; Zepeda, T. A.; Fierro-González, J. C.; Fuentes, G. A. Insight into the Deactivation of Au/CeO_2 Catalysts Studied by In Situ Spectroscopy during the CO-PROX Reaction. *ACS Catal.* **2015**, *5* (7), 4003–4012.

(62) Okumura, M.; Masuyama, N.; Konishi, E.; Ichikawa, S.; Akita, T. CO Oxidation below Room Temperature over Ir/TiO_2 Catalyst Prepared by Deposition Precipitation Method. *J. Catal.* **2002**, *208* (2), 485–489.

(63) Iglesia, E.; Boudart, M. Structure-Sensitivity and Ensemble Effects in Reactions of

Strongly Adsorbed Intermediates: Catalytic Dehydrogenation and Dehydration of Formic Acid on Nickel. *J. Phys. Chem.* **1991**, *95* (18), 7011–7016.

(64) Somorjai, G. A. Modern Concepts in Surface Science and Heterogeneous Catalysis. *J. Phys. Chem.* **1990**, *94* (3), 1013–1023.

(65) Valden, M.; Pak, S.; Lai, X.; Goodman, D. W. Structure Sensitivity of CO Oxidation over Model Au/TiO_2 Catalysts. *Catal. Letters* **1998**, *56* (1), 7–10.

(66) Santos, V. P.; Carabineiro, S. A. C.; Tavares, P. B.; Pereira, M. F. R.; Órfão, J. J. M.; Figueiredo, J. L. Oxidation of CO, Ethanol and Toluene over TiO_2 Supported Noble Metal Catalysts. *Appl. Catal. B Environ.* **2010**, *99* (1–2), 198–205.

(67) Bamwenda, G. R.; Tsubota, S.; Nakamura, T.; Haruta, M. The Influence of the Preparation Methods on the Catalytic Activity of Platinum and Gold Supported on TiO_2 for CO Oxidation. *Catal. Letters* **1997**, *44* (1), 83–87.

(68) Bethke, G. K.; Kung, H. H. Selective CO Oxidation in a Hydrogen-Rich Stream over Au/γ-Al2O3 Catalysts. *Appl. Catal. A Gen.* **2000**, *194–195*, 43–53.

(69) Chen, M. S.; Goodman, D. W. The Structure of Catalytically Active Gold on Titania. *Science (80-.).* **2004**, *306* (5694), 252 LP – 255.

(70) Beck, A.; Yang, A. C.; Leland, A. R.; Riscoe, A. R.; Lopez, F. A.; Goodman, E. D.; Cargnello, M. Understanding the Preferential Oxidation of Carbon Monoxide (PrOx) Using Size-Controlled Au Nanocrystal Catalyst. *AIChE J.* **2018**, *64* (8), 3159–3167.

(71) Yao, S.; Mudiyanselage, K.; Xu, W.; Johnston-Peck, A. C.; Hanson, J. C.; Wu, T.; Stacchiola, D.; Rodriguez, J. A.; Zhao, H.; Beyer, K. A.; et al. Unraveling the Dynamic Nature of a CuO/CeO_2 catalyst for CO Oxidation in Operando: A Combined Study of XANES (Fluorescence) and Drifts. *ACS Catal.* **2014**, *4* (6), 1650–1661.

(72) Luo, J. Y.; Meng, M.; Zha, Y. Q.; Guo, L. H. Identification of the Active Sites for CO and C_3H_8 Total Oxidation over Nanostructured CuO-CeO_2 and Co_3O_4-CeO_2 Catalysts. *J. Phys. Chem. C* **2008**, *112* (23), 8694–8701.

(73) Gamarra, D.; Cámara, A. L.; Monte, M.; Rasmussen, S. B.; Chinchilla, L. E.; Hungría, A. B.; Munuera, G.; Gyorffy, N.; Schay, Z.; Corberán, V. C.; et al. Preferential Oxidation of CO in Excess H_2 over CuO/CeO_2 Catalysts: Characterization and Performance as a Function of the Exposed Face Present in the CeO_2 Support. *Appl. Catal. B Environ.* **2013**, *130–131*, 224–238.

(74) Gamarra, D.; Belver, C.; Fernández-García, M.; Martínez-Arias, A. Selective CO Oxidation in Excess H_2 over Copper-Ceria Catalysts: Identification of Active Entities/Species. *J. Am. Chem. Soc.* **2007**, *129* (40), 12064–12065.

(75) Gamarra, D.; Fernández-García, M.; Belver, C.; Martínez-Arias, A. Operando DRIFTS and XANES Study of Deactivating Effect of CO_2 on a $Ce_{0.8}Cu_{0.2}O_2$ CO-PROX

Catalyst. *J. Phys. Chem. C* **2010**, *114* (43), 18576–18582.

(76) Bazin, D.; Rehr, J. J. Comment on "Operando DRIFTS and XANES Study of Deactivating Effect of CO_2 on a $Ce_{0.8}Cu_{0.2}$ O_2 CO-PROX Catalyst." *J. Phys. Chem. C* **2011**, *115* (46), 23233–23236.

(77) Martínez-Arias, A.; Fernández-García, M. Reply to "Comment on 'Operando DRIFTS and XANES Study of Deactivating Effect of CO_2 on a $Ce_{0.8}$ $Cu_{0.2}$ O_2 CO-PROX Catalyst.'" *J. Phys. Chem. C* **2011**, *115* (46), 23237–23238.

(78) Li, D.; Liu, X.; Zhang, Q.; Wang, Y.; Wan, H. Cobalt and Copper Composite Oxides as Efficient Catalysts for Preferential Oxidation of CO in H2-Rich Stream. *Catal. Letters* **2009**, *127* (3–4), 377–385.

(79) Kang, M.; Song, M. W.; Lee, C. H. Catalytic Carbon Monoxide Oxidation over CoOx/CeO2composite Catalysts. *Appl. Catal. A Gen.* **2003**, *251* (1), 143–156.

(80) Zhao, Z.; Yung, M. M.; Ozkan, U. S. Effect of Support on the Preferential Oxidation of CO over Cobalt Catalysts. *Catal. Commun.* **2008**, *9* (6), 1465–1471.

(81) Zhao, Z.; Jin, R.; Bao, T.; Lin, X.; Wang, G. Mesoporous Ceria-Zirconia Supported Cobalt Oxide Catalysts for CO Preferential Oxidation Reaction in Excess H_2. *Appl. Catal. B Environ.* **2011**, *110*, 154–163.

(82) Zhao, Z.; Lin, X.; Jin, R.; Dai, Y.; Wang, G. High Catalytic Activity in CO PROX Reaction of Low Cobalt-Oxide Loading Catalysts Supported on Nano-Particulate CeO_2-ZrO_2 Oxides. *Catal. Commun.* **2011**, *12* (15), 1448–1451.

(83) Zhao, Z.; Lin, X.; Jin, R.; Wang, G.; Muhammad, T. MO x (M=Mn, Fe, Ni or Cr) Improved Supported Co_3O_4 Catalysts on Ceria-Zirconia Nanoparticulate for CO Preferential Oxidation in H_2-Rich Gases. *Appl. Catal. B Environ.* **2012**, *115–116*, 53–62.

(84) Guo, Q.; Wu, M.; Liu, Y.; Bai, X. Mesoporous CeO2-Supported Co_3O_4 Catalysts for CO Preferential Oxidation in H_2-Rich Gases. *Chinese J. Catal.* **2007**, *28* (11), 953–957.

(85) Woods, M. P.; Gawade, P.; Tan, B.; Ozkan, U. S. Preferential Oxidation of Carbon Monoxide on Co/CeO_2 Nanoparticles. *Appl. Catal. B Environ.* **2010**, *97* (1–2), 28–35.

(86) Grzybek, G.; Ciura, K.; Gryboś, J.; Indyka, P.; Davó-Quiñonero, A.; Lozano-Castelló, D.; Bueno-Lopez, A.; Kotarba, A.; Sojka, Z. CO-PROX Reaction over Co_3O_4 |Al_2O_3 Catalysts—Impact of the Spinel Active Phase Faceting on the Catalytic Performance . *J. Phys. Chem. C* **2019**, *123* (33), 20221–20232.

(87) Nyathi, T. M.; Fischer, N.; York, A. P. E.; Claeys, M. Effect of Crystallite Size on the Performance and Phase Transformation of Co_3O_4 /Al_2O_3 Catalysts during CO-PrOx – an in Situ Study. *Faraday Discuss.* **2017**, *197*, 269–285.

(88) Nyathi, T. M.; Fischer, N.; York, A. P. E.; Morgan, D. J.; Hutchings, G. J.; Gibson, E. K.; Wells, P. P.; Catlow, C. R. A.; Claeys, M. Impact of Nanoparticle–Support Interactions in

Co_3O_4 /Al_2O_3 Catalysts for the Preferential Oxidation of Carbon Monoxide . *ACS Catal.* **2019**, *9* (8), 7166–7178.

(89) Gamba, O.; Moreno, S.; Molina, R. Catalytic Performance of Ni-Pr Supported on Delaminated Clay in the Dry Reforming of Methane. *Int. J. Hydrogen Energy* **2011**, *36* (2), 1540–1550.

(90) Rasmussen, P. B.; Holmblad, P. M.; Askgaard, T.; Ovesen, C. V; Stoltze, P.; Nørskov, J. K.; Chorkendorff, I. Methanol Synthesis on Cu(100) from a Binary Gas Mixture of CO_2 and H2. *Catal. Letters* **1994**, *26* (3), 373–381.

(91) Chorkendorff, I.; Taylor, P. A.; Rasmussen, P. B. SYNTHESIS AND HYDROGENATION OF FORMATE ON CU(100) AT HIGH-PRESSURES. *J. Vac. Sci. Technol. a-Vacuum Surfaces Film.* **1992**, *10* (4), 2277–2281.

(92) Szanyi, J.; Goodman, D. W. Methanol Synthesis on a Cu(100) Catalyst. *Catal. Letters* **1991**, *10* (5), 383–390.

(93) Eren, B.; Weatherup, R. S.; Liakakos, N.; Somorjai, G. A.; Salmeron, M. Dissociative Carbon Dioxide Adsorption and Morphological Changes on Cu(100) and Cu(111) at Ambient Pressures. *J. Am. Chem. Soc.* **2016**, *138* (26), 8207–8211.

(94) Posada-Borbon, A.; Hagman, B.; Schaefer, A.; Zhang, C.; Shipilin, M.; Hellman, A.; Gustafson, J.; Gronbeck, H.; Posada-Borbón, A.; Hagman, B.; et al. Initial Oxidation of Cu(100) Studied by X-Ray Photo-Electron Spectroscopy and Density Functional Theory Calculations. *Surf. Sci.* **2018**, *675*, 64–69.

(95) Hagman, B.; Posada-Borbón, A.; Schaefer, A.; Shipilin, M.; Zhang, C.; Merte, L. R.; Hellman, A.; Lundgren, E.; Grönbeck, H.; Gustafson, J. Steps Control the Dissociation of CO_2 on Cu(100). *J. Am. Chem. Soc.* **2018**, *140* (40), 12974–12979.

(96) Koitaya, T.; Yamamoto, S.; Shiozawa, Y.; Takeuchi, K.; Liu, R.-Y.; Mukai, K.; Yoshimoto, S.; Akikubo, K.; Matsuda, I.; Yoshinobu, J. Real-Time Observation of Reaction Processes of CO_2 on Cu(997) by Ambient-Pressure X-Ray Photoelectron Spectroscopy. *Top. Catal.* **2016**, *59* (5–7), 526–531.

(97) Ren, Y.; Yuan, K.; Zhou, X.; Sun, H.; Wu, K.; Bernasek, S. L.; Chen, W.; Xu, G. Q. Catalytic Intermediates of CO_2 Hydrogenation on Cu(111) Probed by In Operando Near-Ambient Pressure Technique. *Chem. - A Eur. J.* **2018**, *24* (60), 16097–16103.

(98) Regoutz, A.; Kerherve, G.; Villar-Garcia, I.; Williams, C. K.; Payne, D. J. The Influence of Oxygen on the Surface Interaction between CO_2 and Copper Studied by Ambient Pressure X-Ray Photoelectron Spectroscopy. *Surf. Sci.* **2018**, *677*, 121–127.

(99) Li, C.; Zhang, P.; Wang, J.; Boscoboinik, J. A.; Zhou, G. Tuning the Deoxygenation of Bulk-Dissolved Oxygen in Copper. *J. Phys. Chem. C* **2018**, *122* (15), 8254–8261.

(100) Bluhm, H.; Hävecker, M.; Knop-Gericke, A.; Kleimenov, E.; Schlögl, R.; Teschner,

D.; Bukhtiyarov, V. I.; Ogletree, D. F.; Salmeron, M. Methanol Oxidation on a Copper Catalyst Investigated Using in Situ X-Ray Photoelectron Spectroscopy. *J. Phys. Chem. B* **2004**, *108* (38), 14340–14347.

(101) Favaro, M.; Xiao, H.; Cheng, T.; Goddard, W. A.; Yano, J.; Crumlin, E. J. Subsurface Oxide Plays a Critical Role in CO_2 Activation by Cu(111) Surfaces to Form Chemisorbed CO_2, the First Step in Reduction of CO_2. *Proc. Natl. Acad. Sci. U. S. A.* **2017**, *114* (26), 6706–6711.

(102) Lin, L. L.; Yao, S. Y.; Liu, Z. Y.; Zhang, F.; Li, N.; Vovchok, D.; Martinez-Arias, A.; Castaneda, R.; Lin, J. Y.; Senanayake, S. D.; et al. In Situ Characterization of Cu/CeO_2 Nanocatalysts for CO_2 Hydrogenation: Morphological Effects of Nanostructured Ceria on the Catalytic Activity. *J. Phys. Chem. C* **2018**, *122* (24), 12934–12943.

(103) Wang, J.; Gao, R.; Zhou, D.; Chen, Z.; Wu, Z.; Schumacher, G.; Hu, Z.; Liu, X. Boosting the Electrocatalytic Activity of Co_3O_4 Nanosheets for a Li-O2 Battery through Modulating Inner Oxygen Vacancy and Exterior Co^{3+}/Co^{2+} Ratio. *ACS Catal.* **2017**, *7* (10), 6533–6541.

(104) Deng, X. Y.; Verdaguer, A.; Herranz, T.; Weis, C.; Bluhm, H.; Salmeron, M. Surface Chemistry of Cu in the Presence of CO_2 and H2O. *Langmuir* **2008**, *24* (17), 9474–9478.

(105) Palomino, R. M.; Ramirez, P. J.; Liu, Z. Y.; Hamlyn, R.; Waluyo, I.; Mahapatra, M.; Orozco, I.; Hunt, A.; Simonovis, J. P.; Senanayake, S. D.; et al. Hydrogenation of CO_2 on ZnO/Cu(100) and ZnO/Cu(111) Catalysts: Role of Copper Structure and Metal-Oxide Interface in Methanol Synthesis. *J. Phys. Chem. B* **2018**, *122* (2), 794–800.

(106) Yang, Y.; Mei, D.; Peden, C. H. F.; Campbell, C. T.; Mims, C. A. Surface-Bound Intermediates in Low-Temperature Methanol Synthesis on Copper: Participants and Spectators. *ACS Catal.* **2015**, *5* (12), 7328–7337.

(107) Trotochaud, L.; Head, A. R.; Pletincx, S.; Karslıoğlu, O.; Yu, Y.; Waldner, A.; Kyhl, L.; Hauffman, T.; Terryn, H.; Eichhorn, B.; et al. Water Adsorption and Dissociation on Polycrystalline Copper Oxides: Effects of Environmental Contamination and Experimental Protocol. *J. Phys. Chem. B* **2018**, *122* (2), 1000–1008.

(108) Bozzini, B.; Amati, M.; Mele, C.; Knop-Gericke, A.; Vesselli, E. An in Situ Near-Ambient Pressure X-Ray Photoelectron Spectroscopy Study of CO_2 Reduction at Cu in a SOE Cell. *J. Electroanal. Chem.* **2017**, *799*, 17–25.

(109) Graciani, J.; Mudiyanselage, K.; Xu, F.; Baber, A. E.; Evans, J.; Senanayake, S. D.; Stacchiola, D. J.; Liu, P.; Hrbek, J.; Sanz, J. F.; et al. Highly Active Copper-Ceria and Copper-Ceria-Titania Catalysts for Methanol Synthesis from CO_2. *Science (80-.).* **2014**, *345* (6196), 546 LP – 550.

(110) Senanayake, S. D.; Ramírez, P. J.; Waluyo, I.; Kundu, S.; Mudiyanselage, K.; Liu, Z.; Liu, Z.; Axnanda, S.; Stacchiola, D. J.; Evans, J.; et al. Hydrogenation of CO_2 to Methanol on CeOx/Cu(111) and ZnO/Cu(111) Catalysts: Role of the Metal-Oxide Interface and Importance

of Ce3+Sites. *J. Phys. Chem. C* **2016**, *120* (3), 1778–1784.

(111) Vesselli, E.; De Rogatis, L.; Ding, X.; Baraldi, A.; Savio, L.; Vattuone, L.; Rocca, M.; Fornasiero, P.; Peressi, M.; Baldereschi, A.; et al. Carbon Dioxide Hydrogenation on Ni(110). *J. Am. Chem. Soc.* **2008**, *130* (34), 11417–11422.

(112) Freund, H.-J.; Roberts, M. W. Surface Chemistry of Carbon Dioxide. *Surf. Sci. Rep.* **1996**, *25* (8), 225–273.

(113) Heine, C.; Lechner, B. A. J.; Bluhm, H.; Salmeron, M. Recycling of CO_2: Probing the Chemical State of the Ni(111) Surface during the Methanation Reaction with Ambient-Pressure X-Ray Photoelectron Spectroscopy. *J. Am. Chem. Soc.* **2016**, *138* (40), 13246–13252.

(114) Bi, Q.; Huang, X.; Yin, G.; Chen, T.; Du, X.; Cai, J.; Xu, J.; Liu, Z.; Han, Y.; Huang, F. Cooperative Catalysis of Nickel and Nickel Oxide for Efficient Reduction of CO_2 to CH_4. *ChemCatChem* **2019**, *11* (4), 1295–1302.

(115) Ralston, W. T.; An, K.; Brooks, C.; Li, C.; Ye, Y.; Liu, Y.; Zhu, J.; Guo, J.; Alayoglu, S.; Somorjai, G. A. High-Performance Hybrid Oxide Catalyst of Manganese and Cobalt for Low-Pressure Methanol Synthesis. **2015**, 1–5.

(116) Liu, Q.; Han, Y.; Cai, J.; Crumlin, E. J.; Li, Y. M.; Liu, Z. CO_2 Activation on Cobalt Surface in the Presence of H_2O: An Ambient-Pressure X-Ray Photoelectron Spectroscopy Study. *Catal. Letters* **2018**, *148* (6), 1686–1691.

(117) Liu, L.; Puga, A. V.; Cored, J.; Concepción, P.; Pérez-Dieste, V.; García, H.; Corma, A. Sunlight-Assisted Hydrogenation of CO_2 into Ethanol and C^{2+} Hydrocarbons by Sodium-Promoted Co@C Nanocomposites. *Appl. Catal. B Environ.* **2018**, *235*, 186–196.

(118) Genovese, C.; Schuster, M. E.; Gibson, E. K.; Gianolio, D.; Posligua, V.; Grau-Crespo, R.; Cibin, G.; Wells, P. P.; Garai, D.; Solokha, V.; et al. Operando Spectroscopy Study of the Carbon Dioxide Electro-Reduction by Iron Species on Nitrogen-Doped Carbon. *Nat. Commun.* **2018**, *9* (1), 935.

(119) Mohandas, J. C.; Gnanamani, M. K.; Jacobs, G.; Ma, W.; Ji, Y.; Khalid, S.; Davis, B. H. Fischer À Tropsch Synthesis : Characterization and Reaction Testing of Cobalt Carbide. **2011**, 1581–1588.

(120) Li, J. F.; Cheng, X. F.; Zhang, C. H.; Chang, Q.; Wang, J.; Wang, X. P.; Lv, Z. G.; Dong, W. S.; Yang, Y.; Li, Y. W. Effect of Alkalis on Iron-Based Fischer-Tropsch Synthesis Catalysts: Alkali-FeOx Interaction, Reduction, and Catalytic Performance. *Appl. Catal. a-General* **2016**, *528*, 131–141.

(121) Jahangiri, H.; Bennett, J.; Mahjoubi, P.; Wilson, K.; Gu, S. A Review of Advanced Catalyst Development for Fischer-Tropsch Synthesis of Hydrocarbons from Biomass Derived Syn-Gas. *Catal. Sci. Technol.* **2014**, *4* (8), 2210–2229.

(122) Wang, Z.; Yan, Z.; Liu, C.; Goodman, D. W. Surface Science Studies on Cobalt Fischer-Tropsch Catalysts. *ChemCatChem* **2011**, *3* (3), 551–559.

(123) Argyle, M.; Bartholomew, C. Heterogeneous Catalyst Deactivation and Regeneration: A Review. *Catalysts* **2015**, *5* (1), 145–269.

(124) Wu, C. H.; Eren, B.; Bluhm, H.; Salmeron, M. B. Ambient-Pressure X-Ray Photoelectron Spectroscopy Study of Cobalt Foil Model Catalyst under CO, H-2, and Their Mixtures. *ACS Catal.* **2017**, *7* (2), 1150–1157.

(125) Melaet, G.; Ralston, W. T.; Li, C.-S.; Alayoglu, S.; An, K.; Musselwhite, N.; Kalkan, B.; Somorjai, G. A. Evidence of Highly Active Cobalt Oxide Catalyst for the Fischer–Tropsch Synthesis and CO $_2$ Hydrogenation. *J. Am. Chem. Soc.* **2014**, *136* (6), 2260–2263.

(126) de Smit, E.; van Schooneveld, M. M.; Cinquini, F.; Bluhm, H.; Sautet, P.; de Groot, F. M. F.; Weckhuysen, B. M. On the Surface Chemistry of Iron Oxides in Reactive Gas Atmospheres. *Angew. Chemie Int. Ed.* **2011**, *50* (7), 1584–1588.

(127) Zhou, X.; Mannie, G. J. A.; Yin, J.; Yu, X.; Weststrate, C. J.; Wen, X.; Wu, K.; Yang, Y.; Li, Y.; Niemantsverdriet, J. W. Iron Carbidization on Thin-Film Silica and Silicon: A Near-Ambient-Pressure X-Ray Photoelectron Spectroscopy and Scanning Tunneling Microscopy Study. *ACS Catal.* **2018**, *8* (8), 7326–7333.

(128) Behrens, M.; Studt, F.; Kasatkin, I.; Kuhl, S.; Havecker, M.; Abild-Pedersen, F.; Zander, S.; Girgsdies, F.; Kurr, P.; Kniep, B.-L.; et al. The Active Site of Methanol Synthesis over Cu/ZnO/Al_2O_3 Industrial Catalysts. *Science (80-.).* **2012**, *336* (6083), 893–897.

(129) Rodriguez, A.; Grinter, D. C.; Liu, Z.; Palomino, R. M. Ceria-Based Model Catalysts : Fundamental Studies on the Importance of the Metal – Ceria Interface in CO. **2017**, 1824–1841.

(130) Royer, S.; Duprez, D. Catalytic Oxidation of Carbon Monoxide over Transition Metal Oxides. *ChemCatChem* **2011**, *3* (1), 24–65.

(131) van Spronsen, M. A.; Frenken, J. W. M.; Groot, I. M. N. Surface Science under Reaction Conditions: CO Oxidation on Pt and Pd Model Catalysts. *Chem. Soc. Rev.* **2017**, *46* (14), 4347–4374.

(132) Svintsitskiy, D. A.; Kardash, T. Y.; Stonkus, O. A.; Slavinskaya, E. M.; Stadnichenko, A. I.; Koscheev, S. V; Chupakhin, A. P.; Boronin, A. I. In Situ XRD, XPS, TEM, and TPR Study of Highly Active in CO Oxidation CuO Nanopowders. *J. Phys. Chem. C* **2013**, *117* (28), 14588–14599.

(133) Eren, B.; Heine, C.; Bluhm, H.; Somorjai, G. A.; Salmeron, M. Catalyst Chemical State during CO Oxidation Reaction on Cu(111) Studied with Ambient-Pressure X-Ray Photoelectron Spectroscopy and Near Edge X-Ray Adsorption Fine Structure Spectroscopy. *J. Am. Chem. Soc.* **2015**, *137* (34), 11186–11190.

(134) Eren, B.; Lichtenstein, L.; Wu, C. H.; Bluhm, H.; Somorjai, G. A.; Salmeron, M. Reaction of CO with Preadsorbed Oxygen on Low-Index Copper Surfaces: An Ambient Pressure X-Ray Photoelectron Spectroscopy and Scanning Tunneling Microscopy Study. *J. Phys. Chem. C* **2015**, *119* (26), 14669–14674.

(135) Jiang, P.; Prendergast, D.; Borondics, F.; Porsgaard, S.; Giovanetti, L.; Pach, E.; Newberg, J.; Bluhm, H.; Besenbacher, F.; Salmeron, M. Experimental and Theoretical Investigation of the Electronic Structure of Cu_2O and CuO Thin Films on Cu(110) Using x-Ray Photoelectron and Absorption Spectroscopy. *J. Chem. Phys.* **2013**, *138* (2), 024704.

(136) Mudiyanselage, K.; Senanayake, S. D.; Feria, L.; Kundu, S.; Baber, A. E.; Graciani, J.; Vidal, A. B.; Agnoli, S.; Evans, J.; Chang, R.; et al. Importance of the Metal-Oxide Interface in Catalysis: In Situ Studies of the Water-Gas Shift Reaction by Ambient-Pressure X-Ray Photoelectron Spectroscopy. *Angew. Chemie Int. Ed.* **2013**, *52* (19), 5101–5105.

(137) Baber, A. E.; Yang, X.; Kim, H. Y.; Mudiyanselage, K.; Soldemo, M.; Weissenrieder, J.; Senanayake, S. D.; Al-mahboob, A.; Sadowski, J. T.; Evans, J.; et al. Angewandte Stabilization of Catalytically Active Cu + Surface Sites on Titanium – Copper Mixed-Oxide Films . **2014**, *10007*, 5336–5340.

(138) Elias, J. S.; Stoerzinger, K. A.; Hong, W. T.; Risch, M.; Giordano, L.; Mansour, A. N.; Shao-Horn, Y. In Situ Spectroscopy and Mechanistic Insights into CO Oxidation on Transition-Metal-Substituted Ceria Nanoparticles. *ACS Catal.* **2017**, *7* (10), 6843–6857.

(139) Tang, Y.; Ma, L.; Dou, J.; Andolina, C. M.; Li, Y.; Ma, H.; House, S. D.; Zhang, X.; Yang, J.; Tao, F. Transition of Surface Phase of Cobalt Oxide during CO Oxidation. *Phys. Chem. Chem. Phys.* **2018**, *20* (9), 6440–6449.

(140) Lukashuk, L.; Yigit, N.; Kolar, E.; Teschner, D.; Rupprechter, G. Operando Insights into CO Oxidation on Cobalt Oxide Catalysts By. **2018**.

(141) Jain, R.; Reddy, K. P.; Ghosalya, M. K.; Gopinath, C. S. Water Mediated Deactivation of Co3O4 Nanorods Catalyst for CO Oxidation and Resumption of Activity at and above 373 K: Electronic Structural Aspects by NAPPES. *J. Phys. Chem. C.* **2017**, *121* (37), 20296–20305.

(142) Zhu, M.; Rocha, T. C. R.; Lunkenbein, T.; Knop-Gericke, A.; Schlögl, R.; Wachs, I. E. Promotion Mechanisms of Iron Oxide-Based High Temperature Water-Gas Shift Catalysts by Chromium and Copper. *ACS Catal.* **2016**, *6*, 4455–4464.

(143) Keturakis, C. J.; Zhu, M.; Gibson, E. K.; Daturi, M.; Tao, F.; Frenkel, A. I.; Wachs, I. E. Dynamics of CrO_3–Fe_2O_3 Catalysts during the High-Temperature Water-Gas Shift Reaction: Molecular Structures and Reactivity. *ACS Catal.* **2016**, *6* (7), 4786–4798.

(144) Zhang, S. R.; Shan, J. J.; Nie, L. H.; Nguyen, L.; Wu, Z. L.; Tao, F. In Situ Studies of Surface of $NiFe_2O_4$ Catalyst during Complete Oxidation of Methane. *Surf. Sci.* **2016**, *648*, 156–162.

(145) Wolfbeisser, A.; Klötzer, B.; Mayr, L.; Rameshan, R.; Zemlyanov, D.; Bernardi, J.;

Föttinger, K.; Rupprechter, G. Surface Modification Processes during Methane Decomposition on Cu-Promoted Ni-ZrO_2 catalysts. *Catal. Sci. Technol.* **2015**, *5* (2), 967–978.

(146) Dou, J.; Tang, Y.; Nie, L. H.; Andolina, C. M.; Zhang, X. Y.; House, S.; Li, Y. T.; Yang, J.; Tao, F. F. Complete Oxidation of Methane on Co_3O_4/CeO_2 Nanocomposite: A Synergic Effect. *Catal. Today* **2018**, *311*, 48–55.

(147) Zhang, F.; Liu, Z.; Zhang, S.; Akter, N.; Palomino, R. M.; Vovchok, D.; Orozco, I.; Salazar, D.; Rodriguez, J. A.; Llorca, J.; et al. In Situ Elucidation of the Active State of Co–CeO_x Catalysts in the Dry Reforming of Methane: The Important Role of the Reducible Oxide Support and Interactions with Cobalt. *ACS Catal.* **2018**, *8* (4), 3550–3560.

(148) Piccinin, S.; Zafeiratos, S.; Stampfl, C.; Hansen, T. W.; Hävecker, M.; Teschner, D.; Bukhtiyarov, V. I.; Girgsdies, F.; Knop-Gericke, A.; Schlögl, R.; et al. Alloy Catalyst in a Reactive Environment: The Example of Ag-Cu Particles for Ethylene Epoxidation. *Phys. Rev. Lett.* **2010**, *104* (3).

(149) Bukhtiyarov, V. I.; Nizovskii, A. I.; Bluhm, H.; Hävecker, M.; Kleimenov, E.; Knop-Gericke, A.; Schlögl, R. Combined in Situ XPS and PTRMS Study of Ethylene Epoxidation over Silver. *J. Catal.* **2006**, *238* (2), 260–269.

(150) Jones, T. E.; Wyrwich, R.; Böcklein, S.; Carbonio, E. A.; Greiner, M. T.; Klyushin, A. Y.; Moritz, W.; Locatelli, A.; Menteş, T. O.; Niño, M. A.; et al. The Selective Species in Ethylene Epoxidation on Silver. *ACS Catal.* **2018**, *8* (5), 3844–3852.

(151) Greiner, M. T.; Jones, T. E.; Beeg, S.; Zwiener, L.; Scherzer, M.; Girgsdies, F.; Piccinin, S.; Armbrüster, M.; Knop-Gericke, A.; Schlögl, R. Free-Atom-like d States in Single-Atom Alloy Catalysts. *Nat. Chem.* **2018**, *10* (10), 1008–1015.

(152) Greiner, M. T.; Cao, J.; Jones, T. E.; Beeg, S.; Skorupska, K.; Carbonio, E. A.; Sezen, H.; Amati, M.; Gregoratti, L.; Willinger, M.-G. G.; et al. Phase Coexistence of Multiple Copper Oxides on AgCu Catalysts during Ethylene Epoxidation. *ACS Catal.* **2018**, *8* (3), 2286–2295.

(153) Greiner, M. T.; Jones, T. E.; Klyushin, A.; Knop-Gericke, A.; Schlogl, R.; Schlögl, R. Ethylene Epoxidation at the Phase Transition of Copper Oxides. *J. Am. Chem. Soc.* **2017**, *139* (34), 11825–11832.

(154) Greiner, M. T.; Jones, T. E.; Johnson, B. E.; Rocha, T. C. R.; Wang, Z. J.; Armbrüster, M.; Willinger, M.; Knop-Gericke, A.; Schlögl, R. The Oxidation of Copper Catalysts during Ethylene Epoxidation. *Phys. Chem. Chem. Phys.* **2015**, *17* (38), 25073–25089.

(155) Schedel-Niedrig, T.; Neisius, T.; Böttger, I.; Kitzelmann, E.; Weinberg, G.; Demuth, D.; Schlögl, R. Copper (Sub)Oxide Formation: A Surface Sensitive Characterization of Model Catalysts. *Phys. Chem. Chem. Phys.* **2000**, *2* (10), 2407–2417.

(156) Vozniuk, O.; Agnoli, S.; Artiglia, L.; Vassoi, A.; Tanchoux, N.; Di Renzo, F.; Granozzi, G.; Cavani, F. Towards an Improved Process for Hydrogen Production: The

Chemical-Loop Reforming of Ethanol. *Green Chem.* **2016**, *18* (4), 1038–1050.

(157) Bukhtiyarov, V. I.; Prosvirin, I. P.; Tikhomirov, E. P.; Kaichev, V. V; Sorokin, A. M.; Evstigneev, V. V. In Situ Study of Selective Oxidation of Methanol to Formaldehyde over Copper. *React. Kinet. Catal. Lett.* **2003**, *79* (1), 181–188.

(158) Yusuf, A.; Snape, C.; He, J.; Xu, H.; Liu, C.; Zhao, M.; Chen, G. Z.; Tang, B.; Wang, C.; Wang, J.; et al. Advances on Transition Metal Oxides Catalysts for Formaldehyde Oxidation : A Review Advances on Transition Metal Oxides Catalysts For. *Catal. Rev.* **2017**, *59* (3), 189–233.

(159) Prosvirin, I. P.; Tikhomirov, E. P.; Sorokin, A. M.; Kaichev, V. V; Bukhtiyarov, V. I. In Situ Study of the Selective Oxidation of Methanol to Formaldehyde on Copper. *Kinet. Catal.* **2003**, *44* (5), 662–668.

(160) Eren, B.; Kersell, H.; Weatherup, R. S.; Heine, C.; Crumlin, E. J.; Friend, C. M.; Salmeron, M. B. Structure of the Clean and Oxygen-Covered Cu(100) Surface at Room Temperature in the Presence of Methanol Vapor in the 10–200 MTorr Pressure Range. *J. Phys. Chem. B* **2018**, *122* (2), 548–554.

(161) Zafeiratos, S.; Dintzer, T.; Teschner, D.; Blume, R.; Hävecker, M.; Knop-Gericke, A.; Schlögl, R. Methanol Oxidation over Model Cobalt Catalysts: Influence of the Cobalt Oxidation State on the Reactivity. *J. Catal.* **2010**, *269* (2).

(162) Friedrich, M.; Teschner, D.; Knop-Gericke, A.; Armbruster, M. Surface and Subsurface Dynamics of the Intermetallic Compound ZnNi in Methanol Steam Reforming. *J. Phys. Chem. C* **2012**, *116* (28), 14930–14935.

(163) Kugai, J.; Subramani, V.; Song, C. S.; Engelhard, M. H.; Chin, Y. H. Effects of Nanocrystalline CeO2 Supports on the Properties and Performance of Ni-Rh Bimetallic Catalyst for Oxidative Steam Reforming of Ethanol. *J. Catal.* **2006**, *238* (2), 430–440.

(164) Turczyniak, S.; Luo, W.; Papaefthimiou, V.; Ramgir, N. S.; Haevecker, M.; Machocki, A.; Zafeiratos, S. A Comparative Ambient Pressure X-Ray Photoelectron and Absorption Spectroscopy Study of Various Cobalt-Based Catalysts in Reactive Atmospheres. *Top. Catal.* **2016**, *59* (5–7), 532–542.

(165) Turczyniak, S.; Teschner, D.; Machocki, A.; Zafeiratos, S. Effect of the Surface State on the Catalytic Performance of a Co/CeO_2 Ethanol Steam-Reforming Catalyst. *J. Catal.* **2016**, *340*, 321–330.

(166) Ovari, L.; Calderon, S. K.; Lykhach, Y.; Libuda, J.; Erdohelyi, A.; Papp, C.; Kiss, J.; Steinruck, H. P. Near Ambient Pressure XPS Investigation of the Interaction of Ethanol with Co/CeO_2(111). *J. Catal.* **2013**, *307*, 132–139.

(167) Sohn, H.; Celik, G.; Gunduz, S.; Dogu, D.; Zhang, S.; Shan, J.; Tao, F. F.; Ozkan, U. S. Oxygen Mobility in Pre-Reduced Nano- and Macro-Ceria with Co Loading: An AP-XPS, In-Situ DRIFTS and TPR Study. *Catal. Letters* **2017**, *147* (11), 2863–2876.

(168) Sohn, H.; Soykal, I. I.; Zhang, S.; Shan, J.; Tao, F.; Miller, J. T.; Ozkan, U. S. Effect of Cobalt on Reduction Characteristics of Ceria under Ethanol Steam Reforming Conditions: AP-XPS and XANES Studies. *J. Phys. Chem. C* **2016**, *120* (27), 14631–14642.

(169) Casanovas, A.; Marini, C.; Prat, J.; Llorca, J.; Escudero, C. Unraveling the Chemical State of Cobalt in Co-Based Catalysts during Ethanol Steam Reforming : An in Situ Study by Near Ambient Pressure XPS and XANES. **2018**.

(170) Shi, Z.; Yang, H.; Gao, P.; Li, X.; Zhong, L.; Wang, H.; Liu, H.; Wei, W.; Sun, Y. Direct Conversion of CO_2 to Long-Chain Hydrocarbon Fuels over Kâ€ " promoted $CoCu/TiO_2$ Catalysts. *Catal. Today* **2018**, *311*, 65–73.

(171) A. Bharathan, V.; Jain, R.; Gopinath, C. S.; Vinod, C. P. Diverse Reactivity Trends of Ni Surfaces in Au@Ni Core–Shell Nanoparticles Probed by near Ambient Pressure (NAP) XPS. *Catal. Sci. Technol.* **2017**, *7* (19), 4489–4498.

(172) Papaefthimiou, V.; Tournus, F.; Hillion, A.; Khadra, G.; Teschner, D.; Knop-Gericke, A.; Dupuis, V.; Zafeiratos, S. Mixing Patterns and Redox Properties of Iron-Based Alloy Nanoparticles under Oxidation and Reduction Conditions. *Chem. Mater.* **2014**, *26* (4).

(173) Wu, C. H.; Liu, C.; Su, D.; Xin, H. L.; Fang, H.-T.; Eren, B.; Zhang, S.; Murray, C. B.; Salmeron, M. B. Bimetallic Synergy in Cobalt–Palladium Nanocatalysts for CO Oxidation. *Nat. Catal.* **2019**, *2* (1), 78–85.

(174) Zhong, J.-Q.; Zhou, X.; Yuan, K.; Wright, C. A.; Tadich, A.; Qi, D.; Li, H. X.; Wu, K.; Xu, G. Q.; Chen, W. Probing the Effect of the Pt–Ni–Pt(111) Bimetallic Surface Electronic Structures on the Ammonia Decomposition Reaction. *Nanoscale* **2017**, *9* (2), 666–672.

(175) Zafeiratos, S.; Paloukis, F.; Papakonstantinou, G.; Teschner, D.; Havecker, M.; Vass, E.; Schnorch, P.; Knop-Gericke, A.; Schlogl, R.; Moreno, B.; et al. A Comparative in Situ XPS Study of PtRuCo Catalyst in Methanol Steam Reforming and Water Gas Shift Reactions. *Catal. Today* **2010**, *157* (1–4), 250–256.

(176) Alayoglu, S.; Beaumont, S. K.; Zheng, F.; Pushkarev, V. V; Zheng, H. M.; Iablokov, V.; Liu, Z.; Guo, J. H.; Kruse, N.; Somorjai, G. A. CO2 Hydrogenation Studies on Co and CoPt Bimetallic Nanoparticles Under Reaction Conditions Using TEM, XPS and NEXAFS. *Top. Catal.* **2011**, *54* (13–15), 778–785.

(177) Papaefthimiou, V.; Dintzer, T.; Dupuis, V.; Tamion, A.; Tournus, F.; Teschner, D.; Hävecker, M.; Knop-Gericke, A.; Schlögl, R.; Zafeiratos, S. When a Metastable Oxide Stabilizes at the Nanoscale: Wurtzite CoO Formation upon Dealloying of PtCo Nanoparticles. *J. Phys. Chem. Lett.* **2011**, *2* (8), 900–904.

(178) Luo, W.; Baaziz, W.; Cao, Q.; Ba, H.; Baati, R.; Ersen, O.; Pham-Huu, C.; Zafeiratos, S. Design and Fabrication of Highly Reducible PtCo Particles Supported on Graphene-Coated ZnO. *ACS Appl. Mater. Interfaces* **2017**, *9* (39), 34256–34268.

(179) Sapi, A.; Halasi, G.; Kiss, J.; Dobo, D. G.; Juhasz, K. L.; Kolcsar, V. J.; Ferencz, Z.;

Vari, G.; Matolin, V.; Erdohelyi, A.; et al. In Situ DRIFTS and NAP-XPS Exploration of the Complexity of CO_2 Hydrogenation over Size-Controlled Pt Nanoparticles Supported on Mesoporous NiO. *J. Phys. Chem. C* **2018**, *122* (10), 5553–5565.

(180) Kattel, S.; Yu, W.; Yang, X.; Yan, B.; Huang, Y.; Wan, W.; Liu, P.; Chen, J. G. Supported Catalysts Hot Paper CO_2 Hydrogenation over Oxide-Supported PtCo Catalysts : The Role of the Oxide Support in Determining the Product Selectivity Angewandte. **2016**, *116023*, 7968–7973.

(181) Zeng, S.; Nguyen, L.; Cheng, F.; Liu, L.; Yu, Y.; Feng, F. Applied Surface Science Surface Structure and Chemistry of Pt / Cu / Pt (1 1 1) near Surface Alloy Model Catalyst in CO. *Appl. Surf. Sci.* **2014**, *320*, 225–230.

(182) Zafeiratos, S.; Piccinin, S.; Teschner, D. Alloys in Catalysis: Phase Separation and Surface Segregation Phenomena in Response to the Reactive Environment. *Catal. Sci. Technol.* **2012**, *2* (9).

(183) Doh, W. H.; Papaefthimiou, V.; Dintzer, T.; Dupuis, V.; Zafeiratos, S. Synchrotron Radiation X-Ray Photoelectron Spectroscopy as a Tool to Resolve the Dimensions of Spherical Core/Shell Nanoparticles. *J. Phys. Chem. C* **2014**, *118* (46), 26621–26628.

(184) Weckhuysen, B. M.; De Smit, E.; De Groot, F. M. F.; Blume, R.; Hävecker, M.; Knop-Gericke, A. The Role of Cu on the Reduction Behavior and Surface Properties of Fe-Based Fischer-Tropsch Catalysts. *Phys. Chem. Chem. Phys.* **2010**, *12* (3), 667–680.

(185) Carenco, S.; Wu, C. H.; Shavorskiy, A.; Alayoglu, S.; Somorjai, G. A.; Bluhm, H.; Salmeron, M. Synthesis and Structural Evolution of Nickel-Cobalt Nanoparticles Under H-2 and CO2. *Small* **2015**, *11* (25), 3045–3053.

(186) Carenco, S.; Bonifacio, C. S.; Yang, J. C. Ensemble versus Local Restructuring of Core-Shell Nickel–Cobalt Nanoparticles upon Oxidation and Reduction Cycles. *Chem. - A Eur. J.* **2018**, *24* (46), 12037–12043.

(187) Wolfbeisser, A.; Kovács, G.; Kozlov, S. M.; Föttinger, K.; Bernardi, J.; Klötzer, B.; Neyman, K. M.; Rupprechter, G. Surface Composition Changes of CuNi-ZrO_2 during Methane Decomposition: An Operando NAP-XPS and Density Functional Study. *Catal. Today* **2017**, *283*, 134–143.

(188) Beaumont, S. K.; Alayoglu, S.; Pushkarev, V. V.; Liu, Z.; Kruse, N.; Somorjai, G. A. Exploring Surface Science and Restructuring in Reactive Atmospheres of Colloidally Prepared Bimetallic CuNi and CuCo Nanoparticles on SiO_2 in Situ Using Ambient Pressure X-Ray Photoelectron Spectroscopy. *Faraday Discussions*. 2013, pp 31–44.

(189) Pielsticker, L.; Zegkinoglou, I.; Divins, N. J.; Mistry, H.; Chen, Y. T.; Kostka, A.; Boscoboinik, J. A.; Cuenya, B. R. Segregation Phenomena in Size-Selected Bimetallic CuNi Nanoparticle Catalysts. *J. Phys. Chem. B* **2018**, *122* (2), 919–926.

(190) Luo, J.; Monai, M.; Wang, C.; Lee, J. D.; Duchon, T.; Dvorak, F.; Matolin, V.; Murray,

C. B.; Fornasiero, P.; Gorte, R. J. Unraveling the Surface State and Composition of Highly Selective Nanocrystalline Ni-Cu Alloy Catalysts for Hydrodeoxygenation of HMF. *Catal. Sci. Technol.* **2017**, *7* (8), 1735–1743.

(191) Alayoglu, S.; Beaumont, S. K.; Melaet, G.; Lindeman, A. E.; Musselwhite, N.; Brooks, C. J.; Marcus, M. A.; Guo, J. G.; Liu, Z.; Kruse, N.; et al. Surface Composition Changes of Redox Stabilized Bimetallic CoCu Nanoparticles Supported on Silica under H-2 and O-2 Atmospheres and During Reaction between CO_2 and H_2: In Situ X-Ray Spectroscopic Characterization. *J. Phys. Chem. C* **2013**, *117* (42), 21803–21809.

(192) Ralston, W. T.; Liu, W. C.; Alayoglu, S.; Melaet, G. Bimetallic Cobalt Nanoparticles (Co–M): Synthesis, Characterization, and Application in the Fischer–Tropsch Process. *Top. Catal.* **2018**, *61* (9–11), 1002–1015.

(193) Eren, B.; Torres, D.; Karslıoğlu, O.; Liu, Z.; Wu, C. H.; Stacchiola, D.; Bluhm, H.; Somorjai, G. A.; Salmeron, M. Structure of Copper–Cobalt Surface Alloys in Equilibrium with Carbon Monoxide Gas. *J. Am. Chem. Soc.* **2018**, *140* (21), 6575–6581.

(194) Carenco, S.; Wu, C. H.; Shavorskiy, A.; Alayoglu, S.; Somorjai, G. A.; Bluhm, H.; Salmeron, M. Synthesis and Structural Evolution of Nickel-Cobalt Nanoparticles under H_2 and CO_2. *Small* **2015**, *11* (25), 3045–3053.

(195) Law, Y. T.; Dintzer, T.; Zafeiratos, S. Surface Oxidation of NiCo Alloy: A Comparative X-Ray Photoelectron Spectroscopy Study in a Wide Pressure Range. *Appl. Surf. Sci.* **2011**, *258* (4), 1480–1487.

(196) Papaefthimiou, V.; Dintzer, T.; Dupuis, V.; Tamion, A.; Tournus, F.; Hillion, A.; Teschner, D.; Hävecker, M.; Knop-Gericke, A.; Schlögl, R.; et al. Nontrivial Redox Behavior of Nanosized Cobalt: New Insights from Ambient Pressure X-Ray Photoelectron and Absorption Spectroscopies. *ACS Nano* **2011**, *5* (3).

(197) Wang, J. B.; Tsai, D. H.; Huang, T. J. Synergistic Catalysis of Carbon Monoxide Oxidation over Copper Oxide Supported on Samaria-Doped Ceria. *J. Catal.* **2002**, *208* (2), 370–380.

(198) Lee, H. C.; Kim, D. H. Kinetics of CO and H_2 Oxidation over CuO-CeO_2 Catalyst in H2 Mixtures with CO_2 and H_2O. *Catal. Today* **2008**, *132* (1), 109–116.

(199) Nyathi, T. M.; Fischer, N.; York, A. P. E.; Claeys, M. Environment-Dependent Catalytic Performance and Phase Stability of Co 3 O 4 in the Preferential Oxidation of Carbon Monoxide Studied In Situ . *ACS Catal.* **2020**, 11892–11911.

(200) Lukashuk, L.; Yigit, N.; Li, H.; Bernardi, J.; Föttinger, K.; Rupprechter, G. Operando XAS and NAP-XPS Investigation of CO Oxidation on Meso- and Nanoscale CoO Catalysts. *Catal. Today* **2019**, *336* (December 2018), 139–147.

(201) Michel, L.; Sall, S.; Dintzer, T.; Robert, C.; Demange, A.; Caps, V. Graphene-Supported 2D Cobalt Oxides for Catalytic Applications. *Faraday Discuss.* **2019**, *xx*

(xx), Accepted Manuscript.

(202) Yanazawa, H.; Ohshika, K.; Matsuzawa, T. Precision Evaluation in Kr Adsorption for Small BET Surface Area Measurements of Less than 1 M2. *Adsorption* **2000**, *6* (1), 73–77.

(203) Jauncey, G. E. The Scattering of X-Rays and Bragg's Law. *Proc. Natl. Acad. Sci. U. S. A.* **1924**, *10* (2), 57–60.

(204) Monshi, A.; Foroughi, M. R.; Monshi, M. R. Modified Scherrer Equation to Estimate More Accurately Nano-Crystallite Size Using XRD. *World J. Nano Sci. Eng.* **2012**, *02* (03), 154–160.

(205) Sun, B. B.; Wang, Y. B.; Wen, J.; Yang, H.; Sui, M. L.; Wang, J. Q.; Ma, E. Artifacts Induced in Metallic Glasses during TEM Sample Preparation. *Scr. Mater.* **2005**, *53* (7), 805–809.

(206) Luo, W. Tuning the Redox Properties of Cobalt Particles Supported on Oxides by an In-between Graphene Layer Modification, University of strasbourg, 2016.

(207) Hueso, J. L.; Martinez-Martinez, D.; Caballero, A.; Gonzalez-Elipe, A. R.; Mun, B. S.; Salmeron, M. Near-Ambient X-Ray Photoemission Spectroscopy and Kinetic Approach to the Mechanism of Carbon Monoxide Oxidation over Lanthanum Substituted Cobaltites. *Catal. Commun.* **2009**, *10* (14), 1898–1902.

(208) Trotochaud, L.; Head, A. R.; Karslıoğlu, O.; Kyhl, L.; Bluhm, H. Ambient Pressure Photoelectron Spectroscopy: Practical Considerations and Experimental Frontiers. *J. Phys. Condens. Matter* **2017**, *29* (5), 053002.

(209) Hayek, K.; Ribeiro, F. H.; Curtin, T.; Aszalos-Kiss, B.; Zemlyanov, D.; Knop-Gericke, A.; Kleimenov, E.; Zafeiratos, S.; Gabasch, H.; Han, J.; et al. In Situ XPS Study of Pd(111) Oxidation at Elevated Pressure, Part 2: Palladium Oxidation in the 10−1 Mbar Range. *Surf. Sci.* **2006**, *600* (15), 2980–2989.

(210) Zemlyanov, D.; Aszalos-Kiss, B.; Kleimenov, E.; Teschner, D.; Zafeiratos, S.; Hävecker, M.; Knop-Gericke, A.; Schlögl, R.; Gabasch, H.; Unterberger, W.; et al. In Situ XPS Study of Pd(111) Oxidation. Part 1: 2D Oxide Formation in 10−3mbar O_2. *Surf. Sci.* **2006**, *600* (5), 983–994.

(211) Teschner, D.; Pestryakov, A.; Kleimenov, E.; Hävecker, M.; Bluhm, H.; Sauer, H.; Knop-Gericke, A.; Schlögl., R. High-Pressure X-Ray Photoelectron Spectroscopy of Palladium Model Hydrogenation Catalysts. Part 2: Hydrogenation of Trans-2-Pentene on Palladium. *J. Catal.* **2005**, *230* (1), 195–203.

(212) Bluhm, H.; Ogletree, D. F.; Fadley, C. S.; Hussain, Z.; Salmeron, M. The Premelting of Ice Studied with Photoelectron Spectroscopy. *J. Phys. Condens. Matter* **2002**, *14* (8), L227–L233.

(213) Zhang, X. Q.; Ptasinska, S. High-Pressure-Induced Pseudo-Oxidation of Copper

Surfaces by Carbon Monoxide. *ChemCatChem* **2016**, *8* (9), 1632–1635.

(214) Fox, E. B.; Velu, S.; Engelhard, M. H.; Chin, Y. H.; Miller, J. T.; Kropf, J.; Song, C. S. Characterization of CeO_2-Supported Cu-Pd Bimetallic Catalyst for the Oxygen-Assisted Water-Gas Shift Reaction. *J. Catal.* **2008**, *260* (2), 358–370.

(215) Hong, Y. C.; Zhang, S. R.; Tao, F. F.; Wang, Y. Stabilization of Iron-Based Catalysts against Oxidation: An In Situ Ambient-Pressure X-Ray Photoelectron Spectroscopy (AP-XPS) Study. *ACS Catal.* **2017**, *7* (5), 3639–3643.

(216) Rodriguez-Gomez, A.; Holgado, J. P.; Caballero, A. Cobalt Carbide Identified as Catalytic Site for the Dehydrogenation of Ethanol to Acetaldehyde. *ACS Catal.* **2017**, *7* (8), 5243–5247.

(217) Zhang, C.; Grass, M. E.; Yu, Y.; Gaskell, K. J.; DeCaluwe, S. C.; Chang, R.; Jackson, G. S.; Hussain, Z.; Bluhm, H.; Eichhorn, B. W.; et al. Multielement Activity Mapping and Potential Mapping in Solid Oxide Electrochemical Cells through the Use of *Operando* XPS. *ACS Catal.* **2012**, *2* (11), 2297–2304.

(218) Jugnet, Y.; Loffreda, D.; Dupont, C.; Delbecq, F.; Ehret, E.; Cadete Santos Aires, F. J.; Mun, B. S.; Aksoy Akgul, F.; Liu, Z. Promoter Effect of Early Stage Grown Surface Oxides: A Near-Ambient-Pressure XPS Study of CO Oxidation on PtSn Bimetallics. *J. Phys. Chem. Lett.* **2012**, *3* (24), 3707–3714.

(219) Lukashuk, L.; Foettinger, K. *In Situ* and *Operando* Spectroscopy: A Powerful Approach Towards Understanding Catalysts. *Johnson Matthey Technol. Rev.* **2018**, *62* (3), 316–331.

(220) Bañares, M. A. Operando Methodology: Combination of in Situ Spectroscopy and Simultaneous Activity Measurements under Catalytic Reaction Conditions. *Catal. Today* **2005**, *100* (1–2), 71–77.

(221) Lwin, S.; Diao, W.; Baroi, C.; Gaffney, A.; Fushimi, R. Characterization of MoVTeNbOx Catalysts during Oxidation Reactions Using In Situ/Operando Techniques: A Review. *Catalysts* **2017**, *7* (12), 109.

(222) Salmeron, M.; Schlögl, R. Ambient Pressure Photoelectron Spectroscopy: A New Tool for Surface Science and Nanotechnology. *Surface Science Reports*. 2008, pp 169–199.

(223) Arble, C.; Jia, M.; Newberg, J. T. Lab-Based Ambient Pressure X-Ray Photoelectron Spectroscopy from Past to Present. *Surf. Sci. Rep.* **2018**, *73* (2), 37–57.

(224) Klyushin, A. Y.; Rocha, T. C. R.; Havecker, M.; Knop-Gericke, A.; Schlogl, R. A near Ambient Pressure XPS Study of Au Oxidation. *Phys. Chem. Chem. Phys.* **2014**, *16* (17), 7881–7886.

(225) Blume, R.; Rosenthal, D.; Tessonnier, J.-P.; Li, H.; Knop-Gericke, A.; Schlögl, R. Characterizing Graphitic Carbon with X-Ray Photoelectron Spectroscopy: A Step-by-Step

Approach. *ChemCatChem* **2015**, *7* (18), 2871–2881.

(226) Rameshan, C.; Stadlmayr, W.; Weilach, C.; Penner, S.; Lorenz, H.; Hävecker, M.; Blume, R.; Rocha, T.; Teschner, D.; Knop-Gericke, A.; et al. Subsurface-Controlled CO2selectivity of PdZn near-Surface Alloys in H_2 generation by Methanol Steam Reforming. *Angew. Chemie - Int. Ed.* **2010**, *49* (18), 3224–3227.

(227) Lukashuk, L.; Yigit, N.; Rameshan, R.; Kolar, E.; Teschner, D.; Hävecker, M.; Knop-Gericke, A.; Schlögl, R.; Föttinger, K.; Rupprechter, G. Operando Insights into CO Oxidation on Cobalt Oxide Catalysts by NAP-XPS, FTIR, and XRD. *ACS Catal.* **2018**, *8* (9), 8630–8641.

(228) Doh, W. H.; Papaefthimiou, V.; Zafeiratos, S. *Applications of Synchrotron-Based X-Ray Photoelectron Spectroscopy in the Characterization of Nanomaterials*; 2015.

(229) Asplund, L.; Kelfve, P.; Siegbahn, H.; Goscinski, O.; Fellner-Feldegg, H.; Hamrin, K.; Blomster, B.; Siegbahn, K. Chemical Shifts of Auger Electron Lines and Electron Binding Energies in Free Molecules. Sulfur Compounds. *Chem. Phys. Lett.* **1976**, *40* (3), 353–356.

(230) Ogletree, D. F.; Bluhm, H.; Lebedev, G.; Fadley, C. S.; Hussain, Z.; Salmeron, M. A Differentially Pumped Electrostatic Lens System for Photoemission Studies in the Millibar Range. *Rev. Sci. Instrum.* **2002**, *73* (11), 3872–3877.

(231) Knop-Gericke, A.; Kleimenov, E.; Hävecker, M.; Blume, R.; Teschner, D.; Zafeiratos, S.; Schlögl, R.; Bukhtiyarov, V. I.; Kaichev, V. V.; Prosvirin, I. P.; et al. Chapter 4 X-Ray Photoelectron Spectroscopy for Investigation of Heterogeneous Catalytic Processes. *Adv. Catal.* **2009**, *52*, 213–272.

(232) Starr, D. E.; Liu, Z.; Hävecker, M.; Knop-Gericke, A.; Bluhm, H. Investigation of Solid/Vapor Interfaces Using Ambient Pressure X-Ray Photoelectron Spectroscopy. *Chem. Soc. Rev.* **2013**, *42* (13), 5833–5857.

(233) Knudsen, J.; Andersen, J. N.; Schnadt, J. A Versatile Instrument for Ambient Pressure X-Ray Photoelectron Spectroscopy: The Lund Cell Approach. *Surf. Sci.* **2016**, *646*, 160–169.

(234) Rameshan, C.; Weilach, C.; Stadlmayr, W.; Penner, S.; Lorenz, H.; Havecker, M.; Blume, R.; Rocha, T.; Teschner, D.; Knop-Gericke, A.; et al. Steam Reforming of Methanol on PdZn Near-Surface Alloys on Pd(111) and Pd Foil Studied by in-Situ XPS, LEIS and PM-IRAS. *J. Catal.* **2010**, *276* (1), 101–113.

(235) Price, R.; Eralp-Erden, T.; Crumlin, E.; Rani, S.; Garcia, S.; Smith, R.; Deacon, L.; Euaruksakul, C.; Held, G. The Partial Oxidation of Methane Over Pd/Al_2O_3 Catalyst Nanoparticles Studied In-Situ by Near Ambient-Pressure X-Ray Photoelectron Spectroscopy. *Top. Catal.* **2016**, *59* (5–7), 516–525.

(236) Friedrich, M.; Teschner, D.; Knop-Gericke, A.; Armbruster, M. Influence of Bulk Composition of the Intermetallic Compound ZnPd on Surface Composition and Methanol Steam Reforming Properties. *J. Catal.* **2012**, *285* (1), 41–47.

(237) Takagi, Y.; Uruga, T.; Tada, M.; Iwasawa, Y.; Yokoyama, T. Ambient Pressure Hard X-Ray Photoelectron Spectroscopy for Functional Material Systems as Fuel Cells under Working Conditions. *Acc. Chem. Res.* **2018**, *51* (3), 719–727.

(238) Roy, K.; Artiglia, L.; Bokhoven, J. A. Van. Ambient Pressure Photoelectron Spectroscopy : Opportunities in Catalysis from Solids to Liquids and Introducing Time Resolution. **2018**, 666–682.

(239) Weatherup, R. S.; Eren, B.; Hao, Y.; Bluhm, H.; Salmeron, M. B. Graphene Membranes for Atmospheric Pressure Photoelectron Spectroscopy. *J. Phys. Chem. Lett.* **2016**, *7* (9), 1622–1627.

(240) Weatherup, R. S. 2D Material Membranes for Operando Atmospheric Pressure Photoelectron Spectroscopy. *Top. Catal.* **2018**, *61* (20), 2085–2102.

(241) Bluhm, H. Photoelectron Spectroscopy of Surfaces under Humid Conditions. *J. Electron Spectros. Relat. Phenomena* **2010**, *177* (2–3), 71–84.

(242) Axnanda, S.; Scheele, M.; Crumlin, E.; Mao, B.; Chang, R.; Rani, S.; Faiz, M.; Wang, S.; Alivisatos, A. P.; Liu, Z. Direct Work Function Measurement by Gas Phase Photoelectron Spectroscopy and Its Application on PbS Nanoparticles. *Nano Lett.* **2013**, *13* (12), 6176–6182.

(243) Johansson, N.; Merte, L. R.; Grånäs, E.; Wendt, S.; Andersen, J. N.; Schnadt, J.; Knudsen, J. Oxidation of Ultrathin FeO(111) Grown on Pt(111): Spectroscopic Evidence for Hydroxylation. *Top. Catal.* **2016**, *59* (5–7), 506–515.

(244) Yu, Y.; Kim, D.; Lim, H.; Kim, G.; Koh, Y. E.; Kim, D.; Ueda, K.; Hiwasa, S.; Mase, K.; Bournel, F.; et al. ***Operando*** Study of Pd(100) Surface during CO Oxidation Using Ambient Pressure x-Ray Photoemission Spectroscopy. *AIP Adv.* **2019**, *9* (1), 015314.

(245) Liu, Z.; Duchoň, T.; Wang, H.; Grinter, D. C.; Waluyo, I.; Zhou, J.; Liu, Q.; Jeong, B.; Crumlin, E. J.; Matolín, V.; et al. Ambient Pressure XPS and IRRAS Investigation of Ethanol Steam Reforming on Ni–CeO_2 (111) Catalysts: An in Situ Study of C–C and O–H Bond Scission. *Phys. Chem. Chem. Phys.* **2016**, *18* (25), 16621–16628.

(246) https://www.specs-group.com/nc/specs/products/detail/devisim-nap/.

(247) https://www.helmholtz-berlin.de/pubbin/igama_output?modus=einzel&sprache=en&gid=1607.

(248) Https://Www.Helmholtz-Berlin.de/Pubbin/Igama_output?Modus=einzel&sprache=en&gid=1984&typoid=72494.

(249) Castán-Guerrero, C.; Krizmancic, D.; Bonanni, V.; Edla, R.; Deluisa, A.; Salvador, F.; Rossi, G.; Panaccione, G.; Torelli, P. A Reaction Cell for Ambient Pressure Soft X-Ray Absorption Spectroscopy. *Rev. Sci. Instrum.* **2018**, *89*, 054101.

(250) Cabrera-German, D.; Gomez-Sosa, G.; Herrera-Gomez, A. Accurate Peak Fitting and Subsequent Quantitative Composition Analysis of the Spectrum of Co 2p Obtained with Al Kα Radiation: I: Cobalt Spinel. *Surf. Interface Anal.* **2016**, *48* (5), 252–256.

(251) Yeh, J.-J. *Atomic Calculation of Photoionization Cross-Sections and Asymmetry Parameters*; 1993.

(252) Chen, Y.; Liu, D.; Yang, L.; Meng, M.; Zhang, J.; Zheng, L.; Chu, S.; Hu, T. Ternary Composite Oxide Catalysts CuO/Co_3O_4-CeO_2 with Wide Temperature-Window for the Preferential Oxidation of CO in H_2-Rich Stream. *Chem. Eng. J.* **2013**, *234*, 88–98.

(253) Cwele, T.; Mahadevaiah, N.; Singh, S.; Friedrich, H. B. Effect of Cu Additives on the Performance of a Cobalt Substituted Ceria ($Ce_{0.90}Co_{0.10}O_{2-\delta}$) Catalyst in Total and Preferential CO Oxidation. *Appl. Catal. B Environ.* **2016**, *182*, 1–14.

(254) Gómez, L. E.; Tiscornia, I. S.; Boix, A. V.; Miró, E. E. Co/ZrO_2 Catalysts Coated on Cordierite Monoliths for CO Preferential Oxidation. *Appl. Catal. A Gen.* **2011**, *401* (1–2), 124–133.

(255) Gómez, L. E.; Tiscornia, I. S.; Boix, A. V.; Miró, E. E. CO Preferential Oxidation on Cordierite Monoliths Coated with Co/CeO_2 Catalysts. *Int. J. Hydrogen Energy* **2012**, *37* (19), 14812–14819.

(256) Guo, Q.; Chen, S.; Liu, Y.; Wang, Y. Stability of Co-Ce-Mn Mixed-Oxide Catalysts for CO Preferential Oxidation in H2-Rich Gases. *Chem. Eng. J.* **2010**, *165* (3), 846–850.

(257) Peiretti, L. F.; NavascuÃ©s, N.; Tiscornia, I. S.; MirÃ^3, E. E. CeO_2 and Co_3O_4–CeO_2 Nanoparticles: Effect of the Synthesis Method on the Structure and Catalytic Properties in COPrOx and Methanation Reactions. *J. Mater. Sci.* **2016**, *51* (8), 3989–4001.

(258) Woods, M. P.; Gawade, P.; Tan, B.; Ozkan, U. S. Preferential Oxidation of Carbon Monoxide on Co/CeO2nanoparticles. *Appl. Catal. B Environ.* **2010**, *97* (1–2), 28–35.

(259) Gawade, P.; Bayram, B.; Alexander, A. C.; Ozkan, U. S. Applied Catalysis B : Environmental Preferential Oxidation of CO (PROX) over CoO x / CeO 2 in Hydrogen-Rich Streams : Effect of Cobalt Loading. *"Applied Catal. B, Environ.* **2012**, *128*, 21–30.

(260) Broqvist, P.; Panas, I.; Persson, H. A DFT Study on CO Oxidation over Co_3O_4. *J. Catal.* **2002**.

(261) Nagarajan, V.; Chandiramouli, R. A DFT Study on Adsorption Behaviour of CO on Co3O4nanostructures. *Appl. Surf. Sci.* **2016**, *385*, 113–121.

(262) Wang, H. F.; Kavanagh, R.; Guo, Y. L.; Guo, Y.; Lu, G.; Hu, P. Origin of Extraordinarily High Catalytic Activity of Co3O4and Its Morphological Chemistry for CO Oxidation at Low Temperature. *J. Catal.* **2012**, *296*, 110–119.

(263) Zhou, G.; Xie, H.; Gui, B.; Zhang, G.; Zheng, X. Influence of NiO on the Performance of CoO-Based Catalysts for the Selective Oxidation of CO in H_2-Rich Gas. *Catal. Commun.*

2012, *19*, 42–45.

(264) Petitto, S. C.; Marsh, E. M.; Carson, G. A.; Langell, M. A. Cobalt Oxide Surface Chemistry: The Interaction of CoO(1 0 0), Co_3O_4(1 1 0) and Co_3O_4(1 1 1) with Oxygen and Water. *J. Mol. Catal. A Chem.* **2008**, *281* (1–2), 49–58.

(265) Wang, X.; Liu, Y.; Zhang, T.; Luo, Y.; Lan, Z.; Zhang, K.; Zuo, J.; Jiang, L.; Wang, R. Geometrical-Site-Dependent Catalytic Activity of Ordered Mesoporous Co-Based Spinel for Benzene Oxidation: In Situ DRIFTS Study Coupled with Raman and XAFS Spectroscopy. *ACS Catal.* **2017**, *7* (3), 1626–1636.

(266) YUNG-FANG, Y. Y. The Oxidtaion of Hydrocarbons and CO over Metal Oxides III. Co_3O_4. *J. Catal.* **1973**, *33*, 108–122.

(267) Perkas, N.; Teo, J.; Shen, S.; Wang, Z.; Highfield, J.; Zhong, Z.; Gedanken, A. Supported Ru Catalysts Prepared by Two Sonication-Assisted Methods for Preferential Oxidation of CO in H_2. *Phys. Chem. Chem. Phys.* **2011**, *13*, 15690.

(268) Kok, E.; Scott, J.; Cant, N.; Trimm, D. The Impact of Ruthenium, Lanthanum and Activation Conditions on the Methanation Activity of Alumina-Supported Cobalt Catalysts. *Catal. Today* **2011**, *164* (1), 297–301.

(269) Gunasooriya, G. T. K. K.; van Bavel, A. P.; Kuipers, H. P. C. E.; Saeys, M. Key Role of Surface Hydroxyl Groups in C–O Activation during Fischer–Tropsch Synthesis. *ACS Catal.* **2016**, *6*, 3660–3664.

(270) Singh, S. A.; Mukherjee, S.; Madras, G. Role of CO2 Methanation into the Kinetics of Preferential CO Oxidation on Cu/Co3O4. *Mol. Catal.* **2019**, *466* (November 2018), 167–180.

(271) Ha, D. H.; Moreau, L. M.; Honrao, S.; Hennig, R. G.; Robinson, R. D. The Oxidation of Cobalt Nanoparticles into Kirkendall-Hollowed CoO and Co_3O_4: The Diffusion Mechanisms and Atomic Structural Transformations. *J. Phys. Chem. C* **2013**, *117* (27), 14303–14312.

(272) Xia, W.; Yang, Y.; Meng, Q.; Deng, Z.; Gong, M.; Wang, J.; Wang, D.; Zhu, Y.; Sun, L.; Xu, F.; et al. Bimetallic Nanoparticle Oxidation in Three Dimensions by Chemically Sensitive Electron Tomography and In-Situ Transmission Electron Microscopy. *ACS Nano* **2018**, *12* (8), 7866–7874.

(273) Wang, L.; Zhang, S.; Zhu, Y.; Patlolla, A.; Shan, J.; Yoshida, H.; Takeda, S.; Frenkel, A. I.; Tao, F. (Feng). Catalysis and In Situ Studies of Rh1/Co3O4 Nanorods in Reduction of NO with H2. *ACS Catal.* **2013**, *3* (5), 1011–1019.

(274) Powell, C. J.; Jablonski, A. Progress in Quantitative Surface Analysis by X-Ray Photoelectron Spectroscopy: Current Status and Perspectives. *J. Electron Spectros. Relat. Phenomena* **2010**, *178–179*, 331–346.

(275) *Inorganic Two-Dimensional Nanomaterials*; Wu, C., Ed.; Smart Materials Series; The

Royal Society of Chemistry, 2017.

(276) Luo, W.; Zafeiratos, S. CHAPTER 5 XPS Characterization of Metal-Free Functionalized Carbons. In *Metal-free Functionalized Carbons in Catalysis: Synthesis, Characterization and Applications*; The Royal Society of Chemistry, 2018; Vol. 2018-Janua, pp 138–176.

(277) Zhang, X. Q.; Chen, Y. S.; Kamat, P. V; Ptasinska, S. Probing Interfacial Electrochemistry on a Co3O4 Water Oxidation Catalyst Using Lab-Based Ambient Pressure X-Ray Photoelectron Spectroscopy. *J. Phys. Chem. C* **2018**, *122* (25), 13894–13901.

(278) Ralston, W. T.; Musselwhite, N.; Kennedy, G.; An, K.; Horowitz, Y.; Cordones, A. A.; Rude, B.; Ahmed, M.; Melaet, G.; Alayoglu, S. Soft X-Ray Spectroscopy Studies of Adsorption and Reaction of CO in the Presence of H_2 over 6 Nm MnO Nanoparticles Supported on Mesoporous Co3O4. *Surf. Sci.* **2016**, *648*, 14–22.

(279) Piccolo, L.; Daly, H.; Valcarcel, A.; Meunier, F. C. Promotional Effect of H2 on CO Oxidation over Au/TiO2 Studied by Operando Infrared Spectroscopy. *Appl. Catal. B Environ.* **2009**, *86*, 190–195.

(280) Chen, X.; Delgado, J. J.; Gatica, J. M.; Zerrad, S.; Cies, J. M.; Bernal, S. Preferential Oxidation of CO in the Presence of Excess of Hydrogen on Ru/Al2O3 Catalyst: Promoting Effect of Ceria–Terbia Mixed Oxide. *J. Catal.* **2013**, *299*, 272–283.

(281) Smith, M. L.; Kumar, N.; Spivey, J. J. CO Adsorption Behavior of Cu/SiO2 , Co/SiO2 , and CuCo/SiO2 Catalysts Studied by in Situ DRIFTS. *J. Phys. Chem. C* **2012**, *116*, 7931–7939.

(282) Jansson, J.; Palmqvist, A. E. C.; Fridell, E.; Skoglundh, M.; Österlund, L.; Thormählen, P.; Langer, V. On the Catalytic Activity of Co3O4 in Low-Temperature CO Oxidation. *J. Catal.* **2002**, *211* (2), 387–397.

(283) Jiang, M.; Koizumi, N.; Ozaki, T.; Yamada, M. Adsorption Properties of Cobalt and Cobalt-Manganese Catalysts Studied by in Situ Diffuse Reflectance FTIR Using CO and CO+H2as Probes. *Appl. Catal. A Gen.* **2001**, *209* (1–2), 59–70.

(284) Ji, L.; Lin, J.; Zeng, H. C. Metal−Support Interactions in Co/Al 2 O 3 Catalysts: A Comparative Study on Reactivity of Support. *J. Phys. Chem. B* **2000**, *104*, 1783–1790.

(285) Zhu, Y.; Li, H.; Koltypin, Y.; Gedanken, A. Preparation of Nanosized Cobalt Hydroxides and Oxyhydroxide Assisted by Sonication. **2002**, 729–733.

(286) Hadjiivanov, K. *Identification and Characterization of Surface Hydroxyl Groups by Infrared Spectroscopy*, 1st ed.; Elsevier Inc., 2014; Vol. 57.

(287) Parler, C. M.; Ritter, J. A.; Amiridis, M. D. Infrared Spectroscopic Study of Sol–Gel Derived Mixed-Metal Oxides. *J. Non. Cryst. Solids* **2001**, *279* (2), 119–125.

(288) Huang, J.; Qian, W.; Zhang, H.; Ying, W. In Situ Investigation on Co-Phase Evolution

and Its Performance for Fischer-Tropsch Synthesis over Nb-Promoted Cobalt Catalysts. *Catal. Sci. Technol.* **2017**, *7* (23), 5530–5539.

(289) Paredes-Nunez, A.; Lorito, D.; Guilhaume, N.; Mirodatos, C.; Schuurman, Y.; Meunier, F. C. Nature and Reactivity of the Surface Species Observed over a Supported Cobalt Catalyst under CO/H_2 Mixtures. *Catal. Today* **2015**, *242* (Part A), 178–183.

(290) Kwak, G.; Woo, M. H.; Kang, S. C.; Park, H.; Lee, Y.; Jun, K.; Ha, K. In Situ Monitoring during the Transition of Cobalt Carbide to Metal State and Its Application as Fischer – Tropsch Catalyst in Slurry Phase. *J. Catal.* **2013**, *307*, 27–36.

(291) Chagas, C. A.; de Souza, E. F.; de Carvalho, M. C. N. A.; Martins, R. L.; Schmal, M. Cobalt Ferrite Nanoparticles for the Preferential Oxidation of CO. *Appl. Catal. A Gen.* **2016**, *519*, 139–145.

(292) Ma, L.; Seo, C. Y.; Chen, X.; Sun, K.; Schwank, J. W. Indium-Doped Co_3O_4 Nanorods for Catalytic Oxidation of CO and C_3H_6 towards Diesel Exhaust. *Appl. Catal. B Environ.* **2018**, *222*, 44–58.

(293) Natile, M. M.; Glisenti, A. Study of Surface Reactivity of Cobalt Oxides: Interaction with Methanol. *Chem. Mater.* **2002**, *14* (7), 3090–3099.

(294) Chen, S.; Luo, L.; Jiang, Z.; Huang, W. Size-Dependent Reaction Pathways of Low-Temperature CO Oxidation on Au/CeO_2 Catalysts. *ACS Catal.* **2015**, *5* (3), 1653–1662.

(295) Tanaka, K.; Shou, M.; He, H.; Shi, X.; Zhang, X. Dynamic Characterization of the Intermediates for Low-Temperature PROX Reaction of CO in H_2 s Oxidation of CO with OH via HCOO Intermediate. **2009**, 12427–12433.

(296) Davó-Quiñonero, A.; Navlani-García, M.; Lozano-Castelló, D.; Bueno-López, A.; Anderson, J. A. Role of Hydroxyl Groups in the Preferential Oxidation of CO over Copper Oxide-Cerium Oxide Catalysts. *ACS Catal.* **2016**, *6* (3), 1723–1731.

(297) Schubert, M. .; Kahlich, M. .; Gasteiger, H. .; Behm, R. . Correlation between CO Surface Coverage and Selectivity/Kinetics for the Preferential CO Oxidation over $Pt/\gamma\text{-}Al_2O_3$ and $Au/\alpha\text{-}Fe_2O_3$: An in-Situ DRIFTS Study. *J. Power Sources* **1999**, *84*, 175–182.

(298) Turczyniak, S.; Teschner, D.; Machocki, A.; Zafeiratos, S. Effect of the Surface State on the Catalytic Performance of a Co/CeO_2: Ethanol Steam-Reforming Catalyst. *J. Catal.* **2016**, *340*.

(299) Miguel-García, I.; Navlani-García, M.; García-Aguilar, J.; Berenguer-Murcia, Á.; Lozano-Castelló, D.; Cazorla-Amorós, D. Capillary Microreactors Based on Hierarchical SiO_2 Monoliths Incorporating Noble Metal Nanoparticles for the Preferential Oxidation of CO. *Chem. Eng. J.* **2015**, *275*, 71–78.

(300) Zhang, Q.; Liu, X.; Fan, W.; Wang, Y. Manganese-Promoted Cobalt Oxide as Efficient and Stable Non-Noble Metal Catalyst for Preferential Oxidation of CO in H2stream.

Appl. Catal. B Environ. **2011**, *102* (1–2), 207–214.

(301) Zhao, Z.; Bao, T.; Zeng, Y.; Wang, G.; Muhammad, T. Efficient Cobalt-Manganese Oxide Catalyst Deposited on Modified AC with Unprecedented Catalytic Performance in CO Preferential Oxidation. *Catal. Commun.* **2013**, *32*, 47–51.

(302) Hernández, W. Y.; Centeno, M. A.; Romero-Sarria, F.; Ivanova, S.; Montes, M.; Odriozola, J. A. Modified Cryptomelane-Type Manganese Dioxide Nanomaterials for Preferential Oxidation of CO in the Presence of Hydrogen. *Catal. Today* **2010**, *157* (1–4), 160–165.

(303) Zhao, Z.; Jin, R.; Bao, T.; Yang, H.; Lin, X.; Wang, G. Mesoporous $Ce_xMn_{1-x}O_2$ Composites as Novel Alternative Carriers of Supported Co_3O_4 Catalysts for CO Preferential Oxidation in H_2 Stream. *Int. J. Hydrogen Energy* **2012**, *37* (6), 4774–4786.

(304) Gómez, L. E.; Boix, A. V.; Miró, E. E. Co/ZrO_2, Co/CeO_2 and MnCoCe Structured Catalysts for COPrOx. *Catal. Today* **2013**, *216*, 246–253.

(305) Zhao, Z.; Jin, R.; Li, Y.; Dai, Y.; Muhammad, T. Mesostructured Co-Ce-Zr-Mn-O Composite as a Potential Catalyst for Efficient Removal of Carbon Monoxide from Hydrogen-Rich Stream. *Catal. Sci. Technol.* **2013**, *3* (8), 2130–2139.

(306) Gómez, L. E.; Miró, E. E.; Boix, A. V. Spectroscopic Characterization of Mn-Co-Ce Mixed Oxides, Active Catalysts for COPROX Reaction. *Int. J. Hydrogen Energy* **2013**, *38* (14), 5645–5654.

(307) Le, M. T.; Nguyen, T. T.; Pham, P. T. M.; Bruneel, E.; Van Driessche, I. Activated MnO_2-Co_3O_4-CeO_2 Catalysts for the Treatment of CO at Room Temperature. *Appl. Catal. A Gen.* **2014**, *480*, 34–41.

(308) Park, J. E.; Park, E. D. Effects of Surface Area of Co-Mn-O Catalysts on the Selective CO Oxidation in H2. *Catal. Letters* **2014**, *144* (4), 607–614.

(309) Zhang, Q.; Liu, X.; Fan, W.; Wang, Y. Manganese-Promoted Cobalt Oxide as Efficient and Stable Non-Noble Metal Catalyst for Preferential Oxidation of CO in H_2 Stream. *Appl. Catal. B Environ.* **2011**, *102* (1–2), 207–214.

(310) Zhao, Z.; Li, Y.; Bao, T.; Wang, G.; Muhammad, T. Hierarchically Nanoporous Co-Mn-O/FeOx as a High Performance Catalyst for CO Preferential Oxidation in H_2-Rich Stream. *Catal. Commun.* **2014**, *46*, 28–31.

(311) Zhong, L.; Kropp, T.; Baaziz, W.; Ersen, O.; Teschner, D.; Schlögl, R.; Mavrikakis, M.; Zafeiratos, S.; Bazziz, W.; Ersen, O.; et al. Correlation Between Reactivity and Oxidation State of Cobalt Oxide Catalysts for CO Preferential Oxidation. *ACS Catal.* **2019**, *9* (9), 8325–8336.

(312) Frey, K.; Iablokov, V.; Sáfrán, G.; Osán, J.; Sajó, I.; Szukiewicz, R.; Chenakin, S.; Kruse, N. Nanostructured MnO_x as Highly Active Catalyst for CO Oxidation. *J. Catal.* **2012**,

287, 30–36.

(313) Ramesh, K.; Chen, L.; Chen, F.; Liu, Y.; Wang, Z.; Han, Y. F. Re-Investigating the CO Oxidation Mechanism over Unsupported MnO, Mn_2O_3 and MnO_2 Catalysts. *Catal. Today* **2008**, *131* (1–4), 477–482.

(314) Wang, L. C.; Liu, Q.; Huang, X. S.; Liu, Y. M.; Cao, Y.; Fan, K. N. Gold Nanoparticles Supported on Manganese Oxides for Low-Temperature CO Oxidation. *Appl. Catal. B Environ.* **2009**, *88* (1–2), 204–212.

(315) Bishnoi, A.; Kumar, S.; Joshi, N. Chapter 9 - Wide-Angle X-Ray Diffraction (WXRD): Technique for Characterization of Nanomaterials and Polymer Nanocomposites. In *Micro and Nano Technologies*; Thomas, S., Thomas, R., Zachariah, A. K., Mishra, R. K. B. T.-M. M. in N. C., Eds.; Elsevier, 2017; pp 313–337.

(316) Cheng, Q.; Tian, Y.; Lyu, S.; Zhao, N.; Ma, K.; Ding, T.; Jiang, Z.; Wang, L.; Zhang, J.; Zheng, L.; et al. Confined Small-Sized Cobalt Catalysts Stimulate Carbon-Chain Growth Reversely by Modifying ASF Law of Fischer–Tropsch Synthesis. *Nat. Commun.* **2018**, *9* (1).

(317) Ramesh, K.; Chen, L.; Chen, F.; Liu, Y.; Wang, Z.; Han, Y. F. Re-Investigating the CO Oxidation Mechanism over Unsupported MnO, Mn_2O_3 and MnO_2 Catalysts. *Catal. Today* **2008**, *131* (1–4), 477–482.

(318) Bulavchenko, O. A.; Gerasimov, E. Y.; Afonasenko, T. N. Reduction of Double Manganese-Cobalt Oxides:: In Situ XRD and TPR Study. *Dalt. Trans.* **2018**, *47* (47), 17153–17159.

(319) Feltes, T. E.; Espinosa-Alonso, L.; Smit, E. de; D'Souza, L.; Meyer, R. J.; Weckhuysen, B. M.; Regalbuto, J. R. Selective Adsorption of Manganese onto Cobalt for Optimized Mn/Co/TiO_2 Fischer-Tropsch Catalysts. *J. Catal.* **2010**, *270* (1), 95–102.

(320) Yang, R.; Xia, Z.; Zhao, Z.; Sun, F.; Du, X.; Yu, H.; Gu, S.; Zhong, L.; Zhao, J.; Ding, Y.; et al. Characterization of CoMn Catalyst by in Situ X-Ray Absorption Spectroscopy and Wavelet Analysis for Fischer–Tropsch to Olefins Reaction. *J. Energy Chem.* **2019**, *32*, 118–123.

(321) Han, W.; Dong, F.; Han, W.; Tang, Z. Fabrication of Homogeneous and Highly Dispersed CoMn Catalysts for Outstanding Low Temperature Catalytic Oxidation Performance. *New J. Chem.* **2019**, *43* (32), 12846–12857.

(322) Golikov, Y. V.; Tubin, S. Y.; Barkhatov, V. P.; Balakirev, V. F. Phase Diagrams of the CoMnO System in Air. *J. Phys. Chem. Solids* **1985**, *46* (5), 539–544.

(323) Rios, E.; Gautier, J. L.; Poillerat, G.; Chartier, P. Mixed Valency Spinel Oxides of Transition Metals and Electrocatalysis: Case of the $MnxCo_{3-X}O_4$ System. *Electrochim. Acta* **1998**, *44* (8–9), 1491–1497.

(324) Morales, F.; Grandjean, D.; Mens, A.; De Groot, F. M. F.; Weckhuysen, B. M. X-Ray

Absorption Spectroscopy of Mn/Co/TiO_2 Fischer-Tropsch Catalysts: Relationships between Preparation Method, Molecular Structure, and Catalyst Performance. *J. Phys. Chem. B* **2006**, *110* (17), 8626–8639.

(325) Mateos, J. M. J.; Morales, J.; Tirado, J. L. Cation-Deficient Mn, Co Spinel Oxides Obtained by Thermal Decomposition of Carbonate Precursors. *J. Solid State Chem.* **1989**, *82* (1), 87–94.

(326) Papaefthimiou, V.; Dintzer, T.; Dupuis, V.; Tamion, A.; Tournus, F.; Hillion, A.; Teschner, D.; Hävecker, M.; Knop-Gericke, A.; Schlögl, R.; et al. Nontrivial Redox Behavior of Nanosized Cobalt: New Insights from Ambient Pressure X-Ray Photoelectron and Absorption Spectroscopies. *ACS Nano* **2011**, *5* (3), 2182–2190.

(327) Long, X.; Yu, P.; Zhang, N.; Li, C.; Feng, X.; Ren, G.; Zheng, S.; Fu, J.; Cheng, F.; Liu, X. Direct Spectroscopy for Probing the Critical Role of Partial Covalency in Oxygen Reduction Reaction for Cobalt-Manganese Spinel Oxides. *Nanomaterials* **2019**, *9* (4), 577.

(328) Biesinger, M. C.; Payne, B. P.; Grosvenor, A. P.; Lau, L. W. M.; Gerson, A. R.; Smart, R. S. C. Resolving Surface Chemical States in XPS Analysis of First Row Transition Metals, Oxides and Hydroxides: Cr, Mn, Fe, Co and Ni. *Appl. Surf. Sci.* **2011**, *257* (7), 2717–2730.

(329) Di Castro, V.; Polzonetti, G. XPS Study of MnO Oxidation. *J. Electron Spectros. Relat. Phenomena* **1989**, *48* (1), 117–123.

(330) Nesbitt, H. W.; Banerjee, D. Interpretation of XPS Mn(2p) Spectra of Mn Oxyhydroxides and Constraints on the Mechanism of MnO_2 Precipitation. *Am. Mineral.* **1998**, *83* (3–4), 305–315.

(331) Qiao, R.; Chin, T.; Harris, S. J.; Yan, S.; Yang, W. Spectroscopic Fingerprints of Valence and Spin States in Manganese Oxides and Fluorides. *Curr. Appl. Phys.* **2013**, *13* (3), 544–548.

(332) Tanuma, S.; Powell, C. J.; Penn, D. R. Calculations of Electron Inelastic Mean Free Paths (IMFPS). IV. Evaluation of Calculated IMFPs and of the Predictive IMFP Formula TPP-2 for Electron Energies between 50 and 2000 EV. *Surf. Interface Anal.* **1993**, *20* (1), 77–89.

(333) Nakamura, I.; Haneda, M.; Hamada, H.; Fujitani, T. Direct Decomposition of Nitrogen Monoxide over a K-Deposited Co(0 0 0 1) Surface: Comparison to K-Doped Cobalt Oxide Catalysts. *J. Electron Spectros. Relat. Phenomena* **2006**, *150* (2–3), 150–154.

(334) Craciun, R.; Nentwick, B.; Hadjiivanov, K.; Knözinger, H. Structure and Redox Properties of MnOx/Yttrium-Stabilized Zirconia (YSZ) Catalyst and Its Used in CO and CH4 Oxidation. *Appl. Catal. A Gen.* **2003**, *243* (1), 67–79.

(335) Liu, J.; Jiang, L.; Zhang, B.; Jin, J.; Su, D. S.; Wang, S.; Sun, G. Controllable Synthesis of Cobalt Monoxide Nanoparticles and the Size-Dependent Activity for Oxygen Reduction Reaction. **2014**, 8–11.

(336) Khasu, M.; Nyathi, T.; Morgan, D. J.; Hutchings, G. J.; Claeys, M.; Fischer, N. Co_3O_4 Morphology in the Preferential Oxidation of CO. *Catal. Sci. Technol.* **2017**, *7* (20), 4806–4817.

(337) Zhou, Y.; Jin, C.; Li, Y.; Shen, W. Dynamic Behavior of Metal Nanoparticles for Catalysis. *Nano Today* **2018**, *20*, 101–120.

(338) Zheng, F.; Alayoglu, S.; Guo, J.; Pushkarev, V.; Li, Y.; Glans, P.-A.; Chen, J.; Somorjai, G. In-Situ X-Ray Absorption Study of Evolution of Oxidation States and Structure of Cobalt in Co and CoPt Bimetallic Nanoparticles (4 Nm) under Reducing (H_2) and Oxidizing (O2) Environments. *Nano Lett.* **2011**, *11* (2), 847–853.

(339) Wang, K.; Liu, B.; Cao, Y.; Li, Y.; Jia, D. V-Modified Co_3O_4 Nanorods with Superior Catalytic Activity and Thermostability for CO Oxidation. *CrystEngComm* **2018**, *20* (35), 5191–5199.

(340) Wang, T.; Ding, Y.; Xiong, J.; Yan, L.; Zhu, H.; Lu, Y.; Lin, L. Effect of Vanadium Promotion on Activated Carbon-Supported Cobalt Catalysts in Fischer-Tropsch Synthesis. *Catal. Letters* **2006**, *107* (1–2), 47–52.

(341) Bao, T.; Zhao, Z.; Dai, Y.; Lin, X.; Jin, R.; Wang, G.; Muhammad, T. Supported Co_3O_4-CeO_2 Catalysts on Modified Activated Carbon for CO Preferential Oxidation in H 2-Rich Gases. *Appl. Catal. B Environ.* **2012**, *119–120*, 62–73.

(342) Potemkin, D. I.; Filatov, E. Y.; Zadesenets, A. V.; Gorlova, A. M.; Nikitina, N. A.; Pichugina, D. A. A Comparative Study of CO Preferential Oxidation over Pt and $Pt_{0.5}Co_{0.5}$ Nanoparticles: Kinetic Study and Quantum-Chemical Calculations. *Mater. Lett.* **2020**, *260*, 126915.

(343) Barroso-Martín, I.; Alberoni, C.; Rodríguez-Castellón, E.; Infantes-Molina, A.; Moretti, E. Recent Advances in Photo-Assisted Preferential CO Oxidation in H_2-Rich Stream. *Curr. Opin. Green Sustain. Chem.* **2020**, *21*, 9–15.

(344) Groot, F. De. Multiplet Effects in X-Ray Spectroscopy. *Coordination Chemistry Reviews*. 2005.

(345) De Groot, F. High-Resolution X-Ray Emission and X-Ray Absorption Spectroscopy. *Chemical Reviews*. 2001, pp 1779–1808.

(346) Stavitski, E.; de Groot, F. M. F. The CTM4XAS Program for EELS and XAS Spectral Shape Analysis of Transition Metal L Edges. *Micron*. 2010, pp 687–694.

(347) Laverock, J.; Chen, B. B.; Preston, A. R. H.; Smith, K. E.; Wilson, N. R.; Balakrishnan, G.; Glans, P. A.; Guo, J. H. Electronic Structure of the Kagome Staircase Compounds $Ni_3V_2O_8$ and $Co_3V_2O_8$. *Phys. Rev. B - Condens. Matter Mater. Phys.* **2013**, *87*, 125133.

(348) Laverock, J.; Preston, A. R. H.; Chen, B.; McNulty, J.; Smith, K. E.; Piper, L. F. J.; Glans, P. A.; Guo, J. H.; Marin, C.; Janod, E.; et al. Orbital Anisotropy and Low-Energy

Excitations of the Quasi-One-Dimensional Conductor β-$Sr_{0.17}V_2O_5$. *Phys. Rev. B - Condens. Matter Mater. Phys.* **2011**, *84*, 155103.

(349) Ward, M. R.; Boyes, E. D.; Gai, P. L. In Situ Aberration-Corrected Environmental TEM: Reduction of Model Co_3O_4 in H_2 at the Atomic Level. *ChemCatChem* **2013**, *5* (9), 2655–2661.

(350) Van Steen, E.; Sewell, G. S.; Makhothe, R. A.; Micklethwaite, C.; Manstein, H.; De Lange, M.; O'Connor, C. T. TPR Study on the Preparation of Impregnated Co/SiO_2 Catalysts. *J. Catal.* **1996**, *162* (2), 220–229.

(351) Deng, W.; Tang, Q.; Huang, S.; Zhang, L.; Jia, Z.; Guo, L. Low Temperature Catalytic Combustion of Chlorobenzene over Cobalt Based Mixed Oxides Derived from Layered Double Hydroxides. *Appl. Catal. B Environ.* **2020**, *278*, 119336.

(352) Kosmala, T.; Calvillo, L.; Agnoli, S.; Granozzi, G. Enhancing the Oxygen Electroreduction Activity through Electron Tunnelling: CoOx Ultrathin Films on Pd(100). *ACS Catal.* **2018**, *8* (3), 2343–2352.

(353) Chen, J. G.; Eng, J.; Kelty, S. P. NEXAFS Determination of Electronic and Catalytic Properties of Transition Metal Carbides and Nitrides: From Single Crystal Surfaces to Powder Catalysts. *Catal. Today* **1998**, *43* (1–2), 147–158.

(354) Joachim Stöhr. *NEXAFS Spectroscopy*, Surface Sc.; Robert Gomer, Ed.; Springer, 1996.

(355) Biener, J.; Bäumer, M.; Madix, R. J.; Liu, P.; Nelson, E.; Kendelewisz, T.; Brown, G. Growth and Electronic Structure of Vanadium on α-Al_2O_3(0001). *Surf. Sci.* **2000**, *449* (1–3), 50–60.

(356) Chen, J. G. NEXAFS Investigations of Transition Metal Oxides, Nitrides, Carbides, Sulfides and Other Interstitial Compounds. *Surf. Sci. Rep.* **1997**, *30* (1–3), 1–152.

(357) Xing, M.; Kong, L. Bin; Liu, M. C.; Liu, L. Y.; Kang, L.; Luo, Y. C. Cobalt Vanadate as Highly Active, Stable, Noble Metal-Free Oxygen Evolution Electrocatalyst. *J. Mater. Chem. A* **2014**, *2* (43), 18435–18443.

(358) Chakrapani, K.; Bendt, G.; Hajiyani, H.; Lunkenbein, T.; Greiner, M. T.; Masliuk, L.; Salamon, S.; Landers, J.; Schlögl, R.; Wende, H.; et al. The Role of Composition of Uniform and Highly Dispersed Cobalt Vanadium Iron Spinel Nanocrystals for Oxygen Electrocatalysis. *ACS Catal.* **2018**, *8* (2), 1259–1267.

(359) Mu, C.; Mao, J.; Guo, J.; Guo, Q.; Li, Z.; Qin, W.; Hu, Z.; Davey, K.; Ling, T.; Qiao, S. Z. Rational Design of Spinel Cobalt Vanadate Oxide Co_2VO_4 for Superior Electrocatalysis. *Adv. Mater.* **2020**, *32* (10), 1–8.

(360) Nonaka, Y.; Shibata, G.; Koborinai, R.; Ishigami, K.; Sakamoto, S.; Ikeda, K.; Chi, Z.; Koide, T.; Tanaka, A.; Katsufuji, T.; et al. Electronic States and Possible Origin of the

Orbital-Glass State in a Nearly Metallic Spinel Cobalt Vanadate: An x-Ray Magnetic Circular Dichroism Study. *Phys. Rev. B* **2018**, *97* (20), 1–7.

(361) Bora, D. K.; Cheng, X.; Kapilashrami, M.; Glans, P. A.; Luo, Y.; Guo, J. H. Influence of Crystal Structure, Ligand Environment and Morphology on Co L-Edge XAS Spectral Characteristics in Cobalt Compounds. *J. Synchrotron Radiat.* **2015**, *22*, 1450–1458.

(362) Liu, B.; Glass, E. N.; Wang, R. P.; Cui, Y. T.; Harada, Y.; Huang, D. J.; Schuppler, S.; Hill, C. L.; De Groot, F. M. F. Cobalt-to-Vanadium Charge Transfer in Polyoxometalate Water Oxidation Catalysts Revealed by 2p 3d Resonant Inelastic X-Ray Scattering. *Phys. Chem. Chem. Phys.* **2018**, *20*, 4554–4562.

(363) Wang, Q.; Madix, R. J. Preparation and Reactions of V 2 O 5 Supported on TiO 2 (1 1 0). **2001**, *474*, 3–6.

(364) Go, D.; Romanyshyn, Y.; Sturm, J. M.; Naschitzki, M.; Kuhlenbeck, H.; Freund, H. Growth and Characterization of Ultrathin V_2O_y ($y \approx 5$) Films on Au (111) Se. **2008**, No. 111, 12363–12373.

(365) Silversmit, G.; Depla, D.; Poelman, H.; Marin, G. B.; Gryse, R. De. Determination of the V2p XPS Binding Energies for Different Vanadium Oxidation States (V^{5+} to V^{0+}). **2004**, *135*, 167–175.

(366) Beke, S. A Review of the Growth of V_2O_5 Films from 1885 to 2010. *Thin Solid Films* **2011**, *519* (6), 1761–1771.

(367) Maganas, D.; Roemelt, M.; Weyhermüller, T.; Blume, R.; Hävecker, M.; Knop-Gericke, A.; Debeer, S.; Schlögl, R.; Neese, F. L-Edge X-Ray Absorption Study of Mononuclear Vanadium Complexes and Spectral Predictions Using a Restricted Open Shell Configuration Interaction Ansatz. *Phys. Chem. Chem. Phys.* **2014**, *16* (1), 264–276.

(368) Hävecker, M.; Knop-Gericke, A.; Mayer, R. W.; Fait, M.; Bluhm, H.; Schlögl, R. Influence of the Geometric Structure on the V L3 near Edge X-Ray Absorption Fine Structure from Vanadium Phosphorus Oxide Catalysts. *J. Electron Spectros. Relat. Phenomena* **2002**, *125* (2), 79–87.

(369) Taftø, J.; Krivanek, O. L. Site-Specific Valence Determination by Electron Energy-Loss Spectroscopy. *Phys. Rev. Lett.* **1982**, *48* (8), 560–563.

(370) Maganas, D.; Roemelt, M.; Hävecker, M.; Trunschke, A.; Knop-Gericke, A.; Schlögl, R.; Neese, F. First Principles Calculations of the Structure and v L-Edge X-Ray Absorption Spectra of V_2O_5 Using Local Pair Natural Orbital Coupled Cluster Theory and Spin-Orbit Coupled Configuration Interaction Approaches. *Phys. Chem. Chem. Phys.* **2013**, *15* (19), 7260–7276.

(371) Papaefthimiou, V.; Tournus, F.; Hillion, A.; Khadra, G.; Teschner, D.; Knop-Gericke, A.; Dupuis, V.; Zafeiratos, S. Mixing Patterns and Redox Properties of Iron-Based Alloy Nanoparticles under Oxidation and Reduction Conditions. *Chem. Mater.* **2014**, *26* (4),

1553–1560.

(372) Chenakin, S. P.; Szukiewicz, R.; Barbosa, R.; Kruse, N. Surface Analysis of Transition Metal Oxalates: Damage Aspects. *J. Electron Spectros. Relat. Phenomena* **2016**, *209*, 66–77.

(373) Chenakin, S.; Kruse, N. XPS Characterization of Transition Metal Oxalates. *Appl. Surf. Sci.* **2020**, *515*, 146041.

(374) Kuld, S.; Thorhauge, M.; Falsig, H.; Elkjær, C. F.; Helveg, S.; Chorkendorff, I.; Sehested, J. Quantifying the Promotion of Cu Catalysts by ZnO for Methanol Synthesis. *Science (80).* **2016**, *352* (6288), 969–974.

(375) Baidya, T.; Murayama, T.; Bera, P.; Safonova, O. V.; Steiger, P.; Katiyar, N. K.; Biswas, K.; Haruta, M. Low-Temperature CO Oxidation over Combustion Made Fe- and Cr-Doped Co_3O_4 Catalysts: Role of Dopant's Nature toward Achieving Superior Catalytic Activity and Stability. *J. Phys. Chem. C* **2017**, *217*, 15256−15265.

(376) Moltved, K. A.; Kepp, K. P. The Chemical Bond between Transition Metals and Oxygen: Electronegativity, d-Orbital Effects, and Oxophilicity as Descriptors of Metal-Oxygen Interactions. *J. Phys. Chem. C* **2019**, *123*, 18432–18444.

(377) Védrine, J. C.; Fechete, I. Heterogeneous Partial Oxidation Catalysis on Metal Oxides. *Comptes Rendus Chim.* **2016**, *19*, 1203–1225.

(378) Tang, C. W.; Wang, C. Bin; Chien, S. H. Characterization of Cobalt Oxides Studied by FT-IR, Raman, TPR and TG-MS. *Thermochim. Acta* **2008**, *473* (1–2), 68–73.

(379) Wang, X.; Du, L. Y.; Du, M.; Ma, C.; Zeng, J.; Jia, C. J.; Si, R. Catalytically Active Ceria-Supported Cobalt– Manganese Oxide Nanocatalysts for Oxidation of Carbon Monoxide. *Phys. Chem. Chem. Phys.* **2017**, *19* (22), 14533–14542.

(380) Liu, J.; Ji, Y.; Nai, J.; Niu, X.; Luo, Y.; Guo, L.; Yang, S. Ultrathin Amorphous Cobalt-Vanadium Hydr(Oxy) Oxide Catalysts for the Oxygen Evolution Reaction. *Energy Environ. Sci.* **2018**, *11* (7), 1736–1741.

(381) Ghiyasiyan-Arani, M.; Masjedi-Arani, M.; salavati-Niasari, M. Size Controllable Synthesis of Cobalt Vanadate Nanostructures with Enhanced Photocatalytic Activity for the Degradation of Organic Dyes. *J. Mol. Catal. A Chem.* **2016**, *425*, 31–42.

(382) Stoeffler, D. First Principle Study of the Origin of the Large Orbital Magnetic Moment in A−CoV_2O_6. *Thin Solid Films* **2014**, *563*, 24–27.

(383) Davo, A.; Anderson, J. A. Role of Hydroxyl Groups in the Preferential Oxidation of CO over Copper Oxide − Cerium Oxide Catalysts Agust í n Bueno-Lo P. **2016**.

(384) Tang, C.; Sun, J.; Yao, X.; Cao, Y.; Liu, L.; Ge, C.; Gao, F.; Dong, L. Efficient Fabrication of Active CuO-CeO_2/SBA-15 Catalysts for Preferential Oxidation of CO by Solid State Impregnation. *Appl. Catal. B Environ.* **2014**, *146*, 201–212.

(385) Schumacher, B.; Denkwitz, Y.; Plzak, V.; Kinne, M.; Behm, R. J. Kinetics, Mechanism, and the Influence of H_2 on the CO Oxidation Reaction on a Au/TiO_2 Catalyst. *J. Catal.* **2004**, *224* (2), 449–462.